Faculty of Engineering
Kingston University London

PHD THESIS

Academic Year 2006 – 2009

Hessammaddin Ghasemnejad

Effects of Delamination Failure in Crashworthiness of Laminated Composite Box Structures

Director of Study:

Dr. Homayoun Hadavinia

November 2009

This thesis is submitted in partial fulfilment of the requirements
for the degree of Doctor of Philosophy

Abstract

The brittle nature of the most of fibre reinforced polymer (FRP) composites causes they show high capability in absorbing the impact energy in vehicular structures. This energy absorption is introduced by various fracture mechanisms. In this regard, the fracture study is one of the most important areas to be considered in investigating the energy absorption capability of composite box structures.

Various fracture mechanisms such as fibre breakage and buckling, matrix cracking and crushing, debonding at the fibre-matrix interface and especially plies delamination play important roles in progressive failure mode and energy absorption of composite tubes. Delamination occurs as results of shear and tensile separation between fronds. The main objective of this research is to study the effects of interlaminar fracture toughness on the progressive energy absorption of composite structures under quasi-static loading. In this regard, Mode-I, Mode-II and mixed-Mode I/II interlaminar fracture toughness of various types of FRP composites with various laminate designs are studied experimentally to investigate the relationship between interlaminar crack propagation and the energy absorption capability and crushing modes of composite structural elements.

Plan view of crushed CFRP and GFRP composite box struts

The combination of brittle fracture, lamina bending, local buckling and transverse shearing crushing modes was found from experimental studies. New analytical solutions based on friction, bending and fracture mechanisms were proposed to predict the mean crushing force for each of these failure modes. The crushing process of composite boxes was also simulated by finite element software LS-DYNA and the results were verified with the relevant experimental and analytical results.

Lovingly dedicated to my Parents

Acknowledgement

I would like to express my deepest gratitude to Dr. Homayoun Hadavinia for his encouragement, valuable advice, and guidance through my research work.

I would like to particularly thank Dr. Akbar Aboutorabi for his support and great friendship along these past three years. Great thanks also to Dr George Simpson for providing helpful suggestions.

I express my special thanks to engineering officers, Mr Dean Wells, Mr Alex Vine & Mr Colin Bradsell for their availability and technical advice.

I also wish best of luck to my friends Benjamin, James & Karl for their future career.

Last but not least, I am deeply grateful to my parents for their continuous support and encouragement.

Table of contents

List of Figures

Chapter 4

List of Tables

Chapter 1:

Introduction & Objective

Nomenclature

ADCB	asymmetric double-cantilever beam
a	crack length
a_e	effective crack length
b	side of box
C	compliance
CFE	crush force efficiency
CFRP	carbon fibre reinforced plastic
DCB	double-cantilever beam
3ENF	three-point-end-notched flexure
E	Young's modulus
F	load
F_{max}	initial maximum load
F_m	mean load
G_{12}	shear modulus
G_{IC}	Mode-I interlaminar fracture toughness
G_{IIC}	Mode-II interlaminar fracture toughness
GFRP	glass fibre-reinforced polymer
h	ENF specimen half-thickness
L	half span of ENF specimen
SEA	specific energy absorption
t	crush box wall thickness
V_f	fibre volume fraction
U_e	external work
U_f	energy dissipated by friction

U_b energy dissipated in bending

U_{bu} energy dissipated in local buckling

U_{bf} energy dissipated by bundle fracture

U_c energy dissipated in axial splitting

U_d energy dissipated by delamination

U_s energy dissipated in shear deformation

$U_{LB/BF}$ energy dissipated for lamina bending/brittle fracture crushing modes

$U_{BU/TS}$ energy dissipated for local buckling/transverse shearing crushing modes

x sliding distance on the platen

Y geometry factor

z crushing distance

ν Poisson's ratio

λ crush length of a single stroke

β weight factor

μ coefficient of friction

δ displacement

σ_u ultimate tensile stress

σ_b flexural strength

τ_s shear strength

θ fibre orientation

φ semi-angle of the wedge

Δ crack length correction factor in DCB test

1. Introduction

Crashworthiness of fibre-reinforced polymer (FRP) composite materials and structures is classified on how they deform, fail and absorb the crashing energy in a controllable behaviour. The high energy absorbing capabilities of fibre reinforced polymer composite (FRP) materials is one of the main factors in their application in high performance automotives and airframe substructures. They also provide other functional and economic benefits such as enhanced strength, durability, weight reduction and hence lower fuel consumption. For structural vehicle crashworthiness, FRP composites are able to collapse in a progressive, controlled manner which results in high specific energy absorption in the event of a crash. Unlike metals and polymers, the progressive energy absorption of composite structures is dominated by extensive micro-fracture instead of plastic deformation. In this Chapter the frame work of research and research objectives are explained in detail.

1.1. Frame work of research

Various fracture mechanisms such as fibre breakage and buckling, matrix cracking and crushing, debonding at the fibre-matrix interface and especially plies delamination play important roles in progressive failure mode and energy absorption of composite tubes. Delamination occurs as a result of shear and tensile separation between fronds. The main objective of this research is to study the effects of interlaminar fracture toughness on the progressive energy absorption of composite structures under quasi-static loading. In this regard, Mode-I, Mode-II and mixed-Mode I/II interlaminar fracture toughness of various types of FRP composites with various laminate designs are studied experimentally to investigate the relationship between interlaminar crack propagation and the energy absorption capability and crushing modes of composite structural elements.

The combination of brittle fracture, lamina bending, local buckling and transverse shearing crushing modes was found from experimental studies. New analytical solutions based on friction, bending and fracture mechanisms were proposed to predict the mean crushing force for each of these failure crushing modes. The crushing process of composite boxes was also simulated by finite element software LS-DYNA and the results were verified with the relevant experimental and analytical results.

1.2. Research objective

The main objective of this research is to investigate the effect of interlaminar fracture toughness on the energy absorption of composite box structures in a crashing event. New analytical models were introduced to predict the mean crushing force in each progressive failure mode of composite box components.

The main goals of this work can be summarised as follows,

- Effect of Mode-I interlaminar fracture toughness on the progressive crushing of composite box,
- Effect of Mode-II interlaminar fracture toughness on the progressive crushing of composite box,
- Effect of mixed-Mode-I/II interlaminar fracture toughness on the off-axis crushing of composite box,
- Energy absorption and progressive crushing behaviour of hybrid composite box structures,
- Theoretical prediction of mean crushing force in progressive failure of FRP composite box structures;
- Finite Element analysis of progressive failure crushing of composite box structures in LSDYNA.

1.3. Thesis structure

This section presents a concise overview of the different chapters appearing in this thesis.

Chapter 2: *Literature Review*

The energy absorption capabilities of composite tubular structures are generally reviewed in this chapter. The influence of various parameters such as material selection, laminate design, impact speed, structural geometry, strain rate sensitivity and all failure collapse mechanisms are discussed in detail.

Chapter 3: *Mode-I interlaminar fracture toughness and energy absorption of composite box structures*

This chapter mainly focuses on the effect of fibre orientation and stacking sequence on G_{IC} and SEA. The manufacture and testing of DCB and crush box specimens is described with different lay-ups of composite material *i.e.* GFRP and CFRP but with the same geometry. The experimental results are compared together to find the relationship between G_{IC} and SEA.

Chapter 4: *Mode-II interlaminar fracture toughness and energy absorption of composite box structures*

This chapter is in continuation of Chapter-3 to study the effect of fibre orientation and stacking sequence on Mode-II interlaminar fracture toughness, G_{IIC}, and specific energy absorption, SEA. The manufacture and testing of 3-ENF and crush box specimens is described with different lay-ups of woven CFRP and GFRP composite material. The experimental results are compared together to find the relationship between G_{IIC} and SEA.

Chapter 5: *Mixed-Mode I/II interlaminar fracture toughness and off-axis crashworthiness of composite box structures*

This chapter contains a description of work to investigate the energy absorption capability of woven GFRP composite box under various off-axis crushing loadings.

In this regard, the effect of delamination cracks growth in Mode-II, G_{IIC}, and Mixed-Mode I/II, $G_{I/IIC}$, was investigated on the specific energy absorption, SEA. The manufacture and testing of 3-ENF and ADCB and crush box specimens is described with different lay-ups of woven GFRP composite material. The experimental results are compared together to find the relationship between delamination crack growth in Mode-II and mixed-Mode-I/II and SEA.

Chapter 6: *Effects of delamination failure in crashworthiness analysis of hybrid composite box structures*

This chapter contains a description of work carried out to investigate the effects of delamination failure of hybrid composite box structures to examine their crashworthy behaviour compared to pure ones. In this work the combinations of twill-weave and unidirectional CFRP composite materials are used to laminate the composite boxes.

Chapter 7: *Theoretical prediction of mean crushing force in progressive failure of composite box structures*

In this chapter a theoretical prediction based on friction, bending and fracture mechanisms to predict the mean crushing force for the combination of failure crushing modes is proposed.

Chapter 8: *Finite Element analysis of progressive failure crushing of composite box structures.*

In this chapter an analysis and investigation of the crushing characteristics of thin-walled GFRP and CFRP composite crush components, by simulating the response of composite box subjected to quasi-static axial and off-axis compression loading, using LS-DYNA finite element code is described.

Chapter 9: *Conclusion and future work*

In this chapter the accomplishments and contribution to knowledge of the work described in this thesis are summarised. At the end suggestions for different ways of possible future research continuing from this work are proposed.

Chapter 2:

Literature Review

1. Introduction

The present chapter is mainly focused on the literature review of principals of composite material structures and also previous researches related to crashworthiness of composite tubular structures.

2. Research objective

Crashworthiness of fibre-reinforced polymer (FRP) composite materials and structures is classified on how they deform, fail and absorb the crashing energy in a controllable behaviour. The high energy absorbing capabilities of fibre reinforced polymer composite (FRP) materials is one of the main factors in their application in high performance automotives and airframe substructures (see Figure 2.1). This energy absorption is accompanied by various intralaminar and interlaminar fracture mechanisms. In this regard, the fracture based on delamination growth study is one of the most important areas to be considered in investigating the energy absorption capability of composite structures. Various fracture mechanisms such as fibre breakage and buckling, matrix cracking and crushing, debonding at the fibre-matrix interface and especially plies delamination play important roles on progressive failure mode and energy absorption of composite structures. Delamination occurs as results of shear and tensile separation between fronds.

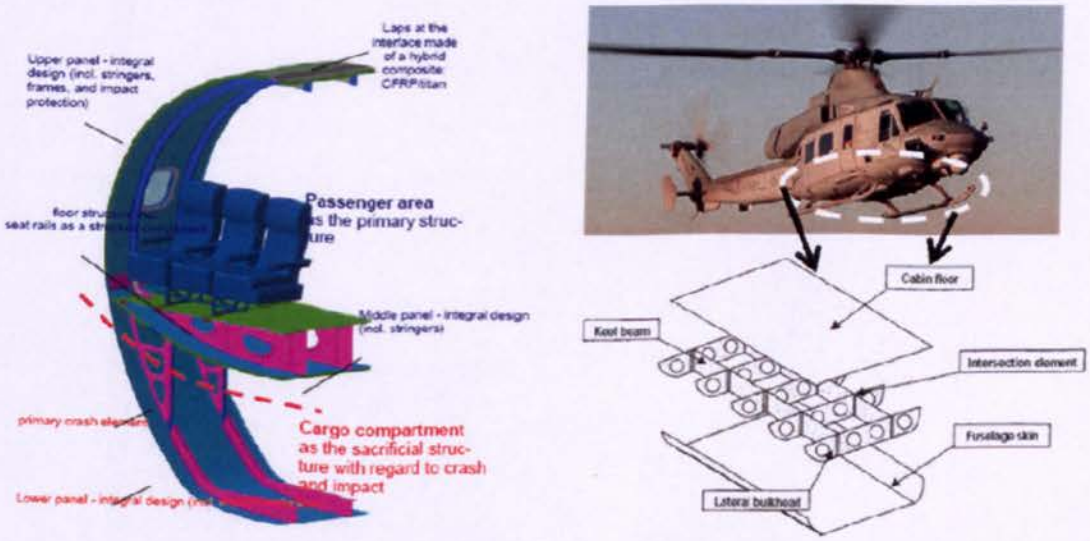

Fig. 2.1. Crashworthiness of FRP composite airframe substructures [2].

The main objective of this research is to study the effects of interlaminar fracture toughness on the progressive energy absorption of composite structures under quasi-static loading. In this regard, Mode-I, Mode-II and mixed-Mode I/II interlaminar fracture toughness of various FRP composites with different laminate designs are studied experimentally to investigate the relationship between interlaminar crack propagation and the energy absorption capability and crushing modes of composite box structures.

The combination of brittle fracture, lamina bending, local buckling and transverse shearing crushing modes was found from experimental studies. New analytical solutions based on friction, bending and fracture mechanisms were proposed to predict the mean crushing force for each of these failure modes. The crushing process of composite boxes was also investigated by explicit finite element software LS-DYNA and the results were verified with the relevant experimental and analytical results.

2.1. Energy absorption capability of composite materials

Collapsible impact energy absorbers made of fibre reinforced composite materials are structural elements used in a broad range of automotive and aerospace applications, since they provide considerable functional and economic benefits such as enhanced strength and durability, weight reduction and lower fuel consumption. Moreover, they have been found to ensure an enhanced level of structural vehicle crashworthiness, being capable of collapsing progressively in a controlled manner that ensures high crash energy absorption in the event of a sudden collision.

In contrast to the response of metals and polymers however, progressive crushing of composite collapsible energy absorbers is dominated by extensive fracture mechanisms instead of plastic deformation [1-3].

The main advantages of fibre reinforced composite materials over more conventional isotropic materials, however, are the very high specific strengths and vary the variety of fibre, matrix and fibre orientation to produce composites with improved material properties.

There are several ways to absorb the impact energy. Deformation of solids is the most common; usually energy is absorbed in plastic flow, although appreciable amounts of energy can also be absorbed in controlled brittle fracture. Absorbers can be reusable like a hydraulic damper; rechargeable with the energy absorbing component being replaced in a permanent

container; or expandable, as in the collapse of a vehicle structure during a crash. Composite materials have significant potential for absorbing kinetic energy during a crash. The energy absorbers application depends on the type of impact force. This can be distributed over the whole of the impact body, as in explosion loading, or it can be localized, with a small or pointed body hitting a large one. The large body may deform in an overall manner in the same way as if the load were distributed, or the small body may penetrate it locally.

The energy absorption capability of composite materials offers an exceptional combination of reduced structural weight and improved vehicle safety by higher or at least equivalent crash resistance compared with metal structures. Crash resistance covers the energy absorbing capability of crushing structural parts as well as the demand to supply a protective shell around vehicle occupants. The basic principle of occupant crash protection has been used in the automotive field since the early 1950s, and crash safety has meanwhile become a well-established car design requirement. In aeronautics, the first structural design requirements for better crash protection were studied for military helicopters and light fixed-wing aircraft in the form of the aircraft crash survival design guide [5]. In aerospace application the material structures considered are higher-performance types such as epoxy resins reinforced with glass fibres and, increasingly, aramid and carbon fibres on hybrids composites. In the automotive area reinforced polymers must satisfy a complex set of design requirements-among others the crash energy absorption management in the front-end and side structures of cars [6-7].

2.2. Impact speed

The impact speeds can be divided generally to three main ranges, as can be seen in Figure 2.2. These ranges are relevant to general interest for energy dissipation. At speeds between 1 to 15 m s^{-1}, impact behaviour can be related to static or vibration behaviour. At speeds in this range large objects with weights measured in tonnes can possibly be stopped without departing from normal methods of construction. The survivable vehicle accident is an example for this range with the purpose to stop the crashing vehicle without damaging or releasing its components.

At speeds from 150 to 1500 m s^{-1}, dynamic effects make impact manner significantly different from static manner. Thus, material properties can probably be related to their static properties. This range covers the conventional terminal ballistics with bullets, bombs and

shells. Regarding the density of rigid objects, weight can be varied from a few grams to a few hundred kilograms, which need to be stopped without excessive damage to the target.

The last range is related to speeds from 3000 to 30000 m s^{-1}. In this case the material behaviour is completely different from static behaviour. Materials are vaporized and solid flows as liquids. This range includes jets of liquid metal from shaped explosive charges penetrating heavy armour, and micrometeorites impacting lightly constructed spacecraft [4].

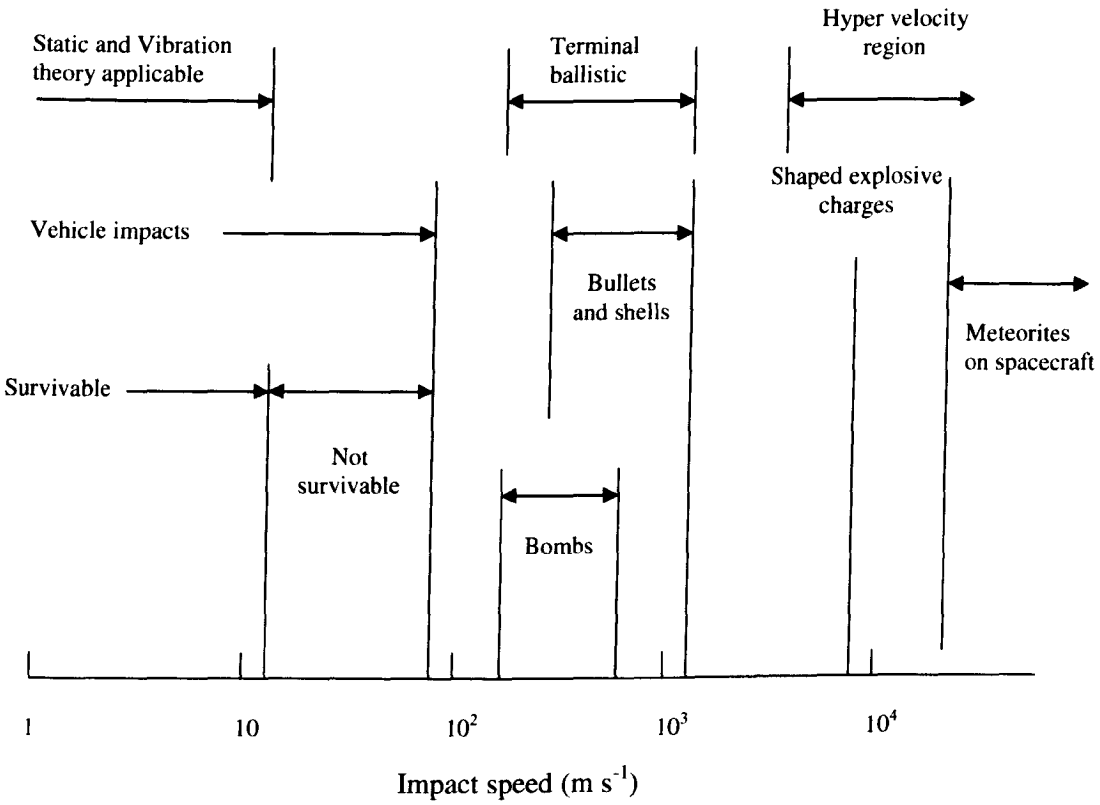

Fig. 2.2. Impact speeds for energy absorbers [4].

2.3. Valuation criteria for crushing behaviour

There are many important variables which must be considered in the study of energy absorption capabilities. These include material; manufacturing method; microstructure; geometry of specimen, including any crush initiator used; and rate of crush. One of the most important parameters is the specific energy absorption (SEA) performance of collapsing or crushing material specimens or structural parts. This value is related to the absorbed energy compared to the mass of the absorber or structure. Thus, it is an important criterion for lightweight designs. Another important factor in the study of energy absorption for energy management capabilities is the shape of the force-crush distance curve. One measure which is used to characterise the shape of the curve is called crush-force efficiency (CFE). This value relates the average crush force (F_m) to the maximum force (F_{max}) of the crush characteristic. The highest force occurs normally at the initiation phase. An absorber with a rectangular-shaped force-crush distance curve and theoretical maximum energy absorption has a crush force efficiency of 100%. One does not want the maximum force to be much greater than the average crush force, because the goal in energy management is to absorb all the energy without imparting large force to the passengers.

Stroke efficiency (SE) is another parameter in energy absorption management which is defined as the ratio of the stroke at bottoming out to the initial length of the absorbers, and high ratio indicates efficient use of the material.

2.4. Properties and applications of fibre-reinforced plastics (FRP)

Density, stiffness and strength are the most important properties of fibre-reinforced plastic (FRP), and these would definitely be the design drivers for materials' selection for transport applications such as aircraft, motor vehicles and trains [8]. A fibrous reinforcement is characterised by its length being much greater than its cross section dimensions. Hence, the ratio of length to a cross-section dimension, known as the aspect ratio can vary significantly. In single-layer composites long fibres with high aspect ratios give what are called continuous fibre-reinforced composites, whereas discontinuous fibre composites are fabricated using short fibres of low aspect ratio [8]. Figure 2.3 illustrates a generally employed classification scheme for composite materials which utilises this description for the reinforcement.

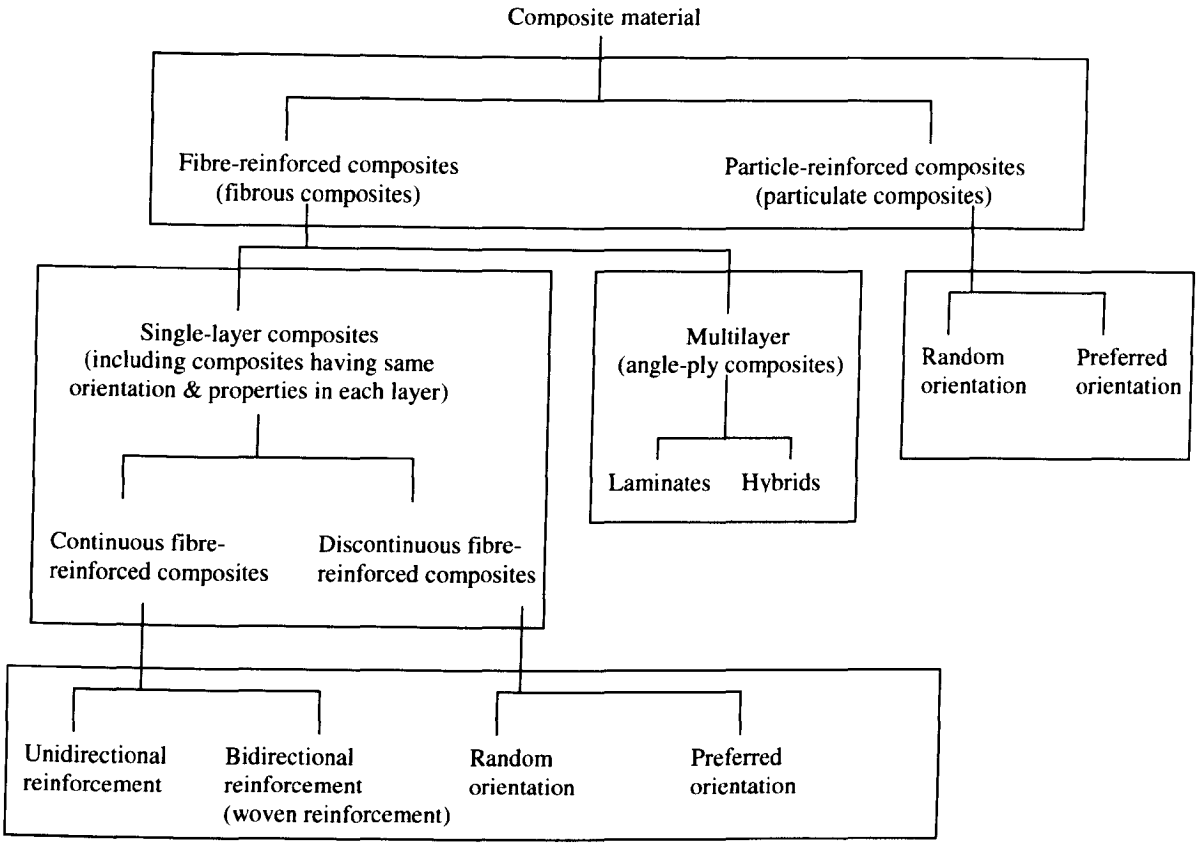

Fig. 2.3. Classification of composite materials [8].

2.4.1. Synthetic inorganic fibres

Glass and carbon are two of the most important synthetic inorganic fibres. Glass is a non-crystalline material with a short-range network structure. As such it has no unique microstructure and the properties, which are determined mainly by composition and surface finish, are isotropic. There are many groups of glasses, for example silica, oxynitride, phosphate and halide glasses, but currently in composite technology only the silica glasses are important. Carbon has two common crystalline forms (diamond and graphite), but it also exists in quasi-crystalline and glassy states. In fibre technology, graphite is the most important structural form of carbon. The graphitic structure consists of strongly bonded hexagonal layers, which are called the basal planes, with weak interlayer van der Waals bonds [8].

2.4.2. Polymer matrix

Polymer materials are the most common matrix material for composites. Polymers are categorised to three classes of thermosets, thermoplastics and rubbers. There are two main reasons for this category. Firstly, in general the mechanical properties of polymers are insufficient for many structural purposes. In particular their strength and stiffness are low compared with metals and ceramics. This means that there is a considerable benefit to be gained by reinforcing polymers, and the reinforcement does not have to have special properties. Secondly, and most essentially, the processing of polymer matrix composites (PMCs) need not involve high pressure and does not require high temperatures. It follows that problems based on the degradation of the reinforcement during manufacture are less significant for PMCs than for composites with other matrices [8].

Thermosets such as epoxy, polyester, polyamide and phenolic are brittle at room temperature and have low fracture toughness values. Because of the cross-links, thermosets cannot be reheated and reshaped, thermosets just degrade on reheating, and in some cases may burn, but do not soften sufficiently for reshaping and they have better creep properties than thermoplastics. Resistance to chemical attack of thermosets is also more than most thermoplastics.

Thermoplastics such as acrylic, nylon (polyamide), polystyrene, polyethylene, polypropylene and polyetheretherketone (PEEK), flow under stress at elevated temperatures, which allows them to be fabricated into the required component, and become solid and keep their shape when cooled to room temperature [8].

2.5. Factors affecting the energy absorption capability

In this section several variables related to the energy absorption of composite thin-walled structural components are described. For the analysis and design of different structures which are subjected to various loads, studying the material behaviour is essential. In the case of composite materials it would be attractive to start the design with constituent material properties and arrive at the composite macromechanical properties through micromechanics analysis [3]. Regarding different applications of composite materials, their suitability is determined not only by the usual design parameters, but by their impact and energy absorbing properties.

However, composite material constituents of fibres and matrix and the design of laminate layup have a major effect on the crashworthiness capability of composite structures. Temperature is another important factor which has considerable effects on material crashworthy response.

2.5.1. Fibre and matrix materials

The vast majority of literatures on crashworthiness of composites are focused on fibres of carbon, glass or aramid in thermosetting resin such as epoxy. Farley [9], Thornton [10], Schmueser and Wickliffe [11] and Farley and Jones [12] all studied and compared the energy absorbing capabilities of various specimens made of carbon-epoxy, glass-epoxy and aramid-epoxy. Hybrid composites were investigated to optimise the energy absorption characteristics of different fibres into a single laminate. Thornton and Edwards [13] reported that glass-aramid and carbon-aramid hybrids cause an unstable collapse by folding which would not have otherwise occurred had the samples been composed of glass or carbon fibres alone. New fibre and matrix materials such as Dyneema PE fibre/carbon fibre hybrid [14] have been introduced to obtain ever higher values for specific energy absorption. The majority of these investigations have been carried out with thermosetting matrix materials, usually an epoxy. Other thermoplastic matrix materials such as polyester and polyetheretherketone (PEEK) have been used as matrix material [15-16].

Hamada *et al.* [16] studied the use of a thermoplastic polyetheretherketone (PEEK) matrix with a carbon fibre which gave an exceptionally high specific energy absorption value of 180 kJ/kg. This value of energy absorption is at least double the value of carbon-epoxy. This is attributed to the PEEK matrix offering a high resistance to crack growth between the fibres, preventing failure by this mode until the onset of stable progressive crushing. Nilson [17] reported in processing PEEK one can meet high pressures and temperatures and difficulty with fibre wet-out.

2.5.2. Laminate design

Various reports have been carried out to study the effect of laminate design on energy absorption of composite structures. Thornton and Edwards [13] showed in a stable collapse a $[45/45]_n$ lay-up developed consistently lower values of energy absorbing than $[0/90]_n$ lay-ups.

Farley [9] reported that in quasi-static tests on $[0/\pm\theta]$ carbon-epoxy circular tubes for $0^\circ < \theta < 45^\circ$, energy absorption decreasing as θ increased.

Furthermore, in $[0/\pm\theta]$ aramid-epoxy and glass-epoxy circular tubes for $45^\circ < \theta < 90^\circ$, the specific energy absorption generally increases with increasing θ. Schmueser and Wickliffe [26] showed variations in specific energy absorption of carbon-epoxy, glass-epoxy and aramid-epoxy $[0_2/\pm\theta]$ specimens all generally increase with increasing θ. Mamalis *et al.* [18] worked on various thin-walled circular and square tubes made of two different materials, and reported that specimens made of a commercial glass fibre and vinyester composite material which consists of nine plies in the sequence $[(90/0/2R_c)/(2R_c/0/90)/R_{c.75}]$, showed better energy absorption behaviour than those made of a fibreglass composite material in which the glass fibres were in the form of chopped-strand mat with random fibre orientation in the plane of the mat. Hamada *et al.* [15] reported that the specific energy absorption for 0° carbon / PEEK tubes was due to the high fracture toughness of PEEK.

2.5.3. Structural geometry

The effect of specimen geometry on the energy absorption capability was investigated by varying the various geometric parameters of the shells such as wall thickness, t, axial length, L, mean diameter, D, or circumference, C [3]. Farley [19] showed that the energy absorption capability is a non-linear function of diameter to thickness, D/t, ratio for carbon-epoxy and aramid-epoxy circular tubes. Furthermore, Farley [19] reported that carbon-epoxy tubes are dependent on D/t for tubes with various internal diameters. Mamalis *et al.* [1] indicated that the energy absorption of glass polyester circular tubes in static axial loading increases with increasing t/D. Thornton and Edwards [13] reported that the capability of square and rectangular cross-section tubes for energy absorption is less than circular ones. The main reason for reduction of energy absorption is generally attributed to corners response as stress concentration leading to the formation of splitting cracks.

Static crushing tests were conducted by Farley [19] on graphite/epoxy and Kevlar/epoxy square cross section tubes to study the influence of specimen geometry on the energy absorption capability and scalability of composite materials. It was found that the energy absorption generally increased with decreasing w/t. Czaplicki *et al.* [20] reported that energy absorption of tulip-triggered specimens was significantly higher than for bevel-triggered

specimens of the same geometry and material. Trigger mechanism can affect the crushing process. The most common type of crush initiator is an external bevel or chamfer ground into one end of the specimen [21].Various types of crush initiator are shown in Figure 2.4.

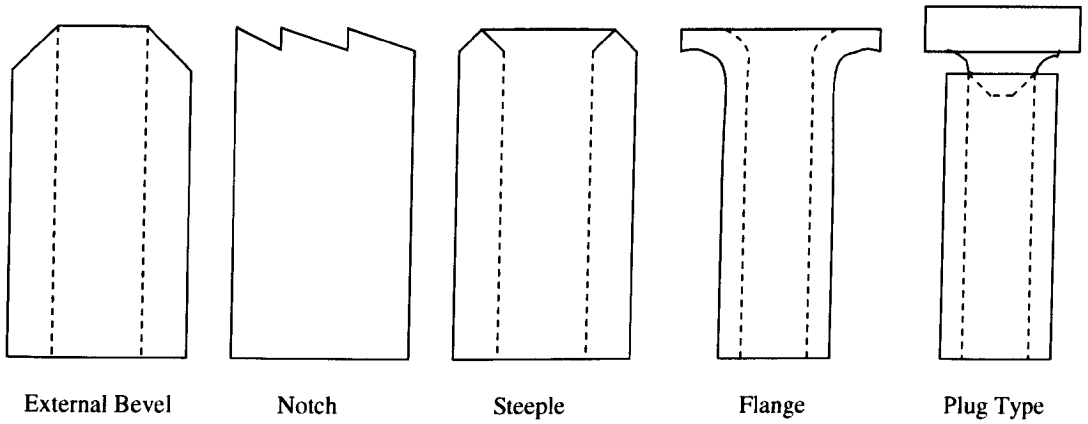

Fig. 2.4. Various types of trigger mechanism [21].

2.5.4. Strain rate sensitivity

Extensive works have been studied by many researchers to investigate the influence of strain-rate on energy absorption of composite thin-walled structures. Farley [22] showed that matrix stiffness and failure strain can be a function of strain-rate; therefore, the energy absorption related with interlaminar crack growth (delamination) may be considered as a function of crushing speed. He reported that the energy absorption in $[0/\pm\theta]_2$ carbon-epoxy tubes was not found to be a function of crushing speed, and also that the energy absorption in $[\pm\theta]_3$ carbon-epoxy specimen was found to be a weak function of crushing speed with an increase in energy absorption of as much as 35% over the speed range tested. Generally, the mechanical properties of brittle fibres are insensitive to strain-rate; therefore, interlaminar crack growth is not a function of crushing speed. Mamalis et *al.* [3] showed that the friction mechanisms which are developed between the composite material and the crushing surface and between the different new surfaces which are created after interlaminar crack growth are also affected by the strain-rate.

2.5.5. Impact of composite materials

In engineering application generally the loading classification are static, fatigue, high speed/rapid loading and impact. These loads are categorised according to the rise time of the load. For static loading this time is 3 times greater than the fundamental period of the mechanical system. Fatigue loading occurs when the rise time from one magnitude to another magnitude is greater than 3 times of the fundamental period. The time for high speed loading is between 1.5 to 3 times the fundamental periods of the mechanical system. The rise time for impact loading is less than 0.5 times the fundamental period of the mechanical system. Impact is an important area of applied mechanics which is strongly related to engineering practice, such as structural engineering, manufacturing engineering, aerospace engineering and material engineering. The application of impact is endless and has resulted in significant achievements both technically and economically [23].

The impact process may involve relatively high contact forces acting over a small area for a period of short time. Local strains generated at the point of contact between the two solids result in the absorption of energy. If energy absorption exceeds a threshold, the impact event can result in damage. When the projectile strikes a laminated composite, fracture processes such as delaminating, matrix cracking and fibre fracture frequently take place. Impact is defined for studying of force acting locally as a resulting of the impact event. The development of impact analysis was started with the establishment of a contact law [24], initially developed for the simple case of the impact of a beam by a steel sphere [25]. The contact law provides a relationship between the contact force and the indentation, defined as the difference between the displacement of the projectile and that of the back face of the laminate.

The first effect of impact loading is to produce some damage close to the surface of the laminate. However, the internal layers of the composite are damaged as well as the projectile penetrates into the laminate, the material stiffness changes locally [26]. The contact force cannot be assumed to be constant for all of the duration of the impact event [27]. From an observation of the indentation process on composite laminates, it was concluded that the loading and unloading phases exhibit different characteristics, and hence should be described by different laws [28]. Moreover, in an attempt to reproduce the real loading situation,

different projectile geometries were employed in order to measure the modifications of the reaction of the composite [29].

In a quasi-static model, the impact response is represented by a time-dependent force and the target composite is represented by an equivalent mass with equivalent stiffness [31]. However, to achieve an acceptable agreement between a model and the impact loading is sometimes difficult. A common problem is that impact loading can result in the generation of different forms of damage in the composite. All of these forms of damages should be considered, because all of them are likely to influence the residual mechanical properties of the material.

Future progress in understanding and predicting impact behaviour and in using composites in spite of their perceived impact properties will depend on one or more of the following [32]:

- Matching the design to the material and the proposed use.
- Careful control of the materials and manufacturing process, to preclude fibre movement during resin flow for instance, to give optimised properties.
- Numerical modelling of specific situations to extract any advantage from local fibre placement, modified resin properties, etc.
- Greater use of protective or sacrificial coatings for structures though at a loss of some mass efficiency.
- Incorporation of damage monitoring devices in critical structures.
- Third direction reinforcement even at the cost of reducing planar properties.
- Development of resins with an intrinsic strength and interfacial bond strength that match the transverse strength of the fibre, while remaining easily worked and not too expensive.

2.6. Woven composites

Woven composites introduce a different approach to the fabrication of thick sections for use in primary and secondary structural applications. Woven composites are shaped by

interlacing two mutually perpendicular sets of yarn. The lengthwise clothes are called warp and the crosswise clothes fill or weft (see Figure 2.5).

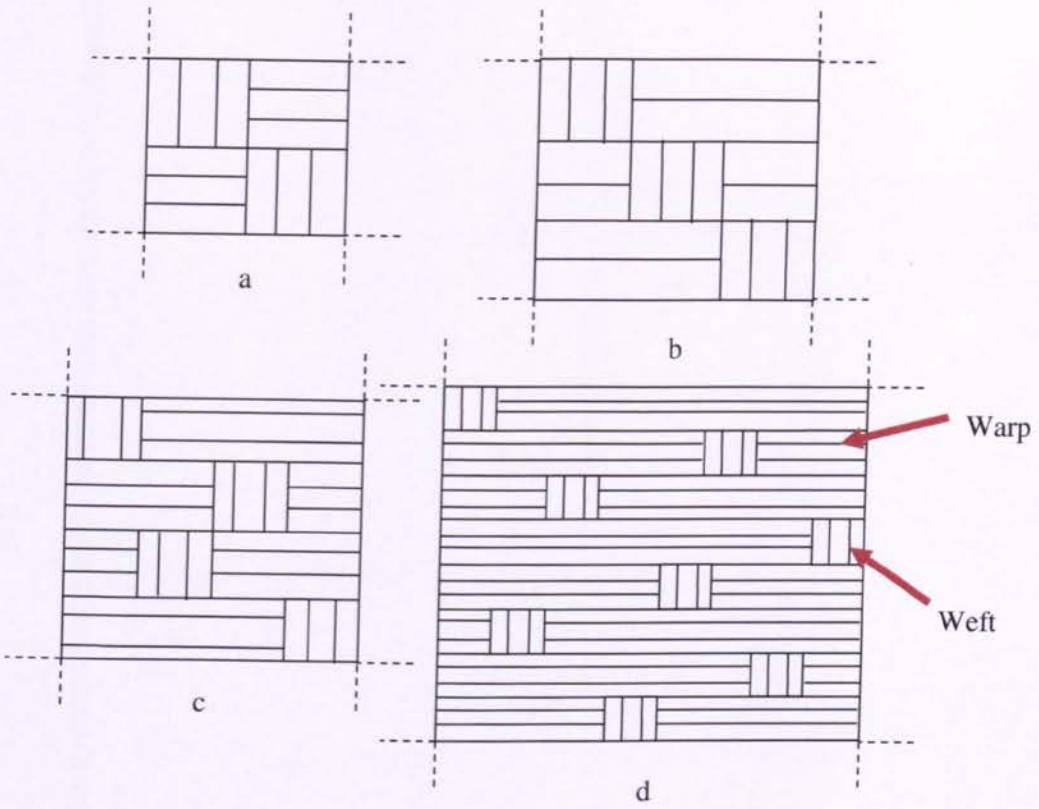

Fig. 2.5. 2D-Weave composites: (a) plain, (b) twill, (c) 4-harness, and (d) 8-harness.

The interlacing pattern of the warp and weft is known as the weave. Two-dimensional fundamental weaves are plain, twill and satin. These materials also provide more balanced properties in the fabric plane than a unidirectional laminate [32-35]. The interlacing of fibre bundles in woven composites can often increase out-of-plane strength as in the case of 3-dimentional woven fabrics. Woven fabrics are thicker than unidirectional lamina; therefore, fabrication of thick composites is less sensitive and less prone to assembly error. These properties are improved by introducing of in-plane stiffness and strength. The loss of in-plane stiffness and strength is dependent on the weave architecture.

This architecture is complex and therefore several parameters control the mechanical and thermal properties of woven composites. The mechanical properties of a woven composite cannot be accurately predicted using classical laminate theory. This is because many specific

factors, such as the type of weaving and the curvature and density of fibre bundles, need to be considered [36]. In addition, irregularity in manufacturing of the composite structure is more common in a woven composite, while they can be ignored in a non-woven laminate.

In brief, two approaches which are usually employed to study non-woven composite laminates are *micromechanics*, and *macromechanics*. The micromechanics study the mechanical properties of a laminate in details such as fibre, matrix and interface, while the macromechanics considers the material properties of laminate as a whole. Another approach which is an intermediate scale of study is called *mesomechanics*. This approach is provided to consider the mechanical properties of weave [37]. The major problem in studying mesomechanics is the large variety of textile performances that are employed (weaves, braids, knits, mats, the properties of weave stitched fabrics, two-dimensional or three dimensional).

2.7. Collapse Modes and Failure Mechanisms

Three main modes of brittle collapse, categorized as mode I, II and III, respectively, were studied in the series of static and dynamic axial compression tests of square tubes [38]. According to Hull classification [1] Euler overall column buckling or progressive folding with hinge formation were not found for fibre-reinforced plastic (FRP) composite tubes. Most of fibre-reinforced composites absorb energy through a combination of fracture and friction [39]. Catastrophic and progressive failures are the two main failure mechanisms of composite tube (see Figure 2.6). A stable progressive crush is established by localised failure that initiates at one end of the specimen and progresses through the specimen without significant damage past this crush front. To reach this failure mechanism, a crush initiator is used for FRP tubes. During catastrophic failure the initial maximum force is very high and drops rapidly, therefore the average force is low.

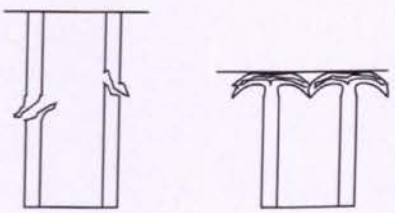

a b

Fig. 2.6. Typical collapse modes for composite tubes (a) catastrophic failure (b) progressive failure [39].

2.8. Failure mechanisms

a) *Macroscopic collapse modes*

According to Mamalis *et al.* [38] the failure modes observed are, in general, greatly affected by the shell geometry, the arrangement of the fibres, the properties of the matrix and fibres of the composite material and the stacking sequences. Furthermore, the following macroscopic collapse modes were classified by Mamalis *et al.* [38-40] from a very extensive experimental treatment of axisymmetric tubes of various geometries made of fibre-reinforced polymer matrix composite materials.

1. Progressive failure

Progressive crushing with microfragmentation of the composite material, associated with large amounts of crush energy, is designated as the first crushing mode (mode-I). This mode is characterised by the progressive end-crushing with laminate splaying of the tube starting at one end of the tested specimen, and the formation of continuous fronds which spread outwards and inwards.

2. Catastrophic failure

Brittle fracture of the component resulting in catastrophic failure with little energy absorption is designated either as Mode-II or Mode-III depended on the crack form. Mode-II is characterised by the development of a spiral or longitudinal crack propagation along the shell circumference. Mode-III is described as mid-length collapse mode, and characterised by the formation of circumferential fracturing of the specimens approximately equal to the mid-height of the shell into irregular shapes.

3. Progressive folding

Progressive folding and hinging similar to the crushing behaviour of thin-walled metal and plastic tubes showing a very low energy absorbing capacity is introduced as Mode-IV. Mamalis *et al.* [6, 7] also reported that the modes of collapse can be classified as stable and unstable collapse modes; and also, stable collapse modes show similar features to those obtained during the static loading of the same geometries.

b) *Microfracturing*

According to Mamalis *et al.* [38] in some applications a very small deformation could be considered as a failure, whereas in others only total fracture or separation constitutes failure. In the case of composite materials, internal material failure generally initiates before any change in its macroscopic appearance or behaviour is observed. Various fracture modes can be defined for a laminate composite.

These modes are divided into intralaminar and interlaminar fracture modes. The intralaminar mode consists of longitudinal matrix fracture, transverse matrix fracture, fibre-matrix debonding and fibre fracture, and the interlaminar mode which is called delamination, is described as separation of layers from one another (see Figure 2.7). The fracture mechanisms included depend upon the nature of the constituents, the architecture of the layers, and the mode of mechanical loading [41].

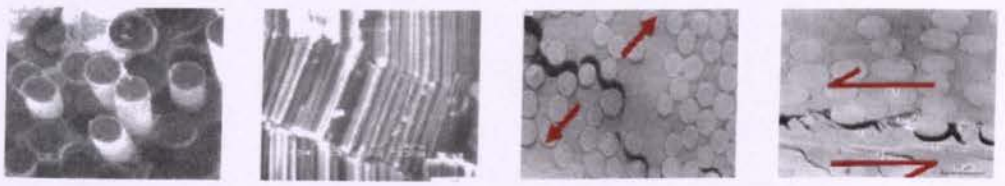

Longitudinal fracture of matrix | Fibre compressive failure –kink band | Matrix micro-cracking under transverse tension | Fibre/matrix debonding under shearing

a

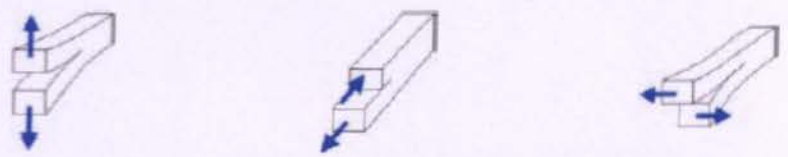

Delamination in Mode-I | Delamination in Mode-II | Delamination in Mode-III

b

Fig.2.7. Fracture mechanisms observed in laminates (a) Intralaminar, (b) Interlaminar Failures [41].

Mamalis *et al.* [4,5] reported that the main features of this microfracture mechanism of composite tubes are similar to that obtained for circular tubes. These microfracture mechanisms are:

- An annular wedge of highly fragmented material, forced down axially through the shell wall;

- An intrawall microcrack which develops ahead of the crush-zone at the apex of the annular wedge and propagates at a rate approximating the compression rate;
- Two continuous fronds, as a result of the plies delamination in the crush zone, mainly caused by the central bundle wedge which spreads radially inwards and outwards from the wall;
- A severely strained zone which extends between the central crack and the shell wall edges showing a combined tensile-compressive type of deformation.

Three main crushing modes in accordance with Farley and Jones [42] classification are categorised for progressive failure of composite box in crushing process as follows,

- Transverse shearing

The first one is transverse shearing (fragmentation) mode which is characterised by a wedge-shaped laminate cross section with one or multiple short interlaminar and longitudinal cracks. In this mechanism interlaminar crack propagation and bundle fracture control the energy absorption.

- Lamina bending

The second one is lamina bending mode which is shaped with long interlaminar, intralaminar, and parallel to fibre cracks. This mechanism causes the formation of continuous fronds which spread inwards and outwards. Friction and inter/intra laminar fracture controls the energy absorption of lamina bending mode. However, the combination of fragmentation and lamina bending modes is called brittle fracture mode. The highest energy absorption of composite tubes has been observed in combination of brittle fracture and lamina bending crushing mode.

- Local buckling

The local buckling crushing mode consists of the formation of local buckles by means of plastic deformation of the material. The post crushing integrity of ductile fibre-reinforced composites is a result of fibre and matrix plasticity without any fracture and fibre splitting. Brittle fibre-reinforced composites can exhibit the local buckling when the interlaminar stresses are small relative to the strength of the matrix, or the matrix has a higher failure strain than the fibre, and when the matrix exhibit plastic deformation under high stress.

The transverse shearing and lamina bending crushing modes are exhibited completely by brittle fibre-reinforced composites, whilst ductile fibre-reinforced composite materials show the local buckling crushing mode similar to that showed by ductile metals (see Figure 2.8).

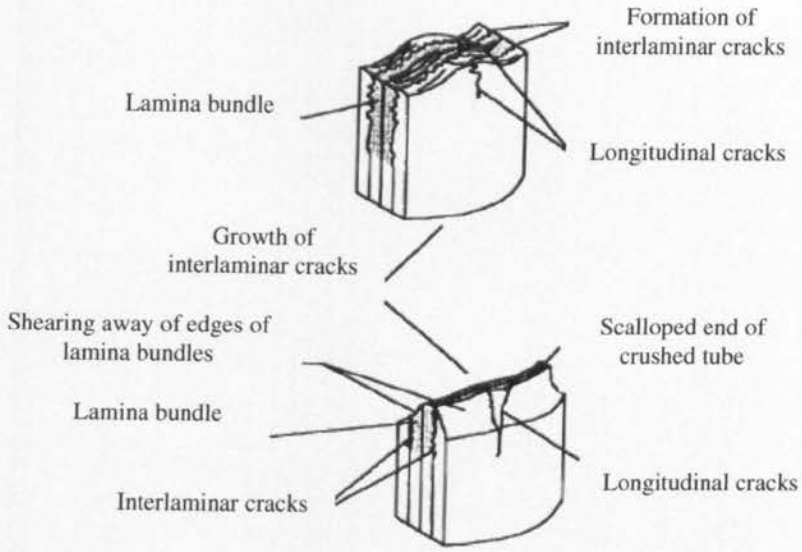
Formation of
interlaminar cracks
Lamina bundle
Longitudinal cracks
Growth of
interlaminar cracks
Shearing away of edges of
lamina bundles
Scalloped end of
crushed tube
Lamina bundle
Interlaminar cracks
Longitudinal cracks

a

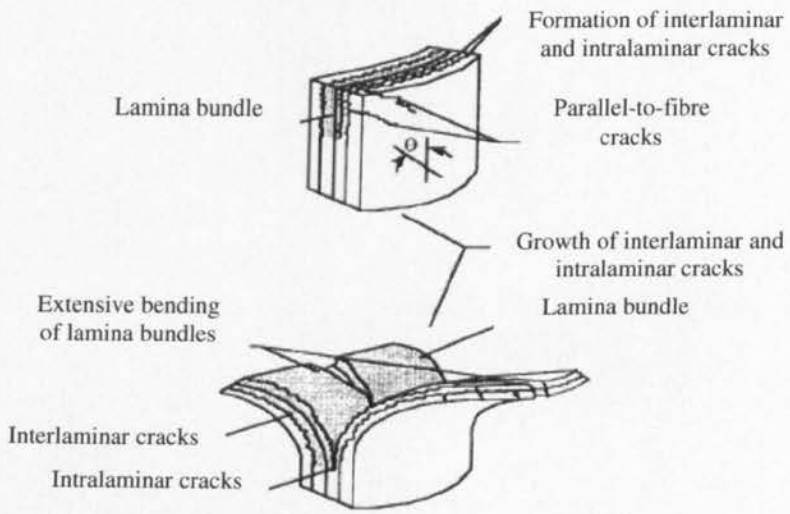
Formation of interlaminar
and intralaminar cracks
Lamina bundle
Parallel-to-fibre
cracks
Growth of interlaminar and
intralaminar cracks
Extensive bending
of lamina bundles
Lamina bundle
Interlaminar cracks
Intralaminar cracks

b

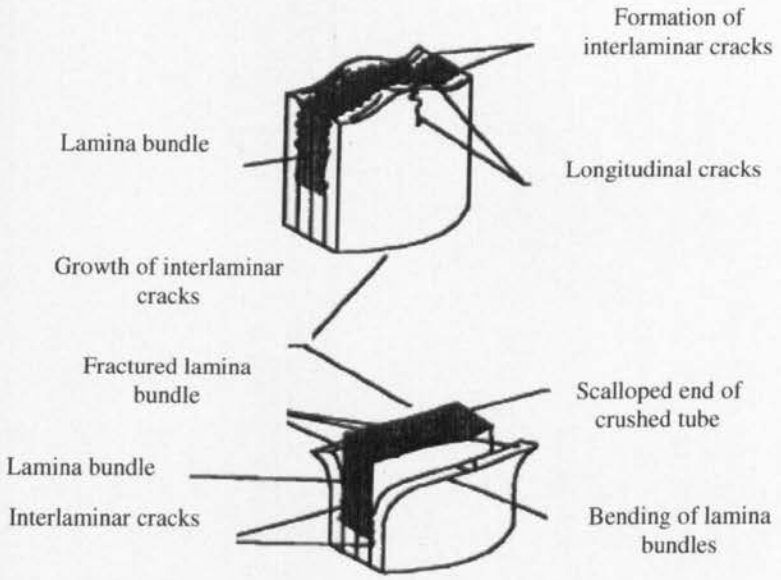

c

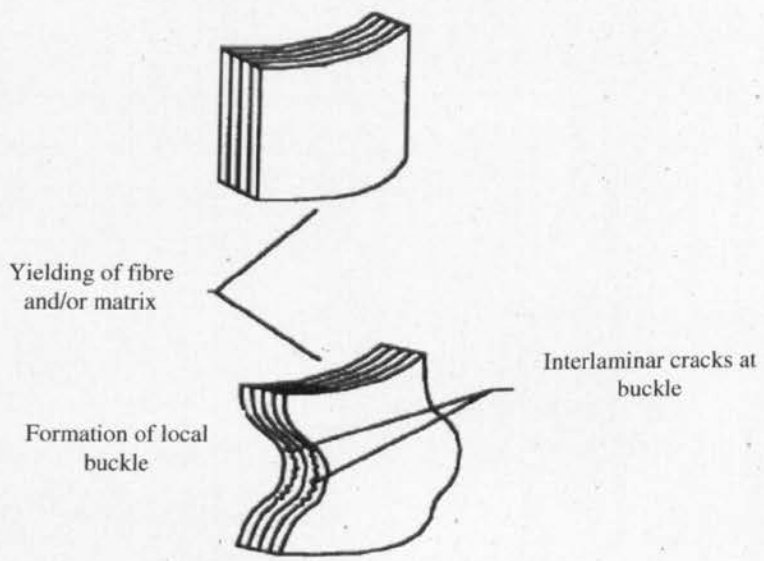

d

Fig. 2.8. (a) Transverse shearing crushing mode, (b) Lamina bending crushing mode, (c) Brittle fracture crushing mode, (d) Local buckling crushing mode [43].

2.9. Theoretical prediction of crushing energy

Various theoretical approaches have been proposed to study the energy absorption of static axial collapse of composite multi-layered shells. Farley and Jones [42] proposed the following simplified phenomena to model the crushing process:

- Friction between the annular wedge and the fronds and between the fronds and the platen of the press,
- Fronds bending,
- Crack propagation and,
- Axial splitting.

Mamalis *et al.* [44] introduced another analysis of composite circular tubes subjected to static axial compression which has been modified and used to analyse the collapse mechanism. Using this model the related energy absorbed during the axial crushing of the square tubes was estimated. According to Mamalis *et al.* [45], during the elastic deformation of the shell the load rises at a steady rate to a peak value, $F_{max.}$ At this stage, cracks of length, L_c, form at the four corners of the tube and propagate downwards along the tube axis, splitting the shell wall, and they are attended by the development of a circumferential central intrawall crack at the top end of the shell. It is assumed that the crack follows an ellipsis configuration. The maximum value of the crack length, L_c, is attained at the middle of each side of the square cross section and it is equal to the corresponding one observed in the case of the equivalent circular tube loaded under the same condition. The associated part of energy absorbed which equals the external work as can be achieved by measuring the area under the force-crush distance curve in the elastic regime is,

$$U_{LC} = 2.\left[\pi.L_C.\left(\frac{b}{2}\right)\right].R_{ad} + n.\left(\frac{t}{2}\right).G.L_C = \frac{1}{2}F_{\max}.s_1 \qquad (2.1)$$

where R_{ad} is fracture energy required to fracture a unit area of the adhesive at the interface between two adjacent layers calculated by applying fracture theory and,

b = Tube side width

n = Number of layers

t = Shell wall thickness

G = Fracture toughness

s_1 = Elastic crush distance

The energy required for the deformation mechanism regarding the history of the formation of the crush zone equals the external work absorbed by the deforming shell in this regime (see Figure 2.9),

$$U_{tr} = \left[2\int_0^{\varphi} \sigma_0 . L_s . \left(\frac{L_s}{2} \right) d\theta \right] . 4b = \int_{s_1}^{s_2} F . ds \qquad (2.2)$$

where

σ_0 = The normal stress applied by the wedge to frond,

L_S = The side length of the wedge inscribed to the bent fronds,

φ = The semi-angle of the wedge,

s_2 = The related shell shortening corresponding to the completion of the wedge formation.

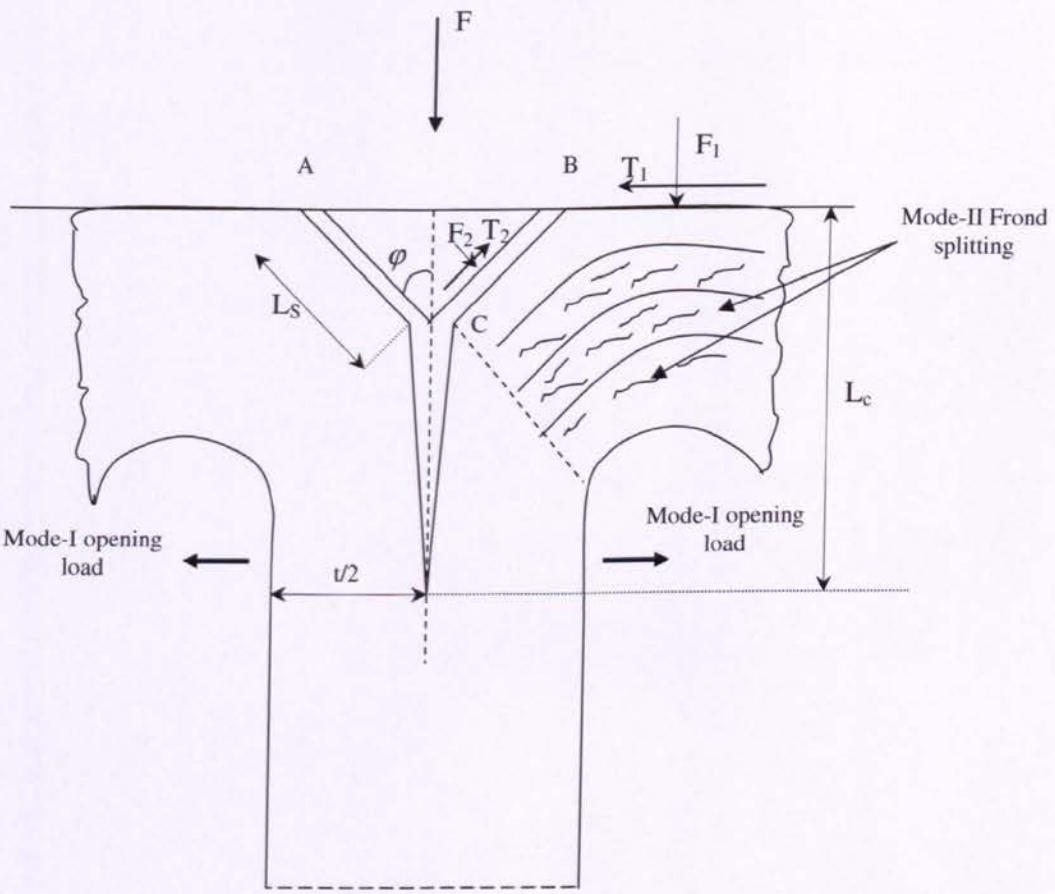

Fig. 2.9. Configuration of the crush zone in the middle of the tube side [45].

The total dissipated energy for a crush distance due to friction between the annular wedge and fronds and between fronds and platen can be written as:

$$U_1 = 2 \cdot \left(F_1 \cdot \mu_{s_1} + F_2 \cdot \mu_{s_2}\right) \cdot (4 \cdot b) \cdot (s - s_1) \tag{2.3}$$

where F_1 is the normal force per unit length applied by the platen to the internal and external frond, F_2 is the normal force per unit length applied to the sides of the wedge, s is the total crush distance, μ_{s_1} is the coefficient of friction between frond and platen and μ_{s_2} is the coefficient of friction between the wedge and the fronds. F_2 and σ_0 are equal to,

$$F_2 = \sigma_0 . l_s \tag{2.4}$$

and

$$\sigma_0 = k . \sigma_u \tag{2.5}$$

where k is a constant and σ_u is the ultimate tensile stress of the composite material.

Other energies dissipated due to fronds bending, crack propagation, and axial splitting are;

$$U_2 = 2 \cdot \left[\int_0^{\varphi} (F_2) \left(\frac{l_s}{2}\right) d\theta + \int_{s_2}^{s} (F_2) \theta . ds \right] \cdot 4 \cdot b \tag{2.6}$$

$$U_3 = G_{IC} \cdot [4 \cdot b \cdot (s - s_1) + \pi . L_c . b] \tag{2.7}$$

$$U_4 = 4 \cdot \left(\frac{t}{2}\right) \cdot G_I \cdot s \tag{2.8}$$

$$G_I = \frac{K^2}{E} \tag{2.9}$$

From Eqs. (3), (6), (7) and (8), the total energy dissipated for the deformation of the shell is obtained as,

$$U_{total} = U_1 + U_2 + U_3 + U_4 \tag{2.10}$$

Therefore, the total force applied by the platen to the shell can be calculated as,

$$F_m = \frac{U_{total}}{s} \tag{2.11}$$

2.10. Off-axis crashworthy behaviour of FRP composite box structures

Most of previous work has studied crushing under axial loading. In a real crash event the more likely scenario is a non-axial collision rather than an axial one. A few researchers have investigated the energy absorbing capabilities of elements such as box under two types of non-axial loadings. These non-axial loadings are known as off-axis loading and angled loading. Off-axis loading occurs when a spinning vehicle impacts an object from a direction not along its longitudinal axis. Angled loading occurs when a vehicle moving forward along its longitudinal axis impacts an object tilted away from being perpendicular to the vehicle's longitudinal axis. In this regards, it is essential to study the effect of collision angle on the energy absorbing capability of crashworthy composite structures.

In off-axis crushing, different form of fracture mechanisms are observed from those seen in axial crushing. During non-axial progressive collapse, non-symmetrical crack propagation at the interwall box and between the fronds plays an important role in dissipation of crushing energy.

The effects of off-axis crushing on the energy absorption of composite materials and structures have been investigated by few other researchers [45-47]. Czaplicki et al. [45] studied the crushing process of E-glass/polyester pultruded tubes under off-axis loading and angled loading. They found that these two loading conditions dissipated energy in different friction mechanisms but they observed similar energy absorption tendency by increasing the inclination angle. They also concluded that the mean crushing force increased at 10° off-axis angle in comparison with mean crushing force of axial crushing and then continuously decreased as the angle of inclination increases. Song and Du [46] investigated the effect of off-axis loading on the energy absorbing capability of glass/epoxy and glass/polyester composite tube laminated from various lay-ups. According to their results three characteristic crushing stages were identified as the triggering stage (Tr), the sustained crushing stage and the toppling stage. In general, they found that the energy absorption decreased as the off-axis inclination angle increased, due to changing two factors of toppling tendency and fracture pattern. They also concluded that 0° ply could prevent the circumferential cracks and therefore longitudinal resistance to delay the toppling stage.

Ochelski and Gotowicki [47] experimentally studied the effect of fibre reinforcement type, type of structure, orientation of fibres in a layer and stacking sequence of layers on the energy absorption capabilities of tubes and truncated cones. They also analysed the effect of specimen's thickness and the direction of the applied loading on the specific energy absorption (SEA).

2.11. Interlaminar fracture toughness and energy absorbing of composite structures

The brittle nature of most fibre reinforced polymer (FRP) composites causes they show high capability in absorbing the impact energy in vehicular structures. This energy absorption is introduced by various fracture mechanisms.

In this regard, the fracture study is one of the most important areas to be considered in investigating the energy absorption capability of composite structures. Various fracture mechanisms such as fibre breakage and buckling, matrix cracking and crushing, debonding at the fibre-matrix interface and especially plies delamination play important roles in progressive failure mode and energy absorption of composite tubes. Delamination occurs as results of shear and tensile separation between fronds. During progressive collapse, formation of frond bending and delamination among fronds layers causes a significant amount of energy absorption. Frond bending is caused by shaping a main central interwall crack. The propagation of this main crack is respectively similar to Mode-I interlaminar crack propagation. Frond layer sliding which occurs between lamina bundles during frond bending, dissipates the energy in Mode-II crack propagation.

Various works have been published on the effects of fractures on the energy absorption of composite materials and structures. Cauchi Savona *et al.* [48] studied the relation between specific sustained crushing stress (SSCS) of glass fibre reinforced plastic composite plates with their Mode-I and Mode-II fracture toughness properties. According to their results, materials which show low Mode-I and Mode-II fracture toughness, yield low crushing energies. They also concluded that the G_{IC} and G_{IIC} of initiation are more influential than the G_{IC} and G_{IIC} of propagation in the energy absorption mechanism. Solaimurugan *et al.* [49-51] studied the effect of stitching, fibre orientation and stacking sequence on G_{IC}, SEA, and of progressively crushing of glass/polyester composite cylindrical shells under axial compression.

They reported that axial fibres placed close to the outer surface of the tube led to more petal formation and to a stable crushing process, while axial fibres close to the inner surface of the tube caused higher energy absorption. Furthermore, they found that the energy absorption in the form of circumferential delamination increased for higher values of Mode-I fracture toughness.

They also reported that stitching increased the Mode-I interlaminar fracture toughness which caused higher energy absorption cylindrical tube. Warrior *et al.* [52] studied the influence of toughened resins, thermoplastic resin additives, through-thickness stitching and thermoplastic interleaving on the interlaminar fracture toughness (G_{IC}) and the SEA for continuous filament random mat (CoFRM) and 0/90 non-crimp fabric (NCF) E-glass reinforced polyester composite tubes. They reported that all the above-mentioned factors increased G_{IC}, but only toughened resin and through-thickness stitching increased SEA. In general a tougher matrix was found to give a higher G_{IC} for the composite and this is a benefit in crashworthiness design.

Farley [53] concluded that the matrix stiffness had only a small effect on energy absorption of materials which crushed by a brittle fracture and transverse shearing mechanism, and matrix stiffness has more effect on materials which crushed by lamina bending mechanism.

2.12. Finite Element Analysis (FEA)

In crashworthiness evaluations of composite box structures nonlinear material and geometric properties must be simulated and must be designed to simulate short-time large deformations in crash conditions. FEA involving short-time large deformation dynamics such as crashworthiness evaluation requires the solution of transient dynamic problems over a short time length. Explicit computational algorithms typically use the central differences method for integration, wherein the internal and external forces are assumed at each node point, and a nodal acceleration is computed by dividing by the nodal mass. The solution is continued by integrating this acceleration in time. The advantage of this method is that the time-step size may be selected by the user. The disadvantage is the large numerical effort required to form, store, and factorise the stiffness matrix.

The explicit solution technique is stable only if the time-step Δt is smaller than Δt_{cr} which is the critical time step. Δt_{cr} for shell element, is obtained from $\Delta t_{cr} = L_s / C$, where L_s is the

characteristic length and C is the speed of sound, $C = \sqrt{E/\rho(1-\nu^2)}$. The implicit method is not solved by the time-step size and then is unconditionally stable for larger time steps. This situation results in the implicit method typically engages a large number of expensive time steps. For an explicit solution the number of time-steps can be larger than that of implicit methods, the small time-step size requirement causes the explicit method suitable for short transient solutions. The most important advantage of the explicit method is that there is no requirement for solving simultaneous equations. Thus, no global matrix inversion is needed and a reduction of computational time is obtained [54].

2.13. Conclusion

In the present research the effects of delamination failure of composite box structures on their crashworthy behaviour will be studied. Various types of composite materials with different fibre orientations will be used to optimise the energy absorption capabilities of composite box structures. Delamination study in Mode-I, Mode-II and Mixed-Mode I/II with the same lay-ups will be carried out to investigate the effect of delamination crack growth on energy absorption of hybrid composite box structures. Regarding the delamination study of the variation of the specific energy absorption (SEA) versus G_{IC}, G_{IIC} and $G_{I/IIC}$ will be plotted to combine the effect of Mode-I, Mode-II and Mixed-Mode I/II interlaminar fracture toughness on the SEA. The new theoretical model based on friction, bending and fracture mechanisms to predict the mean crushing force for the combination of failure crushing modes will be proposed. The crushing process of composite boxes will also be simulated by finite element software LS-DYNA and the results were verified with the relevant experimental result.

References

[1] Hull D. A unified approach to progressive crushing of fibre reinforced tubes. *Composite Sci. Technol.* 1991:40;377–421.

[2] Farley G. Jones R. Crushing characteristics of continuous fibre reinforced composite tubes. *Journal of Composite Materials* 1992:26;37–50.

[3] Mamalis A. Manolakos D. Viegelahn G. Crashworthy behaviour of thin-walled tubes of fibreglass composite material subjected to axial loading. *Journal of Composite Material* 1990:24;72.

[4] Macaulay MA. Introduction to impact engineering. Published by Chapman and Hall, USA, 1987.

[5] Desjardins SP. *et al.* Aircraft crash survival design guide. USA VSCOM TR 89-D-22A-E, Vol I-IV, December 1989.

[6] Thornton PH. and Jeryan RA. Composite structure for automotive energy management. Presented at Autocom'87, 1-4 June 1987, Dearbon, MI.

[7] Beardmore P. and Johnson CF. The potential for composites in structural automotive applications. *Journal of Composite Sci. Technol.*, 1986:26;251-81.

[8] Matthews FL., Davies GAO., Hitchings D., and Soutis C. Finite element modelling of composite materials and structures. Woodhead Published Limited, USA, 2000.

[9] Farley GL. Energy absorption of composite materials. *Composite Materials* 1983:17;167.

[10] Thornton PH. Energy absorption in composite structures. *Journal of Comp. Mats.* 1979:13;247.

[11] Schmueser DW. and Wickliffe LE. Impact energy absorption of continuous fiber composite tubes. *Journal of Eng. Mat. Trans.* ASME 1987:72;77.

[12] Farley GL. and Jones RM. Crushing characteristics of continuous fibre- reinforced composite tubes. *Journal of Composite Materials* 1992:26;37.

[13] Thornton PH. and Edwards PJ. Energy absorption in composite tubes. *Journal of Composite Materials,* 1982:16;521.

[14] PE fibre reinforcement prevents crush. News article in British Plastics and Rubber, January, 1990;10.

[15] Hamada H., Coppala JC., Hull D., Maekawa Z. and Sato H. Comparison of energy absorption of carbon/epoxy and carbon/PEEK composite tubes. *Composites*, Vol. 23. Number 4. July 1992, pp. 245-252.

[16] Hamada H., Coppola JC., Hull D., Maekawa Z. and Sato H. Comparison of energy absorption of carbon-epoxy and carbon-PEEK composite tubes. *Composites* 1992:23;245.

[17] Nilson S. Polyetheretherketone matrix resins and composites. Int. Encyclopaedia of Composites, VCH Publishers Inc, 1991:6;282.

[18] Mamalis AG., Manolakos DE., Demosthenous GA. and Ioannidis MB. The static and dynamic axial crumbling of thin-walled fibreglass composite square tubes. *Composites* Part B, 1997;28(4):439-451.

[19] Farley GL. Effect of specimen geometry on the energy absorption of composite materials. *Journal of Composite Mats*, 1986:20;390.

[20] Czaplicki MJ., Robertson RE. and Thorton PH. Comparison of bevel and tulip triggered pultruded tubes for energy absorption. *Composites Science and Technology* 1991:40;31.

[21] Thuis HGSJ., Metz VH. The influence of trigger configurations and laminate lay-Up on the failure mode of composite crush cylinders. *Composite Structures,* Vol. 25, pp. 37-43.

[22] Farley GL. The effect of crushing speed on the energy-absorption capability of composite tubes. *Journal of Composite Mats*, 1991:25;1314. .

[23] Zhang L. Engineering plasticity and impact dynamic. Published by World Scientific, 2001.

[24] Abrate S. Impact on composite structures. Cambridge University Press, 1998.

[25] Timoshenko S. Theory of plates and shells. Mc Graw Hill, New York, 1959.

[26] Davies G. and Morton J. (ed.). Structural impact and crashworthiness. 2 volumes, Elsevier, 1984.

[27] Kim KJ. and Yu TX. (ed.). Impact response and dynamic failure of composites and laminate materials. TTP, Trans-Tech Publications, 1998.

[28] Sierakowski RL. and Newaz GM. Damage tolerance in advanced composites. Technomic Publishing Company, 1995.

[29] Wu HY. and Springer GS. Impact induced stresses, strains and delaminations in composite plates. *Journal of Composite Materials* 1988:22;533-560.

[30] Pang SS., Yang C. and Zhao Y. Impact response of single-lap composite joints. *Composites Engineering* 1995:5;1011-1027.

[31] Hancox NL. An overview of the impact behaviour of fibre-reinforced composites. in "Impact behaviour of fibre-reinforced composite materials and structures", Reid SR. and Zhou G., Woodhead publishing Ltd., Cambridge, UK, 2000.

[32] Naik N.K. and Ganesh V.K. Prediction of On-Axes Elastic Properties of Plain Weave Fabric Composites. *Composite Science and Technology*, 1992:45;135-152.

[33] Ishikawa T. and Chou T.W. Stiffness and strength of woven fabric composites. *Journal of Materials Science*, 1982:17;3211-3220.

[34] Yang Y.C. and Harding J. A numerical micromechanics analysis of the mechanical properties of a plain weave composite, *Computers and Structures*, 1990:36(5);839-844.

[35] Whitcomb J.D. Three-dimensional stress analysis of plain weave composites. *Composite Materials and Fracture* (Third Volume), ASTM STP 1110, O'Brien T.K. American Society for Testing and Materials, Philadelphia, USA, 1991:417-438.

[36] Santulli C. Impact damage evaluation in woven composites using acoustic and thermoelastic techniques. PhD Thesis, Liverpool University, 2000.

[37] Riva E. Mechanics of woven composites. PhD thesis, 97-98, University of Parma.

[38] Mamalis AG., Robinson M., Manolakos DE., Demosethenous GA., Ioannidis MB. and Carruthers J. Crashworthy capability of composite material structures. *Composite Structures*, 1996:13-5;263-8223.

[39] Mamalis AG, Manolakos DE, Demosthenous GA and Ioannidis MB. Crashworthiness of Composite thin-walled structural components. Publisher CRC; 1st edition, 1998.

[40] Mamalis AG., Manolakos DE. and Viegelahn GL. Crashworthy behaviour of thin-walled tubes of fibreglass composite material subjected to axial loading. *Journal of Composite Materials* 1990:24;72.

[41] Berthelot JM. Composite materials, mechanical behaviour and structural analysis. ISBN 0-387-98426-7 Spring-Verlag New York, USA, 1999.

[42] Farley GL. and Jones RM. Analogy for the effect of material and geometrical variables on energy absorption capability of composite tubes. *Journal of Composite Materials*, 1992:26(1);78.

[43] Jacob GC., Fellers JF., Simunivic S. and Starbuck M. energy absorption in polymer composites for automotive crashworthiness. *Journal of Composite Materials* 2002:36;813.

[44] Mamalis AG., Manolakos DE., Demosthenous GA. and Ioannidis MB. Analysis of failure mechanisms observed in axial collapse of thin-walled circular fibreglass composite tubes. *Thinwalled Structures*, 1994:26.

[45] Mamalis AG, Manolakos DE, Demosthenous GA and Ioannidis MB. The static and dynamic collapse of fibreglass composite automotive frame rails. *Composite Structures*, 1996;34:77-90.

[46] Czaplicki MJ, Robertson RE and Thornton PH. Non-axial crushing of E-glass/polyester pultruded tubes. *Journal of Composite Materials,* 1990;24.

[47] Hong-Wei Song and Xing-Wen Du. Off-axis crushing of GFRP tubes. *Compos Sci Technol,* 2002;62:2065–2073.

[48] Ochelski S, Gotowicki P. Experimental assessment of energy absorption capability of carbon-epoxy and glass-epoxy composites, *Composite structures*, in press, 2009.

[49] Cauchi Savona S, Hogg PJ. Effect of fracture toughness properties on the crushing of flat composite plates. *Compos Sci Technol,* 2006;66:2317-2328.

[50] Solaimurugan S and Velmurugan R. Influence of fibre orientation and stacking sequence on petalling of glass/polyester composite cylindrical shell under axial compression. *Int Jnl of Sol and Struc* 2007;44:6999-7020.

[51] Solaimurugan S and Velmurugan R. Progressive crushing of stitched glass/polyester composite cylindrical shells. *Compos Sci Technol* 2007;67:422-437.

[52] Warrior NA, Turner TA, Robitaille F, Rudd CD. The effect of interlaminar toughening strategies on the energy absorption of composite tubes. *Composites: Part A* 2004;35:431-437.

[53] Farley GL. Energy absorption in composite materials for crashworthy structures. In: Matthews FL, Buskell NCR, Hodgkingson JM, and Mortan J. (eds.), in: *Proceedings of the ICCM 6.* London: Elsevier Science Publishers Limited. pp. 3.57-3.66.

[54] LS-DYNA User's Manual (Non-linear Dynamic Analysis of Structures in Three Dimensions), Livermore Software Technology Corporation, 1997, Livermore, USA.

Chapter 3:

Effect of Mode-I Delamination Failure in Crashworthiness Analysis of Composite Box Structures

Nomenclature

a	crack length
b	side of box
C	compliance
CFE	crush force efficiency
$CFRP$	carbon fibre reinforced plastic
DCB	double cantilever beam
E	Young's modulus
F	force
F_{max}	initial maximum force
F_m	mean force
G_{12}	shear modulus
G_{IC}	mode-I interlaminar fracture toughness
$GFRP$	glass fibre reinforced plastic
SEA	specific energy absorption
S	shear strength
t	thickness
V_f	volume fraction
υ	Poisson's ratio
σ_1	longitudinal stress
σ_2	transverse stress
σ_{12}	transverse shear stress
δ	displacement
σ_u	ultimate tensile stress

θ fibre orientation

Δ extension correction factor for DCB sample

α trigger angle

3. Introduction

The present chapter is mainly focused on the effect of fibre orientation and stacking sequence on G_{IC} and SEA. The manufacture and testing of DCB and crush box specimens is described with different lay-ups of composite material *i.e.* GFRP and CFRP but with the same geometry. The experimental results are compared together to find the relationship between G_{IC} and SEA.

3.1. Experimental studies

Five different types of test were conducted to characterize the mechanical characteristics of unidirectional GFRP and twill/weave CFRP materials. These were tensile, shear, double-cantilever beam (DCB), fibre volume fraction determination and quasi-static crush box tests. All tensile, shear, DCB and fibre volume fraction tests were carried out in accordance with the relevant standards [1-4]. The GFRP and CFRP specimens were manufactured from glass and carbon fibre material of densities 2.1 g/cm^3 and 1.8 g/cm^3 with epoxy resin.

3.2. Mechanical properties

A separate laminate was made for each type of test and specimens were cut from the laminate for testing. The dimensions of each panel were determined by the size and quantity of specimen required for each test. As all three types of test specimen had the same dimensions, they could all be prepared in the same way, using the same templates and equipment. Five specimens were made for each test which meant the panels from which they were to be cut would need to be 125mm wide by the required length, 250 mm. With allowances for machining and possible defects around the edge these numbers were rounded up to 300mm × 200mm. The thickness of each specimen was 2 mm with 250 mm length and 25 mm width. All specimens were cured first in a curing cycle of 30 minutes at 60° C with a heating rate of 3-5°C per minute and the temperature was held at 125° C for 60 minutes. Tensile tests were carried out on specimens with [0] and [90] layup with the aim of finding Young's modulus, E_1 and E_2, Poisson's ratio ν_{12} and ν_{21}, and the ultimate tensile strengths according to BS ISO 2747 standard [1]. There are several test methods for measuring the shear modulus of composite materials. The $[\pm 45]_S$ tensile shear test was chosen for the shear testing as this type of test can be carried out using a conventional tensile testing machine. The state of stress in

each laminate was not pure shear but a combination of normal stresses, in addition to the desired shear stress.

Firstly, the shear stress-strain responses of many composite materials are non-linear, and may exhibit strain softening characteristics, due to rearrangement of dislocations. So, although the biaxial stress in the specimen is likely to cause the measured value of shear strength to be lower than the true value, the reduction may be small because of the nonlinear softening response. Secondly, the magnitudes of the interlaminar stresses for laminates containing lamina with high orthotropic ratios are a maximum at ply angles of 15° to 25°, and the interlaminar stresses for 45° ply angles are considerably smaller.

These tests were conducted in accordance with BS ISO 14129 standard [2]. The tests were carried out on a Denison-Mayes 100 kN universal testing machine with crosshead speed of 2 mm/min. For measuring Young's modulus in the axial and transverse direction a biaxial rosette strain gauge Showa N22-FA-8 with a resistance of 120 Ohms and gauge length of 8 mm was placed at the central part of the specimen and for measuring the shear modulus a 0/45/90 rosette strain gauge was used.

The fibre volume fraction of the GFRP and the CFRP was determined by the resin burn-off method. It is particularly suitable for FRP composite because they are resistant to oxidation at elevated temperatures. This test followed ASTM D 3171 standard [3]. Three small specimens of composite, approximately 15x15x2mm, were cut from a larger panel. The width, thickness and length were measured in three places using a micrometer, a mean average taken and the volume of the specimen calculated. Three ceramic crucibles were weighed on scales accurate to one hundredth of a gram. The composite specimens were then placed one on each crucible and the crucible and specimen weighed together. The mass of the composite was obtained from subtracting this value from the weight of the crucible. The mass of the composite was divided by its volume to calculate the specimen's density. The three crucibles containing the specimens were then placed in a preheated oven at 500°C for five hours. This high temperature burned-off the epoxy matrix leaving just the fibres behind. After five hours the specimens are removed and reweighed. This mass was subtracted from the crucible mass to obtain the weight of the fibres in the specimen. The results showed excellent correlation with each other. The fibre volume fraction for this material was found to be 40.3% for the GFRP and 45% for the CFRP. The manufacturers reported values of fibre volume fracture for these

composites were found to closely match the experimental results. A summary of the findings for these tests is reported in Table 3.1.

Table 3.1. Material properties of a) the GFRP and b) CFRP.

E_1 (GPa)	E_2 (GPa)	G_{12} (GPa)	υ_{12}	σ_u 0° MPa	σ_u 90° MPa	τ_s MPa	V_f (%)
35.1±5	9.6±1.5	4±0.2	0.32	807±35	21.3±1.5	97.9±3	40.3

(a)

E_1 GPa	E_2 GPa	G_{12} GPa	ν_{12}	σ_u 0° MPa	σ_u 90° MPa	τ_s MPa	V_f %
61±3.5	58±3	3.4±0.2	0.1	634±22	560±14	94±5	45

(b)

3.3. Determination of Mode-I fracture toughness

The fabrication of GFRP and CFRP DCB specimens were laid-up according to the laminate design of each GFRP and CFRP composite crush box which will be discussed later. The mid-plane interface of GFRP was 0/90, 90/90, 0/45 and +60/-60 to determine the Mode-I interlaminar fracture toughness for three fracture locations. The mid-plane interfaces of CFRP DCB specimens were respectively 0/0, 0/45 and 45/45 with respect to weft direction. The crack propagation was set along the weft direction which was defined as 0 direction (see Figure 3.1).

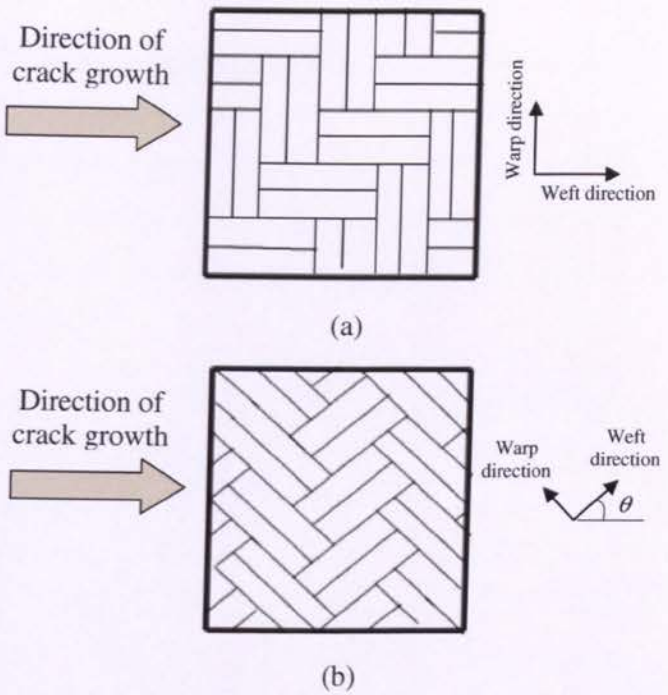

Fig. 3.1. Direction of crack propagation in CFRP specimen (a) 0° and (b) 45° ply.

For determining the Mode-I interlaminar fracture toughness G_{IC}, BS ISO 15024 standard [4] was followed together with the corrections developed elsewhere to take into account for the end-block, DCB arm bending and root rotation [5-8]. The recommended specimen size is at least 125mm long and 20-25mm wide with an initial crack length (i.e. length of the insert from the load line) of 50mm (see Figure 3.2).

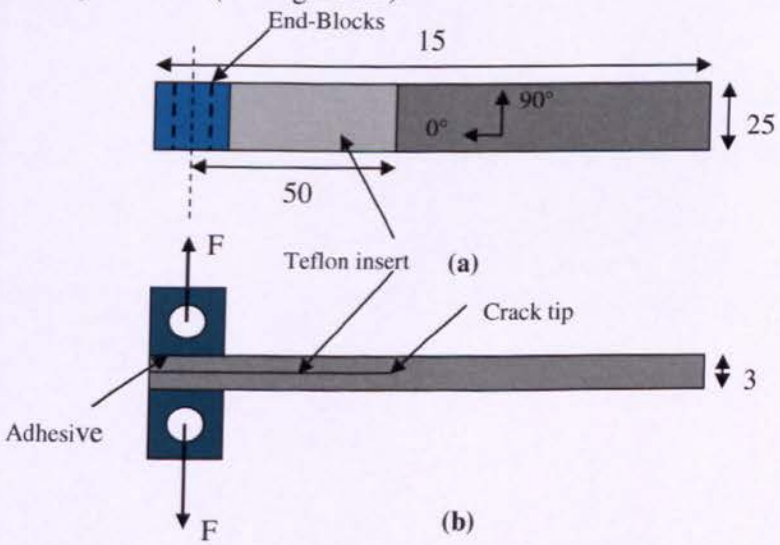

Fig. 3.2. Double Cantilever Beam (DCB) specimen, (a) plane view (b) side view (All dimensions in mm).

For curing the specimens the temperature was initially raised to 60°C and held for 30 minutes and then the temperature was increased to 125°C and held for 60 minutes. This stepped heat-up meant the temperature was raised gradually to 125°C, allowing the epoxy matrix to fully infuse the reinforcement before hardening. After curing, the specimen was left in the oven to cool to room temperature. Each specimen was labelled prior to testing with the specimen lay-up and specimen number.

White paint was applied to both longitudinal edges of each specimen and allowed to dry. The painted sides were then marked with a fine pen at the edge of the polymer insert to indicate the edge of the pre-crack. To aid in recording crack growth, the first 5mm from the insert were marked every 1mm with a thin pen line and the next 55mm were marked at 5mm intervals. Hence crack growth was recorded for 60mm along the specimens. The load end-blocks were bonded to the DCB specimens using Betamate 1493 adhesive at the end containing the insert. Load was applied to the specimens through end-blocks to propagate the crack (see Figure 3.3).

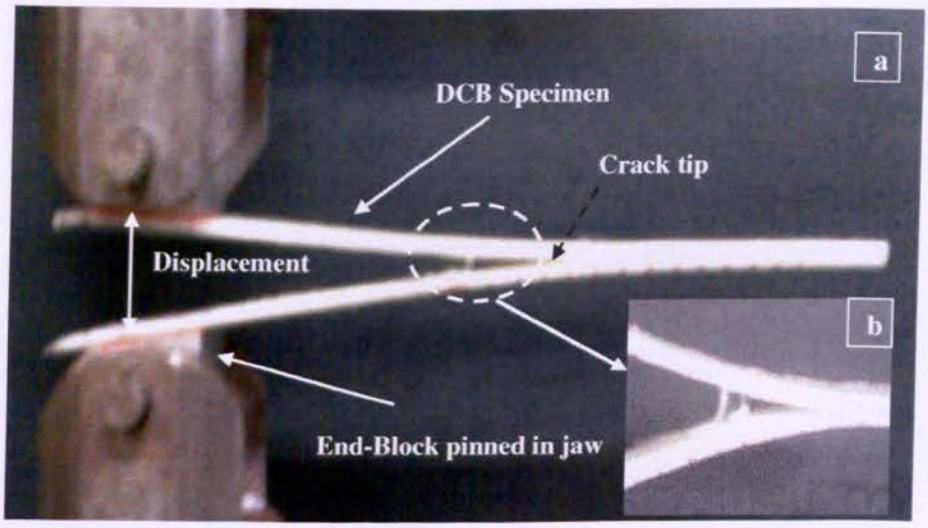

Fig. 3.3. a) GFRP DCB test specimen in universal testing machine, b) Fiber bridging across the interface layers.

A travelling optical microscope with 10X magnification was used to accurately measure the length of the initial crack by sliding it along a horizontal scale similar to that used on callipers. A cross-hair is lined up with the path of the load through the hinges (load line).

The position of the microscope was noted to the nearest tenth of a millimetre. The travelling microscope was then moved, by turning a knob, to the end of the polymer insert, sighted using the pre-mentioned pen line. The position of the microscope was again noted, and the difference of these two measurements gave the initial crack length. Loading was carried out at a constant crosshead displacement rate of 2 mm/min. The position of the crack tip was monitored through the microscope as the crack advanced. When the crack first visibly propagated, the displacement of the crosshead was recorded. As the crack propagation past the subsequent marked lines, the crack length and crosshead displacement were recorded. The force at each crack length was retrospectively obtained from the force-displacement diagram to calculate G_{IC}.

3.4. Composite crush box

The crush box specimens were made of glass fibre/epoxy and carbon fibre/epoxy by hand lay-up with various fibre orientations which followed the same lay ups as described in DCB tests in the previous section. A cardboard template was made for marking out the panel plies on the prepreg roll. The 0° and 90° angle plies were marked using a set square and the 45 and ±60 angle plies were marked using a protractor to orientate the template on the roll and achieve the required fibre direction.

The pieces were then labelled with fibre direction and angle to avoid later confusion. Once marked out, the panel plies were cut from the roll using a sharp Stanley knife and steel ruler. The two protective layers covering each ply of prepreg were removed and the first layer was placed around a rigid wooden mould covered with a non-stick polymer sheet. The layer then covered with another sheet of non-stick polymer to prevent contamination and a roller was used to roll and shape the material around the mould as flat as possible, and removing any air pockets. The polymer sheet was then removed and the second ply was laid-up on top of the first ply according to desired lay-up. Four laminate with fibre orientations of $[\pm 60]_{10}$, $[0_2/\pm 45]_5$, $[0/90]_{10}$ and $[0/90]_{5S}$ were chosen for GFRP composite boxes. The 0 direction was aligned with the axial axis of the crush box. The lay-ups of CFRP composite boxes were chosen with fibre orientations of $[0]_4$, $[0/45]_2$ and $[45]_4$. Once the boxes had been successfully laid-up, they were placed between four pre-cut aluminium plates to keep them flat during the curing process.

The plates were pre-treated with a mould cleaner to remove grease and debris and a monocoat wax was applied to prevent escaped epoxy from the prepreg bonding to the metal plates. The plates were then covered in non-stick polymer sheets to further decrease the chance of epoxy bonding to the plates.

The plates were placed on either side of the uncured composite, then covered top and bottom with three sheets of 'breather cloth' and placed inside a heat resistant polymer bag. The breather cloth has the appearance of cotton wool and allows air to circulate around the bag preventing the formation of air pockets. The bagging material was cut from a roll and was open at either end. A high temperature, double-sided epoxy tape was used to seal the ends. Once sealed, an air suction valve was inserted through the bag and a pipe connected the valve to a vacuum pump.

The vacuum pump was used to evacuate the bag, with the aid of the breather cloth. This had the effect of pressing the aluminium plates tightly together and forcing the plies of prepreg together, allowing good adhesion between the plies and eliminating air that could cause voids in the composite. The pressure gauge was inserted via a second valve to monitor the pressure in the bag. This was used to ensure the correct pressure was applied to the bag (following the manufacture's guidelines). The pressure gauge was also used to measure any pressure drop in the vacuum bag once the pump had been switched off and hence to check if the bag was properly sealed. All GFRP composite boxes were cured for 30 minutes at 65°C and then for 120 minutes at 130°C while CFRP composite boxes were cured for 30 minutes at 90°C and then for 120 minutes at 180°C. Then they were cut to the required lengths. The dimensions of all boxes were the same and chosen according to the previous reported works which have shown progressive failure [10].

The *b/t* ratio was 26.7 with thickness of about 3 mm and the total length was 100 mm. To avoid stress concentration at the box corners, an internal fillet with a radius of 6 mm was inserted at the internal corners of the box. Also one end of each specimen was bevelled to make a trigger for progressive crushing with an angle of 60° (Figure 3.4). Each specimen was crushed between two parallel plates for 50 mm stroke using a universal testing machine with 500 kN load cell.

The crush speed was set at 2 mm/min, the same speed as used for the DCB tests. For each test configuration three specimens were tested. The force-crush distance diagrams were recorded automatically for each test.

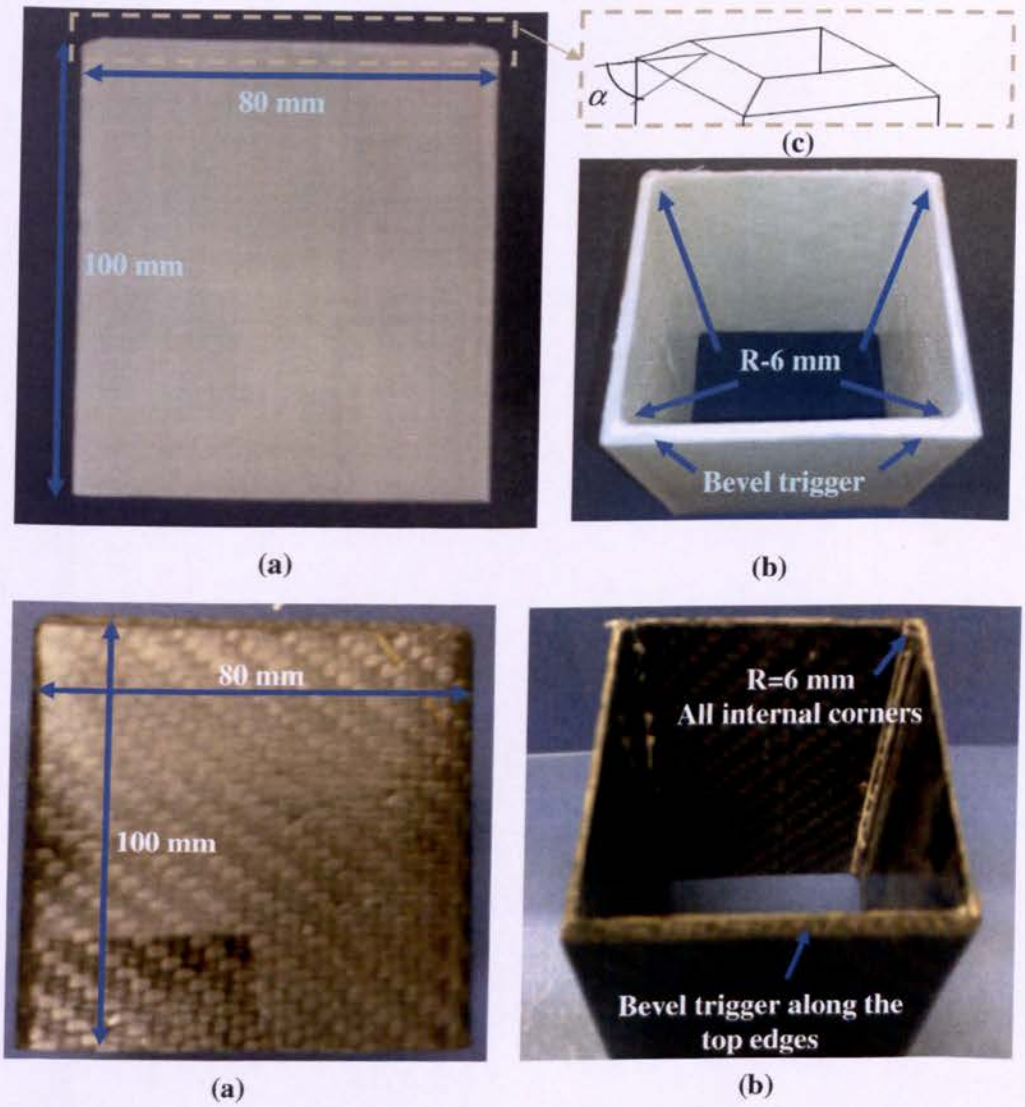

Fig. 3.4. GFRP and CFRP composite crush box specimens, (a) front view (b) top view and (c) trigger mechanism. Internal fillets of 6mm were introduced at the internal box corners. The box wall thickness is t=3mm.

3.5. Results and discussion

3.5.1. Mode-I interlaminar fracture toughness

The Mode-I interlaminar fracture toughness G_{IC}, for each fibre orientation was calculated using the *Modified Beam Theory (MBT)* method and the *Modified Compliance Calibration (MCC)* method [4-9]. For MBT method, the cube root of compliance, $C^{1/3}$, was plotted as a function of crack length, a. The intercept with the x-axis was considered as the crack length correction, Δ. The G_{IC} value was calculated from:

$$G_{IC} = \frac{3F\delta}{2b(a+|\Delta|)} \tag{3.1}$$

In the MCC method a least squares plot of a/t as a function of the cube root of the compliance, $C^{1/3}$, is generated using the visually observed delamination onset values and all the propagation values. The slope of this line is A [9]. The G_{IC} value was then obtained from:

$$G_{IC} = \frac{3F^2C^{\frac{2}{3}}}{2Abt} \tag{3.2}$$

The experimental G_{IC} results of GFRP obtained from MBT and MCC for different fibre orientation are shown in Table 3.2. Transverse cracking of θ-oriented lamina at interface of GFRP specimens caused some fibre bridging for most of GFRP-DCB tests as shown in Figures 3.2b. The development of fibre bridging caused the force to continuously increase as the crack advanced resulting in a rising R-curve. A sample experimental resistance curve (i.e. G_{IC} versus crack length) for GFRP specimen is shown in Figure 3.5.

Table 3.2. Interlaminar fracture toughness obtained from DCB tests for various interface fibre orientations.

Laminate lay-up	Fracture plane interface	G_{IC} (J/m^2) MCC	G_{IC} (J/m^2) MBT
$[0/90]_{10}$	0/90	923±22	1243±53
$[0_2/\pm45]_5$	0/45	884±32	1060±36
$[0/90]_{5S}$	90/90	778±25	1168±46
$[\pm60]_{10}$	+60/−60	450±21	540±12

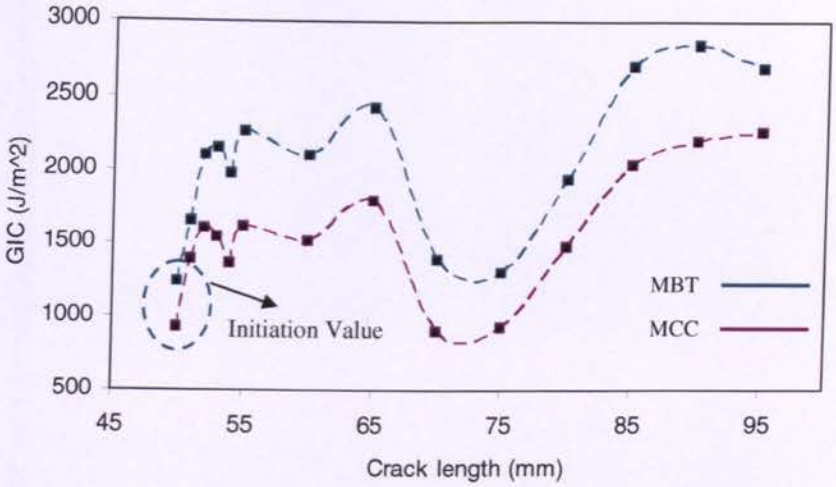

Fig. 3.5. Resistance curve (R-curve) in a DCB specimen with 0/90 fracture plane interface using MBT and MCC methods.

Mode-I interlaminar fracture toughness of the interface layers of (0/90)-GFRP showed the highest values of GIC for all tested specimens, and the interlaminar fracture toughness of interface layers of (+60/−60)-GFRP showed the lowest value. The combination of $0/\theta$ and θ/θ at interface layers of GFRP caused the maximum interlaminar fracture toughness.

Various reasons such as intralaminar delamination, mixed mode fracture, fibre-bridging, micro-cracking, residual stresses, or a combination of these effects of θ-oriented lamina at interface caused the development of transverse intralaminar and unstable crack propagation in DCB tests. In all CFRP-DCB tests intralaminar delamination, fibre-matrix debonding and/or fibre breakage were observed in fracture surface areas as shown in Figure 3.6. The development of transverse cracking also caused the force to show several continuous increases after initial crack propagation resulting in a rising R-curve (see Figures 3.7 and 3.8). Regarding the results and recommendations of other works on DCB-tests on multidirectional laminates [11-13], G_{IC} values of initiation are reported as interlaminar fracture toughness.

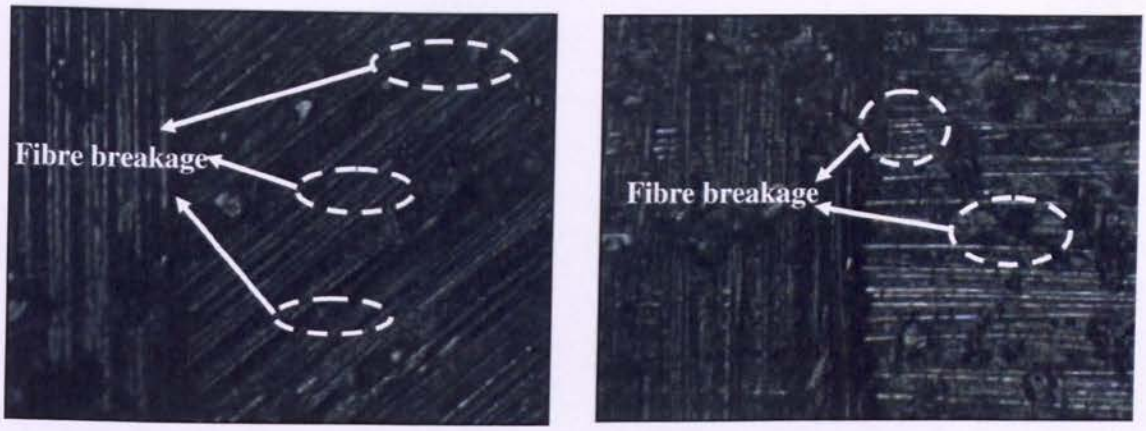

Fig. 3.6. Optical micrograph from fracture surface of CFRP-DCB specimens showing fibre breakage combination of intralaminar (a) 0/45 interface and (b) 0/0 interface.

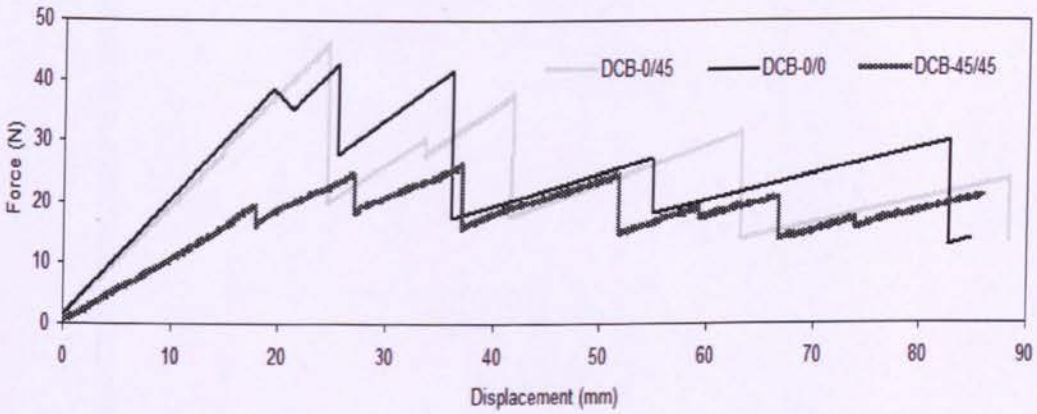

DCB tests

Fig. 3.7. Force-load line displacement from CFRP-DCB tests for various mid-plane interfaces.

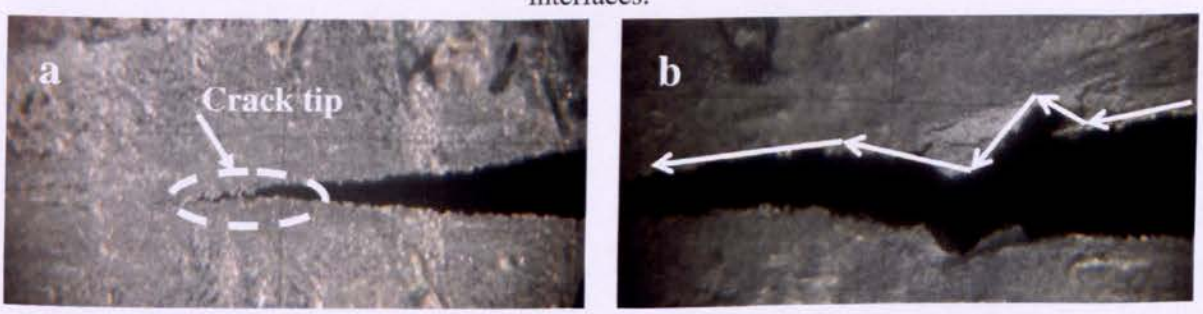

Fig. 3.8. Transverse cracking in DCB specimen, (a) at crack tip and (b) typical pattern of crack propagation.

Three different methods to determine crack length for the initiation values from the precrack as the distance between the force-displacement and the precrack are considered. The first non-linearity (NL) method determines the point of deviation from linearity, by sketching a straight line from the origin. The second uses the visual observation (VIS) which is the first point at which the crack is observed to move from the tip of the Teflon insert. The last is the MAX/5 %, a point on the force-displacement curve at which the compliance has increased by 5% of its initial value. In this work the visual observation (VIS) was chosen to determine the initiation crack length. It was observed that fibre orientation in the layers adjacent to crack plane affects the G_{IC}. Mode-I interlaminar fracture toughness of the interface layers of (0/45)-CFRP showed the highest values of G_{IC}, and interface layers of (45/45)-CFRP showed the lowest value (see Figure 3.9).

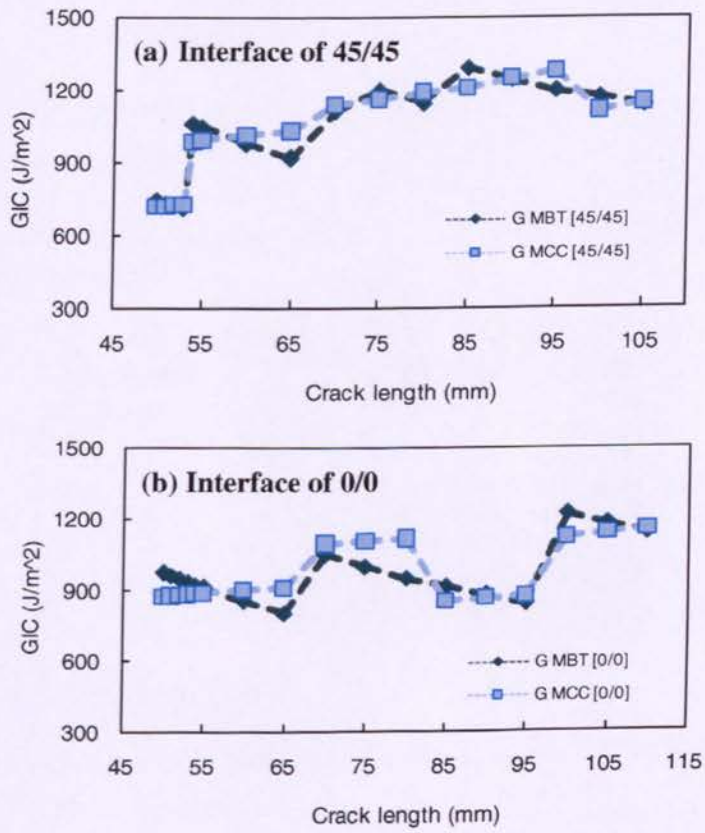

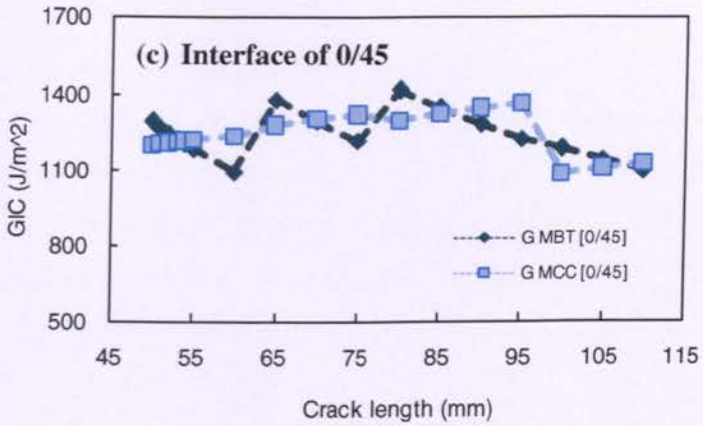

Fig. 3.9. Resistance curve (R-curve) in CFRP-DCB specimens with (a) 45/45, (b) 0/0 and (c) 0/45 fracture plane interfaces using MBT and MCC methods.

The experimental G_{IC} results of CFRP obtained from MBT and MCC for different fibre orientation are shown in Table 3.3.

Table 3.3. Interlaminar fracture toughness obtained from DCB test for various interface fibre orientations of woven CFRP.

Laminate lay-up	**Fracture plane interface**	G_{IC} **(MCC)** J/m^2	G_{IC} **(MBT)** J/m^2
$[0]_4$	0/0	900±20	1000±30
$[0/45]_2$	0/45	1200±50	1300±40
$[45]_4$	45/45	700±20	700±20

MCC: Modified Compliance Calibration, MBT: Modified Beam Theory

3.5.2. Progressive crushing process

Three main crushing modes in accordance with Farley and Jones [10] classification are categorised for progressive failure of composite box in crushing process. The first one is the fragmentation mode which is characterised by a wedge-shaped laminate cross section with one or multiple short interlaminar and longitudinal cracks. The second one is the lamina bending mode which is shaped with long interlaminar, intralaminar, and parallel to fibre cracks. This mechanism causes the formation of continuous fronds which spread inwards and

outwards. The third one is the combination of fragmentation and lamina bending modes and it is called brittle fracture mode.

Different modes of crush were observed during quasi-static crush test. As can be seen in Figure 3.10, the combination of two distinct crush modes, brittle fracture (fragmentation) and lamina bending, observed for all the GFRP specimens. This was combined mode is an ideal crushing mechanism to dissipate the energy during crushing in composites [14]. For fibre orientation of $[0/90]_{5S}$ and $[\pm60]_{10}$, the fronds were broken into short pieces. The other two fibre orientations $[0_2/\pm45]_5$ and $[0/90]_{10}$ showed more interlaminar separation during the crushing process.

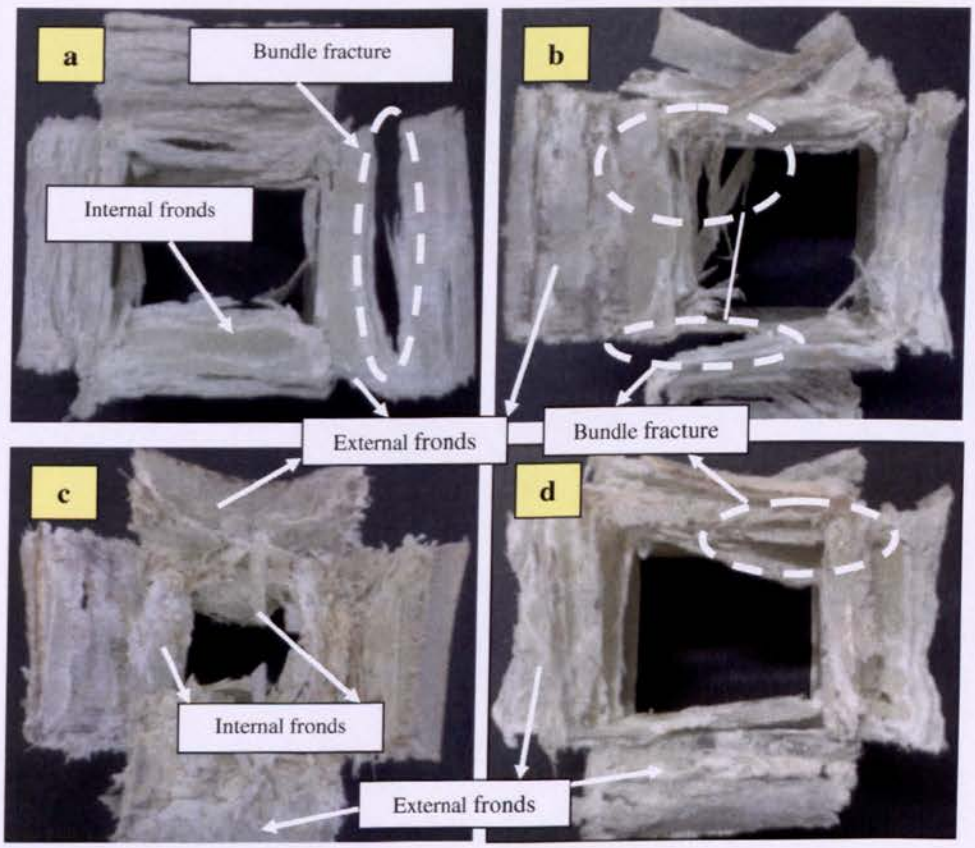

Fig. 3.10. Plane view of crushed GFRP composite box. a) $[0/90]_{10}$, b) $[0/90]_{5S}$, c) $[0_2/\pm45]_5$, d) $[\pm60]_{10}$.

The combinations of three distinct crushing modes were observed for CFRP crush box during quasi-static crush tests. As can be seen in Figure 3.11, the combination of lamina bending and brittle fracture modes were observed for fibre orientations of $[0]_4$ and $[0/45]_2$ and also the

combination of transverse shearing and local buckling was found for laminate design of $[45]_4$. The combination of lamina bending and brittle fracture crushing modes showed the highest energy absorption in comparison with the other observed modes.

This high energy absorption is caused by a larger crush area and therefore a higher potential to absorb energy by frictional effects at the platen/specimen interface. The force-crush distance of lamina bending crushing mode showed that the majority of serrations with small amplitude. This situation causes the required stresses to initiate crack propagation to increase and consequently causes high energy absorption. In brittle fracture and lamina bending many interlaminar and intralaminar cracks were formed in the crush zone.

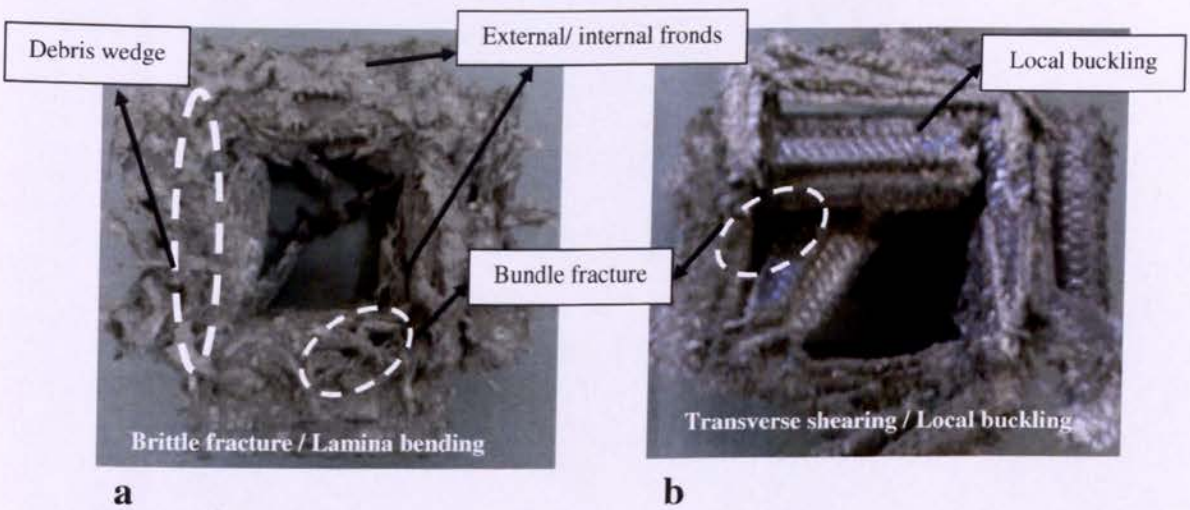

Fig. 3.11. Plane view of crushed CFRP composite box. a) $[0]_4$ and b) $[45]_4$.

For combination of the brittle fracture/ lamina bending crushing mode, at the initial stages of the crushing, four axial cracks were formed at corners of each box which caused bending of the internal and external fronds. It was observed that the external fronds were longer than internal fronds. No axial tear was observed during the crush process. The deformation of all boxes was elastic at the beginning of crushing process while the load increased rapidly to its maximum. Because of the friction between crushing plate and deformed fronds, the debris wedge was shaped. After this many interlaminar and intralaminar cracks were formed in the crush zone (Figure 3.12). The crack continued to propagate along the main central interwall (Figure 3.13), and lamina bundles were formed. The load dropped from its peak and

stabilised around a mean force, F_m. The magnitude of the mean force was found to depend on the propagation of the interlaminar and intralaminar cracks.

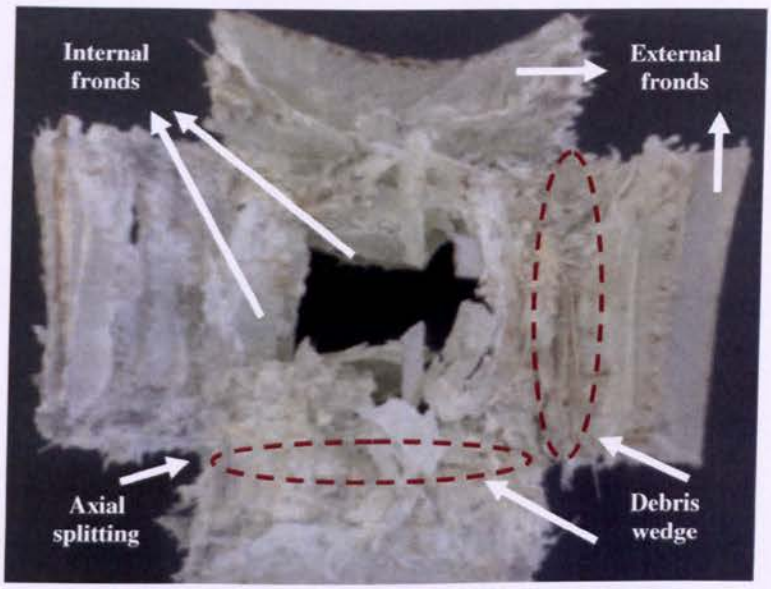

Fig. 3.12. Crush zone of GFRP composite box (Plain view).

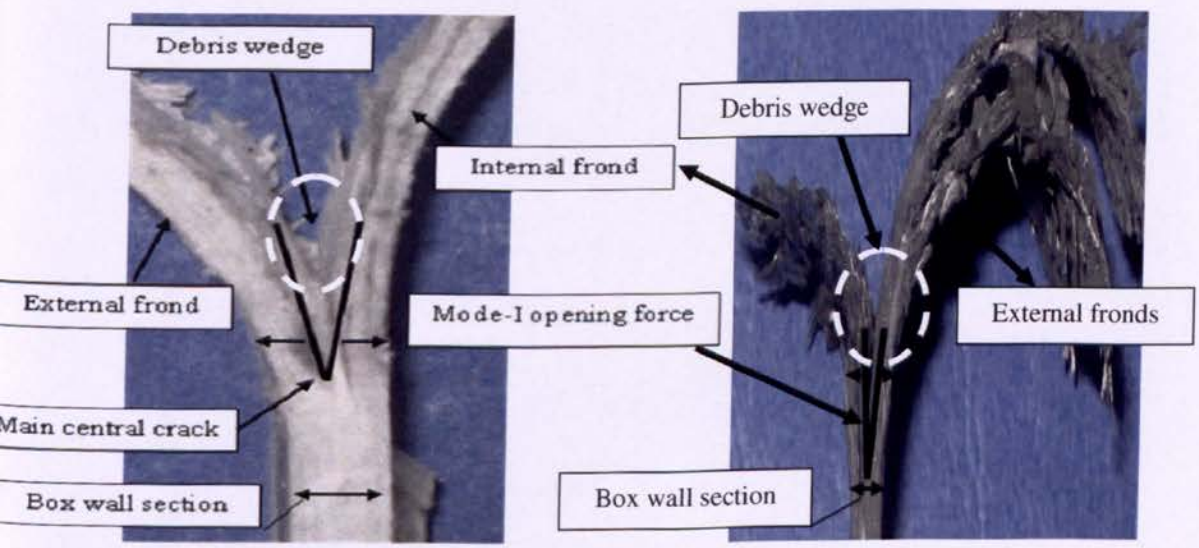

Fig. 3.13. Mode-I interlaminar crack propagation at the middle of box wall, a) GFRP and b) CFRP.

In this stage which is called post-crushing regime, the internal and external fronds were buckled when the applied force reached a critical value. The energy absorption and the force stability of composite boxes are related to fracture behaviour of the main central interwall crack (Figure 3.13). The main central crack which causes to shape lamina bundles has an important role on resistance against crushing energy.

The propagation of this crack is similar to crack propagation in Mode-I delamination in composite laminates discussed earlier in section 3.1 that the fibre orientation at the interface planes has significant effect on Mode-I interlaminar fracture toughness. Also the SEA varied with fibre orientation and fracture behaviour of the main interlaminar cracks. These evidences show that the fracture behaviour of a central interlaminar opening crack is correlated to Mode-I interlaminar fracture toughness.

As discussed previously, the fibre orientation and consequently interlaminar fracture toughness affect the progressive crushing modes. For those fibre orientations which show higher fracture energy from DCB test, higher mean force and absorbed energy were observed during crushing. Obviously the resistance crack propagation contributes to greater energy absorption. As the material and geometry are the same for all specimens; the effect of friction on the dissipation of energy can be assumed to be approximately the same in all crushing processes. The experimental results of force-crush distance for all lay ups are shown and compared in Figure 3.14.

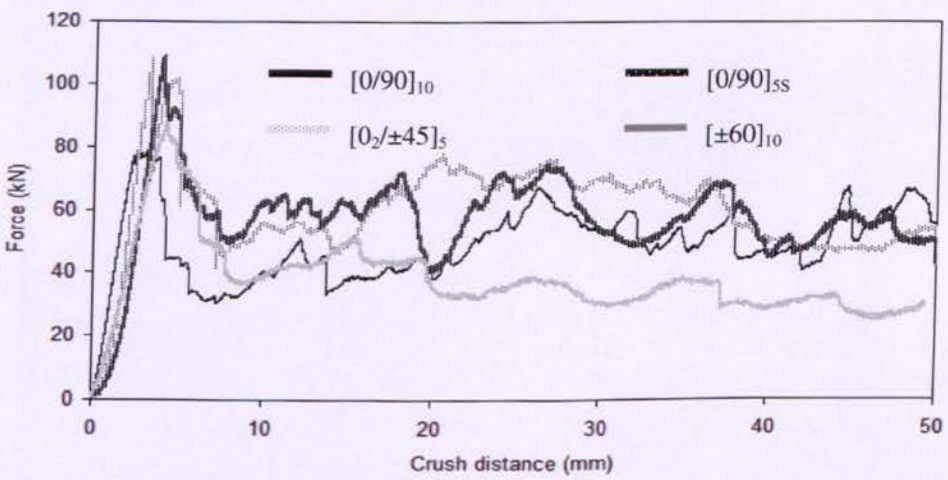

Fig. 3.14. The comparison of force-crush distance in a square GFRP crush box for various lay-ups.

The results show that the $[0_2/\pm45]_5$ has the highest mean force and consequently highest energy absorption in comparison with other lay-ups. This high energy absorption is related to high Mode-I interlaminar fracture toughness. The lowest interlaminar fracture toughness from DCB tests was observed for $[\pm60]_{10}$ lay-up.

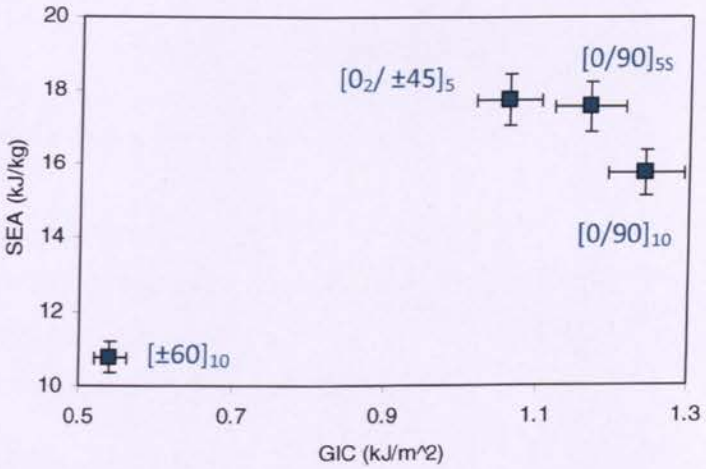

Fig. 3.15. Variation of specific energy absorption (SEA) with interlaminar fracture toughness, G_{IC} for various box lay-ups.

This was reflected on the lowest values of mean force and energy absorption in the crash box with the same lay-ups. Variation of specific energy absorption (SEA) from crush test versus Mode-I interlaminar fracture toughness, G_{IC}, from DCB tests for various lay-ups is plotted in Figure 3.15. It can be seen that the interlaminar fracture toughness for interface fracture planes of 0/90, 90/90 and 0/45 are clustered close to each other while the equivalent value for +60/–60 interface plane is much lower. This shows that the specific energy absorptions (SEA) of fibre orientations which are laminated with $0/\theta$ angles are close together.

Choosing a suitable fibre orientation in the interface plane is one of the main factors for improving the energy absorption of composite crush boxes in progressive failure. The ratio between initial maximum collapse force and mean force is known as the crush force efficiency (CFE). The higher value of CFE parameter shows a better energy absorption capability. The crush force efficiency (CFE) of all composite crush boxes was also obtained and the results are shown in Table 3.4.

Table 3.4. Comparison of SEA and Mode-I interlaminar fracture toughness for GFRP crush boxes.

Lay up	F_{max} (kN)	F_m (kN)	CFE %	SEA (kJ/kg)	G_{IC} (J/m^2) MCC
$[0/90]_{10}$	78	52	67	15.8	923±20
$[0/90]_{5S}$	110	60	55	17.5	884±30
$[0_2/\pm45]_5$	105	61	58	17.7	778±25
$[\pm60]_{10}$	87	38	43	10.8	450±20

The $[0/90]_{10}$ lay-up has the highest CFE. The reason comes from its lower initial maximum collapse force compared with other fibre orientations. This situation is more suitable for crashworthiness design cases which need to absorb the energy with a lower initial collapse force but not necessarily with the highest energy absorption capability.

In the lamina bending crushing mode of CFRP composite crush box, due to through the thickness transverse stress, Mode-I interlaminar fracture will occur. However, this fracture mode was not observed in laminate design of $[45]_4$. The combination of local buckling and transverse shearing crushing modes was more likely to shape than other crushing modes. In combination of lamina bending and brittle fracture modes, the high friction and the high fracture toughness values far outweigh other crushing mechanisms in absorbing the crushing energy.

The experimental results of force-crush distance for all lay ups are compared in Figure 3.16. The results show that $[0/45]_2$ has the highest mean force and consequently the highest energy absorption capability in comparison with other lay-ups. The lowest value of mean force and energy absorption was observed in the crash box of $[45]_4$ lay-ups in which the frictional effect was low and no frond bending occurred.

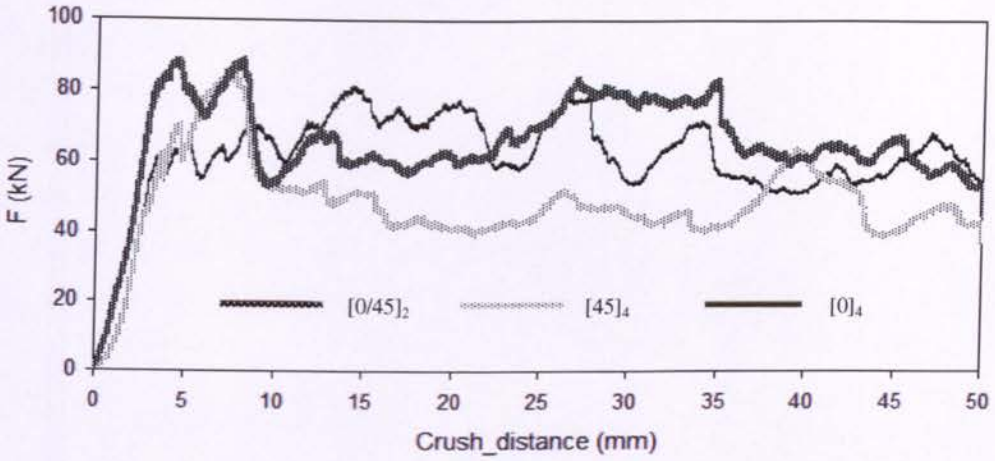

Fig. 3.16. Comparison of force-crush distance of CFRP composite boxes with different layup.

Comparison of specific energy absorption (SEA) from crush test versus G_{IC} for various lay-ups is plotted in Table 3.5. It can be seen that the total interlaminar fracture toughness in Mode-I of 0/0 is higher than the equivalent values of 0/45 and 45/45 interface planes, but 0/45 box has the highest SEA. This shows that the effect of other mechanisms such as friction and bending will increase as the total fracture energy increase beyond a certain limit. It should be mentioned that due to absence of Mode I crack in 45/45 laminated crushed box during quasi-static crushing tests, G_{IC} for this lay-up was not considered.

Table 3.5. Comparison of experimental SEA and summation of Mode-I interlaminar fracture toughness.

Laminate Lay-up	F_{max} kN	F_m kN	**CFE** %	**SEA** kJ/kg	G_{IC} **(MCC)** J/m^2	G_{IC} **(MBT)** J/m^2
$[0]_4$	67	65	97	25	900±20	1000±30
$[0/45]_2$	87	67	77	26	1200±50	1300±40
$[45]_4$	85	52	61	20	700±30	700±20

The ratio between initial maximum collapse force and mean force is known as the crush force efficiency (CFE) and the higher the value of this parameter, the better energy absorption capability.

The experimental crush force efficiency (CFE) of all composite crush boxes was obtained and the results of CFE versus interlaminar fracture toughness for various lay-ups are shown in Figure 3.17. It can be seen the CFE increases as the total interlaminar fracture toughness in Mode-I increases. The $[0]_4$ lay-up has the highest CFE. This is due to its lower initial maximum collapse force compared with other fibre orientations. This situation is more suitable for crashworthiness design cases which need to absorb the energy with a lower initial collapse force but not necessarily with the highest energy absorption capability.

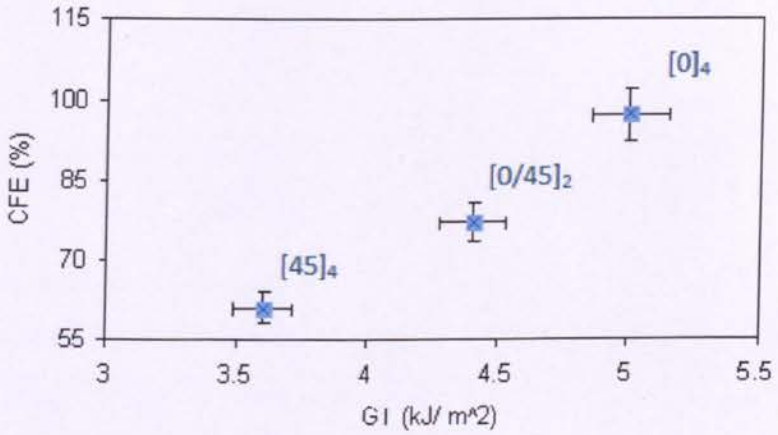

Fig. 3.17. Variation of crush force efficiency (CFE) versus interlaminar fracture toughness in Mode-I.

3.6. Conclusion

It was found that the interlaminar fracture toughness for GFRP interface fracture planes of 0/90, 90/90 and 0/45 are clustered close to each other while the equivalent value for +60/–60 interface plane is much lower. This shows that the specific energy absorptions (SEA) of fibre orientations which are laminated with $0/\theta$ angles are close together. In the lamina bending crushing mode of CFRP composite crush box, due to through the thickness transverse stress, Mode-I interlaminar fracture will occur (see Figure 3.18).

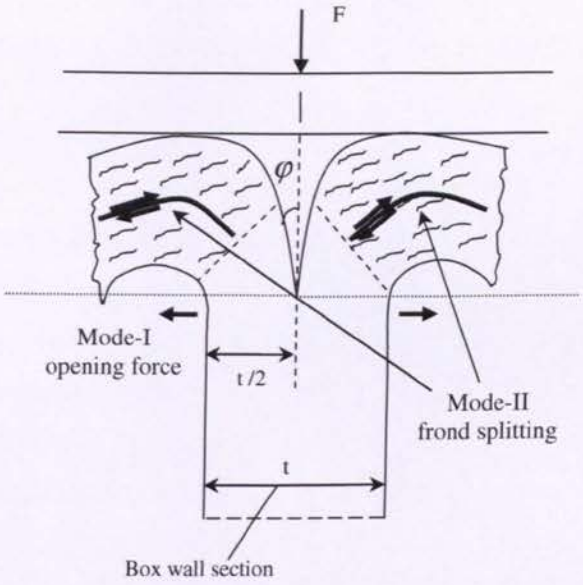

Fig. 3.18. Illustration of lamina bending crushing mode in CFRP composite box with laminate design of $[0]_4$ and $[0/45]_2$.

However, this fracture mode was not observed in laminate design of $[45]_4$. Choosing a suitable fibre orientation in the interface plane is one of the main factors for improving the energy absorption of composite crush boxes in progressive failure.

References

[1] BS EN ISO 2747, Glass Fibre Reinforced Plastics-Tensile Test, British Standard Institute, London, 1998.

[2] BS EN ISO 14129, Fibre Reinforced Plastics Composite-Determination of the In-plane Shear Stress/Shear Strain Response, Including the In-plane Shear Modulus and Strength by the ±45 Tension Test Method, British Standard Institute, London, 1998.

[3] ASTM D 3171-99, Standard test method for constituent content of composite materials. Annual book of ASTM standards, West Conshohocken, PA, 2002.

[4] BS EN ISO 15024:2001, Fibre-reinforced plastic composites. Determination of mode I interlaminar fracture toughness, G_{IC}, for unidirectional reinforced materials. BSI, 2002.

[5] Blackman BRK, Brunner AJ., Mode I fracture toughness testing of fibre reinforced polymer composites: unidirectional versus cross ply layup, In: Brown MW, de la Rios ER, Miller KJ., editor, ECF-12 Fracture from Defects, EMAS, 1998, Pages: 1471 - 1475

[6] Hashemi S, Kinloch AJ, Williams JG. Corrections needed in double-cantilever beam tests for assessing the interlaminar failure of fibre-composites, J Mater Sci Lett, 1989;8:125 – 129.

[7] Hashemi S, Kinloch AJ, Williams, JG. The analysis of interlaminar fracture in uniaxial fiber-polymer composites, P Roy Soc Lond A Mat, 1990;427:173 – 199.

[8] Williams JG. End corrections for orthotropic DCB specimens, Compos Sci Technol, 1989;35:367 – 376.

[9] Shetty MR, Vijay Kumar KR, Sudhir S, Raghu P and Madhuranath AD. Effect of fibre orientation on Mode-I interlaminar fracture toughness of Glass Epoxy composites. *Journal of Reinforced Plastic and Composites* 2000; 19:606-620.

[10] Farley GL. and Jones RM. Energy absorption capability of composite tubes and beams. *NASA TM-101634, AVSCOM TR-89-B-003*, 1989.

[11] Choi NS, Kinloch AJ, Willams JG. Delamination fracture of multidirectional carbon-fiber/epoxy composites under mode I, mode II and mixed mode I/II loading. *J Compos Mater* 1999;33(1):73–100.

[12] de Morais AB. Double cantilever beam testing of multidirectional laminates. Compos Part A: *Appl Sci* 2003;A34(12):1135–42.

[13] Pereira AB, de Morais AB. Mode I interlaminar fracture of carbon/epoxy multidirectional laminates. *Compos Sci Technol,* 2004;64(13–14):2261–70.

[14] Farley GL. Energy absorption in composite materials for crashworthy structures. In: Matthews FL, Buskell NCR, Hodgkingson JM, and Mortan J. (eds.), in: *Proceedings of the ICCM 6*. London: Elsevier Science Publishers Limited. pp. 3.57-3.66.

Chapter 4:

Effect of Mode-II Delamination Failure in Crashworthiness Analysis of Composite Box Structures

Nomenclature

a	crack length
a_e	effective crack length
b	side of box
C	compliance
$3ENF$	three-point-end-notched flexure
E	Young's modulus
f	large displacement correction factor
F	force
F_i	internal force
F_{max}	initial maximum force
F_m	mean force
G_{12}	shear modulus
G_{IIC}	Mode-II interlaminar fracture toughness
h	specimen half-thickness of ENF specimen
L	half span of ENF specimen
L_F	free length of the specimen
L_T	trigger length
N	number of fractured bundles

N'	internal force
n	number of crack in Mode-II
SEA	specific energy absorption
t	crush box wall thickness
V_f	fibre volume fraction
v	Poisson's ratio
σ_u	ultimate tensile stress
σ_b	flexural strength
τ_s	shear strength
θ	off-axis angle
φ	semi-angle of the wedge
χ	correction factor for beam root rotation

4. Introduction

Chapter-4 is in continuation of Chapter-3 and describes a study of the effect of fibre orientation and stacking sequence on Mode-II interlaminar fracture toughness, G_{IIC}, and specific energy absorption, SEA of woven fabric composite box. The manufacture and testing of 3-ENF and crush box specimens is decribed with different lay-ups of woven CFRP and GFRP composite material. From experimental results the relationship between G_{IIC} and SEA is obtained. Also the relationship between the combination of G_{IC} + G_{IIC} and SEA is discussed in detail.

4.1. Experimental studies

Five different types of test were conducted to characterize the mechanical characteristic of twill/weave CFRP and GFRP composite materials. These were tensile, shear, 3-point-end-notched flexure (3-ENF), fibre volume fraction determination, 3 point bending test (3PB) and quasi-static crush box tests. All tensile, shear, 3-ENF and fibre volume fraction tests were carried out in accordance with the relevant standards. The GFRP and CFRP specimens were manufactured from glass and carbon fibre material of densities 1.4 g/cm^3 and 1.8 g/cm^3 with epoxy resin.

4.1.1. Mechanical properties

The mechanical characteristics of glass/carbon/epoxy twill-weave fabrics were obtained by testing in accordance with the relevant standards [1-4]. These tests were tensile, shear, fibre volume fraction, coefficient of friction, 3-point-end-notched flexure (3ENF) and quasi-static crush box. All specimens were manufactured from twill/weave fabric GFRP and CFRP material of density 1.4 g/cm^3 and 1.8 g/cm^3 with epoxy resin. For twill/weave composite it was observed that crack propagation along the weft yarns was associated with more resistance than propagation along the warp direction [5]. In this regard, the weft direction was aligned with the longitudinal axis of composite boxes which crack propagates. Details of the test procedures were explained in Chapter 3. A summary of the findings for tensile, shear and fibre volume fracture are summarised in Table 4.1.

Table 4.1. Material properties of the woven a) GFRP and b) CFRP composite materials.

E_1 (GPa)	E_2 (GPa)	G_{12} (GPa)	υ_{12}	σ_u 0° (MPa)	σ_u 90° (MPa)	τ_s (MPa)	V_f (%)	σ_b MPa
27±2.2	26±3	6±0.1	0.14	516±28.1	466±29	220±21	65	450±22

(a)

E_1 (GPa)	E_2 (GPa)	G_{12} (GPa)	υ_{12}	σ_u 0° (MPa)	σ_u 90° (MPa)	τ_s (MPa)	V_f %	σ_b MPa
61±3	58±3	3.4±0.1	0.1	634±27	560±33	94±12	45	570±24

(b)

4.2. Mode-II interlaminar fracture toughness

The Mode-II interlaminar fracture toughness, G_{IIC}, can be measured by the three-point-end-notched flexure (3ENF), the end-loaded split (ELS) and the four-point-end-notched flexure (4ENF) tests (see Figure 4.1) [6]. The ENF test is categorised with 3-point bending flexure but this specimen leads to unstable initiation, thus preventing the measurement of propagation toughness. The 4-ENF specimen is able to offer significant advantages such as stable crack propagation, a simple test fixture and a straight forward data analysis. However, the measured toughness of 4-ENF specimen is sensitive to geometrical non-linearity associated with changes in roller contact points and loading point rotation [7]. In this regard, the effects of friction and fixture compliance need to be taken into account. The ELS specimen geometry shows stable initiation while this specimen is affected by clamp variability and is more prone to large displacement [8,9].

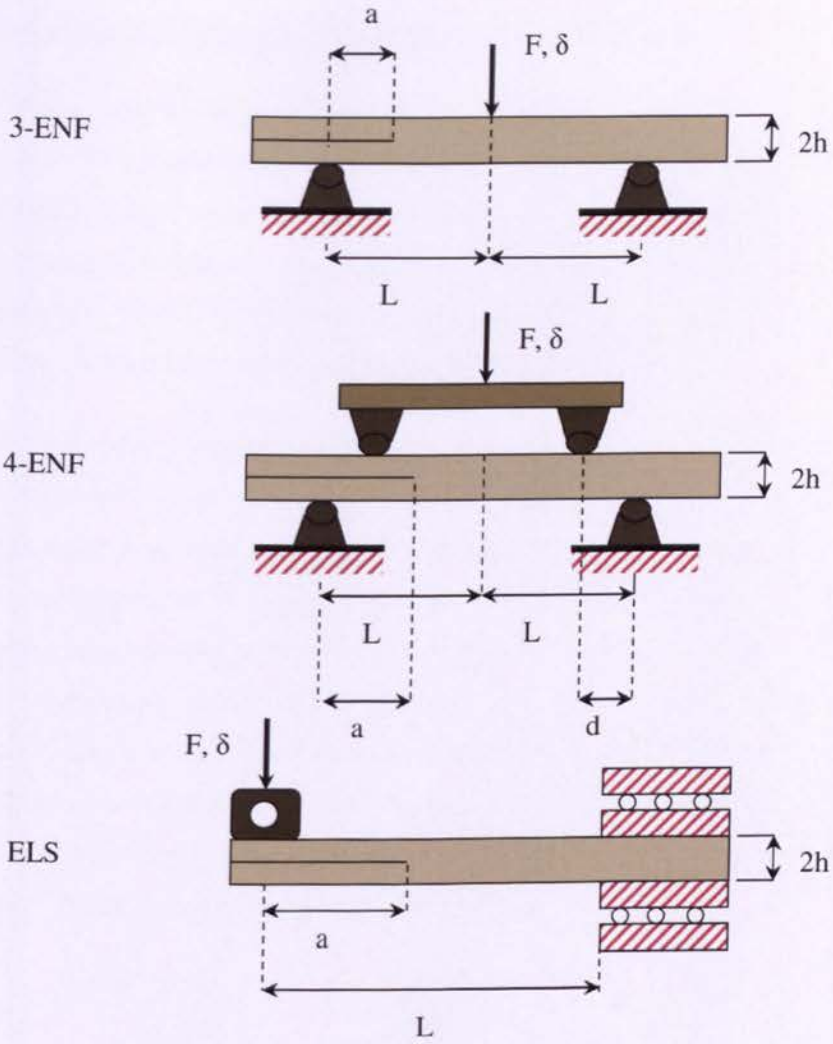

Fig. 4.1. The mode-II delamination specimens.

Because of the simplicity of the 3ENF test setup, this method is the most used [10]. Measuring the Mode-II fracture toughness from film inserts yields a higher toughness than from precracks. This is in contrast to Mode-I testing where fibre bridging causes higher fracture toughness from precracks [11]. In the present work, as the initiation values of G_{IC} and G_{IIC} is more relevant than propagation values, the 3ENF test method was used to study the effect of Mode-II fracture toughness on the energy absorption of the composite box.

4.3. Determination of Mode-II interlaminar fracture toughness

The fabrication of GFRP and CFRP 3-ENF specimens were laid-up according to the laminate design of each GFRP and CFRP composite crush box which will be discussed later. The mid-plane interface of GFRP was 0//0 to determine the Mode-II interlaminar fracture toughness for three fracture locations. The mid-plane interfaces of CFRP ENF specimens were respectively 0//0, 0//45 and 45//45 with respect to the weft direction. The crack propagation was set along the weft direction which was defined as 0 direction.

The 3ENF specimens were made according to ESIS protocol [4] with the width of 20mm and the total length of 160mm, while the thickness varied from 5 to 6mm. This thickness was required to avoid large displacement, plastic deformation and intraply damage. A precrack length of 55mm from the free end of specimen was inserted using a Teflon film (see Figure 4.2). Loading was carried out at a constant crosshead displacement rate of 2 mm/min. The details of specimen preparation and testing method were explained in Chapter 2. However, due to rapid crack propagation without any clear mouth opening in 3ENF Mode-II tests, the initiation fracture toughness which was obtained is more accurate than the propagation result. The force at each crack length was retrospectively obtained from the recorded force-displacement diagram to calculate G_{IIC} (see Figure 4.3).

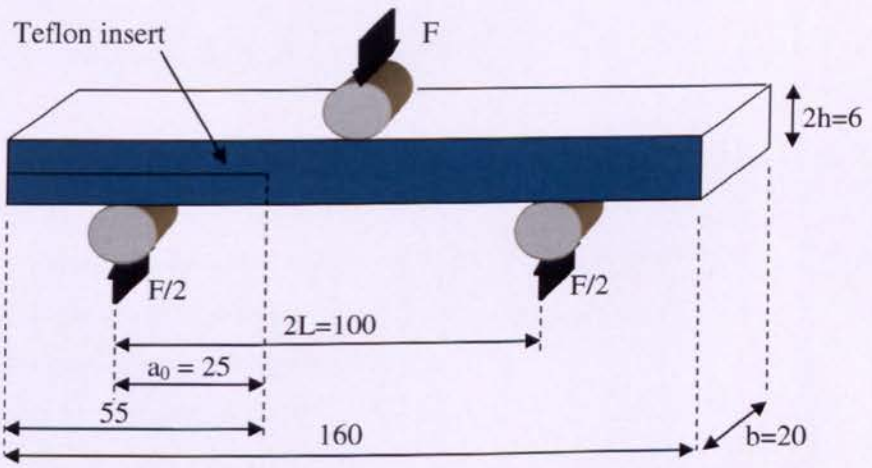

Fig. 4.2. Geometries of 3-ENF specimens (All dimensions in mm).

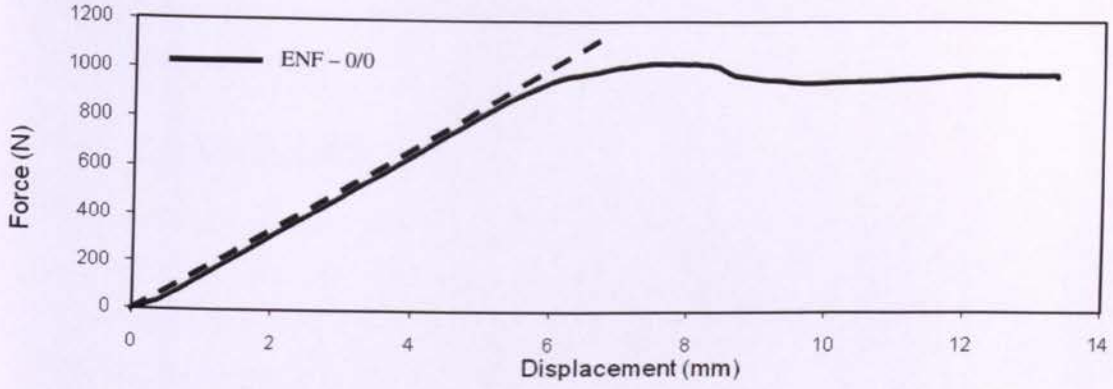

(a) GFRP

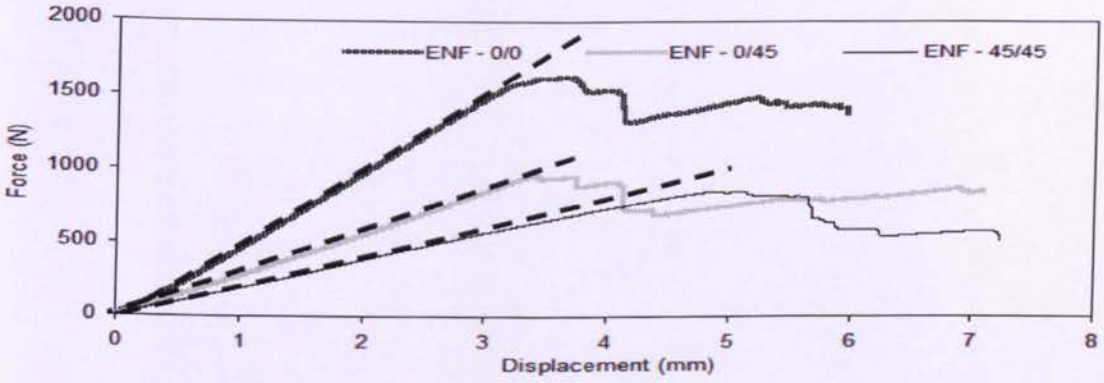

(b) CFRP

Fig. 4.3. Force-load line displacement from 3ENF tests for various mid-plane interfaces (a) GFRP and (b) CFRP.

A travelling optical microscope was used to accurately measure the length of the initial crack. The travelling microscope, with 10X magnification, slides along a horizontal scale similar to that used on callipers. A cross-hair is lined up with the path of the load through the hinges (load line). The position of the microscope was noted to the nearest tenth of a millimetre. The travelling microscope was then moved, by turning a knob, to the end of the polymer insert, sighted using the pre-mentioned pen line. The position of the microscope was again noted, and the difference of these two measurements gave the initial crack length. Loading was carried out at a constant crosshead displacement rate of 2 mm/min. The position of the crack tip was monitored through the microscope as the crack advanced. When the crack first visibly propagated, the displacement of the crosshead was recorded. As the crack propagation past the subsequent marked lines, the crack length and crosshead displacement were recorded.

The force at each crack length was retrospectively obtained from the force-displacement diagram to calculate G_{IIC}.

4.4. Composite crush box

The crush box specimens were made of the glass/epoxy and carbon/epoxy twill-weave fabric by hand lay-up with fibre orientations in accordance to those used in 3ENF tests as described in the previous section. The 0° direction which coincided with the axial axis of the crush box was parallel to the weft direction. All details of specimen preparation and testing method were reported in Chapter 3. Each specimen was crushed at the rate of 2mm/min between two parallel platens for 50mm stroke using a Universal Testing Machine with 500 kN load cell. For each test configuration three specimens were tested. The force-crush distance diagrams were recorded automatically for each test (see Figure 4.12).

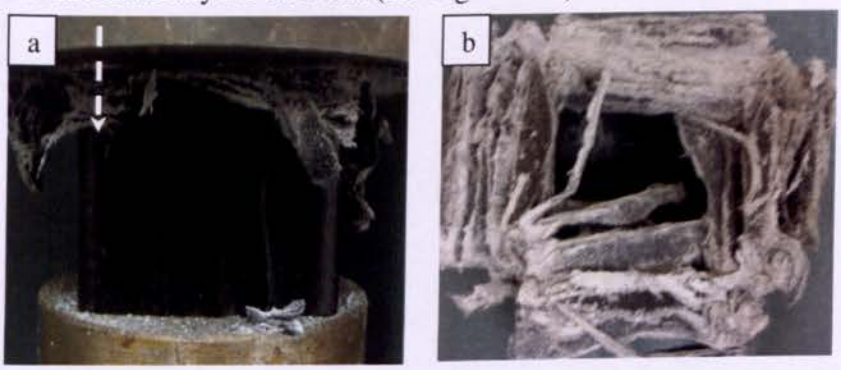

Fig. 4.4. GFRP composite crush box specimens, (a) crushing process (b) plane view of crushed box.

4.5. Compliance of the 3-ENF specimen

The 3-ENF specimen is divided into two sub-problems using the principle of superposition [12]. These sub-problems are; an un-cracked beam under three-point bending and a beam with the same dimension but with a mid-plane crack at one end. This beam is skew symmetric (see Figure 4.5).

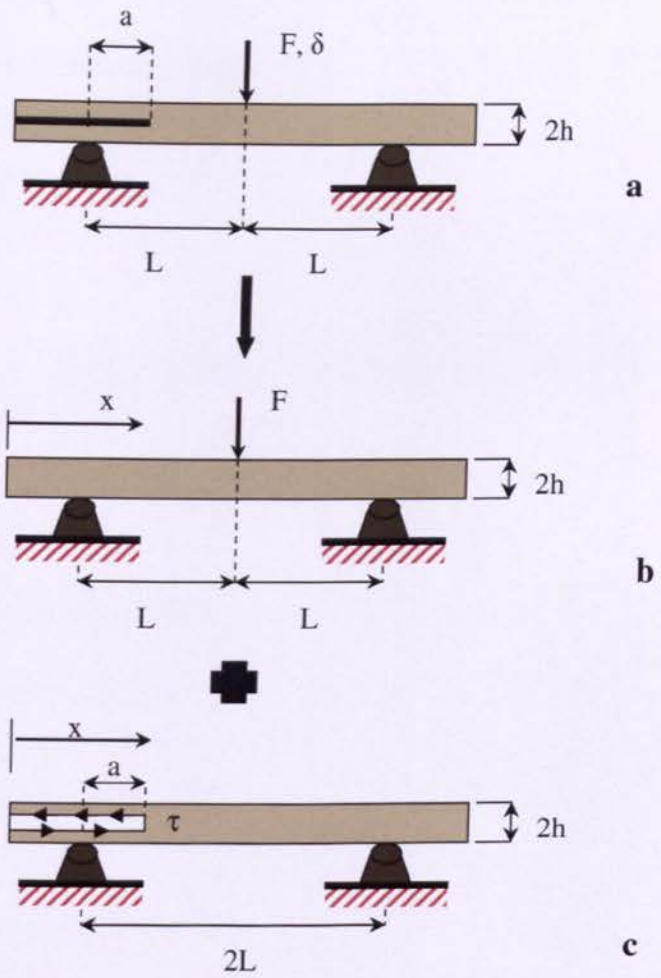

Fig. 4.5. The beam theory model for 3-ENF specimen, (a) ENF specimen, (b) un-cracked beam under 3PB, and (c) skew-symmetric beam under crack surface traction [12].

Based on Timoshenko's beam theory [12], the compliance of the un-cracked beam is calculated as;

$$C' = \frac{L}{4kG_{12}bh} + \frac{L^3}{4E_1bh^3} \tag{4.3}$$

where b and h are the width and half thickness of the beam and k is the shear correction factor.

The compliance of the skew-symmetry is analysed only for the upper half portion of the beam. This analysis is partitioned to two portions. First in the un-cracked portion (x > a), the longitudinal displacements along the bottom are zero since they are located along the neutral axis of the un-crack beam portion. Second the reacting shear traction, τ, applies on the bottom

surface of the upper half beam. In the cracked portion (x < a), the surface of the crack also has a shear traction, τ_0. Based on simple beam theory [13], the direction of the shear stress in the cracked surface is shown in Figure 4.6.

$$\tau_0 = \frac{3F}{8bh} \tag{4.4}$$

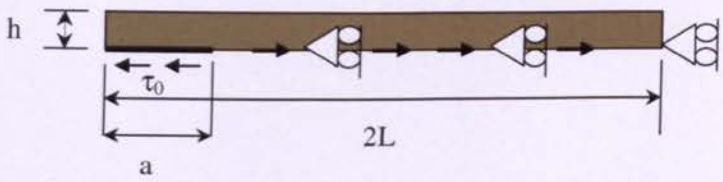

Fig. 4.6. Upper half beam model of second sub-problem [12].

Now, the displacement and rotation fields in the un-cracked (a < x < 2L) and cracked (0 < x < a) portion of sub-problem two are analysed analytically. Then the compliance of the 3-ENF specimen is obtained by summation of the compliances of un-cracked and cracked beam, respectively.

4.5.1. Un-cracked portion (a < x < 2L)

The longitudinal displacement of the un-cracked portion at the neutral plane of the beam is,

$$u(x) = -\frac{1}{E_1 bh}\int F_i\,dx + k\tau - \frac{h}{2}\beta = 0 \tag{4.5}$$

where k is the coefficient of shear compliance for an orthotropic material as [12];

$$k = \frac{h}{3\lambda G_{12}} \tag{4.6}$$

Differentiating Eq. (5) two times becomes,

$$k\frac{d^2\tau}{dx^2} - \frac{1}{E_1 bh}\frac{dF_i}{dx} - \frac{h}{2}\frac{d^2\beta}{dx^2} = 0 \tag{4.7}$$

The relation between the internal forces and stresses (Figure 3.7) in the second sub-problem are;

$$\frac{dF_i}{dx}=b\tau,\quad \frac{dM}{dx}=-\frac{h}{2}b\tau,\quad \frac{d^2w}{dx^2}=\frac{d\beta}{dx}=-\frac{M}{E_1 I},\quad \frac{dw}{dx}-\beta=0,\quad \frac{du}{dx}=-\frac{F_i}{E_1 bh} \tag{4.8}$$

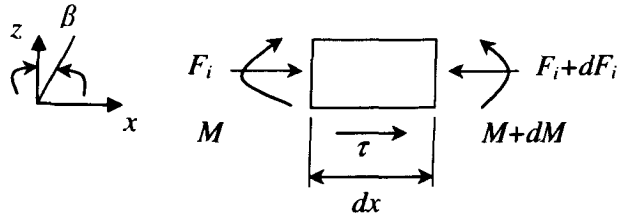

Fig. 4.7. Beam internal forces.

From Eqs. (6), (7) and (8) the following relations are derived,

$$\frac{d^2\beta}{dx^2}=\frac{hb}{2E_1 I}\tau \tag{4.9}$$

$$\frac{d^2\tau}{dx^2}-\frac{12\lambda G_{12}}{E_1 h^2}\tau=0 \tag{4.10}$$

The shear stress is obtained by solving Eq. (10) as,

$$\tau(x)=c_1 e^{-\frac{x-a}{\chi h}}+c_2 e^{\frac{x-a}{\chi h}} \tag{4.11}$$

where,

$$\chi=\sqrt{\frac{E_1}{12\lambda G_{12}}} \tag{4.12}$$

Assuming $L >> h$, the shear stress is small; while in the case of x-a $>> \chi h$, c_2 must be very small constant and consequently it is neglected. From Eqs. (4) and (11) the equilibrium condition along the beam half-height yields to the Eq. (13) as;

$$\int_0^a\left(-\frac{3F}{8bh}\right)bdx+\int_a^L c_1 e^{-\frac{x-a}{\chi h}}bdx=0 \tag{4.13}$$

Thus, the shear stress τ for x >> a is obtained from Eqs. (11) & (13) as,

$$\tau(x)=\frac{3Fa}{8b\chi h^2}e^{-\frac{x-a}{\chi h}} \tag{4.14}$$

The moment at this portion (x >> a) is calculated as,

$$M(x) = -\frac{h}{2}\left(\int_0^a \frac{-3F}{8bh} \right) bdx + \int_0^x \left(\frac{3Fa}{8bxh^2} e^{-\frac{x-a}{xh}} \right) bdx = \frac{3Fa}{16} e^{-\frac{x-a}{xh}} \quad (4.15)$$

Substituting Eq. (15) into Eq. (8), the rotation and deformation of the beam becomes,

$$\beta_1 = -\int \frac{M(x)}{E_1 I} dx = D_1 + \frac{3Faxh}{16E_1 I} e^{-\frac{x-a}{xh}} \quad (4.16)$$

$$w_1 = \int \beta dx = -\frac{3Fa(xh)^2}{16E_1 I} e^{-\frac{x-a}{xh}} + D_1 x + D_2 \quad (4.17)$$

4.5.2. Cracked portion (0 < x < a)

The same procedures are followed to find the rotation and deformation of the cracked portion (0 < x < a) as,

$$\beta_2 = \frac{3x^2}{32E_1 I} + D_3 \quad (4.18)$$

$$w_2 = \frac{x^3}{32E_1 I} + D_3 x + D_4 \quad (4.19)$$

Using the following boundary conditions, the unknown parameters of D_1, D_2, D_3 and D_4 can be found.

$$w_2(x=0) = 0, \quad w_1(x=2L) = 0, \quad w_2(x=a) = w_1(x=a), \quad \beta_2(x=a) = \beta_1(x=a) \quad (4.20)$$

Using superposition principle the compliance, C, is obtained as,

$$C = C' + C_{crack} \quad (4.21)$$

Therefore, the compliance becomes,

$$C = \frac{2L^3 + 3a^3}{8E_1 bh^3} \quad (4.22)$$

Using classical simple beam theory (SBT), the load-point compliance in the 3ENF specimen is [14],

$$C = \frac{\delta}{F} \tag{4.23}$$

Using the compliance equation

$$G = \frac{F^2}{2b}\frac{dC}{da} \tag{4.24}$$

The interlaminar fracture toughness can be found Eqs. (4.3), (4.4) and (4.5):

$$G_{IIC} = \frac{9F\delta a^2}{2b\left(2L^3 + 3a^3\right)} \tag{4.25}$$

Various other methods of the *Compliance Calibration Method (CCM)*, the *Corrected Beam Theory (CBT)* and the *Corrected Beam Theory (CBT^{WW})* after Wang and Williams [15] are used to calculate the Mode-II interlaminar fracture toughness, G_{IIC}. In *CCM* compliance is based on the least squares linear regression as [16],

$$CN_1 = A + ma^3 \tag{4.26}$$

where N_1 is a large displacement correction factor and A and m are data fitting constants. Thus, G_{IIC}, becomes:

$$G_{IIC} = \frac{3mF^2a^2}{2b}\frac{F'}{N_1} \tag{4.27}$$

where F' is an additional large displacements correction factor which was found negligible in 3*ENF* tests [14].

In this work *Simple Beam Theory* (SBT) and *Corrected Calibration Method* (CCM) were used to determine the Mode-II fracture toughness. Due to the difficulties in defining the exact position of crack initiation, the non-linearity (NL) and the 5% offset are used to find the crack initiation.

The results of Mode-II delamination fracture toughness, G_{IIC}, using non-linearity (NL) for each interface, are presented in Table 4.2.

Table 4.2. Interlaminar fracture toughness obtained from 3ENF tests for various interface fibre orientations.

Laminate lay-up	**Fracture plane interface**	G_{IIC} **(CCM)** J/m^2	G_{IIC} **(SBT)** J/m^2
CFRP-$[0]_4$	0//0	2000±50	2400±40
CFRP-$[0/45]_2$	0//45	1600±30	1500±60
CFRP-$[45]_4$	45//45	1200±30	900±20
GFRP-$[0]_{10}$	0//0	3700±50	3200±70

CCM: Compliance Calibration Method, SBT: Simple Beam Theory

The Mode-II interlaminar fracture toughness of the interface layers of (0/0) woven CFRP composite material showed the highest values of G_{IIC} for all specimens, and for interface layers of (45/45) showed the lowest value. The experimental resistance curves of woven GFRP and CFRP composite materials of G_{IIC} versus crack length are presented in Figure 4.8 and 4.9.

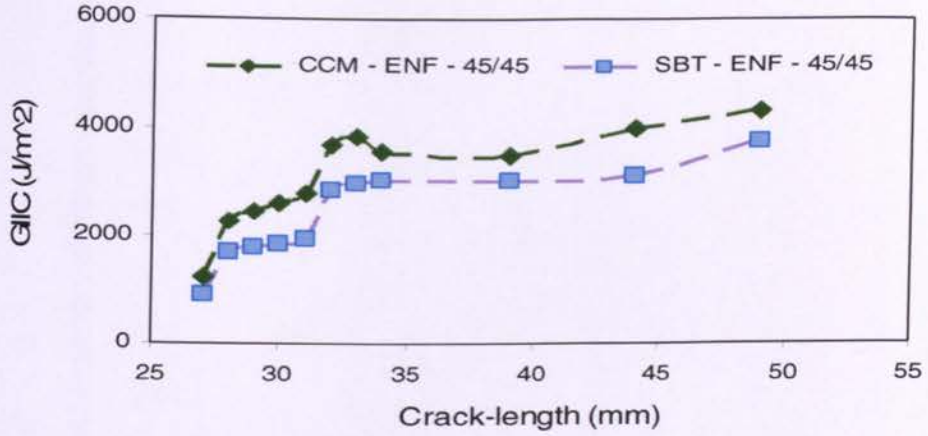

(a) Interface of 45/45

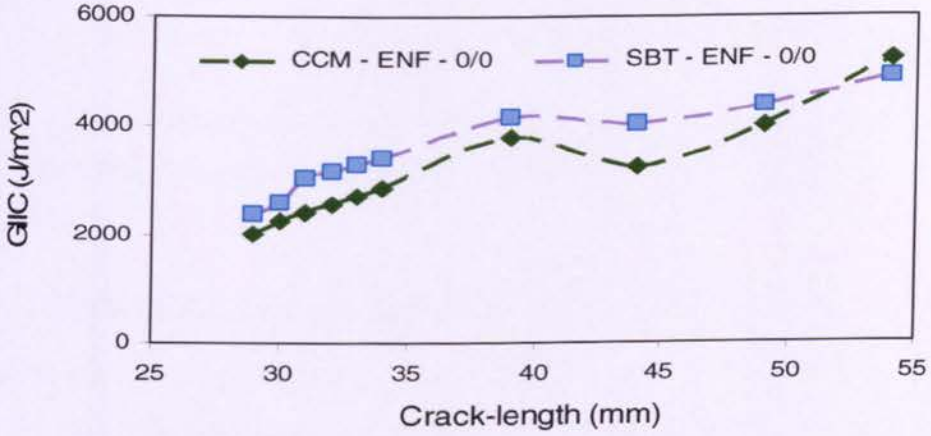

(b) Interface of 0/0

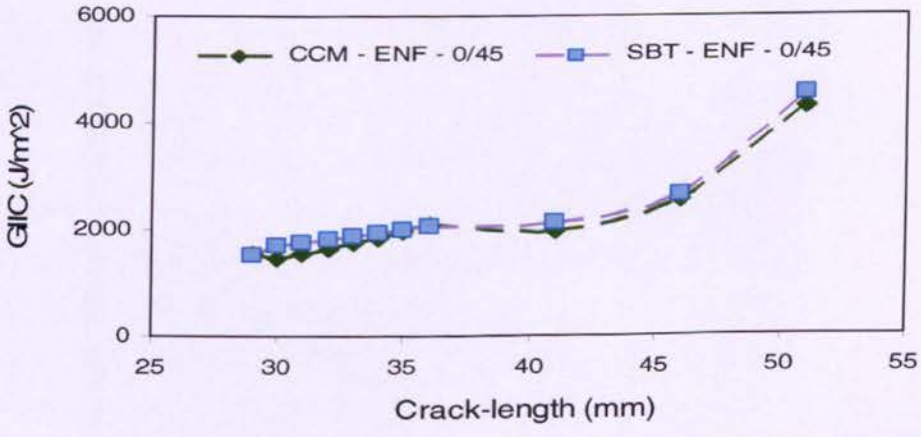

(c) Interface of 0/45

Fig. 4.8. Resistance curve (R-curve) in 3ENF woven CFRP specimens with (a) 45/45, (b) 0/0 and (c) 0/45 fracture plane interfaces using *CCM* and *SBT* methods.

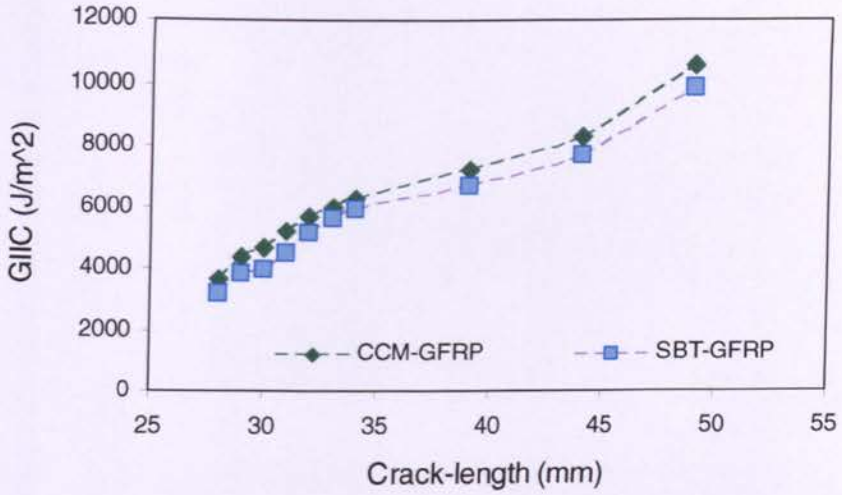

Fig. 4.9. Resistance curve (R-curve) in woven GFRP 3ENF specimens with 0/0 fracture plane interface using Compliance Calibration Method (*CCM*) and Simple Beam Theory (*SBT*) methods.

4.6. Progressive crushing process of woven CFRP composite crush box

Each woven GFRP and CFRP composite box (as described in 3.4) was crushed between two parallel platens for 50mm stroke using a universal testing machine with 500 kN load cell. The crush speed was set at 2 mm/min, the same speed as used for the 3ENF tests. For each test configuration three specimens were tested. The force-crush distance diagrams were recorded automatically for each test.

The combinations of three distinct crushing modes were observed for woven CFRP composite boxes during quasi-static crush tests. As can be seen in Figure 4.10, the combination of lamina bending and brittle fracture modes was observed for fibre orientations of $[0]_4$ and $[0/45]_2$ and also the combination of transverse shearing and local buckling was found for laminate design of $[45]_4$. The combination of lamina bending and brittle fracture crushing modes showed the highest energy absorption in comparison with the other observed modes. This high energy absorption is caused by a larger crush area and therefore a higher potential to absorb energy by frictional effects at the platen/specimen interface.

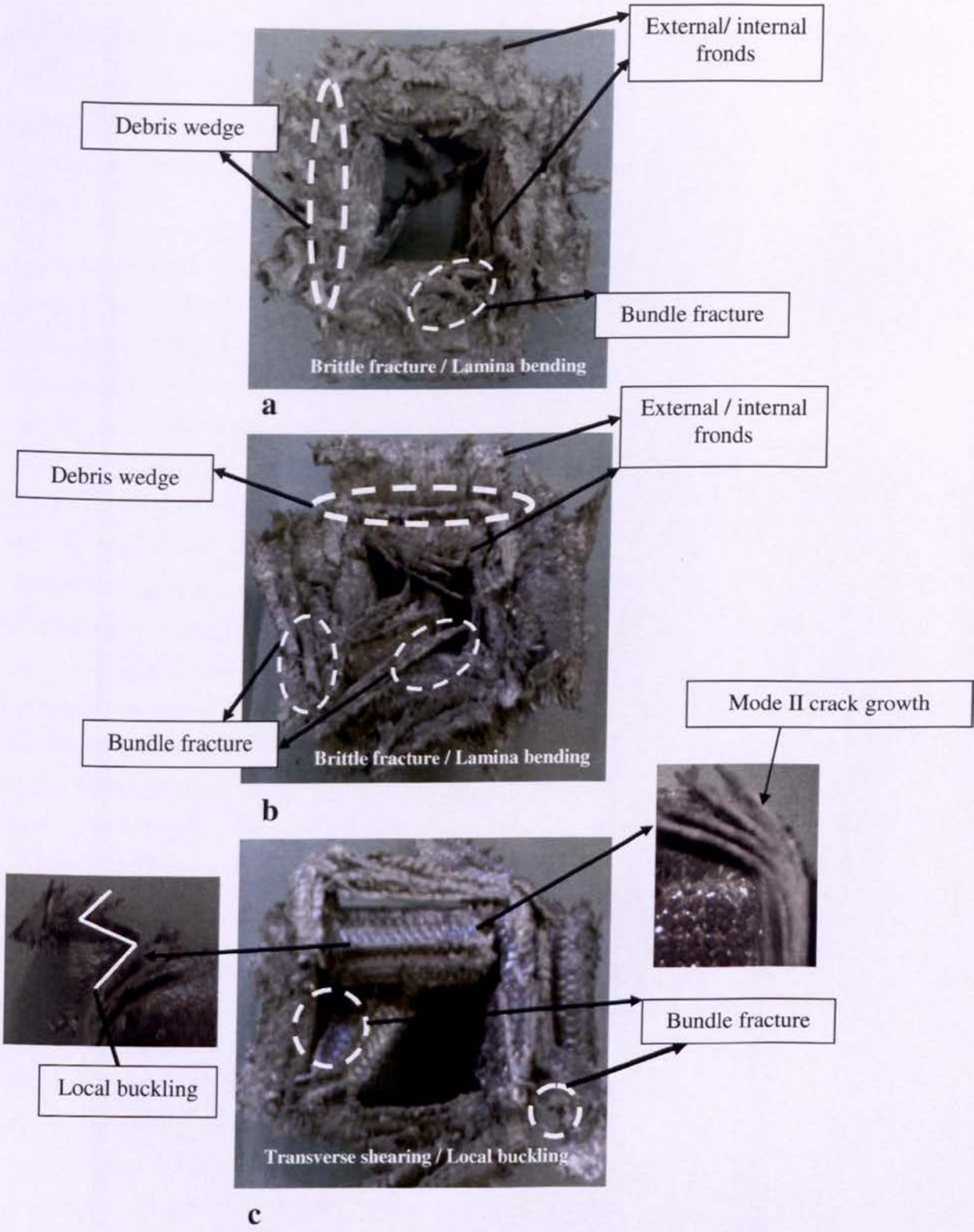

Fig. 4.10. Plane view of crushed CFRP composite box. a) $[0]_4$, b) $[0/45]_2$, and c) $[45]_4$.

The force-crush distance of lamina bending crushing mode showed that the majority of serrations were of small amplitude. This situation causes the stresses required to initiate crack propagation to increase and consequently causes high energy absorption. In brittle fracture and lamina bending many interlaminar and intralaminar cracks were formed in the crush zone.

The deformation of all boxes was elastic at the beginning of crushing process while the load increased rapidly to its maximum. At the initial stages of the crushing, four axial cracks were formed at the corners of each box which caused splitting of the transverse fibres and bending of the internal and external fronds. It was observed that the external fronds were nearly the same size as internal fronds. For all boxes except the laminate design of $[45]_4$ the main cracks started and continued to propagate along the central interwall, and lamina bundles were formed. At this stage the load dropped from its peak and stabilised around a mean force, F_m. The magnitude of the mean force was found to depend on the propagation of the interlaminar and intralaminar cracks. In this stage which is called post-crushing regime, the internal and external fronds were buckled when the applied force reached a critical value. In crushing of $[0]_4$ and $[0/45]_2$ boxes, some lamina bundle fracture mechanisms were observed during frond bending as the central interwall crack propagated. In crushing of $[45]_4$ box, local buckling and many lamina bundle fracture and short interlaminar Mode-II crack propagation occurred (Figure 4.10c). In this case the interlaminar stresses are small relative to the strength of the matrix and no Mode-I crack growth will occur. This situation yields to shape local buckling crushing mode with many bundle fractures in transverse shearing mode.

In lamina bending mode, the main central crack causes to shape lamina bundles which has a significant role on absorbing the impact energy. The propagation of this type of crack is the same as crack propagation in Mode-I delamination in composite laminates discussed earlier in Chapter 3. We saw that the fibre orientation at the interface planes had a significant effect on Mode-I interlaminar fracture toughness. Also in this failure mode the fronds splitting due to lamina bundle bending is similar to interlaminar crack propagation in Mode-II (see Figure 4.11). The G_{IC} and G_{IIC} of initiation are more influential than the G_{IC} and G_{IIC} of propagation in the energy absorption mechanism [17]. Hence, the Mode-I and Mode-II initiation values were chosen to quantify the effect of Mode-I and Mode-II fracture toughness on the energy absorption of the composite box.

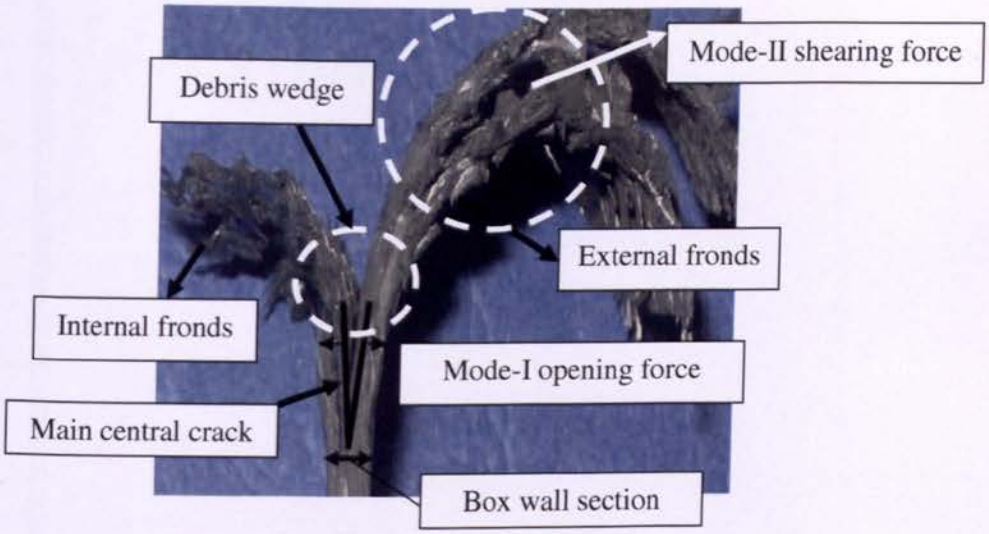

Fig. 4.11. Mode-I & Mode-II interlaminar crack propagation at the central interwall in $[0/45]_2$ and $[0]_4$ CFRP composite boxes.

Regarding the fracture toughness study in previous sections, the interface of 0/45 showed the highest Mode-I fracture toughness and the interface of 0/0 showed the highest Mode-II fracture toughness while the lowest of both Mode-I and Mode-II fracture toughness was observed along interface of 45/45.

In the lamina bending crushing mode due to through the thickness transverse stress, Mode-I interlaminar fracture will occur. However, this fracture mode was not observed in the laminate design of $[45]_4$, (see Figure 4.10c). The combination of local buckling and transverse shearing crushing modes was more likely to shape than other types of crushing modes. In the combination of lamina bending and brittle fracture modes, the high friction and the high fracture toughness values far outweigh other crushing mechanisms in absorbing the crushing energy [18].

The experimental results of force-crush distance for all lay ups of CFRP composite box are compared in Figure 4.12. The results show that $[0/45]_2$ has the highest mean force and consequently the highest energy absorption capability in comparison with other lay-ups. Owing to no frond bending and low frictional effect this was reflected on the lowest values of mean force and energy absorption in the crush box of $[45]_4$ lay-ups.

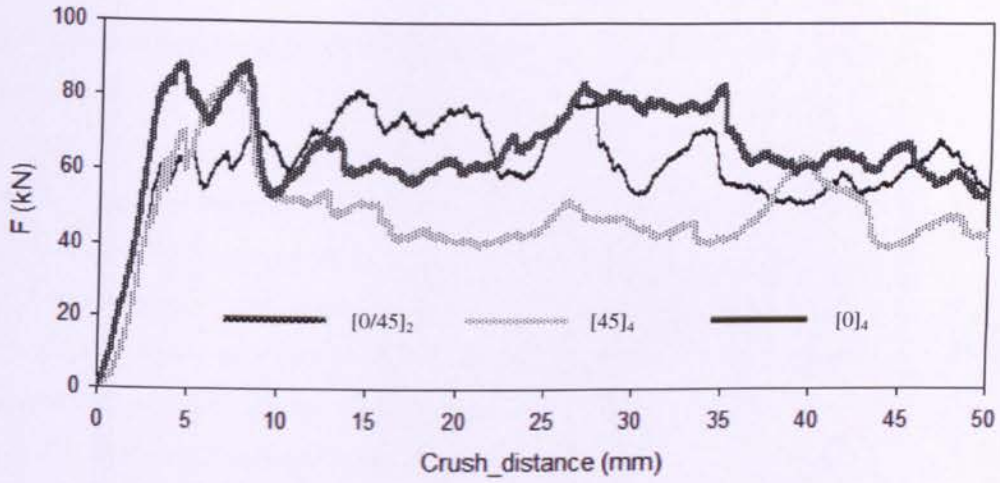

Fig. 4.12. Comparison of force-crush distance of CFRP composite boxes with different layup.

The variation of the specific energy absorption (SEA) from the crush test versus a summation of G_{IC} and G_{IIC} for various lay-ups of CFRP composite box is plotted in Figure 4.13a. It can be seen that the total interlaminar fracture toughness in Mode-I and Mode-II of 0/0 is higher than the equivalent values of 0/45 and 45/45 interface planes, but the 0/45 box has the highest SEA. This shows that the effect of other mechanisms such as friction and bending will increase as the total fracture energy increase beyond a certain limit. It should be mentioned that due to absence of Mode-I crack in 45/45 laminated crushed box during quasi-static crushing tests, G_{IC} for this lay-up was not considered in Figure 4.13. A summary of results is presented in Table 4.3. Choosing a suitable fibre orientation at the interface plane is one of the main factors for improving the energy absorption of composite crush boxes in progressive failure.

Table 4.3. Comparison of experimental SEA and summation of Mode-I and Mode-II interlaminar fracture toughness.

Laminate Lay-up	F_{max} kN	F_m kN	**CFE** %	**SEA** kJ/kg	$G_T^{(1)}$ kJ/m^2
$[0]_4$	67	65	97	25	5
$[0/45]_2$	87	67	77	26	4.4
$[45]_4$	85	52	61	20	3.6

(1) Under the assumption that $G_T = G_{IC} + 2G_{IIC}$ for box lay-ups of $[0/45]_2$ and $[0]_4$ and $G_T = 3G_{IIC}$ for box lay-up of $[45]_4$ as no Mode-I crack was observed in this lay-up.

The ratio between initial maximum collapse force and mean force is known as the crush force efficiency (CFE) and the higher the value of this parameter, the better the energy absorption capability. The experimental crush force efficiency (CFE) of all composite crush boxes was obtained and the results of CFE versus interlaminar fracture toughness for various lay-ups are shown in Figure 4.13b. It can be seen the CFE increases as the total interlaminar fracture toughness in Mode-I and Mode-II increases. The $[0]_4$ lay-up has the highest CFE. This is due to its lower initial maximum collapse force compared with other fibre orientations. This situation is more suitable for crashworthiness design cases which need to absorb the energy with a lower initial collapse force but not necessarily with the highest energy absorption capability [19].

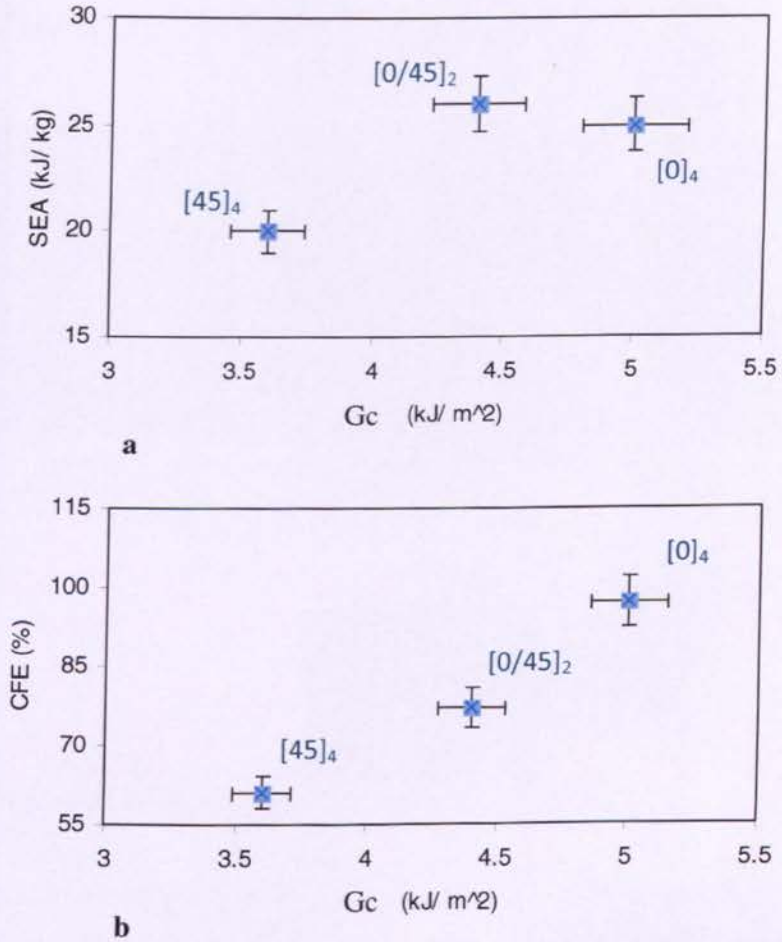

Fig. 4.13. (a) Variation of specific energy absorption (SEA) and (b) crush force efficiency (CFE) versus summation of interlaminar fracture toughness in Mode-I and Mode-II, i.e., G_{IC} $+2G_{IIC}$ for boxes with $[0/45]_2$ and $[0]_4$ lay-ups and $3G_{IIC}$ for boxes with $[45]_4$ lay-up.

4.7. Progressive crushing process of woven GFRP composite crush box

Each woven glass/epoxy composite box was crushed between two platen for 50mm stroke using a Universal Testing Machine with 500 kN load cell. The crush speed was set at 2 mm/min, the same speed as used for the 3ENF tests. For each test configuration three specimens were tested. The force-crush distance diagrams were recorded automatically for each test. The crushing process at axial crushing process was in brittle fracture crushing mode (see Figure 4.14). In brittle fracture crushing mode the crushing process is a combination of transverse shearing and lamina bending crushing modes. In this mode the length of the interlaminar cracks are between 1 to 10 laminate thicknesses. In this case the main energy absorption mechanism is fracturing of lamina bundles. The highest energy absorption of composite tubes was observed in brittle fracture and lamina bending crushing modes.

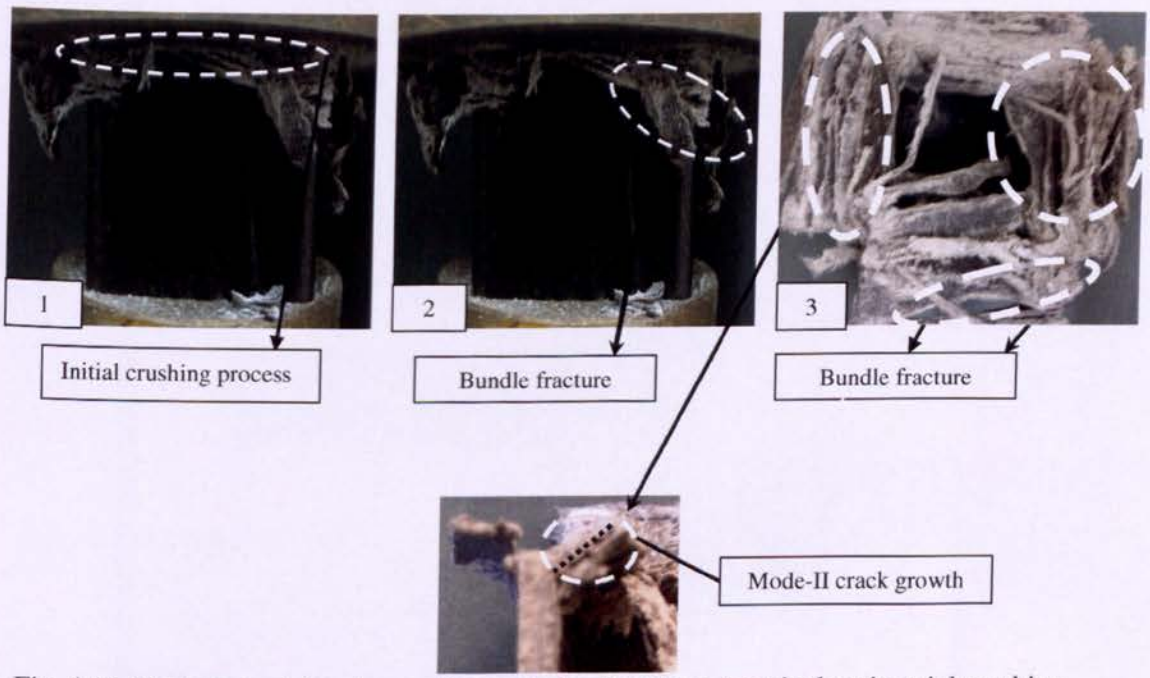

Fig. 4.14. Various crushing stages of woven glass/epoxy composite box in axial crushing.

In brittle fracture crushing mode two main mechanisms of bundle fractures and inter/intra laminar crack propagation control the energy absorption during quasi-static crushing process. For the woven GFRP composite box all these mechanisms were observed in the crushing process (see Figure 4.15).

The interlaminar crack propagation in Mode-II was one of the fracture mechanisms which contributed in the energy absorbing of GFRP composite box. The value of dissipated energy due to Mode-II delamination can be found from Eq. (27),

$$U_D = n(4\lambda b)G_{IIC} \tag{3.27}$$

where, λ is crush distance, b is the width of composite box and n is number of delamination crack growth in Mode-II. The crack propagation in Mode-II also can affect the bending resistance of bundles during the crushing process.

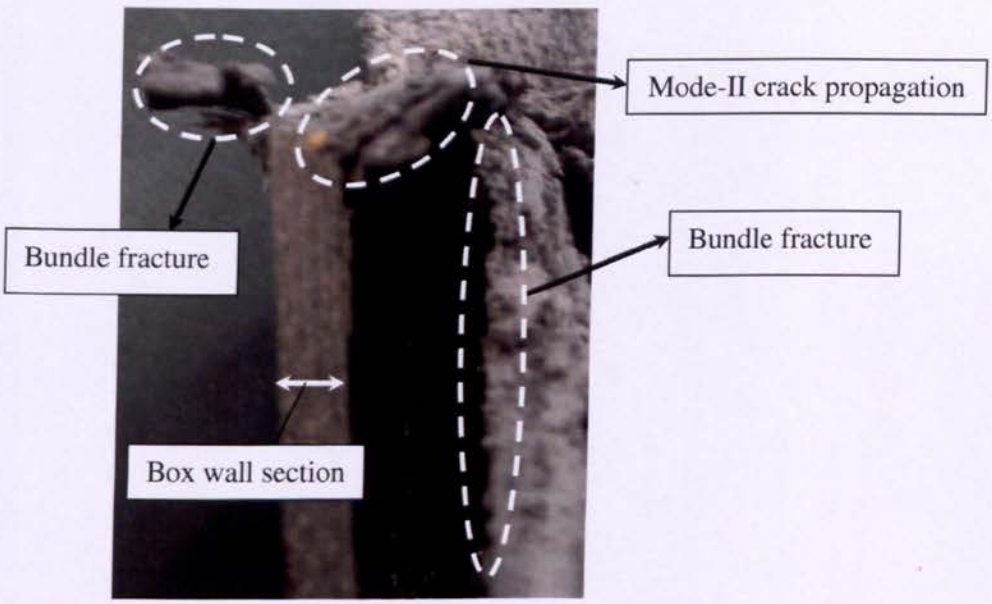

Fig. 4.15. Fracture mechanisms of brittle fracture crushing mode at the central interwall in $[0]_{10}$ GFRP composite box.

4.8. Conclusion

It was shown that the total interlaminar fracture toughness in Mode-I and Mode-II of 0/0 is higher than the equivalent values of 0/45 and 45/45 interface planes of CFRP composites, but 0/45 box has the highest SEA. This indicates that the effect of other mechanisms such as friction and bending will increase as the total fracture energy increase beyond a certain limit. It can be seen the CFE increases as the total interlaminar fracture toughness in Mode-I and

Mode-II increases. The $[0]_4$ lay-up has the highest CFE. This is due to its lower initial maximum collapse force compared with other fibre orientations. This situation is more suitable for crashworthiness design cases which need to absorb the energy with a lower initial collapse force but not necessarily with the highest energy absorption capability.

References

[1] BS EN ISO 2747, Glass Fibre Reinforced Plastics-Tensile Test, British Standard Institute, London, 1998.

[2] BS EN ISO 14129, Fibre Reinforced Plastics Composite-Determination of the In-plane Shear Stress/Shear Strain Response, Including the In-plane Shear Modulus and Strength by the ±45 Tension Test Method, British Standard Institute, London, 1998.

[3] ASTM D 3171-99, Standard test method for constituent content of composite materials. Annual book of ASTM standards, West Conshohocken, PA, 2002.

[4] Davies P, editor. Protocols for interlaminar fracture testing of composites. ESIS-Polymers and Composites Task group; 1993.

[5] Alif N, Carlsson LA, Boogh L. The effect of weave pattern and crack propagation direction on mode I delamination resistance of woven glass and carbon composites. *Composites Part B*, 1998;29(B):603-611.

[6] Russel AJ, Street KN. Factor affecting the interlaminar fracture energy of graphite/epoxy laminates, in *Progress in Science and Engineering of Composites,* Hayashi T, Kawata K, Umekawa S. Eds., ICCM-IV, ASM International, Tokyo, 1982;279-286.

[7] Davidson BD, Sun X. Effects of friction, geometry, and fixture compliance on the perceived toughness from three-and four-point bend end-notched flexure tests. *J Reinf Plastics Compos,* 2005;24:1611–28.

[8] Hashemi S, Kinloch AJ, Williams JG. The analysis of interlaminar fracture in uniaxial fibre-polymer composites. *Proc Royal Soc*, 1990;427(A):173–99.

[9] Wang H, Vu-Khanh T, Le VN. Effects of large deflection on mode II fracture test of composite materials. *J Compos Mater*, 1995;29:833–49.

[10] Davies P, Sims GD, Blackman BRK, Brunner AJ. Comparison of test configurations for determination of mode II interlaminar fracture toughness: results from international collaborative test programme. Plastic, Rubber Comp 1999;28:432-7.

[11] Moore DR, Pavan A, Williams JG, Editors. Fracture mechanics testing methods for polymers, adhesives and composites. ESIS Publication 28. Elsevier Science Ltd, 2001.

[12] Wang J, Qiao P. Novel beam analysis of end notched flexure specimen for mode-II fracture. *Eng Frac Mechans,* 2004;71:219-231.

[13] Reddy JN. Energy and variational methods in applied mechanics. New York: John Wiley & Sons; 1984.

[14] Moura MFSF, Morais AB. Equivalent crack based analysis of ENF and ELS tests, *Eng Frac Mechans,* 2008;75:2584-2596.

[15] Wang Y, Williams JG. Corrections for mode II fracture toughness specimens of composite materials. *Comp Sci Technol,* 1992;43:251-6.

[16] Moore DR, Pavan A, Williams JG, Editors. Fracture mechanics testing methods for polymers, adhesives and composites. ESIS Publication 28. Elsevier Science Ltd, 2001.

[17] Savona SC and Hogg PJ. Effect of fracture toughness properties on the crushing of flat composite plates. *Compos Sci Technol,* 2006;66:2317-2328.

[18] Hadavinia H and Ghasemnejad H. Effects of Mode-I and Mode-II interlaminar fracture toughness on the energy absorption of CFRP twill/weave composite box sections, *Composite Structures*, doi: 10.1016/j.compstruct.2008.08.004, 2009.

[19] Ghasemnejad H, Hadavinia H, Marchant DR, Aboutorabi A. Energy absorption of thin-walled corrugated crash box in axial crushing, *Journal of Structural Durability and Health Monitoring*, 2008;4(1):29-46.

Chapter 5:

Effect of Mixed-Mode-I/II Delamination Failure in Off-axis Crashworthiness Analysis of Composite Box Structures

Nomenclature

a crack length

a_e effective crack length

$ADCB$ asymmetric double cantilever beam

b side of box

C compliance

$3ENF$ three-point-end-notched flexure

E Young's modulus

f large displacement correction factor

F force

G_{12} shear modulus

G_{IIC} Mode-II interlaminar fracture toughness

$G_{I/IIC}$ mixed-Mode-I/II interlaminar fracture toughness

I second moment of inertia

L_F free length of the specimen

L_T trigger length

n number of crack in Mode-II

SEA specific energy absorption

t crush box wall thickness

V_f fibre volume fraction

ν Poisson's ratio

σ_u ultimate tensile stress

σ_b flexural strength

τ_s shear strength

θ off-axis angle

φ semi-angle of the wedge

χ correction factor for beam root rotation

5. Introduction

In a real crash event the more likely scenario is a non-axial collision rather than an axial one. A few researchers have investigated the energy absorbing capabilities of elements such as the box under two types of non-axial loadings. This chapter contains a description of work to investigate the energy absorption capability of the woven GFRP composite box under various off-axis crushing loadings.

In this regard, the effect of delamination cracks growth in Mode-II, G_{IIC}, and mixed-Mode I/II, $G_{I/IIC}$, was investigated on the specific energy absorption, SEA. The 3-ENF and ADCB and the crush box specimens were made and tested with different lay-ups of woven GFRP composite material. The experimental results were compared together to find the relationship between delamination crack growth in Mode-II and mixed-Mode-I/II and SEA.

5.1. Experimental studies

Two different types of asymmetric double cantilever beam (ADCB) and also off-axis quasi-static crush box tests were carried out in accordance with the relevant standards. The GFRP specimens were manufactured from twill weave glass fibre material of densities 1.4 g/cm^3 with epoxy resin. The mechanical properties and interlaminar fracture toughness in Mode-II for woven GFRP material were extensively studied in the work described Chapter 4.

5.2. Determination of mixed-Mode-I/II interlaminar fracture toughness

The fabrication of GFRP ADCB specimens were laid-up according to the laminate design of each GFRP composite crush box which will be discussed later. The mid-plane interface of GFRP was 0//0 to determine the mixed-Mode I/II interlaminar fracture toughness. The crack propagation was set along the weft direction which was defined as 0 direction.

For determining the mixed-Mode I/II interlaminar fracture toughness, $G_{I/IIC}$, ESIS protocol [1] was followed. The Teflon insert in ADCB specimens were located at two different locations. The first position was applied at the mid-plane (10//10) of specimen with equal thickness ($h_1=h_2=2.75mm$) for upper and lower arms. This specimen was called symmetric ADCB (ADCB^B). Second the insert Teflon was located between the 6th and 7th layer.

This means that the thickness of upper arm (h_1) is 1.65mm and thickness of lower arm (h_2) is 3.85mm, respectively. This specimen was called asymmetric ADCB ($ADCB^{UB}$) (see Figure 5.1).

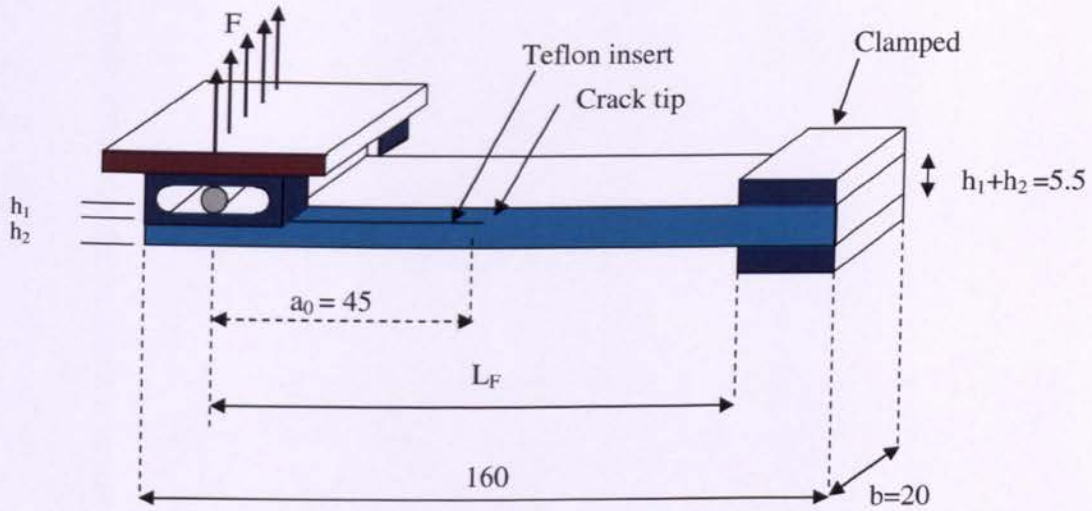

Fig. 5.1. ADCB specimen for mixed-Mode I/II delamination testing (All dimensions in mm).

This ratio was chosen regarding the crack growth in the box wall in off-axis loading of 10°. In this case the crack propagation in mixed-Mode I/II occurs between layers of 3 and 7 (will be discussed later) with the thickness ratio of (0.9/2.1). The corrections for the end-block, ADCB arm bending and root rotation were considered. According to [2] the recommended ADCB specimen size is at least 160mm long and 20mm wide with an initial crack length (i.e. the length of the insert from the load line) of 45mm. The force at each crack length was retrospectively obtained from the recorded force-displacement diagram to calculate $G_{I/IIC}$ (Figure 5.2).

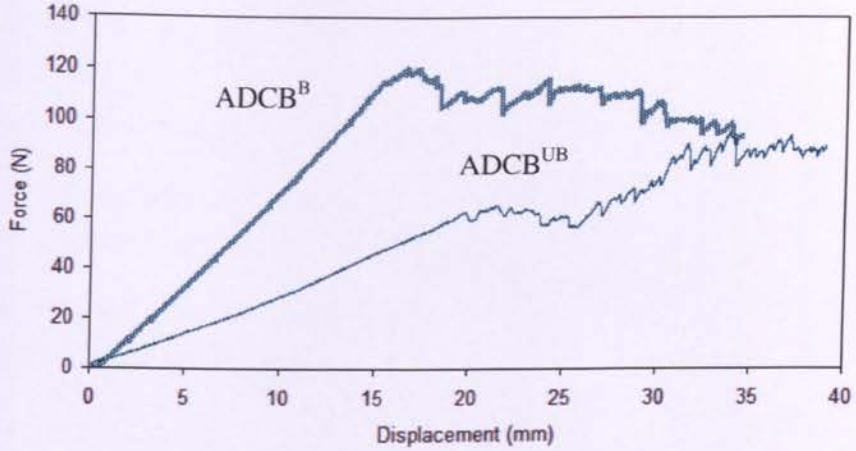

(b) ADCB tests

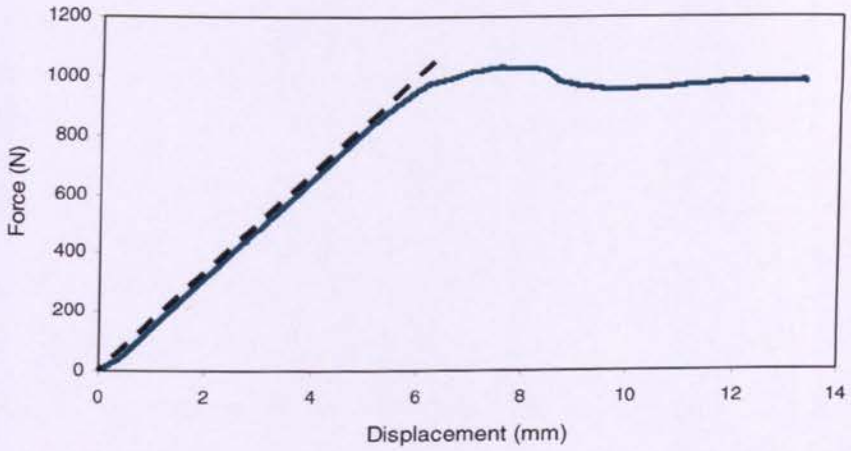

(a) 3ENF tests

Fig. 5.2. Force-load line displacement from (a) symmetric and asymmetric ADCB and (b) 3ENF tests.

5.3. Mixed-Mode I/II interlaminar fracture toughness

Various test methods have been investigated to measure mixed-Mode I/II interlaminar fracture toughness. The mixed-mode bending (MMB) [3] test has been balloted within ASTM as a prospective mixed-Mode standard. The main advantage of the MMB test is that it could change the whole mixed-mode failure envelope from pure Mode-I to pure Mode-II, to be measured using a single apparatus. The asymmetric double cantilever beam (ADCB) [4] is another test method for measuring the mixed-Mode I/II interlaminar fracture toughness.

The ADCB test method yields one single ratio, namely G_I/G_{II} = 4/3 between Mode I and Mode II interlaminar fracture toughness. Due to dissipated energy by asymmetric crack growth in the side-wall of composite box in off-axis crushing angle of 10°, it was necessary to measure the fracture toughness in mixed-Mode I/II crack propagation.

This kind of crack growth was judged to be similar to ADCB test. Thus, this test was chosen for measuring the mixed-Mode fracture toughness.

The ADCB specimens at two different mixed-Mode ratios were manufactured. These mixed-mode ratios were calculated from [4],

$$\frac{G_I}{G_{II}} = \frac{h_1^2(h_1+h_2)^2}{3h_2^4} \cdot \left[\frac{a+\chi_I h_2}{a+\chi_{II} h_1}\right]^2 \tag{5.1}$$

where h_1 is the distance between the plane of insert film and the top of the beam and h_2 is the distance from the plane of insert film to the bottom of the beam and

$$\chi_I = \sqrt{\frac{E_1}{11G_{12}}\left\{3-2\left(\frac{\Gamma}{\Gamma+1}\right)^2\right\}}, \quad \Gamma = 1.18\frac{\sqrt{E_1E_2}}{G_{12}} \tag{5.2}$$

where χ_I is a correction factor for the beam root rotation in Mode-I component, $\chi_{II} = 0.42\chi_I$ the correction factor for Mode-II component.

The mixed-Mode ratio of $ADCB^B$ specimen which was made with insert Teflon at the mid-plane (h_1=h_2), was 1.33 while the mixed-Mode ratio of $ADCB^{UB}$ specimen with upper arm thickness of h_1=1.65mm and lower arm thickness of h_2=3.85mm was 0.125 (see Figure 5.3).

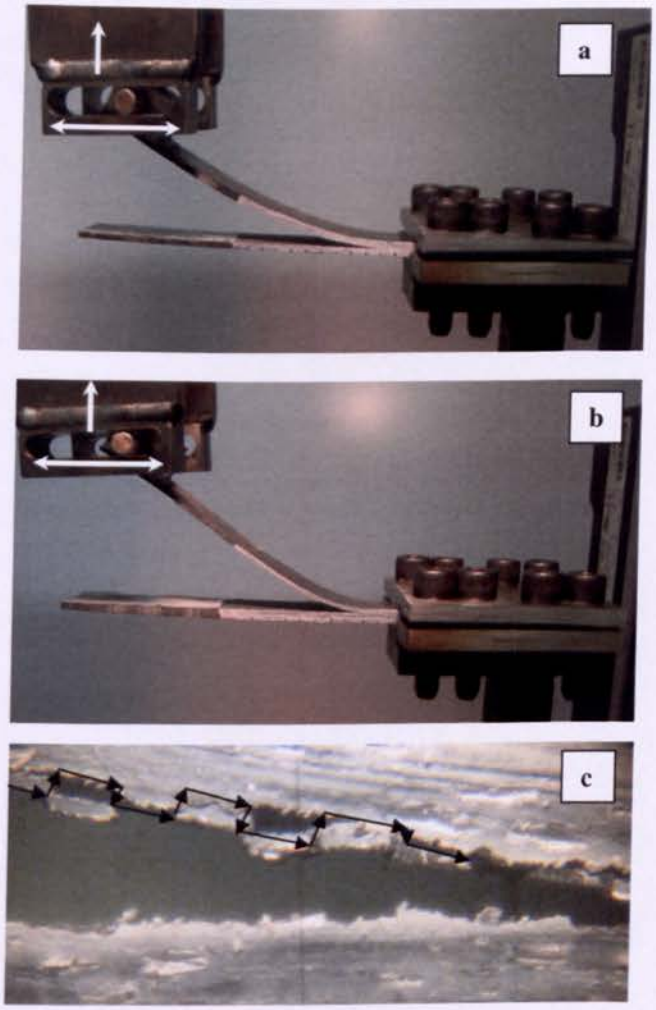

Fig. 5.3. GFRP ADCB test specimens under loading, a) ADCB^{B} and b) ADCB^{UB} and c) Transverse crack propagation.

Using the *Corrected Beam Theory* (CBT) method which uses simple beam theory with correction factors of the beam not being perfectly built-in and large displacement during the test, the total mixed-Mode I/II energy release rate in the ADCB test, $G_{I/IIC}$ can be partitioned to Mode-I and Mode-II components as [4]:

$$G_{I/IIC} = G_{IC}^{mixed} + G_{IIC}^{mixed} \tag{5.3}$$

where $G_{IC}{}^{mixed}$ and $G_{IIC}{}^{mixed}$ are as below,

$$G_{IC}^{mixed} = \frac{6F^2(a+\chi_1 h_2)^2}{b'^2 E_1} \cdot \frac{h_1^3}{h_2^3\left(h_1^3+h_2^3\right)} \cdot f \tag{5.4}$$

$$G_{IIC}^{mixed} = \frac{18F^2(a+\chi_{II}h_1)^2}{b'^2E_1}\cdot\frac{h_1h_2}{(h_1+h_2)^2.(h_1^3+h_2^3)}\cdot f \qquad (5.5)$$

where f is the large displacement correction factor.

In this study *Experimental Calibration Method* (ECM) which uses the plot of the compliance, C, versus the cube of the delamination length, a^3, was also considered to determine the mixed-Mode I/II fracture toughness. The development of transverse cracking caused the force to show several continuous increases after initial crack propagation resulting in a rising R-curve for ADCB specimens (see Figure 5.4).

The results of mixed-Mode I/II delamination fracture toughness, $G_{I/IIC}$, using VIS for each interface, are presented in Table 5.1.

Table 5.1. Interlaminar fracture toughness obtained from $ADCB^B$ and $ADCB^{UB}$ tests.

Specimen	Fracture plane interface	Mixed-Mode ratio (G_{IC}/G_{IIC})	$G_{I/IIC}^{(Initiation)}$ (ECM) J/m^2	$G_{I/IIC}^{(Initiation)}$ (CBT) J/m^2	$G_{I/IIC}^{(Prop.)}$ (ECM) J/m^2	$G_{I/IIC}^{(Prop.)}$ (CBT) J/m^2
$ADCB^B$	0//0	1.33	560±20	720±20	1550±20	2200±30
$ADCB^{UB}$	0//0	0.125	50±4	70±6	550±20	750±20

ECM: Experimental Compliance Method, *CBT*: Corrected Beam Theory

According to standard, mixed-Mode I/II tests have to be complemented by pure Mode I and Mode II tests, if the full failure envelope is to be determined. Thus, Mode-I interlaminar fracture toughness was also measured with fracture interface of 0//0 (see Table 5.2).

Table 5.2. Interlaminar fracture toughness obtained from 3ENF and DCB tests.

Specimen	Fracture plane interface	G_{IC} (MCC) J/m^2	G_{IC} (MBT) J/m^2
DCB	0//0	1200±60	1200±40
Specimen	**Fracture plane interface**	**G_{IIC} (CCM) J/m^2**	**G_{IIC} (SBT) J/m^2**
3-ENF	0//0	3700±30	3200±30

CCM: Compliance Calibration Method, *SBT*: Simple Beam Theory

MCC: Modified Compliance Calibration, *MBT*: Modified Beam Theory

The experimental resistance curves of $G_{I/IIC}$ versus crack length are presented in Figure 5.4.

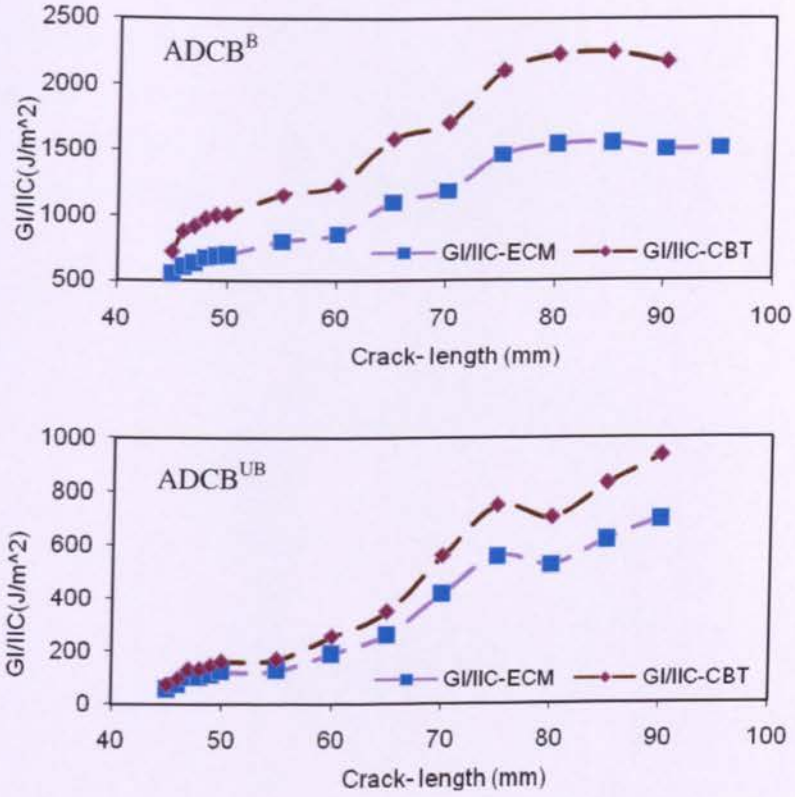

Fig. 5.4. Resistance curve (R-curve) in ADCB specimens with 0//0 fracture plane interface using Experimental Calibration Method *(ECM)* and Corrected Beam Theory *(CBT)* methods.

Regarding the unreliable results of un-balanced (UB) ADCB specimen, the results of balanced ADCB specimen are used to study the effect of mixed-mode I/II delamination on off-axis crashworthiness of composite box.

5.4. Composite crush box

The crush box specimens were made of the glass/epoxy twill-weave fabric by hand lay-up with fibre orientations in accordance to those used in ADCB tests as described in the previous section. The 0° direction which coincided with the axial axis of the crush box was parallel to weft direction. Each box was made with a total height of 100mm, external cross-section of 80×80mm and wall thickness of 3mm. To avoid stress concentration at the box corners, an internal fillet with a radius of 6 mm was inserted at the internal corners of each box. Also one

end of each specimen was bevelled to make a trigger for progressive crushing with an angle of 60°. All details of the specimen preparation and testing method were reported in Chapter 3.

The wedge-shape base of the experimental fixture was made from steel with a dimension of 100mm in length and 100mm in width with various inclination angles of 5°, 10°, 20° and 30° (see Figure 5.5). To prevent the toppling of the specimen during the crush test, the clamped-set with total height of 10mm was welded at the slope-surface of each base.

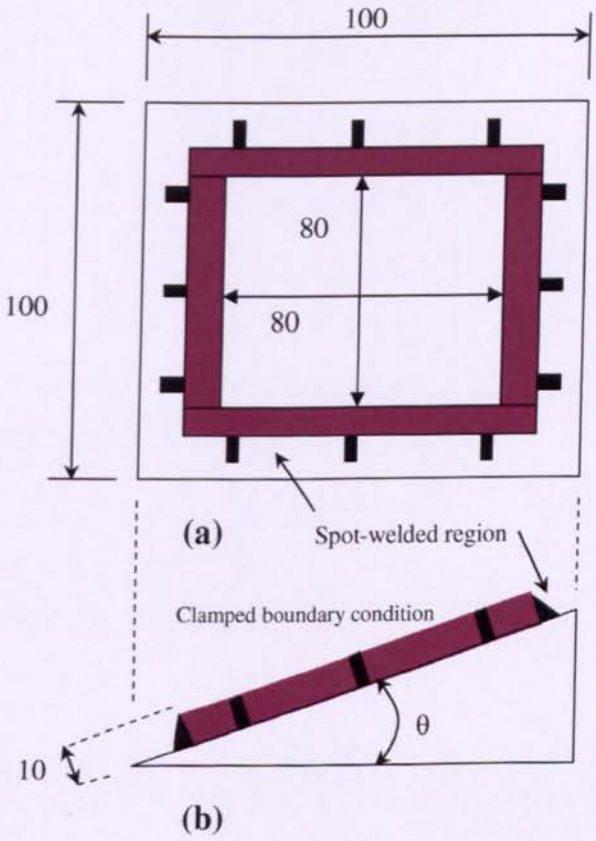

Fig. 5.5. Wedge-shape base for off-axis crushing tests, at off-axis angles of θ = 5°, 10°, 20° and 30°, a) plane view, b) side view (All dimensions in mm).

Each specimen was crushed at a rate of 2mm/min between two parallel platens for 50mm stroke using a universal testing machine with 500 kN load cell. For each test configuration three specimens were tested. The force-crush distance diagrams were recorded automatically for each test (Figure 5.6).

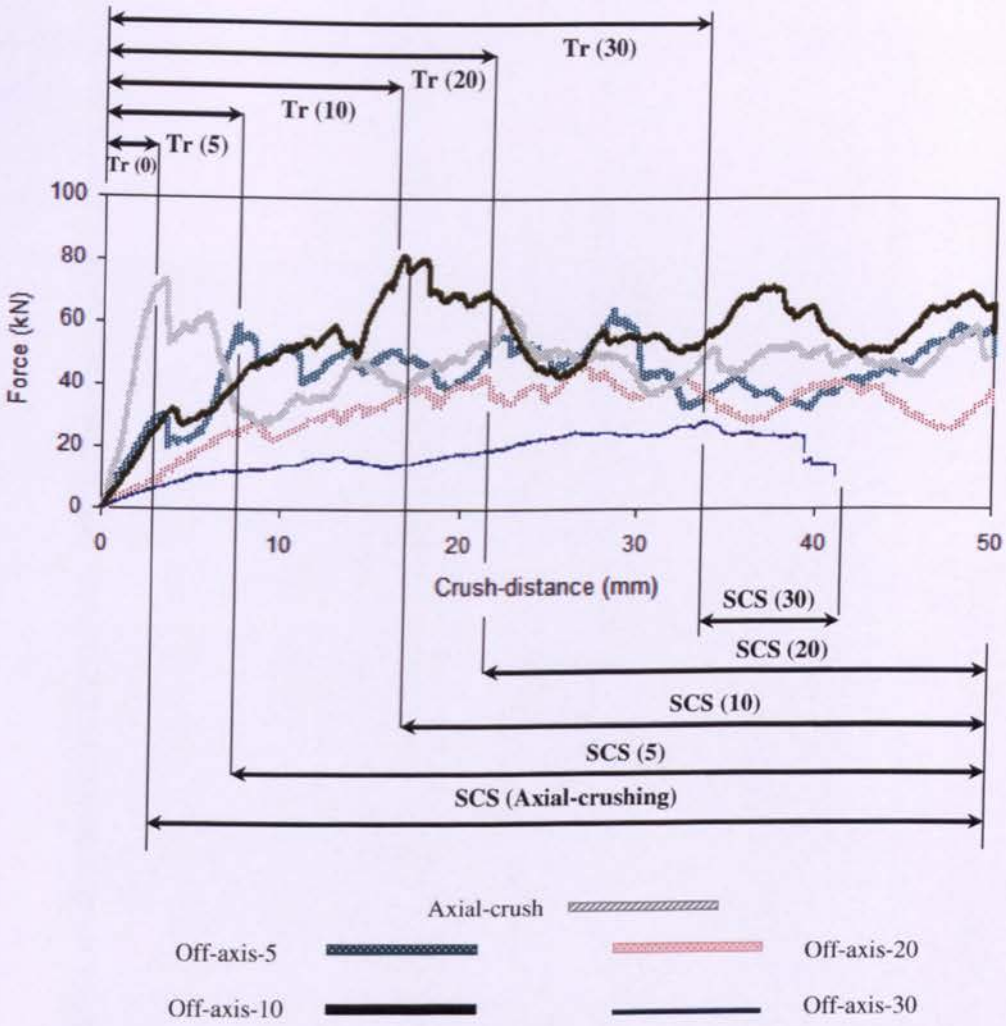

Fig. 5.6. Crushing process of woven glass/epoxy composite boxes under off-axis loading of θ = 5°, 10°, 20° and 30°. Triggering stage at θ offset angle ($Tr_{(\theta)}$) and Sustained Crushing Stage are shown.

5.5. Off-axis crushing process of crush box

For each off-axis angle the wedge-shape base with relevant angle was set for each composite box. Each woven glass/epoxy composite box with fibre orientation of $[0]_{10}$ was crushed between two plates for 50mm stroke using a Universal Testing Machine with 500 kN load cell. The crush speed was set at 2 mm/min, the same speed as used for the ADCB tests. For each test configuration three specimens were tested. The force-crush distance diagrams were recorded automatically for each test.

The crushing process at the 5° off-axis loading was in brittle fracture crushing mode (see Figure 5.7).

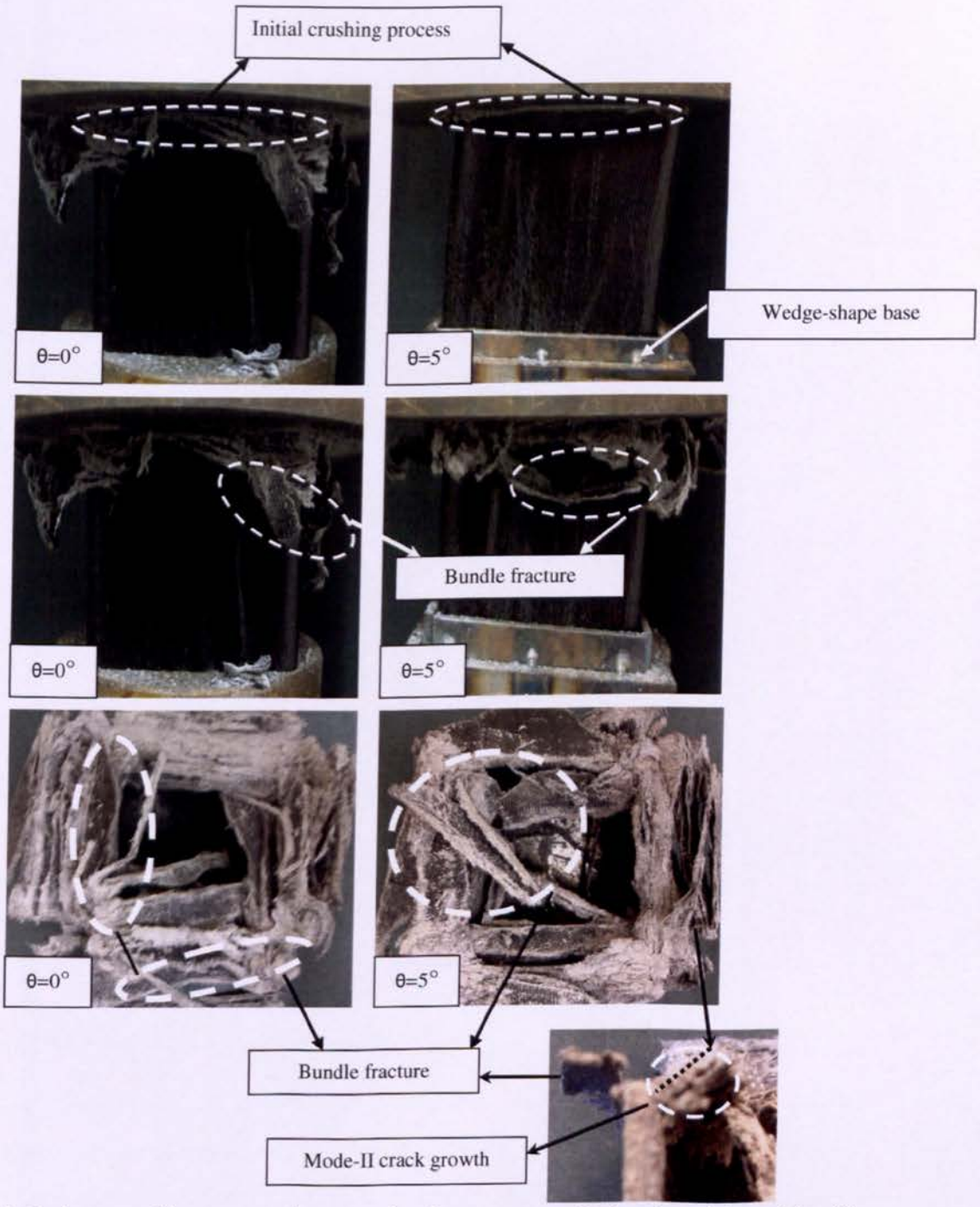

Fig. 5.7. Various crushing stages of woven glass/epoxy composite box in axial crushing (θ =0) and off-axis loading at (θ =5°).

In brittle fracture crushing mode the crushing process is a combination of transverse shearing and lamina bending crushing modes. In this mode the length of the interlaminar cracks are between 1 to 10 laminate thicknesses. In this case the main energy absorption mechanism is fracturing of lamina bundles. The highest energy absorption of composite tubes was observed in brittle fracture and lamina bending crushing modes.

At off-axis angle of 5° the onset of the sustained crushing stage was delayed in comparison with axial crushing process. The triggering stage (Tr) continued until the crushing process reached to its maximum area and took place over a total length of $L_T=bsin\theta$. After this stage the sustained crushing stage began and the shape of crushing zone became rectangular with long side of $b/cos\theta$ and the short side of b (Figure 5.8-b and 5.10-a). However, the length of sustained crushing stage was almost the same as the relevant length of sustained crushing stage in axial crushing.

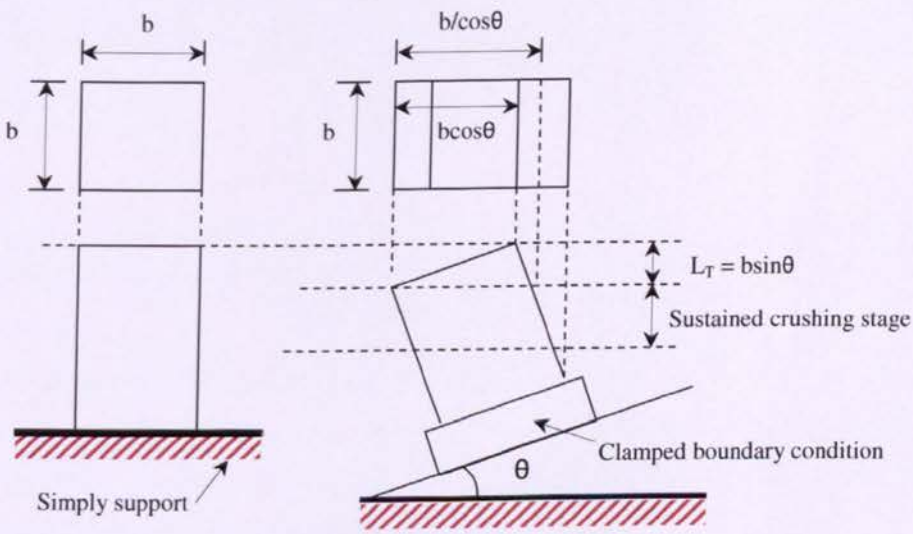

Fig. 5.8. Comparison of axial and off-axis crushing process, a) axial crushing and b) off-axis crushing.

The off-axis loading test was carried for the loading angle of 10°. The behaviour of this loading angle was exceptionally different from the process of off-axis loadings. Initially it was predicted that the sustained crushing stress would be described by increasing the inclination angle. At this angle the triggering stage was longer than the triggering stage of 5°

loading. However, sustained crushing stress was reached at a higher value of mean force than the observed value of mean force in sustained crushing stage of axial crushing.

This situation yields to show the higher SEA at this off-axis loading. The fracture mechanism to absorb the crushing energy was followed by many bundle fracture and interlaminar crack propagation in Mode-II and mixed-Mode I/II in main wall (see Figure 5.9 and 5.10-b).

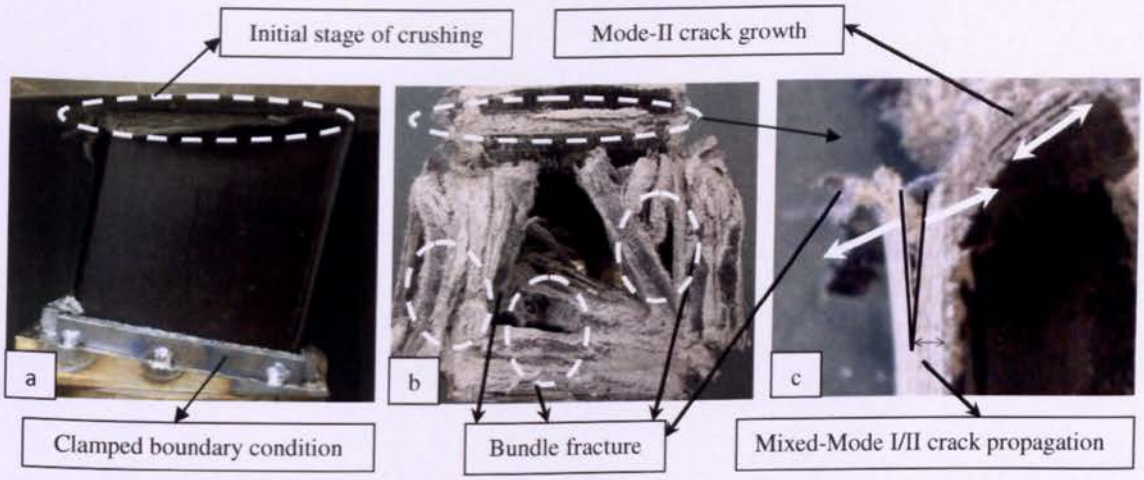

Fig. 5.9. Crushing process analysis of woven glass/epoxy composite box at off-axis loading of 10°, a) crushing process, b) plane view of crushed box and c) crack propagation in the wall of composite box.

However, due to off-axis loading these fracture mechanisms did not occur at the same time. This fracture mechanism was observed only at one side of composite box. The main reason for the increase of the energy absorbing capability of this off-axis loading might be related to crack propagation in mixed-Mode I/II at one side of the composite box.

This kind of crack propagation yields to produce lamina bundles and consequently increasing of friction and bending resistance. Regarding the fracture study in Mode-II and mixed-Mode I/II, an extra amount in energy absorbing of this off-axis angle can be derived as,

$$U_{delamination} = b\lambda(G_{I/IIC} + nG_{IIC}) \tag{5.6}$$

The fracture toughness value in mixed-Mode I/II in the side-wall of the box was calculated from ADCB^{UB} test.

It should be mentioned that this kind of crack propagation was observed only at 10° off-axis loading. This could explain why only at this angle the highest SEA in comparison with other off-axis loadings and axial loading was observed (see Figure 5.11).

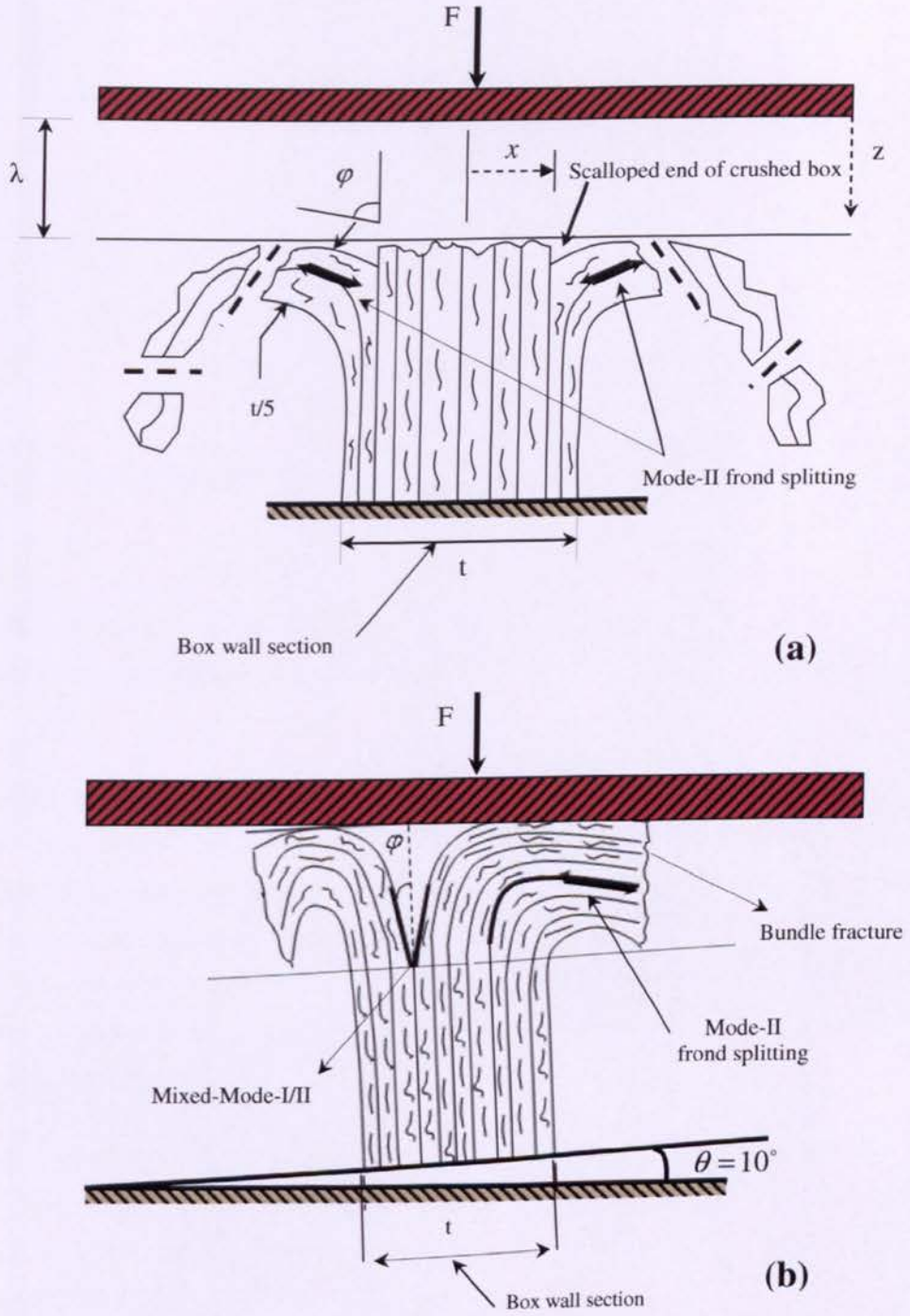

Fig. 5.10. Ideal crush zone, (a) Brittle fracture crushing mode in axial crushing and (b) Crack propagation in mixed-Mode I/II in off-axis angle of 10°.

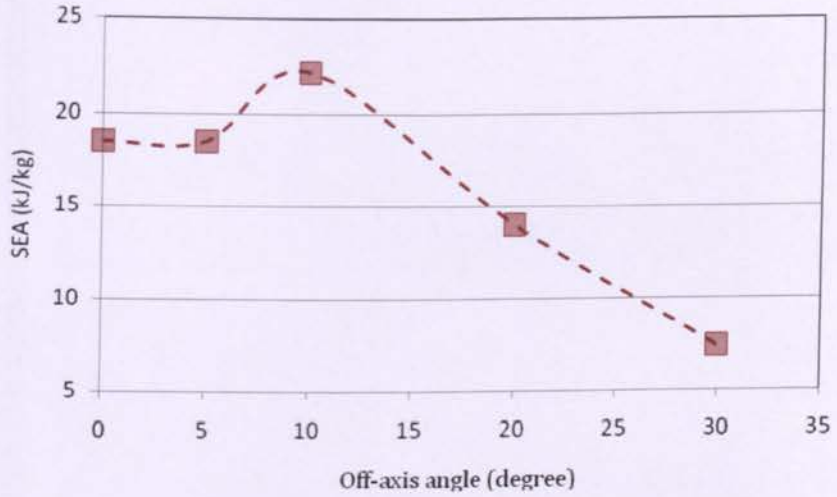

Fig. 5.11. Variation of specific energy absorption (SEA) versus off-axis angle for GFRP composite box.

The off-axis crushing process was performed for the other two angles of 20° and 30°. Increasing the loading angle caused the triggering stage for both angles to increase (Figure 5.6).

The sustained crushing stage was shorter and also lower than the sustained crushing stage of smaller loading angles. The reason for this decreasing of SEA comes from the fracture mechanisms which control the crushing process. At the beginning of the crushing process it was observed that one side of the composite box started to absorb the crushing energy and the other two adjacent sides joined the crushing process after a delay. This situation significantly affected the capability of composite box to absorb the energy. Off-axis loading of 30° showed the minimum amount of SEA.

In contrast to [5], in our experiments, the toppling stage was not observed in any off-axis loadings. Also at 20° and 30° angles, the fracture mechanisms were recognised as crack propagation in Mode-II at one side of composite box which started the absorbing of crushing energy (see Figure 5.12).

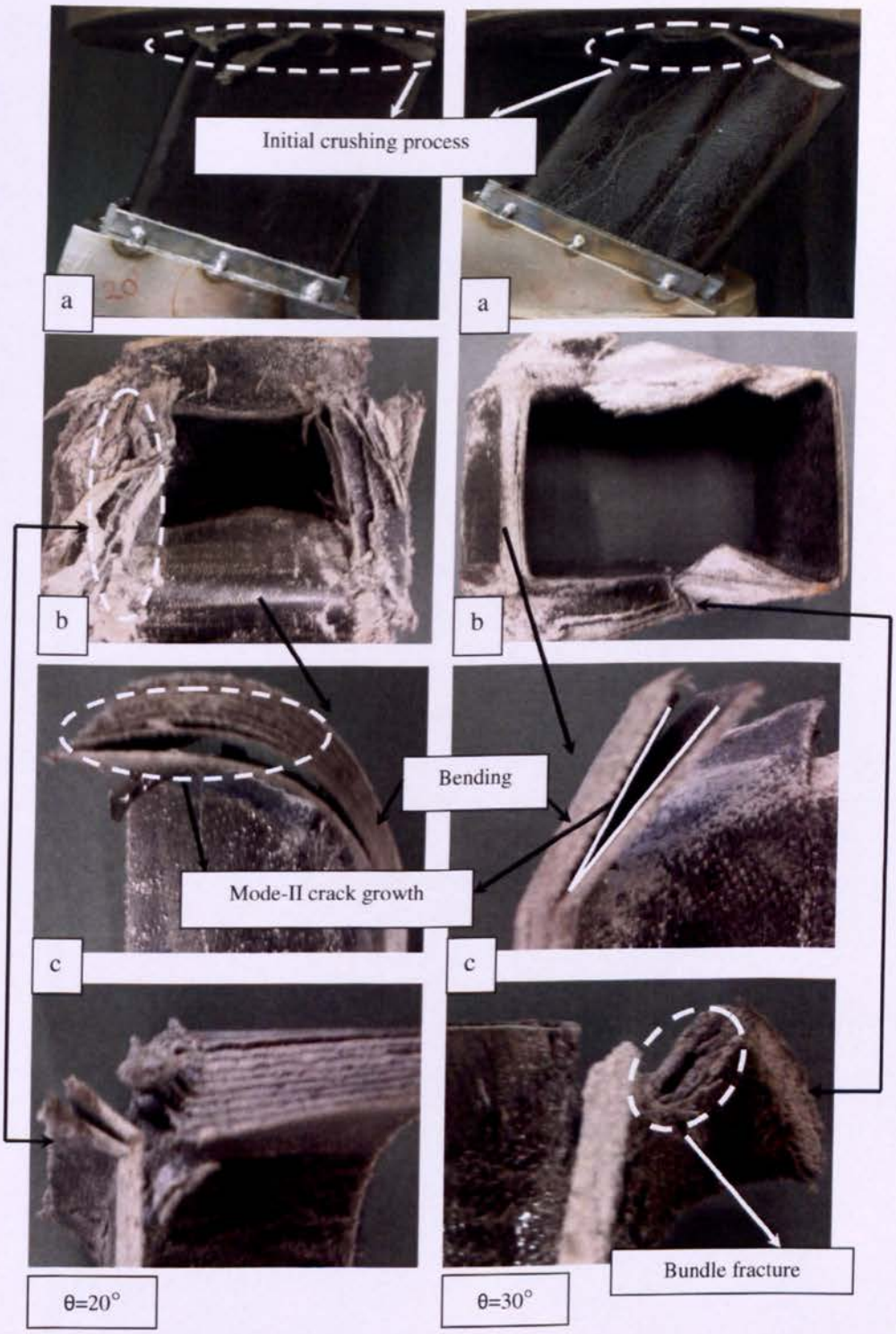

Fig. 5.12. Crushing process analysis of woven glass/epoxy composite box at off-axis loading of 20 and 30°, a) crushing process, b) plane view of crushed box and c) crack propagation in the walls of composite box.

5.6. Conclusion

In the present work, the effect of off-axis loading on the fracture mechanisms and specific energy absorption of glass/epoxy twill-weave composite box was investigated. The brittle fracture mode was observed for composite box in axial crushing and off-axis loading of 5°. The energy absorbing capability at this off-axis loading was almost the same as energy absorption of the composite box under axial loading.

Two fracture mechanisms of bundle fracture and crack propagation in Mode-II were found for all composite boxes at various off-axis loading. Due to crack propagation in mixed-Mode I/II and more friction and bending resistance at the side of composite box which first contacted the crushing platen, the amount of SEA at off-axis loading of 10° was the maximum. The energy absorbing capability of this off-axis loading was increased about 16% in comparison with energy absorption in axial loading. Except for the off-axis angle of 10°, the SEA of glass/epoxy composite box was decreased by increasing the off-axis loading. The delay in arrival of sustained crushing stage caused the energy absorption of CFRP composite box to decrease. The SEA of 20° and 30° related to SEA of axial crushing decreased by 24% and 60%, respectively. The toppling stage was not observed in any of the off-axis loading tests.

References

[1] Choi NS, Kinloch AJ, Willams JG. Delamination fracture of multidirectional carbon-fiber/epoxy composites under mode I, mode II and mixed mode I/II loading. *J Compos Mater,* 1999;33(1):73–100.

[2] Moore DR, Pavan A, Williams JG, Editors. Fracture mechanics testing methods for polymers, adhesives and composites. ESIS Publication 28. Elsevier Science Ltd, 2001.

[3] ASTM D 6671-01, Standard test method for mixed mode I-mode II interlaminar fracture toughness of unidirectional fiber reinforced polymer matrix composites.

[4] Kinloch AJ, Wang Y, Williams JG, Yayla P. The mixed-mode delamination of fiber composite materials. *Compos Sci Technol* 1993;47(3):225–37.

[5] Hong-Wei Song and Xing-Wen Du. Off-axis crushing of GFRP tubes. *Compos Sci Technol,* 2002;62:2065–2073.

[6] Hashemi S, Kinloch AJ, Williams JG. The analysis of interlaminar fracture in uniaxial fibre-polymer composites. Proc. R. Soc. Lond. 1990;427(A):173-199.

Appendix (C5):

Calculation of delamination in ADCB test

Williams [6] proposed beam theory analysis for general problems involving delaminated homogeneous materials. Based on this theoretical framework, the total strain energy release rate can be used to find the delamination problem for different geometries.

Total strain energy release rate is,

$$G = \frac{1}{b}\left(\frac{dU_e}{da} - \frac{dU_S}{da}\right) \tag{C5-7}$$

where, U_e is the external work performed and U_s is the strain energy.

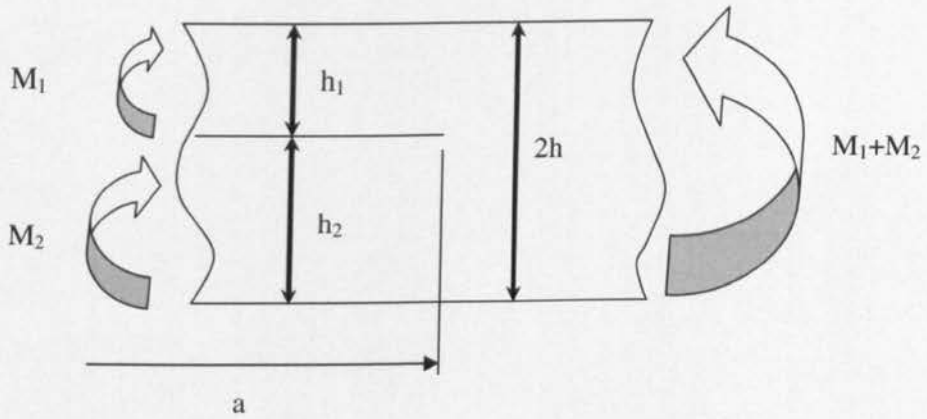

Fig.C5.13. Delaminated laminates under bending [6].

External work is defined as,

$$\frac{dU_e}{da} = \frac{1}{8E_1 I}\left[\frac{M_1^2}{\xi^3} + \frac{M_2^2}{(1-\xi)^3} - (M_1 + M_2)^2\right] \tag{C5-8}$$

where

$$\xi = \frac{h_1}{2h} \tag{C5-9}$$

The strain energy is derived as,

$$\frac{dU_S}{da} = \frac{M_1^2}{2E_1 I_1} + \frac{M_2^2}{2E_1 I_2} - \frac{(M_1 + M_2)^2}{2E_1 I_0} \tag{C5-10}$$

Substituting Eqs. (8) and (10) in (7) the energy release rate becomes,

$$G = \frac{1}{16 b' E_1 I}\left[\frac{M_1^2}{\xi^3} + \frac{M_2^2}{(1-\xi)^3} - (M_1 + M_2)^2\right] \tag{C5-11}$$

According to [6], pure Mode-I exists when symmetric moments act on the laminate legs i.e. $M_I = M_I$ and $M_2 = -M_I$. Also, pure Mode-II requires equal curvature for both legs, a condition that is achieved when $M_I = M_{II}$ and $M_2 = \psi M_{II}$.

where,

$$\psi = \frac{h_2^3}{h_1^3} \tag{C5-12}$$

In ADCB test only one arm is loaded; therefore, $M_2 = 0$ and $M_1 = F(a + \chi h_1)$

$$M_1 = M_I + M_{II} \tag{C5-13}$$

$$M_2 = -M_I + \psi M_{II} = 0 \tag{C5-14}$$

$$M_{II} = \frac{M_1}{(1+\psi)}, \text{ and } M_I = \frac{\psi}{(1+\psi)} M_1 \tag{C5-15}$$

Substituting new values for bending moments, G_I and G_{II} are obtained as,

$$G_{IC}^{mixed} = \frac{6F^2(a + \chi_I h_2)^2}{b'^2 E_1} \cdot \frac{h_1^3}{h_2^3(h_1^3 + h_2^3)} \cdot f \tag{C5-16}$$

$$G_{IIC}^{mixed} = \frac{18F^2(a + \chi_{II} h_1)^2}{b'^2 E_1} \cdot \frac{h_1 h_2}{(h_1 + h_2)^2 . (h_1^3 + h_2^3)} \cdot f \tag{C5-17}$$

Chapter 6:

Effect of Delamination Failure in Crashworthiness Analysis of Hybrid Composite Box Structures

Nomenclature

a	crack length
b	side of box
C	compliance
E	Young's modulus
ELS	end-loaded split
F	force
F_{max}	initial maximum force
F_m	mean force
G_{12}	shear modulus
G_{IC}	mode-I interlaminar fracture toughness
I	second moment of inertia
S	shear strength
SEA	specific energy absorption
$SSCS$	specific sustained crushing stress
t	thickness
U_e	external work
U_S	strain energy
V_f	fibre volume fraction
ν	Poisson's ratio
σ_u	ultimate tensile stress
σ_b	flexural strength

ρ density

τ_s shear strength

θ fibre orientation

Δ_{clamp} end-clamp correction factor

6. Introduction

This chapter contains a description of work carried out to investigate the effects of delamination failure of hybrid composite box structures on crashworthiness behaviour and to investigate their performance compared with non-hybrid ones. In this work the combinations of twill-weave and unidirectional CFRP composite materials were used to laminate the composite boxes. Delamination studies in Mode-I and Mode-II with the same lay-ups were carried out to investigate the effect of delamination crack growth on energy absorption of hybrid composite box structures. The end-loaded split (ELS) and double cantilever beam (DCB) standard test methods were chosen for delamination studies. Also, the effects of stiffened and channel stiffened composite box structures in absorbing the crushing energy were studied and the results were compared to the relevant un-stiffened composite box.

6.1. Experimental studies

6.1.1. Determination of Mode-I interlaminar fracture toughness

The mechanical characteristics of carbon/epoxy twill-weave and unidirectional fabrics were obtained in accordance with the relevant standards discussed in Chapters 2 and 3. These tests were tensile, shear, fibre volume fraction, coefficient of friction (see Table 6.1), double-cantilever beam (DCB) (Table 6.2 and Figure 6.2), end-loaded split (ELS) (Table 6.4 and Figure 6.5) and quasi-static crush box.

Table 6.1. Material properties of the woven a) Unidirectional-CFRP and b) Woven-CFRP composite materials.

E_1 (GPa)	E_2 (GPa)	G_{12} (GPa)	υ_{12}	σ_u 0° MPa	σ_u 90° MPa	τ_s MPa	V_f (%)
138±12	10.5±0.5	6.3±0.4	0.3	330±14	32±2	147±14	42

(a)

E_1 GPa	E_2 GPa	G_{12} GPa	ν_{12}	σ_u 0° MPa	σ_u 90° MPa	τ_s MPa	V_f %
61±5	58±2	3.4±0.3	0.1	634±15	560±21	94±7	45

(b)

For all interface planes the development of transverse cracking also caused the force to show several continuous increases after initial crack propagation resulting in a rising R-curve. Transverse cracking for interface planes of T90//U90, T0//U0, T90//T90, T90//U0 and T0//U90 happened at the beginning of delamination crack growth (see Figure 6.1.a) while this process for interface plane of U90//U90 happened at the end of delamination crack growth (see Figure 6.1.b).

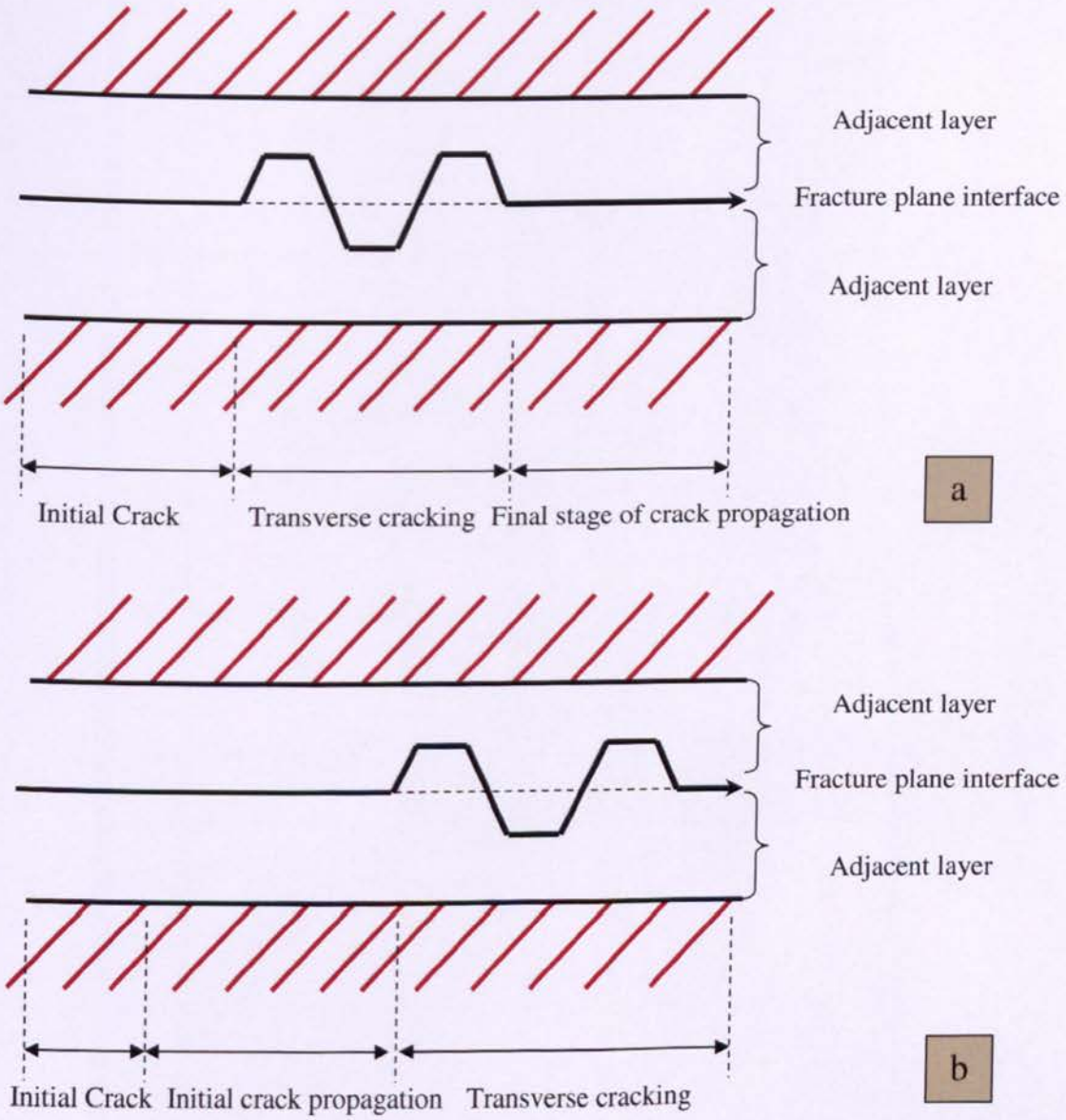

Fig. 6.1. Typical crack propagation in Mode-I delamination at fracture plane interface.

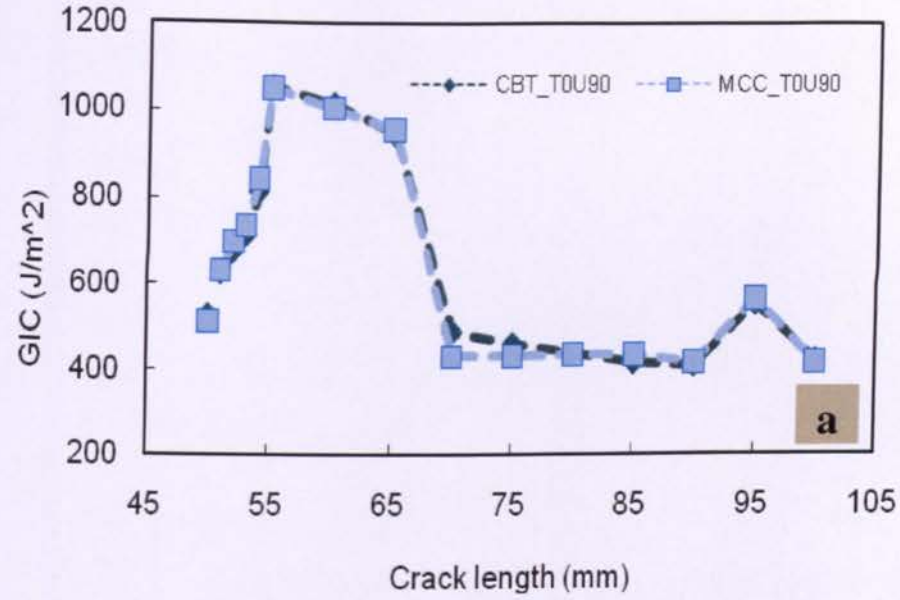
1200
1000
800
600
400
200
GIC (J/m^2)
CBT_T0U90
MCC_T0U90
a
45
55
65
75
85
95
105
Crack length (mm)

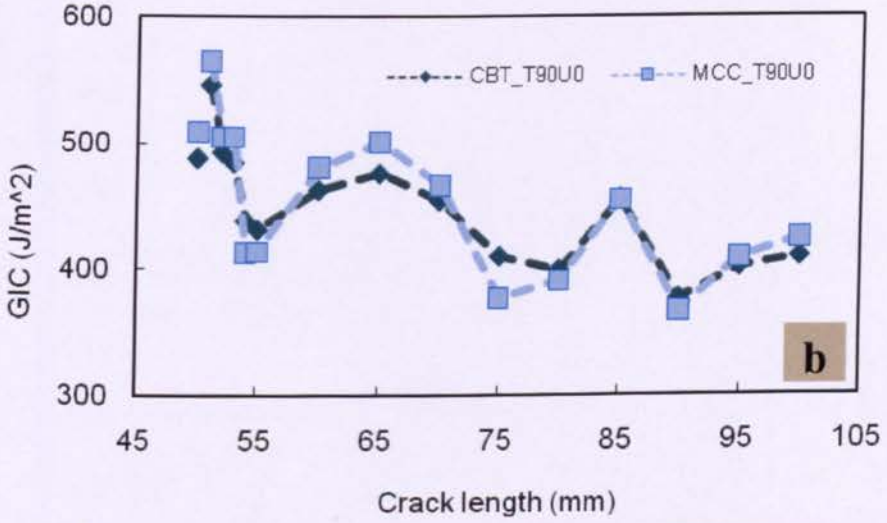
600
500
400
300
GIC (J/m^2)
CBT_T90U0
MCC_T90U0
b
45
55
65
75
85
95
105
Crack length (mm)

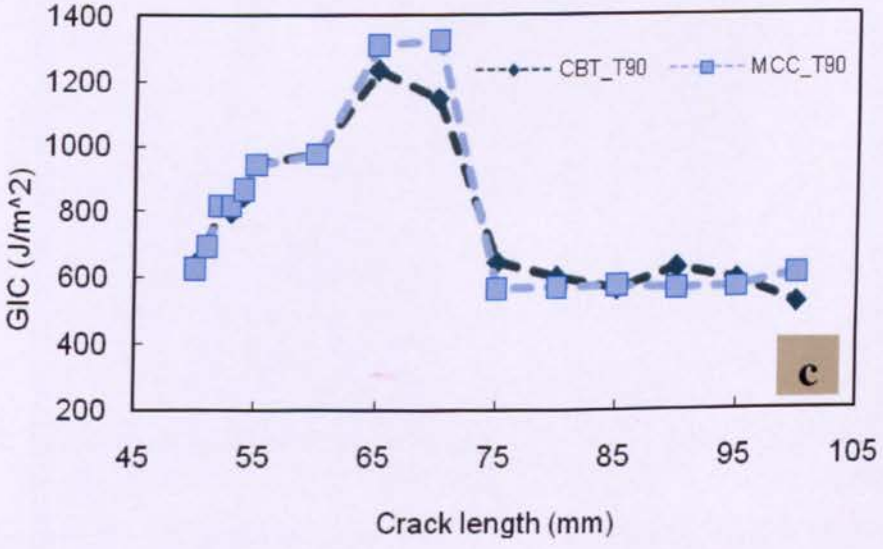
1400
1200
1000
800
600
400
200
GIC (J/m^2)
CBT_T90
MCC_T90
c
45
55
65
75
85
95
105
Crack length (mm)

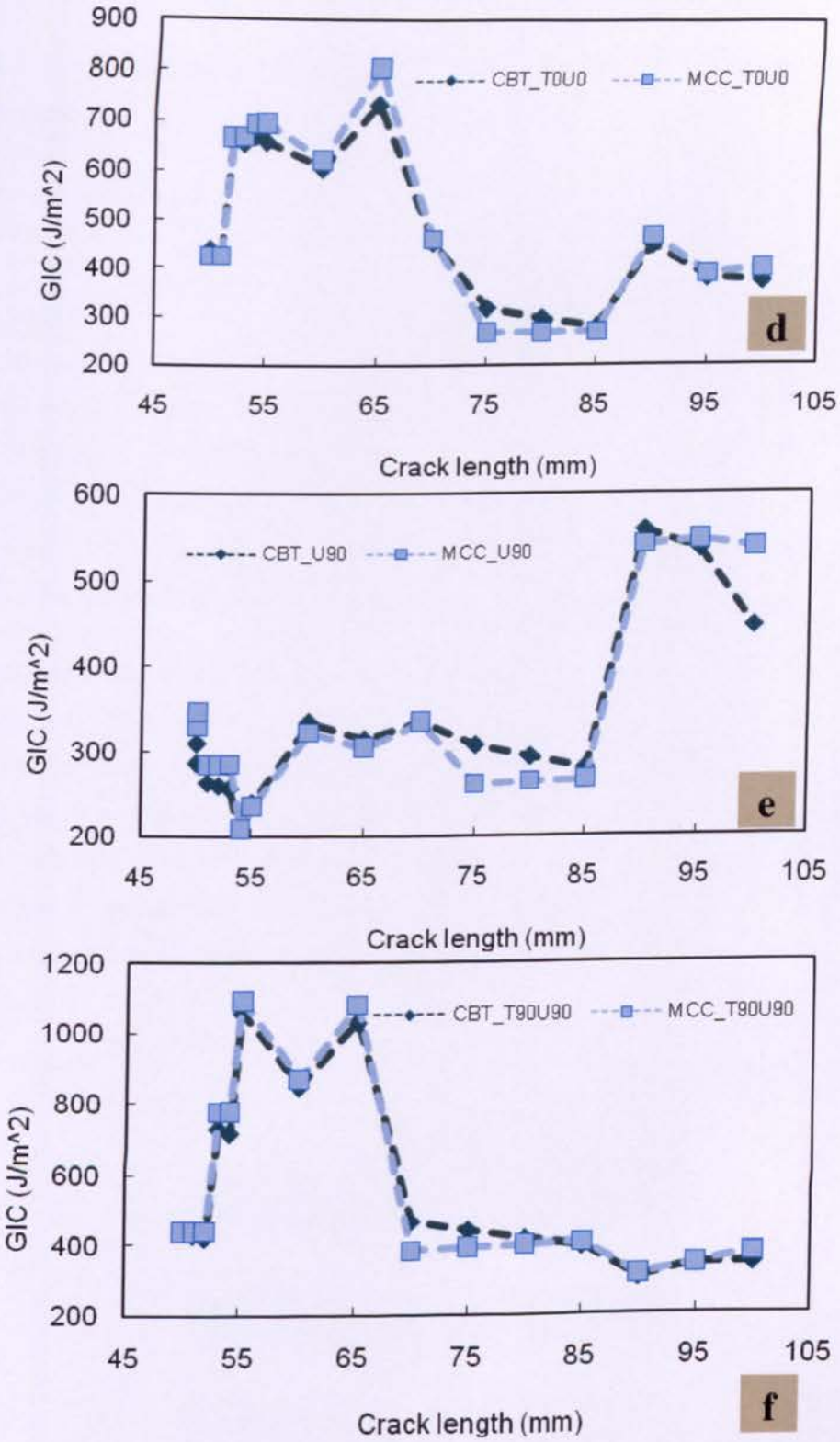

Fig.6.2. Resistance curve (R-curve) in DCB specimens with various fracture plane interfaces using MBT and MCC methods.

Table 6.2. Interlaminar fracture toughness obtained from DCB tests for various interface fibre orientations.

Laminate lay-up	Fracture plane interface	G_{IC} (MCC) J/m^2	G_{IC} (MBT) J/m^2	G_{IProp} (MCC) J/m^2	G_{IProp} (MBT) J/m^2
$[T0/U0]_7$	T0//U0	480±20	450±20	400±20	400±20
$[T0/U90]_7$	T0//U90	510±20	530±20	420±20	420±20
$[T90/U0]_7$	T90//U0	500±20	480±20	430±30	430±20
$[T90/U90]_7$	T90//U90	440±20	430±10	400±20	400±10
$[T90]_{10}$	T90//T90	620±20	610±20	600±20	600±20
$[U90]_{16}$	U90//U90	350±20	340±10	400±20	400±10

MCC: Modified Compliance Calibration Method, MBT: Modified Beam Theory

All specimens were manufactured from unidirectional and twill/weave fabric CFRP materials of density 1.4 g/cm^3 and 1.8 g/cm^3 with epoxy resin. For twill/weave composite it was observed that crack propagation along the weft yarns was associated with more resistance than propagation along the warp direction. For comparison between the energy absorption of hybrid composite box and pure one, two other types of composite box were made: one from the twilled-weave; and the other all from unidirectional CFRP materials. The lay-ups of different hybrid composite boxes are presented in Table 6.3.

Table 6.3. Various lay-ups of hybrid composite box structures.

Hybrid composite box lay-ups
$[T0/U0]_7$
$[T0/U90]_7$
$[T90/U0]_7$
$[T90/U90]_7$
$^*[T90]_{10}$
$^*[U90]_{16}$

T= Twill-weave & U = Unidirectional CFRP materials
(*) = Pure CFRP composite box

6.1.2. Determination of Mode-II interlaminar fracture toughness using ELS specimen

The fabrication of the hybrid twill-weave and the unidirectional CFRP ELS specimens were laid-up according to the laminate design of each hybrid composite crush box. The mid-plane interface of hybrid CFRP ELS specimens were T0//U0, T0//U90, T90//U0 and T90//U90, and for non-hybrid CFRP ELS specimens were T90//T90 and U0//U0 to determine the Mode-II interlaminar fracture toughness. In the twill-weave specimens the weft direction was defined as 0 direction.

The ELS specimens were made according to ESIS protocol [1] with the width of 20mm and the total length of 160mm, while the thickness varied from 5 to 6mm. This thickness was required to avoid large displacement, plastic deformation and intraply damage. A precrack length of 60mm from the free end of specimen was inserted using a Teflon film of thickness 13μm (see Figure 6.3). Loading was carried out at a constant crosshead displacement rate of 2 mm/min.

The details of specimen preparation and testing method were explained in Chapters 3 and 4. The force at each crack length was retrospectively obtained from the recorded force-displacement diagram to calculate G_{IIC} (see Figure 6.4).

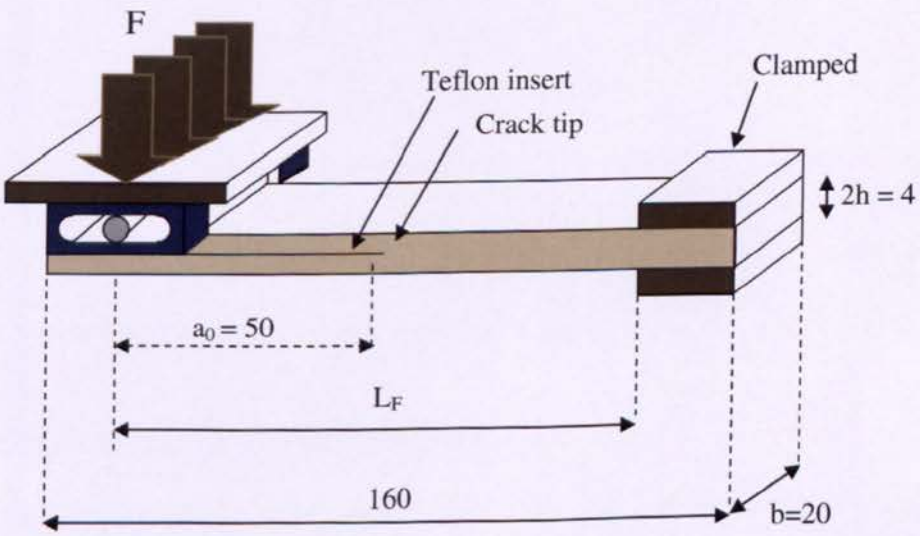

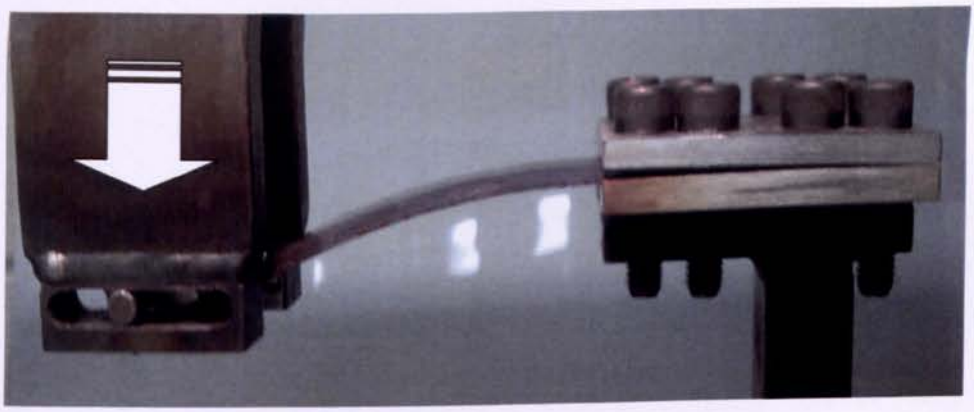

Fig. 6.3. ELS specimen for Mode II delamination testing (All dimensions in mm).

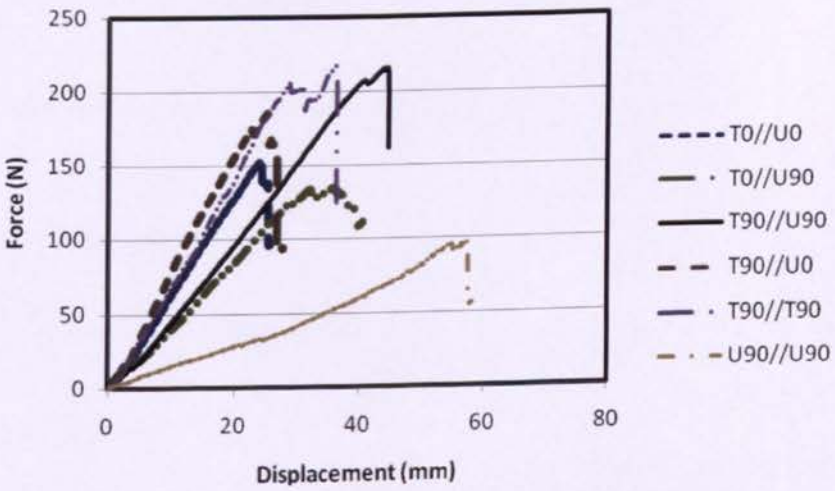

Fig. 6.4. Force-load line displacement from ELS tests for various mid-plane interfaces.

6.2. Mode II interlaminar fracture toughness

Considering the contour ABCD (discussed in Chapter 5) at the tip of the crack O which moves *da* to O' then, total strain energy release rate for corrected-beam theory (CBT) is [2],

$$G = \frac{1}{B}\left(\frac{dU_e}{da} - \frac{dU_S}{da}\right) \tag{6.1}$$

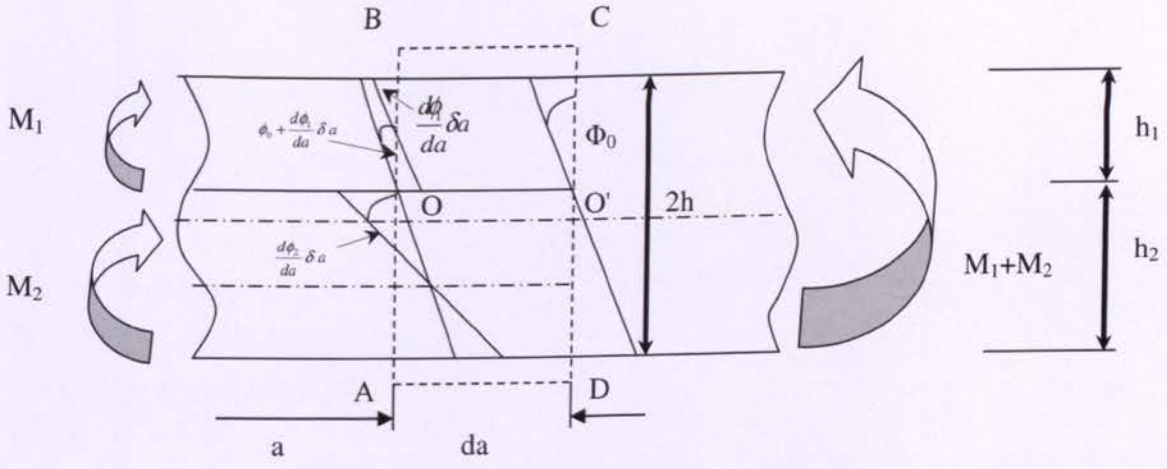

Fig.6.5. Delaminated laminates under bending [2].

where, U_e is the external work performed and U_s is the strain energy.

External work is defined as,

$$\frac{dU_e}{da} = \frac{1}{8E_1 I}\left[\frac{M_1^2}{\xi^3} + \frac{M_2^2}{(1-\xi)^3} - (M_1 + M_2)^2\right] \tag{6.2}$$

The strain energy is derived as,

$$\frac{dU_S}{da} = \frac{M_1^2}{2E_1 I_1} + \frac{M_2^2}{2E_1 I_2} - \frac{(M_1 + M_2)^2}{2E_1 I} \tag{6.3}$$

where

$$I_1 = \frac{Bh_1^3}{12} = \xi^3 I \tag{6.4}$$

$$I_2 = \frac{Bh_2^3}{12} = (1-\xi)^3 I \tag{6.5}$$

$$I = \frac{Bh^3}{12} \quad and \quad \xi = \frac{h_1}{2h} \tag{6.6}$$

In ELS specimen, $h_1=h_2$, therefore, ξ equals 0.5 and E_1 is the longitudinal modulus.

Substituting Eqs. (2) and (4) in (1) the energy release rate becomes,

$$G=\frac{1}{16BE_1I}\left[\frac{M_1^2}{\xi^3}+\frac{M_2^2}{(1-\xi)^3}-(M_1+M_2)^2\right] \tag{6.7}$$

Pure Mode-I exists when symmetric moments act on the laminate legs i.e. $M_I = M_I$ and $M_2=-M_I$. Also, pure Mode-II requires equal curvature for both legs, a condition that is achieved when $M_I = M_{II}$ and $M_2=\psi M_{II}$.

where,

$$\psi=\frac{h_2^3}{h_1^3} \tag{6.8}$$

$$M_{II}=\frac{Fa}{1+\psi} \tag{6.9}$$

$$G_I=\frac{1}{16BE_1I}\left[\frac{M_I^2}{\xi^3}+\frac{M_I^2}{(1-\xi)^3}\right] \tag{6.10}$$

$$G_{II}=\frac{1}{16BE_1I}\left[\frac{M_{II}^2}{\xi^3}+\frac{(\psi M_{II})^2}{(1-\xi)^3}-(M_{II}+\psi M_{II})^2\right] \tag{6.11}$$

In *ELS* test $\psi = 1$ and $M_1 = M_2 = \frac{Fa}{2}$

$$G_{II}=\frac{9F^2(a+\Delta_{II})^2}{4B^2h^3E_1}f \tag{6.12}$$

$$C=\frac{\delta}{F}=\left(\frac{3(a+\Delta_{II})^3+(L+\Delta_{Clamp})^3}{2Bh^3E_1}\right)\cdot N \tag{6.13}$$

Substituting Eq. (11) in Eq. (10), G_{II} is obtained as [3],

$$G_{II}=\frac{9F\delta}{2B}\left[\frac{(a+\Delta_{II})^2}{3(a+\Delta_{II})^3+(L+\Delta_{clamp})^3}\right]\frac{f}{N} \tag{6.14}$$

where, $\Delta_{clamp}=2\Delta_{II}$ [2] is the end-clamp effect and f and N are the correction factors for large displacement, end-block and end-clamp effects (see Appendix C6).

In this work *Corrected Beam Theory* (CBT) and *Experimental Calibration Method* (ECM) were used to determine the Mode-II fracture toughness. The slope of the plot of the compliance versus the cube of the delamination length (a^3) was used to find the interlaminar fracture toughness using ECM. Due to the difficulties in defining the exact position of crack initiation, the non-linearity (NL) and the 5% offset were used to find the crack initiation. Because of some difficulties in curve fitting in ECM some undesirable discrepancies were found between the R-curve obtained from two methods for interface layers of (T0//U0) and (T90//U90). The Mode-II interlaminar fracture toughness of the interface layer of (T90//T90) and (T90//U0) CFRP composite material showed the highest values of G_{IIC} for all specimens, and for interface layers of (U0//U0) unidirectional CFRP composite material showed the lowest value. The experimental resistance curves of hybrid CFRP composite materials of G_{IIC} versus crack length are presented in Figure 6.6.

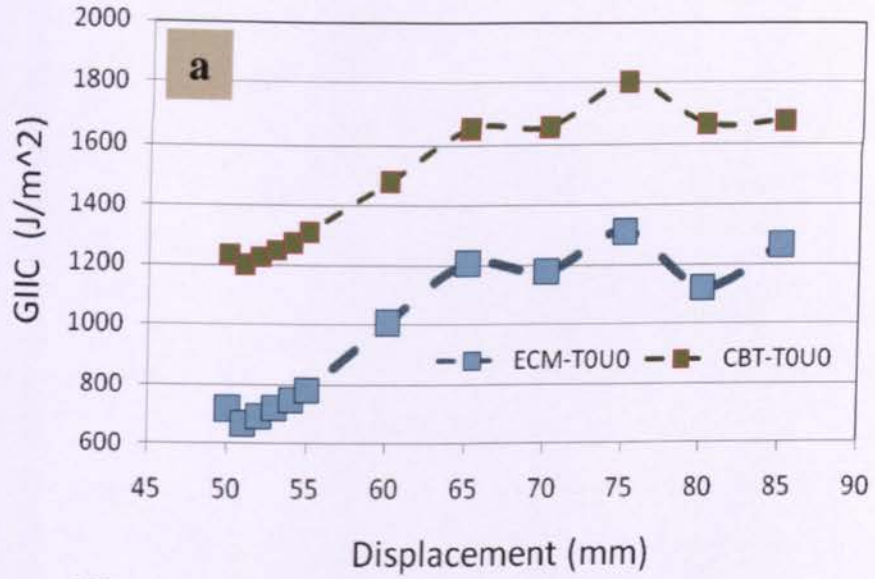
a
GIIC (J/m^2)
2000
1800
1600
1400
1200
1000
800
600
45
50
55
60
65
70
75
80
85
90
ECM-T0U0
CBT-T0U0
Displacement (mm)

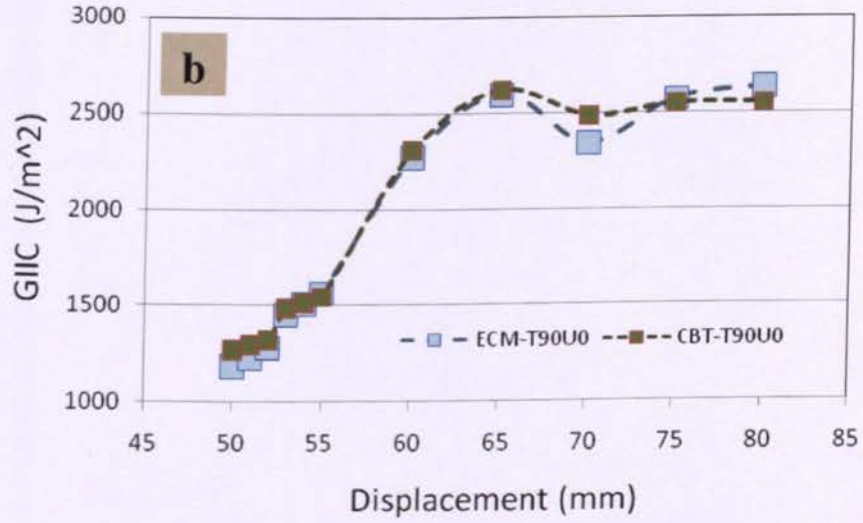
b
GIIC (J/m^2)
3000
2500
2000
1500
1000
45
50
55
60
65
70
75
80
85
ECM-T90U0
CBT-T90U0
Displacement (mm)

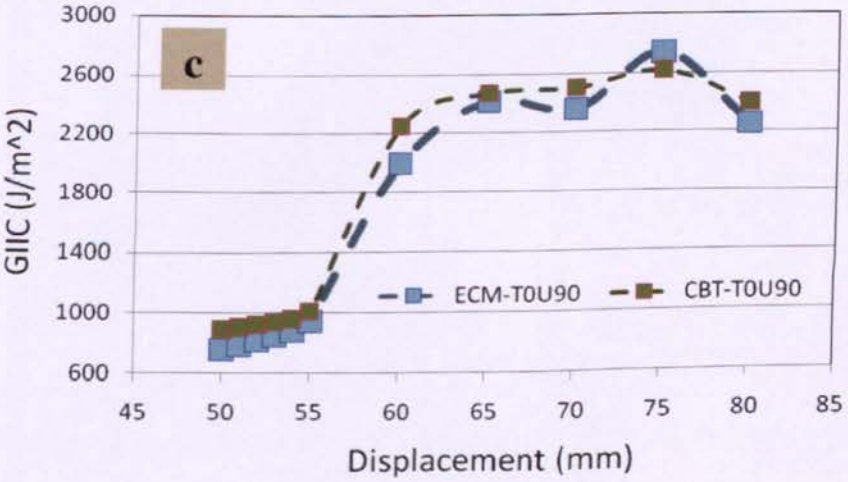
c
GIIC (J/m^2)
3000
2600
2200
1800
1400
1000
600
45
50
55
60
65
70
75
80
85
ECM-T0U90
CBT-T0U90
Displacement (mm)

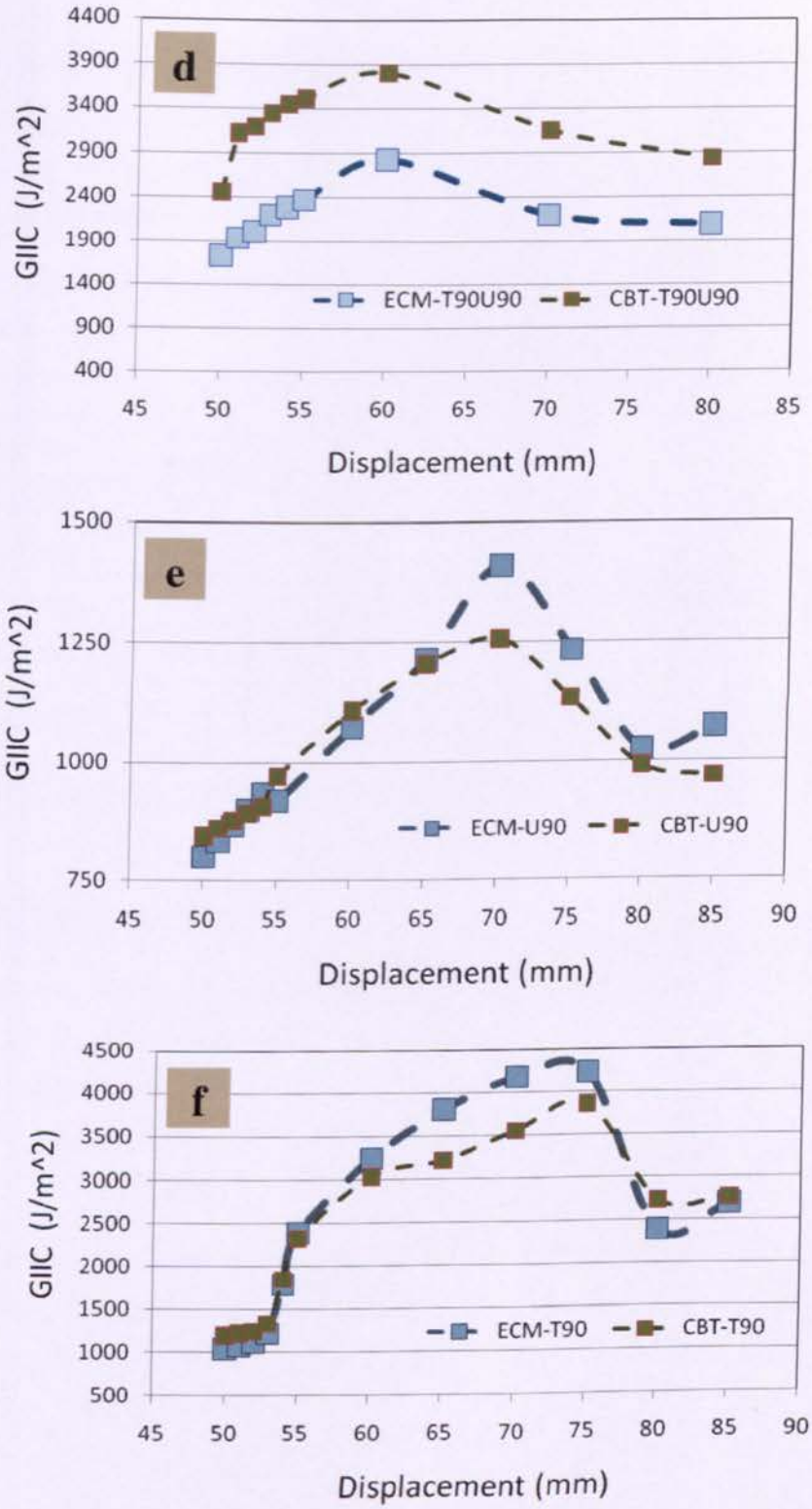

Fig. 6.6. Resistance curve (R-curve) in ELS specimens with various fracture plane interfaces using *ECM* and *CBT* methods.

The results of Mode-II delamination fracture toughness, G_{IIC}, using non-linearity (NL) for each interface, are presented in Table 6.4. The propagation value of fracture toughness in Mode-II was also measured from obtained R-curve of each ELS specimen. This value for fracture interface planes of U90//U90 and T90//T90 was found as an average of R-curve.

Table 6.4. Interlaminar fracture toughness obtained from ELS tests for various interface fibre orientations.

Laminate lay-up	**Fracture plane interface**	G_{IIC} **(ECM)** kJ/m^2	G_{IIC} **(CBT)** kJ/m^2	$G_{IIProp.}$ **(ECM)** kJ/m^2	$G_{IIProp.}$ **(CBT)** kJ/m^2
$[T0/U0]_7$	T0//U0	800±30	1200±40	1300±30	1700±40
$[T0/U90]_7$	T0//U90	900±30	1000±40	2500±30	2600±40
$[T90/U0]_7$	T90//U0	1200±40	1300±30	2500±40	2700±30
$[T90/U90]_7$	T90//U90	900±30	1500±40	2000±20	3000±40
$[T90]_{10}$	T90//T90	1100±30	1300±40	3200±30	3300±40
$[U90]_{12}$	U90//U90	800±30	1000±30	1200±30	1300±30

CCM: Compliance Calibration Method, CBT: Corrected Beam Theory

6.3. Composite crush box

The crush box specimens were made of the hybrid woven and also of unidirectional carbon/epoxy by hand lay-up with fibre orientations in accordance to those used in DCB and ELS tests as described in the previous section. The 0° direction which coincided with the axial axis of the crush box was parallel to the weft direction. All details of the specimen preparation and testing method were reported in Chapter 2.

Each specimen was crushed at the rate of 2mm/min between two parallel platens for 50mm stroke using a universal testing machine with 500 kN load cell. For each test configuration three specimens were tested. The force-crush distance diagrams were recorded automatically for each test.

6.4. Progressive crushing process of hybrid composite crush box

For all hybrid composite crush boxes the lamina bending crushing mode was observed. The lamina bending mode is shaped with long interlaminar, intralaminar, and parallel to fibre cracks. This mechanism causes the formation of continuous fronds which spread inwards and outwards. Friction and inter/intra laminar fracture controls the energy absorption of lamina bending mode.

In lamina bending crushing modes higher energy absorption was observed in comparison with the other observed modes. This high energy absorption is caused by a larger crush area and therefore a higher potential to absorb energy by bending and frictional effects at the platen/specimen interface (see Figure 6.7).

Fig. 6.7. Lamina bending crushing mode of various lay-ups of hybrid composite box.

The comparison of force-crush distance behaviour of hybrid composite boxes together with non-hybrid ones from twill-weave and from unidirectional CFRP materials is shown in Figure 6.8. This comparison shows that hybrid composite boxes absorb energy than non-hybrid unidirectional CFRP composite boxes, while in some cases this energy absorption capability is lower than the relevant capability in non-hybrid woven CFRP composite box. The hybrid boxes with laminate designs of $[T0/U0]_7$ and $[T90/U0]_7$ absorbed the highest crushing energy in all hybrid composite boxes. On the other hand, energy absorption of hybrid boxes with lay-ups of $[T0/U90]_7$ and $[T90/U90]_7$ was almost the same as that of the pure unidirectional CFRP composite box. It should be emphasised that, the weight of all composite boxes is the same *i.e.*, 158 ± 2 gr.

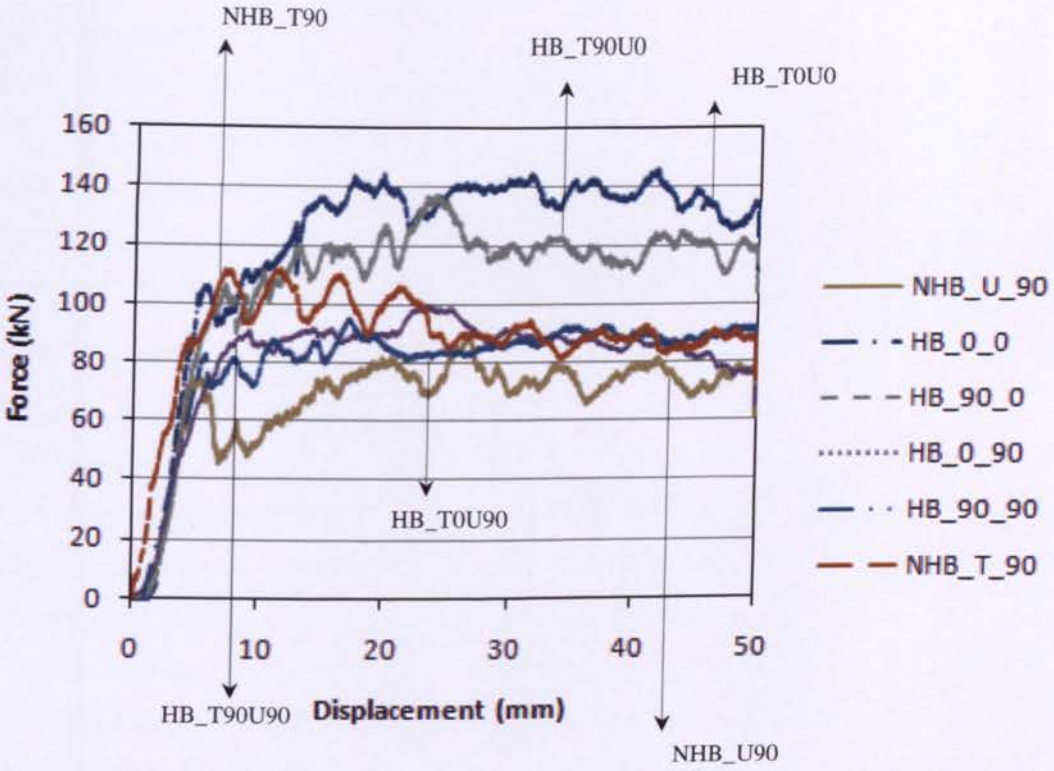

Fig. 6.8. The comparison of force-crush distance in a hybrid composite crush box for various lay-ups.

Comparing the mean force results of all hybrid boxes to non-hybrid composite box indicates that the mean force for pure composite box made of Unidirectional CFRP is the lowest value (*i.e.*, F_m = 78kN), while the mean force of hybrid boxes with laminate designs of $[T90/U0]_7$ and $[T0/U0]_7$ are about 120 and 138 kN, respectively. The non-hybrid composite box with laminate design of $[T90]_{10}$ showed higher energy absorption capability in comparison with composite boxes with laminate design of $[T0/U90]_7$, $[T90/U90]_7$ and $[U90]_{16}$.

In all composite boxes the lamina bending crushing mode was observed. In this case the main central interwall crack which is similar to Mode-I crack delamination (discussed in Chapter 4) starts to propagate at four sidewalls of each composite box. This situation causes to shape lamina bundles and resistance against the crushing load. In lamina bending mode, the main central crack causes to shape lamina bundles which has a significant role on absorbing the crushing energy. Earlier it was shown that the fibre orientation at the interface planes has a significant effect on Mode-I interlaminar fracture toughness. Also in this failure mode the

fronds splitting due to lamina bundle bending is similar to interlaminar crack propagation in Mode-II (see Figure 6.9).

The G_{IC} and G_{IIC} of initiation are more influential than the G_{IC} and G_{IIC} of propagation in the energy absorption mechanism. The Mode-I and Mode-II initiation values were chosen to quantify the effect of Mode-I and Mode-II fracture toughness on the energy absorption of composite box. Regarding the delamination study of hybrid DCB and ELS (discussed earlier) the variation of SEA versus summation of G_{IC} and G_{IIC} and a root mean square of $\sqrt{G_{IC}^2 + 2\,G_{IIC}^2}$ were plotted in Figure 6.10 to combine the effect of Mode-I and Mode-II interlaminar fracture toughness on the SEA. The values of G_{IIC} were doubled as during the lamina bending two crack propagations in Mode-II were observed in internal and external fronds. From these relationships it is calculated that the hybrid laminate designs which showed higher fracture toughness in Mode-I and Mode-II delamination tests, will absorb more energy as a composite box in crushing process. However other mechanisms such as bending and friction also contribute significantly to energy absorption. For the hybrid box with laminate design of $[T0//U0]_7$ these mechanisms are more dominant in absorbing the crushing energy. As a result, delamination crack growth in Mode-I and Mode-II cannot far outweigh the bending and friction mechanisms in energy absorption. Many other intralaminar fracture mechanisms such as fibre/matrix debonding, fibre breakage and matrix cracking are also contributing in dissipating the crushing energy.

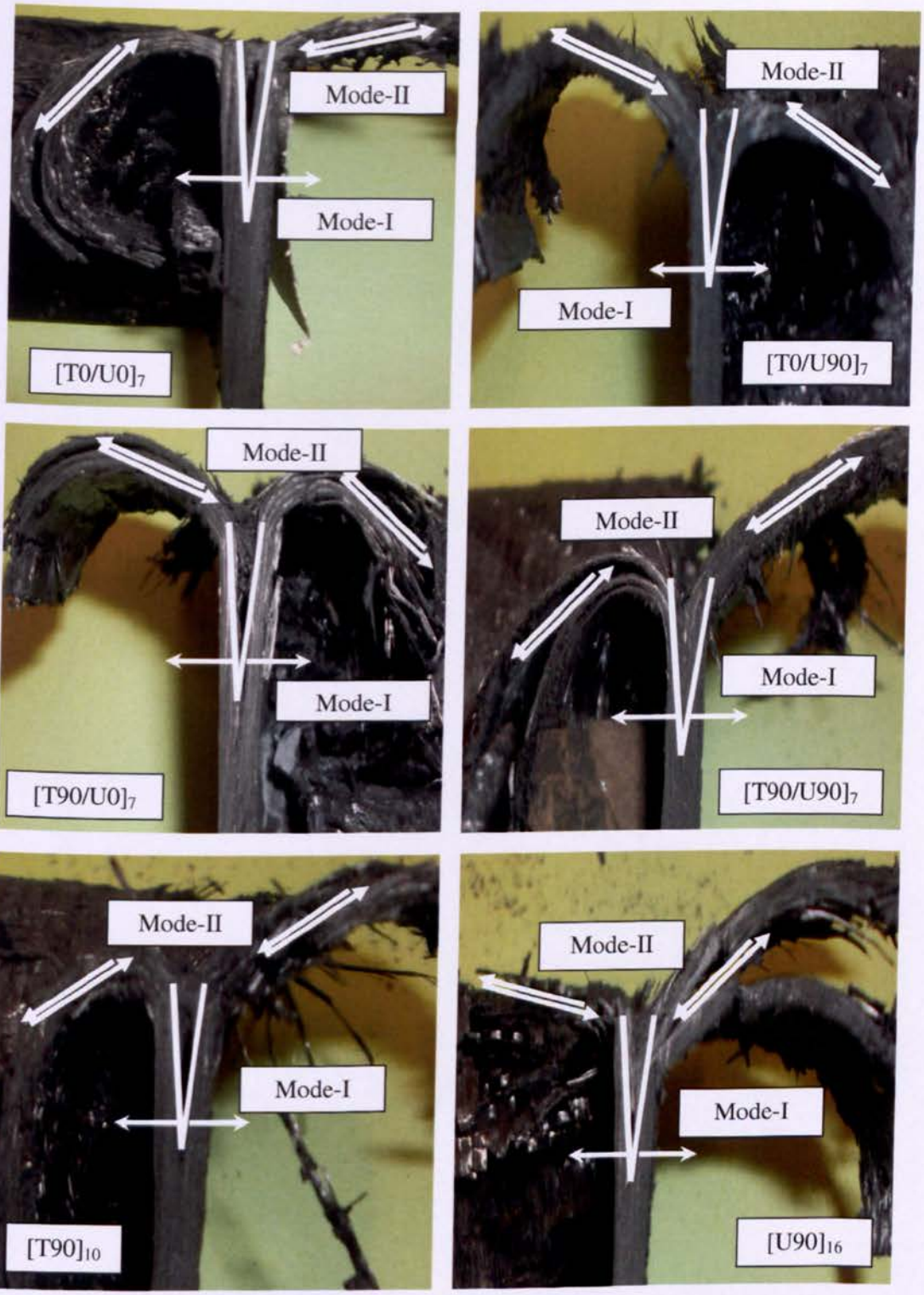

Fig. 6.9. Mode-I and Mode-II interlaminar crack propagation at the central interwall in all composite boxes.

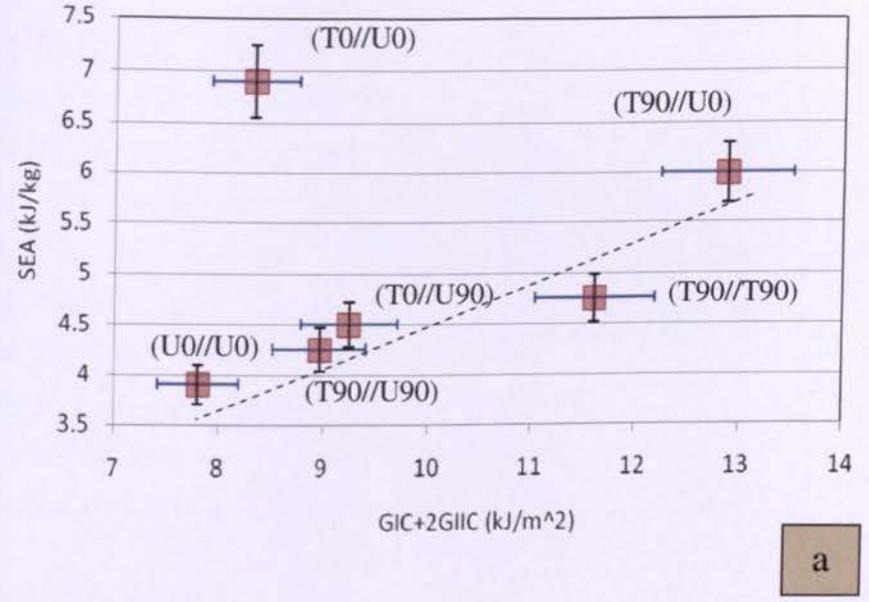

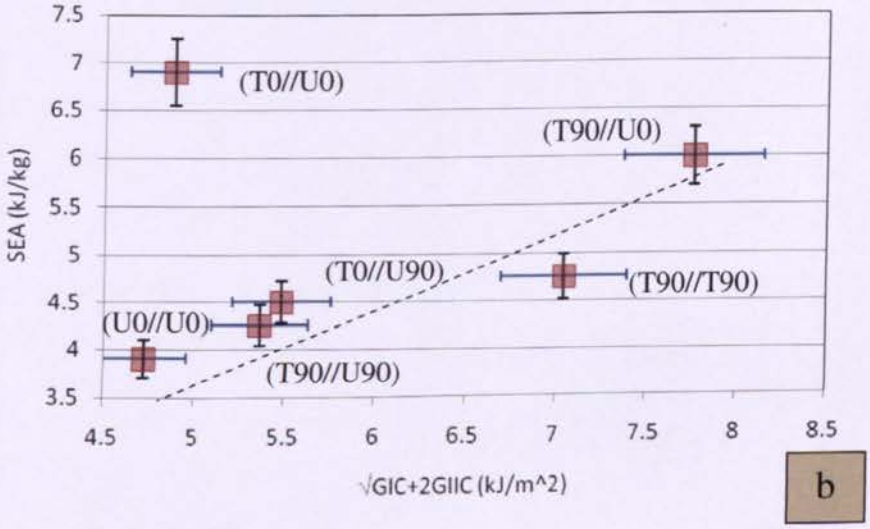

Fig. 6.10. Variation of SEA versus (a) $G_{IC}+G_{IIC}$ and (b) $\sqrt{G_{IC}^2+2\,G_{IIC}^2}$

6.5. Crushing behaviour of stiffened composite box structures

This work was sought to continue in studying the energy absorption of composite stiffeners to conduct expensive and time-consuming design support tests at the element and sub-assembly level prior to fabrication of the fuselage structure in aircraft. In this regard, an optimum composite crash box design was sought by studying the effect of laminate design and stiffeners on the SSCS. Two new assembled composite boxes were made from channels and V-shape stiffener and tested in quasi-static condition. The most effective laminate design which was found in Chapter 3 was chosen in laminating channels and V-shape stiffener. Epoxy adhesive was used in joining the channelled and stiffened boxes. The measured values of SSCS for all models were compared to find the optimum crash box. It was found that the SSCS increased with increasing proportion of 0° plies in the laminate.

6.5.1. Experimental studies

The crush box specimens were made of carbon/epoxy twill-weave fabrics by hand lay-up with that fibre orientation which showed higher energy absorption during the tests described in Chapter 3. The dimensions of all boxes were the same as those which showed progressive failure. The side of each box was 80 mm with thickness around 3 mm and the total length was 100 mm. One end of each specimen was bevelled to make a trigger for progressive crushing with an angle of 60°.

Each specimen was crushed between two parallel plates for 50 mm stroke using universal testing machine with 500 kN load cell. The crush speed was set at 2 mm/min.

The specific sustained crushing stress (SSCS) is a measure of the energy absorption capability of the material which is defined by,

$$SSCS = \frac{\sigma_{sc}}{\rho} \tag{6.13}$$

where, σ_{sc} is the sustained crushing stress which is defined as the ratio of mean force to cross-sectional area, and ρ is the material density. From experimental results, it was found that the SSCS increased with increasing the proportion of 0° plies in the laminate. $[0]_4$

laminate has the highest mean force and consequently the highest SSCS with respect to other laminates made from the same materials and the same cross-sectional area.

Two types of boxes were made from assembling channels and V-shape stiffener using the $[0]_4$ laminate which showed the highest SSCS in the simple box tests. The thickness of the channels was the same as that of the simple composite box but the V-shape stiffener thickness was 2.25 mm. The type I specimens consisted of two bonded channels and the type II specimens were made from bonding two channels and one V-shape stiffener (Figure 6.11). The channels and the stiffener were bonded together using Betamate 1493 epoxy adhesive which was cured for 30 min at 180°C. All boxes were tested at the same conditions as in the simple box tests.

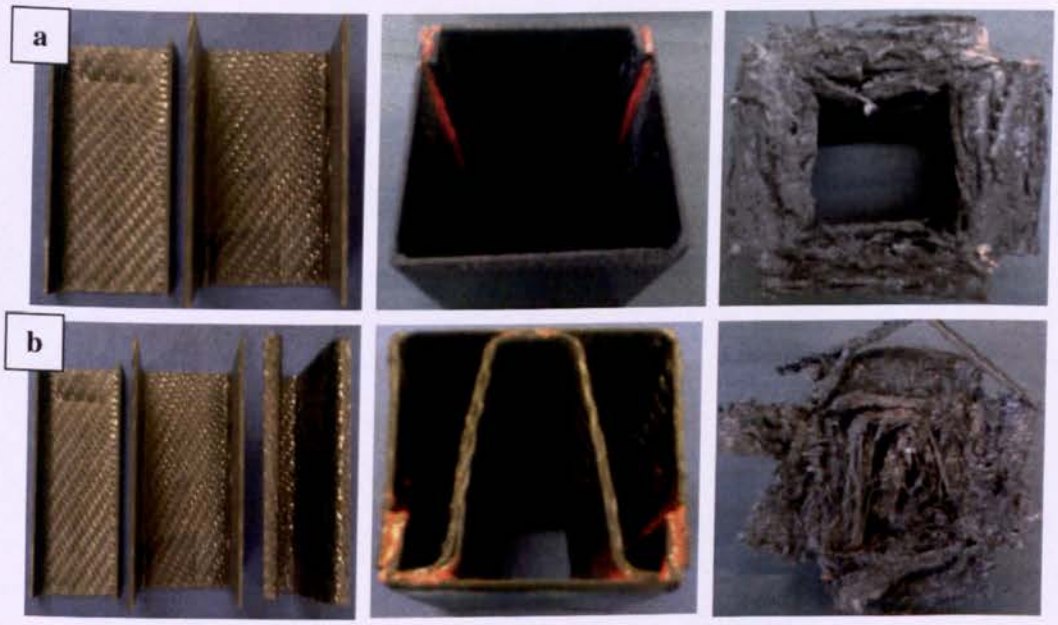

Fig. 6.11. Assembled crash boxes made from bonding (a) Two channels and b) Two channels stiffened with V-shape stiffener before and after crushing.

In Figure 6.12 the force-crush distance diagrams of assembled specimens are compared to the crushing response of simple box with $[0]_4$ laminate.

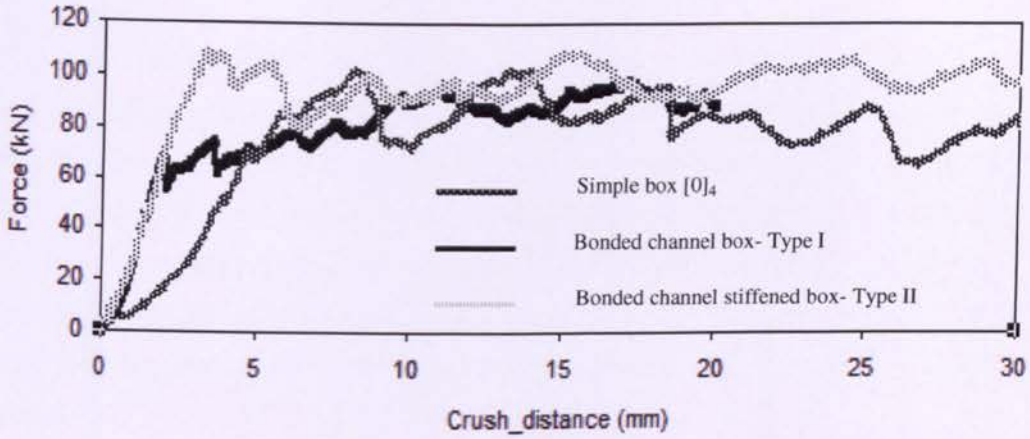

Fig. 6.12. Comparison of force-crush distance of CFRP assembled and simple boxes (All made from $[0]_4$ lay-up).

6.5.2. Crushing response of stiffened composite box structures

The specific sustained crushing stress (SSCS) of simple and stiffened CFRP composite boxes which were laminated from carbon/epoxy twill-weave fabrics was studied experimentally. It was found that the highest specific sustained crushing stress (SSCS) was achieved for the simple composite box with the fibre orientation of $[0]_4$.

The assembled boxes from two channels with the $[0]_4$ lay-up bonded by epoxy adhesive showed roughly the same SSCS as the simple box. The assembled box stiffened with a V-shape stiffener has 4% higher SSCS relative to its higher mean force in comparison with the simple box.

6.6. Conclusion

In all hybrid composite boxes the lamina bending crushing mode was observed. In this case the main central interwall crack which is similar to Mode-I crack delamination started to propagate at four sidewalls of each composite box. In the lamina bending mode, the main central crack causes to form lamina bundles which had a significant role in absorbing the

crushing energy. It was shown that the fibre orientation at the interface planes had a significant effect on Mode-I interlaminar fracture toughness.

Also in this failure mode the fronds splitting due to lamina bundle bending is similar to interlaminar crack propagation in Mode-II. The G_{IC} and G_{IIC} of initiation are more influential than the G_{IC} and G_{IIC} of propagation in the energy absorption mechanism. The Mode-I and Mode-II initiation values were chosen to quantify the effect of Mode-I and Mode-II fracture toughness on the energy absorption of the composite box. From this relationship it was found that the hybrid laminate designs which showed higher fracture toughness in Mode-I and Mode-II delamination tests were able to absorb more energy as a composite box in crushing process.

References

[1] Davies P, editor. Protocols for interlaminar fracture testing of composites. ESIS-Polymers and Composites Task group; 1993.

[2] Hashemi S, Kinloch AJ, Williams JG. The analysis of interlaminar fracture in uniaxial fibre-polymer composites. Proc. R. Soc. Lond. 1990;427(A):173-199.

[3] de Moura MFSF, de Morais AB, Equivalent crack based analysis of ENF and ELS tests. 2008;75: 2584-2596.

Appendix (C6): The correction factors of f and N for the end-loaded split (ELS) specimen.

$$F = 1 - \theta_1 \left(\frac{\delta}{L}\right)^2 - \theta_2 \left(\frac{\delta l_1}{L^2}\right) \tag{C6-1}$$

$$N = 1 - \theta_3 \left(\frac{l_2}{L}\right)^3 - \theta_4 \left(\frac{\delta l_1}{L^2}\right) - \theta_5 \left(\frac{\delta}{L}\right)^2 \tag{C6-2}$$

$$\theta_1 = \frac{3}{20}\left[\frac{15 + 50\left(\frac{a}{L}\right)^2 + 63\left(\frac{a}{L}\right)^2}{\left[1 + 3\left(\frac{a}{L}\right)^3\right]^2}\right] \tag{C6-3}$$

$$\theta_2 = \frac{-3\left(\frac{L}{a}\right)\left(1 + 3\left(\frac{a}{L}\right)^2\right)}{1 + 3\left(\frac{a}{L}\right)^3} \tag{C6-4}$$

$$\theta_3 = \frac{4}{1 + 3\left(\frac{a}{L}\right)^3} \tag{C6-5}$$

$$\theta_4 = \frac{-9}{4}\frac{\left[\left(1 - \left(\frac{a}{L}\right)\right)\left(1 + 3\left(\frac{a}{L}\right)^3\right) + 4\left(\frac{a}{L}\right)^2\left(1 - \left(\frac{l_2}{a}\right)^2\right)\left(1 + 3\left(\frac{a}{L}\right)^2\right)\right]}{\left(1 + 3\left(\frac{a}{L}\right)^3\right)^2} \tag{C6-6}$$

$$\theta_5 = \frac{36}{35}\frac{1+\frac{3}{8}\left(\frac{a}{L}\right)^3\left(35+70\left(\frac{a}{L}\right)^2+63\left(\frac{a}{L}\right)^4\right)}{\left(1+3\left(\frac{a}{L}\right)^3\right)^3} \qquad \text{(C6-7)}$$

Chapter 7:

Analytical Prediction of Mean Crushing Force in Progressive Crushing Failure

Nomenclature

a	crack length
a_e	effective crack length
b	side of box
E	Young's modulus
F	load
F_m	mean load
G_{12}	shear modulus
G_{IC}	Mode-I interlaminar fracture toughness
G_{IIC}	Mode-II interlaminar fracture toughness
SEA	specific energy absorption
t	crush box wall thickness
U_e	external work
U_f	energy dissipated by friction
U_b	energy dissipated in bending
U_{bu}	energy dissipated in local buckling
U_{bf}	energy dissipated by bundle fracture
U_c	energy dissipated in axial splitting
U_d	energy dissipated by delamination
U_s	energy dissipated in shear deformation
$U_{LB/BF}$	energy dissipated for lamina bending/brittle fracture crushing modes
$U_{BU/TS}$	energy dissipated for local buckling/transverse shearing crushing modes
U_{BF}	energy dissipated for brittle fracture crushing modes

x sliding distance on the platen

Y geometry factor

z crushing distance

ν Poisson's ratio

λ crush length in a single stroke

β weight factor

μ coefficient of friction

δ displacement

σ_u ultimate tensile stress

σ_b flexural strength

τ_s shear strength

φ semi-angle of the wedge

7. Introduction

In this chapter a new theoretical model based on friction, bending and fracture mechanisms to predict the mean crushing force for the combination of failure crushing mode is proposed. During the progressive crushing of CFRP and GFRP composite box the combination of brittle fracture, lamina bending, local buckling and transverse shearing crushing modes are observed. The brittle nature of CFRP and GFRP composites shows the high capability in absorbing the crushing energy by various fracture mechanisms, the most important of them are bundle fracture, frond splitting and delamination crack growth. These kind of fractures contribute to shaping lamina bundles and consequently increasing of friction and bending resistance. Compared to other analytical methods, the present work introduces a comprehensive prediction of the mean crushing force for combination of all the failure modes.

7.1. Theoretical prediction

The composite boxes showed the combination of progressive crushing failure of lamina in bending/brittle fracture, local buckling/transverse shearing and brittle fracture modes. Other analytical solutions were proposed for the prediction of static and dynamic mean force of composite tubular specimens in axial crushing [1,2]. In the following section, two analytical models based on energy balance approach will be introduced to obtain the mean crushing force, F_m, in axial crushing of square composite box.

The external work of crushing platen is dissipated by mechanisms of friction, bending, fracture and shear deformation. The idealised crush zone for our analytical model is shown in Figure 7.1.

7.2. Lamina bending/brittle fracture crushing mode

The applied external work by force F during the crush distance z is

$$U_e = F \cdot z \tag{7.1}$$

where $z = \lambda - \lambda\cos\varphi$ is the crush distance as shown in Figure 7.1 and λ is the crush length in a single stroke. The maximum work done by external force happens when $\varphi=\pi/2$, $z = \lambda$.

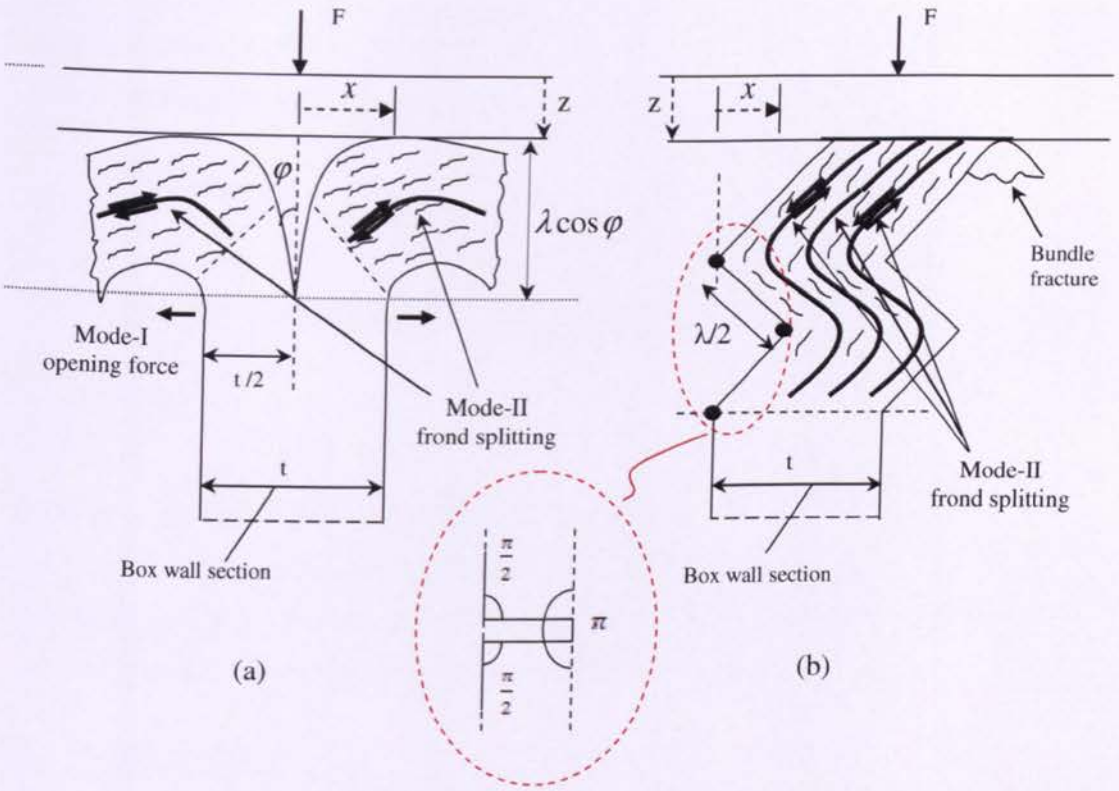

Fig. 7.1. Ideal crush zone, (a) Lamina bending/brittle fracture crushing mode and (b) Local buckling/transverse shearing crushing mode.

The energy dissipated by friction between crushing platen and the debris inside the internal and external fronds in *lamina bending/brittle fracture* crushing mode can be obtained from,

$$U_f = 2(\mu \cdot \frac{F}{2} \cdot x) = \mu \cdot F \cdot x \qquad (7.2)$$

where, $x = \lambda \sin\varphi$. The experimentally measured coefficient of friction for woven CFRP is μ=0.41.

The energy dissipated by frond bending was calculated by assuming that the whole cross section of the frond will reach to the flexural bending strength, σ_b. The bending moment per unit width of internal and external fronds is $M = 2\left[2\int_0^{\frac{t}{4}} \sigma_b \, y \, dy\right] = \frac{\sigma_b t^2}{8}$.

The flexural strengths, σ_b, for each lay-up of CFRP were measured from 3PB experiments and the results are listed in Table 4.1. The energy dissipated in bending for combination of *lamina bending/brittle fracture* crushing mode at stationary hinge lines is

$$U_b = \int_0^{\frac{\pi}{2}} \frac{\sigma_b (4b) t^2 d\varphi}{8} \tag{7.3}$$

Hence, the dissipated energy due to bending becomes,

$$U_b = \frac{\pi b t^2 \sigma_b}{4} \tag{7.4}$$

The energy dissipated by interlaminar crack propagation in Mode-I and Mode-II is calculated from interlaminar fracture energies. In lamina bending/brittle fracture mode there is one interwall Mode-I crack at the centre of each side wall of the box and one Mode-II cracks in each internal and external fronds as shown in Figure 7.2. Therefore,

$$U_d = 4b\lambda(G_{IC} + 2G_{IIC}) \tag{7.5}$$

The Mode-I and Mode-II interlaminar fracture toughness were measured experimentally by DCB and 3ENF tests as discussed earlier in Chapters 3 and 4.

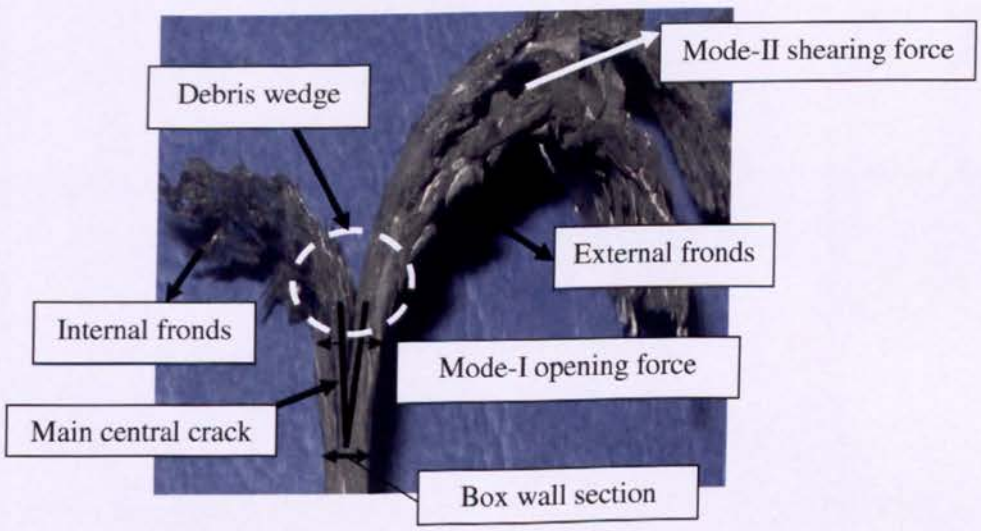

Fig. 7.2. Mode-I and Mode-II interlaminar crack propagation at the central interwall in $[0/45]_2$ and $[0]_4$ boxes.

Dissipated energy by axial splitting at the four corners of the box for *lamina bending/transverse shearing* crushing mode is calculated based on the stress intensity factor.

$$G = \frac{K^2}{E_z} \tag{7.6}$$

where K is the stress intensity factor given by

$$K = Y\sigma\sqrt{\pi\lambda} \tag{7.7}$$

At fibre splitting we assume $\sigma = \sigma_u$. The crack assumed to propagate similar to a crack growth in a single edge notched (SEN) plate where *Y=1.12*. Therefore, the dissipated energy in axial splitting for a fracture area of $A = 4t\lambda$ is,

$$U_c = \frac{5\pi t \lambda^2 \sigma_u^2}{E_z} \tag{7.8}$$

where E_z *is* Young's modulus in axial direction of the crush box.

The energy dissipated in shear deformation of matrix during steady state progressive crushing was estimated from

$$U_s = \frac{1}{2}\int_V \tau\gamma dV = \frac{1}{2}\int_V \frac{\tau^2}{G_{12}} dV \tag{7.9}$$

By assuming during the crushing process the shear stress will reach to its maximum shear strength value of the laminate, $\tau = \tau_s$, the energy dissipated in shear deformation of laminate is

$$U_s = \frac{2bt\lambda\tau_s^2}{G_{12}} \tag{7.10}$$

Dissipated energy due to bundle fracture was obtained by replacing the crush distance, λ with the width of box, *b/2*.

$$U_{bf} = \frac{1.25\pi t b^2 \sigma_u^2}{E_y} \tag{7.11}$$

The fracture area of $A = 8\left(\frac{t}{2}\right)\left(\frac{b}{2}\right) = 2bt$ was assumed for eight internal and external fronds with crack growth assumed to be half the width of the side wall as observed in the experiments and E_y is Young's modulus in transverse direction of the crush box.

The energy balance for the crushing process during a single stroke crush distance is

$$U_e - U_f = U_b + U_d + U_c + U_s + U_{bf} \tag{7.12}$$

Substituting from Eqs. (7.1), (7.2), (7.4), (7.5), (7.8), (7.10) and (7.11) in Eq. (7.12), the energy dissipated by *lamina bending/brittle fracture* crushing mode, $U_{LB/BF}$, is

$$U_{LB/BF} = F(1-\mu)\lambda = \frac{\pi bt^2\sigma_b}{4} + 4b\lambda(G_{IC} + 2G_{IIC}) + \frac{5\pi t\lambda^2\sigma_u^2}{E_z} + \frac{2bt\lambda\tau_s^2}{G_{12}} + \frac{1.25\pi b^2\sigma_u^2}{E_y} \tag{7.13}$$

Therefore, the mean crushing force in a stable progressive crush is:

$$F = \frac{1}{(1-\mu)}\left[\frac{\pi bt^2\sigma_b}{4\lambda} + 4b(G_{IC} + 2G_{IIC}) + \frac{5\pi t\lambda\sigma_u^2}{E_z} + \frac{2bt\tau_s^2}{G_{12}} + \frac{1.25\pi b^2\sigma_u^2}{E_y\lambda}\right] \tag{7.14}$$

A single stroke crush distance for lamina bending case can be found from Eq. (7.14) by setting $\partial F / \partial\lambda = 0$

$$\lambda = \sqrt{\frac{bt\sigma_b E_y + 5b^2\sigma_u^2}{20\sigma_u^2}\frac{E_z}{E_y}} \tag{7.15}$$

The mean force during the progressive crushing can be found by calculating λ from Eq. (7.15) and substituting in Eq. (14).

7.3. Local buckling/transverse shearing crushing mode

According to experimental results for *local buckling/transverse shearing* crushing mode, interwall Mode-I opening crack was not observed in the crushed box. In this case the energy dissipated by friction between crushing platen and fronds when the hinge folded completely can be obtained from (see Figure 7.1),

$$U_f = \mu \cdot F \cdot x = \mu \cdot F \cdot \lambda \tag{7.16}$$

The energy dissipated in bending for *local buckling/transverse shearing* mode happening in three hinge lines can be summed

$$U_{bu} = (4b)\int_0^{\varphi} M\, d\varphi = (4b)\sum_{i=1}^{3} M\, \varphi \tag{7.17}$$

In this situation, the rotational angles at the hinge lines are assumed to be $\pi/2$, π and $\pi/2$, respectively (see Figure 7.1). For this crushing mode the dissipated energy in local buckling is,

$$U_{bu} = \frac{\pi b t^2 \sigma_b}{2} \tag{7.18}$$

In this mode during crushing, box side walls were locally buckled and three Mode-II interlaminar fracture cracks were observed in *local buckling/transverse shearing* in bundles (see Figure 7.3).

The dissipated energy in delamination is calculated from,

$$U_d = 4b\lambda(3G_{IIC}) = 12b\lambda G_{IIC} \tag{7.19}$$

Dissipated energy due to bundle fracture can be obtained from Eq. (7.11)

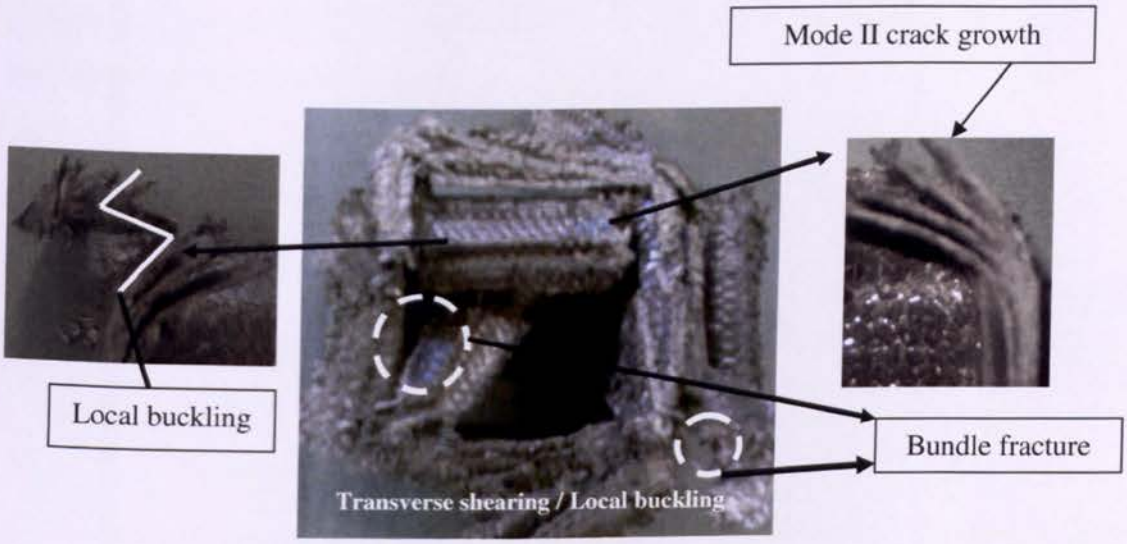

Fig. 7.3. Plane view of crushed CFRP composite box of $[45]_4$.

Dissipated energy due to axial splitting and shear deformation of matrix remains as before and can be calculated from Eqs. (7.8) and (7.10). Assuming the maximum work done, $U_e = F\lambda$, the total energy balance can be written as,

$$U_e - U_f = U_{bu} + U_d + U_c + U_s + U_{bf} \tag{7.20}$$

Finally, the dissipated energy by *local buckling/transverse shearing*, $U_{BU/TS}$ crushing mode can be obtained by substituting from Eqs. (7.8), (7.10), (7.16), (7.18) and (7.19) in Eq. (7.20) as,

$$U_{BU/TS} = F\lambda(1-\mu) = \frac{\pi b t^2 \sigma_b}{2} + 12 b \lambda G_{IIC} + \frac{5\pi t \lambda^2 \sigma_u^2}{E_z} + \frac{2bt\lambda\tau_s^2}{G_{12}} + \frac{1.25\pi t b^2 \sigma_u^2}{E_y} \tag{7.21}$$

The crush length of a single stroke due to lamina bending can be found from Eq. (7.21) by setting $\partial F / \partial \lambda = 0$

$$\lambda = \sqrt{\frac{bt\sigma_b E_y + 2.5 b^2 \sigma_u^2}{10\sigma_u^2} \frac{E_z}{E_y}} \tag{7.22}$$

The results of the mean force from the experimental and theoretical solutions are summarised in Table 7.1. The results are in good agreement and the discrepancy between experimental and theoretical results is less than 8%.

Table 7.1. Comparison of experimental and analytical mean force results of each laminate design. LB/BF= Lamina bending/brittle fracture and BU/TS= Local buckling/transverse shearing.

Laminate Lay-up	**Cushing failure mode**	F_m (Exp.) kN	F_m (Anal.) kN
$[0]_4$	LB/BF	65	59.4
$[0/45]_2$	LB/BF	67	59.3
$[45]_4$	BU/TS	52	58.5

7.4. Brittle fracture crushing mode

In previous sections analytical solutions were proposed for the prediction of static mean force of composite box specimens in axial crushing in combination of *lamina bending/brittle fracture* and *local buckling/transverse shearing* crushing modes. In the experimental investigations in axial crushing of woven GFRP composite box, *brittle fracture* crushing mode was observed. In the following section, an analytical model based on energy balance approach will be introduced to obtain the mean crushing force, F_m, and consequently the SEA in axial brittle fracture crushing of square composite box.

According to experimental results in axial crushing many bundle fractures and crack propagation in Mode-II were observed in crushed box. In this case the energy dissipated by friction between crushing platen and fronds when the frond bent completely can be obtained from (see Figure 7.4),

$$U_f = \mu \cdot F \cdot x \tag{7.23}$$

where, $x = \lambda \sin\varphi$. The experimentally measured coefficient of friction for woven GFRP is μ=0.35.

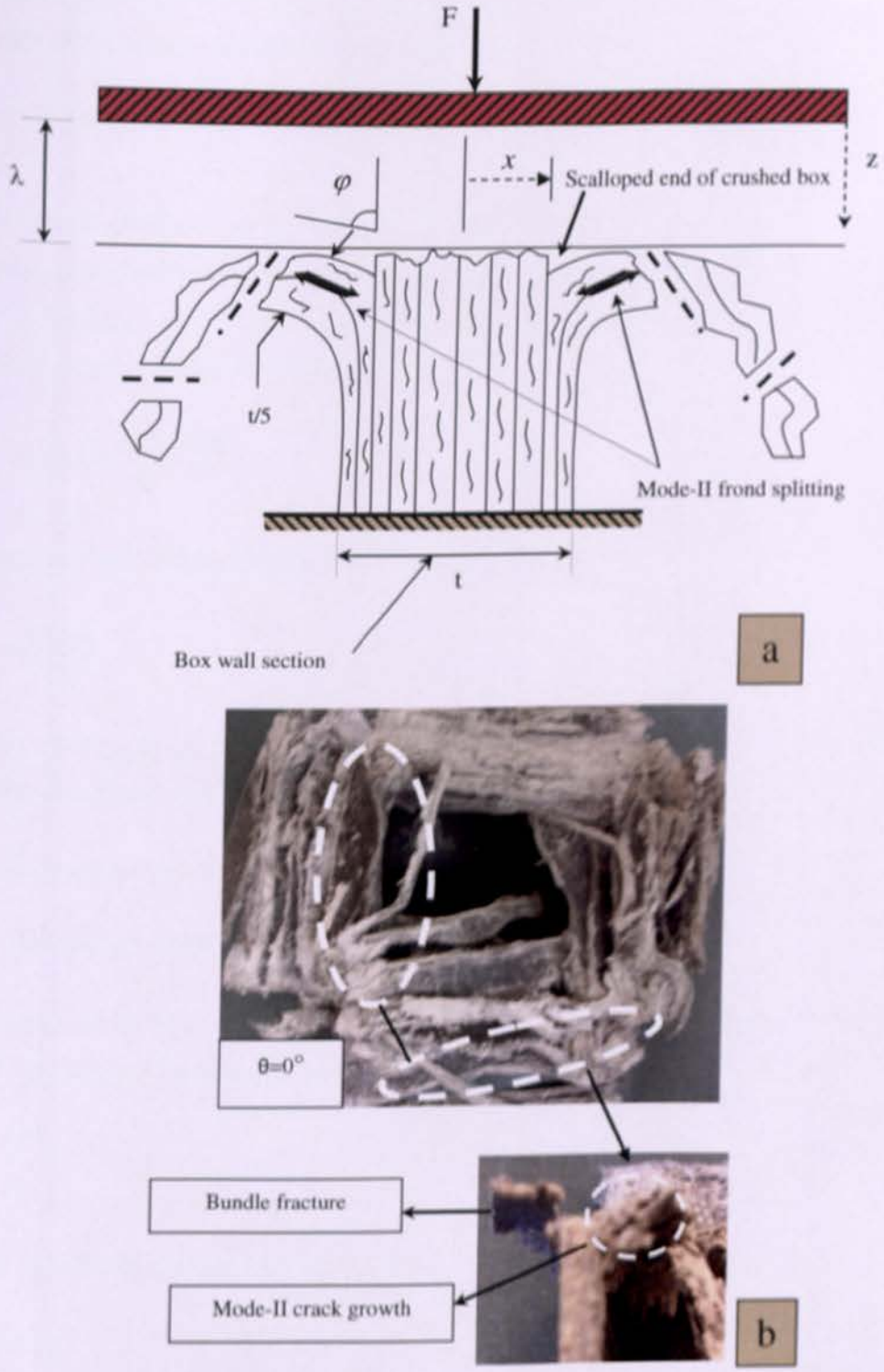

Fig. 7.4. Ideal crush zone, brittle fracture crushing mode in axial crushing, (a) Analytical model (b) Experimental.

The energy dissipated by frond bending was calculated by assuming that the whole cross section of the frond will reach to the flexural bending stiffness, σ_b. The bending moment per unit width of internal and external fronds is $M = 2\left[2\int_0^{\frac{t}{10}} \sigma_b y\, dy\right] = \frac{\sigma_b t^2}{50}$.

The flexural strengths, σ_b, for each lay-up of GFRP were measured from 3PB experiments and the results are listed in Table 7.1. In each side of the box, the internal and external fronds with a thickness of t/5 were formed. The energy dissipated in bending for *brittle fracture* crushing mode at stationary hinge lines is

$$U_b = \int_0^{\frac{\pi}{2}} \frac{\sigma_b (4b) t^2 d\varphi}{50} \tag{7.24}$$

Hence, the dissipated energy due to bending becomes,

$$U_b = \frac{\pi b t^2 \sigma_b}{25} \tag{7.25}$$

At this crushing mode, the Mode-II interlaminar fracture cracks were observed in fractured bundles (see Figure 7.4).

The dissipated energy in delamination is calculated from,

$$U_d = 4b\lambda(2G_{IIC}) = 8b\lambda G_{IIC} \tag{7.26}$$

Dissipated energy by axial splitting at the four corners of the box for *brittle fracture* crushing mode is calculated based on the stress intensity factor.

$$G = \frac{K^2}{E_z} \tag{7.27}$$

where K is the stress intensity factor given by

$$K = Y\sigma\sqrt{\pi\lambda} \tag{7.28}$$

At fibre splitting we assume $\sigma = \sigma_u$. The crack assumed to propagate similar to a crack growth in a single edge notched (SEN) plate where *Y=1.12*.

Therefore, the dissipated energy in axial splitting for a fracture area of $A = 4t\lambda$ is,

$$U_c = \frac{5\pi t \lambda^2 \sigma_u^2}{E_z} \tag{7.29}$$

where E_z is Young's modulus in axial direction of the crush box.

The energy dissipated in shear deformation of matrix during steady state progressive crushing was estimated from

$$U_s = \frac{1}{2}\int_V \tau\gamma dV = \frac{1}{2}\int_V \frac{\tau^2}{G_{12}} dV \tag{7.30}$$

By assuming during the crushing process the shear will reach to its maximum shear strength of the laminate, $\tau = \tau_s$, the energy dissipated in shear deformation of laminate is

$$U_s = \frac{2bt\lambda\tau_s^2}{G_{12}} \tag{7.31}$$

Dissipated energy due to bundle fracture was obtained by replacing the crush distance, λ with the width of box, *b/2*, because crack growth was assumed to be half the width of the side wall.

$$U_{bf} = \frac{0.5\pi t b^2 \sigma_u^2}{E_y} \tag{7.32}$$

The fracture area of $A = 8\left(\frac{t}{5}\right)\left(\frac{b}{2}\right) = \frac{4}{5}bt$ was assumed for eight internal and external fronds with crack growth assumed to be half the width of the side wall as observed in the experiments and E_y is Young's modulus in transverse direction of the crush box.

Assuming the maximum work done, $U_e = F\lambda$, the total energy balance can be written as,

$$U_e - U_f = U_b + U_d + U_c + U_s + U_{bf} \tag{7.33}$$

Finally, the dissipated energy by *brittle fracture, U_{BF}* crushing mode can be obtained by substituting from Eqs. (7.23), (7.25), (7.26), (7.29), (7.31) and (7.32) in Eq. (7.33) as,

$$U_{BF} = F\lambda(1-\mu) = \frac{\pi b t^2 \sigma_b}{25} + 8b\lambda G_{IIC} + \frac{5\pi t \lambda^2 \sigma_u^2}{E_z} + \frac{2bt\lambda\tau_s^2}{G_{12}} + \frac{0.5\pi t b^2 \sigma_u^2}{E_y} \quad (7.34)$$

The crush length of a single stroke can be found from Eq. (7.35) by setting $\partial F / \partial \lambda = 0$

$$\lambda = \sqrt{\frac{0.04bt\sigma_b E_y + 0.5b^2\sigma_u^2}{5\sigma_u^2}\frac{E_z}{E_y}} \quad (7.35)$$

From the theoretical result the mean force in axial crushing was 48kN. This result is in good agreement and the discrepancy between experimental result reported in Table 7.2 and theoretical result is less than 4%.

Table 7.2. Comparison of experimental and analytical mean force (F_m) results of GFRP composite box in brittle fracture crushing mode.

Axial crushing in Brittle fracture	F_m (Exp.) (kN)	F_m (Anal.) (kN)	Error (%)
GFRP-$[0]_{10}$	50	48	4

7.5. Conclusion

The contribution of each failure mechanism to the energy dissipation of composite box in various crushing modes are presented in Table 7.3. In brittle fracture/ lamina bending crushing mode the highest value which plays an important role on energy absorption during crushing process is for axial splitting and after that for bundle fracture. It should be mentioned these mechanisms are coupled together and they act at the same time in a crushing process. This fact shows higher resistance for delamination crack growth in different delamination modes directly affect on the bending and friction resistance of internal and external fronds against the crushing load.

Table 7.3. Contribution of dissipated energy for each failure mechanism of various crushing modes.

Lamina bending/ brittle fracture

Dissipated Energy	***Lamina Bending*** $U_b(J)$	***Axial splitting*** $U_c(J)$	***Ply Delamination*** $U_d(J)$	***Shear deformation*** $U_S(J)$	***Bundle fracture*** $U_{bf}(J)$
CFRP-$[0]_4$	313.7	776	54.4	62.4	522
%	18.1	44.9	3.1	3.6	30.2

Dissipated Energy	***Lamina Bending*** $U_b(J)$	***Axial splitting*** $U_c(J)$	***Ply Delamination*** $U_d(J)$	***Shear deformation*** $U_S(J)$	***Bundle fracture*** $U_{bf}(J)$
CFRP-$[0/45]_2$	322	776	70.4	62.4	522
%	18	44.9	4	3.6	30.2

Local buckling/ transverse shearing

Dissipated Energy	***Lamina Bending*** $U_{bu}(J)$	***Axial splitting*** $U_c(J)$	***Ply Delamination*** $U_d(J)$	***Shear deformation*** $U_S(J)$	***Bundle fracture*** $U_{bf}(J)$
CFRP-$[45]_4$	361.7	776	115.2	62.4	522.2
%	19.7	42.2	6.3	3.4	28.4

Brittle fracture

Dissipated Energy	***Lamina Bending*** $U_b(J)$	***Axial splitting*** $U_c(J)$	***Ply Delamination*** $U_d(J)$	***Shear deformation*** $U_S(J)$	***Bundle fracture*** $U_{bf}(J)$
GFRP-$[0]_{10}$	40.7	338.6	63.2	104.5	308.7
%	4.7	40	7.4	12	36

References

[1] Mamalis AG, Manolakos DE, Demosthenous GA and Ioannidis MB. The static and dynamic collapse of fibreglass composite automotive frame rails. *Composite Structures*, 1996;34:77-90.

[2] Solaimurugan S and Velmurugan R. Influence of fibre orientation and stacking sequence on petalling of glass/polyester composite cylindrical shell under axial compression. *Int Jnl of Sol and Struc*, 2007;44:6999-7020.

Chapter 8:

Finite Element Analysis of Progressive Failure of Composite Crush Box Using LSDYNA

Nomenclature

G_{12}	shear modulus
SEA	specific energy absorption
S	shear strength
X_t	longitudinal tensile strength
X_c	longitudinal compressive strength
Y_t	transverse tensile strength
Y_c	transverse compressive strength
υ	Poisson's ratio
σ_1	longitudinal stress
σ_2	transverse stress
σ_{12}	transverse shear stress
$NFLS$	normal tensile stress
$SFLS$	normal shear stress
β	weight factor
σ_u	ultimate tensile stress

8. Introduction

In this chapter an analysis and investigation of the crushing characteristics of thin-walled GFRP and CFRP composite crush components, by simulating the response of composite box subjected to quasi-static axial and off-axis compression loading, using LS-DYNA finite element code is described. LS-DYNA is a code that was developed by the Lawrence Livermore National Laboratory in particular for impact and non-linear dynamic simulation works, using a Langrangian formulation and explicit time integration with central differences, which provides a wide variety of material models being particularly effective in the modelling of contact between interacting parts and crash simulation. Finally the results are verified with the relevant experimental result.

8.1. Finite Element Analysis (FEA)

In crashworthiness evaluations of composite box structures nonlinear material and geometric properties must be simulated and must be designed to simulate short-time large deformations in crash conditions. FEA involving short-time large deformation dynamics such as crashworthiness evaluation requires the solution of transient dynamic problems over a short time length. Explicit computational algorithms typically use the central differences method for integration, wherein the internal and external forces are assumed at each node point, and a nodal acceleration is computed by dividing by the nodal mass. The solution is continued by integrating this acceleration in time. The advantage of this method is that time-step size may be selected by the user. The disadvantage is the large numerical effort required to form, store, and factorise the stiffness matrix.

The explicit solution technique is stable only if time-step Δt is smaller than Δt_{cr} which is the critical time step Δt_{cr} for shell element, is obtained from $\Delta t_{cr} = L_s / C$, where L_s is the characteristic length and C is the speed of sound, $C = \sqrt{E/\rho(1-\nu^2)}$. The implicit method is not solved by the time-step size and then is unconditionally stable for larger time steps. This situation yields that the implicit method typically engages a large number of expensive time steps. For an explicit solution the number of time-steps can be larger than that of implicit methods, the small time-step size requirement makes the explicit method suitable for short transient solutions. The most important advantage of the explicit method is that there is no

requirement for solving simultaneous equations. Thus, no global matrix inversion is needed and a reduction of computational time is obtained [1].

8.2. Loading conditions

Four loading conditions of static, fatigue, high-speed/rapid loading and impact are generally categorised in engineering science. These loading conditions are recognised by the rate of loading or the rise time upon the mechanical system or component. The load rise time on a system is illustrated in Figure 8.1.

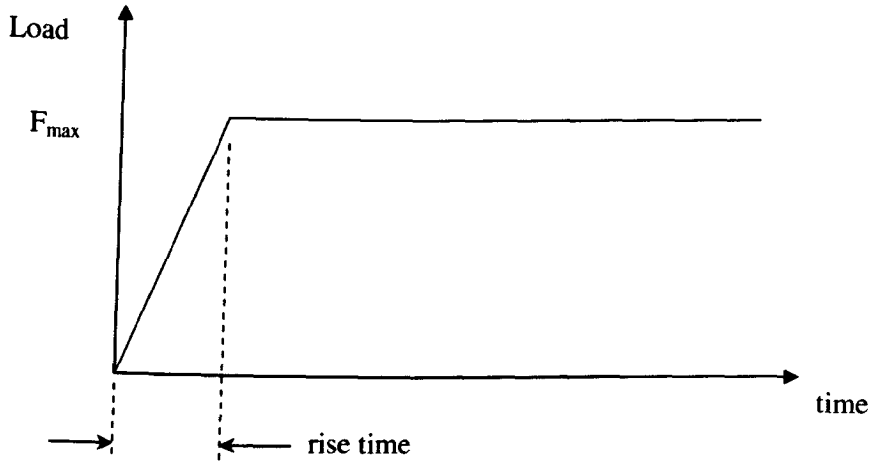

Fig. 8.1. Load rise time in category of various loading conditions.

- *Static loading*: Static loading happens when the rise time of the load is three times greater than the fundamentally period (T_n) of the mechanical system. The usual methods of analysis of stress, strain, and displacements along with static material properties are used to analyse the system.

- *Fatigue loading:* Fatigue is a time-varying load in which the rise time from one magnitude to another magnitude still remains greater than three fundamental periods.

- *High speed or rapid loading:* This occurs when the rise time of load application ranges between 1.5 to 3 times the fundamental periods of the mechanical system. Vibration analysis should be used in the loading category.

- *Impact loading:* If the duration of load application is less than 0.5 times the fundamental period of the mechanical system, the loading is defined as impact. The static methods of stress, strain, and deflection analysis are inappropriate under impact conditions.

This is due to propagation, reflection, and interference of elastic/plastic waves travelling within the engineering solid. Accurate calculations of stresses and strains must be based on wave analysis methods, which are extraordinarily complex for practical use, and thus are used for a limited number of simple cases. Other methods such as contact mechanics, energy methods, and FEA must be used to estimate the effects of impact analysis on mechanical systems that exhibit complexity.

The equations of equilibrium governing the dynamic response of a finite element system are of the form [2]

$$M\ddot{U} + C\dot{U} + KU = R \tag{8.1}$$

where

- M, C and K are the mass, damping and stiffness matrices,
- R is the externally applied load vector,
- U, $\dot{U}$ and $\ddot{U}$ are the displacement, velocity and acceleration vectors of the finite element assemblage, and
- $F_I(t) = M\ddot{U}$, $F_D(t) = C\dot{U}$, $F_E(t) = KU$ and $R(t)$ are the time dependent inertia, damping, elastic and externally applied forces.

LS-DYNA is an explicit finite element code employing the central difference method, which requires for the displacement U_t, velocity $\dot{U}_t$ and acceleration $\ddot{U}_t$, to satisfy the equations;

$$\ddot{U}_t = \frac{1}{\Delta t^2}(U_{t-\Delta t} - 2U_t + U_{t+\Delta t}) \tag{8.2}$$

$$\dot{U}_t = \frac{1}{2\Delta t}(-U_{t-\Delta t} + U_{t+\Delta t}) \tag{8.3}$$

where, Δt is an appropriate time step size required for the numerical integration.

The displacement solution at time $t + \Delta t$ is obtained by considering the Eq. (8.1) at time t,

$$M\ddot{U}_t + C\dot{U}_t + KU_t = R_t \tag{8.4}$$

Substituting the relations for $\ddot{U}_t$ and $\dot{U}_t$ from Eqs. (8.2) and (8.3), respectively, into Eq. (8.4), it will result;

$$\left(\frac{1}{\Delta t^2}M+\frac{1}{2\Delta t}C\right)U_{t+\Delta t}=R_t-\left(\mathrm{K}-\frac{2}{\Delta t^2}M\right)U_t-\left(\frac{1}{\Delta t^2}M-\frac{1}{2\Delta t}C\right)U_{t-\Delta t} \qquad (8.5)$$

which gives the solution for $U_{t+\Delta t}$.

The above mentioned integration procedure is called an explicit integration method because the solution of $U_{t+\Delta t}$ is calculated by using the equilibrium conditions at time t Eq. 8.4. For this reason exactly, an integration scheme does not require decomposition (i.e., factorization or triangularization) of the effective stiffness matrix $\hat{K}=K+\alpha_0 M+\alpha_1 C$ in the step-by-step solution, since the stiffness matrix K does not appear as a factor to the required displacements $U_{t+\Delta t}$ on the left side of Eq. (5) and hence no effective stiffness matrix occurs to be decomposed. Instead, the effective mass matrix $\hat{M}=\alpha_0 M+\alpha_1 C$ formed, where $\alpha_0=1/\Delta t^2$ and $\alpha_0=1/2\Delta t$ are the appropriate integration constants, is necessary to be decomposed in order to obtain the solution for $U_{t+\Delta t}$ after the required calculation of the effective load factor

$$\hat{R}_t=R_t-\left(\mathrm{K}-\frac{2}{\Delta t^2}M\right)U_t-\left(\frac{1}{\Delta t^2}M-\frac{1}{2\Delta t}C\right)U_{t-\Delta t} \qquad (8.6)$$

which requires only matrix multiplications to obtain (see Eq. (8.5)). In an implicit integration scheme, such as Houbolt's, the solution of $U_{t+\Delta t}$ is calculated by using the equilibrium conditions at time $U_{t+\Delta t}$ and not at time t as in the central difference method, leading in the formulation of the effective stiffness matrix $\hat{K}=K+\alpha_0 M+\alpha_1 C$ (where α_0 and α_1 are the related method appropriate integration constants) which appears as a factor to the required displacements $U_{t+\Delta t}$ on the left side of the corresponding Eq. (8.5). Thus, in this case, the decomposition of the effective stiffness matrix is obvious in order to obtain the solution for $U_{t+\Delta t}$. Additionally, since the effective stiffness matrix $\hat{K}=K+\alpha_0 M+\alpha_1 C$ of the element assemblage is not to be decomposed as it is not formed according to the central difference method, it is also not necessary to assemble the stiffness matrix K, because KU_t as required in Eq. (8.5) can be evaluated on the element level by summing the contributions from each element to the effective load vector.

Using the explicit central difference method, the calculation of $U_{t+\Delta t}$ involves U_t and $U_{t+\Delta t}$. Therefore, in order to calculate the solution at time Δt (i.e., at the end of the first time step) a

special starting procedure must be used. Eqs. (8.2) and (8.3), at time *t=0* (i.e., $t-\Delta t=-\Delta t$ and $t+\Delta t=\Delta t$), give

$$U_{-\Delta t}=U_0-\Delta t\dot{U}_0+\frac{\Delta t^2}{2}\ddot{U}_0 \tag{8.7}$$

where, U_0, $\dot{U}_0$ and $\ddot{U}_0$ are known, since, given the U_0 and $\dot{U}_0$ from the initial conditions, $\ddot{U}_0$ can be calculated using the Eq. (8.1) at time 0.

8.3. Finite element modelling process

8.3.1. Geometry and element definition

The GFRP and CFRP composite boxes were modelled with various lay-ups using finite element software LSDYNA [1]. The size of outer cross section of the composite box was 80×80mm with a thickness of 3 mm. The trigger mechanism was modelled by reducing the thickness of the first row of shell elements at the top of each box. The composite box model was based on Belytschko-Lin-Tsay quadrilateral shell elements. This shell element is based on a combined co-rotational and velocity strain. All surfaces of the model were meshed using quadratic shell elements and the size of an element was 2.5×2.5mm (see Figure 8.2). The striker was modelled as a rigid block using solid elements. The mesh of finite elements was featured by local refinements along the height, thickness and circumference of the specimen in order to accurately simulate the main crushing characteristics observed in the experimental works which were discussed in earlier chapters.

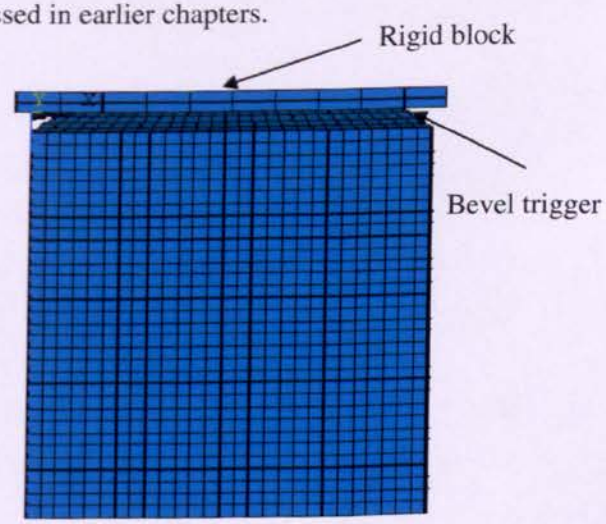

Fig. 8.2. Finite element model of GFRP and CFRP composite box in LS-DYNA.

The box wall was modelled with 10 layers. The composite layers were modelled by defining 10 integration points which were placed equally through the thickness in each layer of Belytschko-Lin-Tsay shell element.
The single layer was modelled with a single integration point located at the mid-surface according to the Gauss-integration rule. The number and locations of the integration points were defined on the SECTION-SHELL and INTEGRATION cards in the key file.

8.3.2. Material modelling and composite failure criteria

Two different types of material models were used in LSDYNA in the development of finite element models described herein:

- Material model 20 "mat_rigid",
- Material model 54 "mat_enhanced_composite_damage".

The first of the two material models (i.e. model 20 "mat_rigid") was used to model the rigid striker. As required by the code the values of the basic material properties (mass density, Young's modulus and Poisson ratio) corresponding to mild steel were given as input to the program.
Material model 54 of LS-DYNA was selected to model the damage of GFRP and CFRP composite box. In ANSYS this material model follows the Chang-Chang [3] failure criterion which is the modification of the Hashin's failure criterion for assessing lamina failure in which the tensile fibre failure, compressive fibre failure, tensile matrix failure and compressive matrix failure are separately considered. Chang-Chang modified the Hashin equations to include the non-linear shear stress-strain behaviour of a composite lamina. They also defined a post-failure degradation rule so that the behaviour of the laminate can be analysed after each successive lamina failure. In this model four failure modes are categorised. These failure indicators are appointed on total failure for the laminas, where both the strength and the stiffness are set equal to zero after failure is encountered. In this model as described below all material properties of lamina are checked using the following laws to determine the failure characteristic. The failure equations chosen for analysis define the failure modes as described below, based on the values of stress components obtained from constitutive laws.

- Tensile fibre failure mode: (fibre rupture)

If $\sigma_1 > 0$

$$\text{then } e_f{}^2 = \left(\frac{\sigma_1}{X_t}\right)^2 + \beta\left(\frac{\sigma_{12}}{S}\right)^2 - 1 \qquad \begin{cases} e_f{}^2 \geq 0 \text{ failed} \\ e_f{}^2 < 0 \text{ elastic} \end{cases} \tag{8.8}$$

where β is a weighting factor for shear term in tensile fibre mode and its range is 0-1 and σ_1 is stress in the fibre direction and σ_{12} is transverse shearing stress. When lamina failure occurs, all material constants are set to zero.

- Compressive fibre failure mode: (fibre buckling)

If $\sigma_1 < 0$

$$\text{then } e_C{}^2 = \left(\frac{\sigma_1}{X_c}\right)^2 - 1 \qquad \begin{cases} e_C{}^2 \geq 0 \text{ failed} \\ e_C{}^2 < 0 \text{ elastic} \end{cases} \tag{8.9}$$

After lamina failure by fibre buckling E_1, ν_{12} and ν_{21} are set to zero.

- Tensile matrix failure: (matrix cracking under transverse tension and in-plane shear)

If $\sigma_2 > 0$

$$\text{then } e_m{}^2 = \left(\frac{\sigma_2}{Y_t}\right)^2 + \beta\left(\frac{\sigma_{12}}{S}\right)^2 - 1 \qquad \begin{cases} e_m{}^2 \geq 0 \text{ failed} \\ e_m{}^2 < 0 \text{ elastic} \end{cases} \tag{8.10}$$

where σ_2 is stress in normal to the fibre direction. After lamina failure by matrix cracking, E_1, ν_{21} and G_{12} are set to zero.

- Compressive matrix failure mode: (matrix cracking under transverse compression and in-plane shear)

If $\sigma_2 < 0$

$$\text{then } e_d^{\,2} = \left(\frac{\sigma_2}{2S}\right)^2 + \left[\left(\frac{Y_c}{2S}\right)^2 - 1\right]\frac{\sigma_2}{Y_c} + \left(\frac{\sigma_{12}}{S}\right)^2 - 1 \qquad \begin{cases} e_d^{\,2} \geq 0 \text{ failed} \\ e_d^{\,2} < 0 \text{ elastic} \end{cases} \tag{8.11}$$

After lamina failure by matrix cracking, E_2, ν_{21}, ν_{12} and G_{12} are set to zero.
In this work the weight factor β which is defined as the ratio between shear stress and shear strength is set to 1. The material properties of GFRP and CFRP were obtained from experimental work reported in earlier chapters.

8.3.3. Delamination modelling

The micro-failure modes normally observed in composite laminates are fibre breakage, fibre micro buckling and matrix cracking, transverse matrix cracking, transverse matrix crushing, debonding at the fibre-matrix interface, and delamination. The first four failure modes can be treated using thin shell theory, since they depend on in-plane stresses. The delamination failure mode needs three-dimensional representation of the constitutive equation and kinematics, and cannot be treated in thin shell theory. The delamination failure mode requires micro-mechanical modelling of the interface between layers and cannot be treated in thin shell theory that deals with stresses at macro levels. Thus, debonding and delamination are usually ignored when thin shell elements are used to model failure in composite modelling. Many methods have been investigated by the researchers to model the delamination growth in composite materials, including the virtual crack extension technique [4], stress intensity factor [5], stresses in a resin layer [6], virtual crack closure technique [7] and cohesive zone modelling (CZM) [8].

The Cohesive Zone Model (CZM) was developed to describe the failure behaviour of very thin layers, such as delaminating of composite structures or adhesive bonding. In crash simulations of adhesively-bonded vehicle structures, the CZM can be used instead of a more complicated and therefore slower continuum approach to model the adhesive layer [9]. In principal, the CZM does not consider the continuum mechanical fracture behaviour of the adhesive layer, but describes its failure by a simple traction-separation law instead of using classical constitutive equations (see Figure 8.3). On the other hand, choices for modelling delamination using finite element crash codes are more restricted.

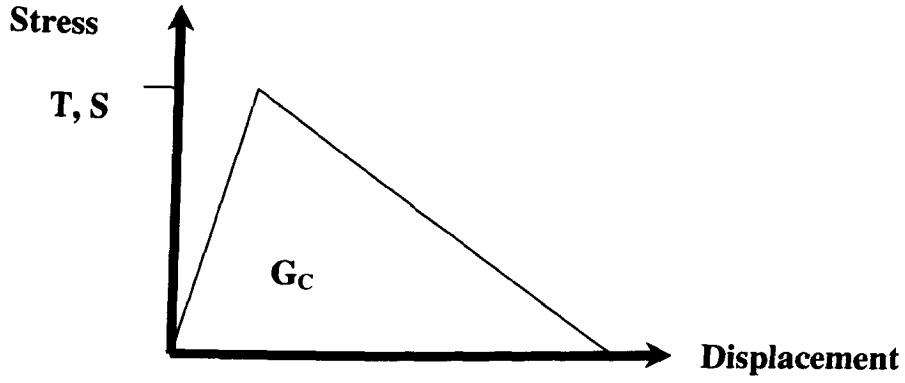

Figure 8.3. Bi-linear Traction-Separation law in pure Mode I loading.

The finite element modelling is satisfactory when the models which do not fully capture all aspects of crushing damage observed experimentally are used. In these models, the aspects of crushing that mostly influence the response are considered. Models of composite structures using in-plane damaging failure to represent crushing behaviour are used in damage material models [1]. The structures whose failure modes are governed by large-scale laminate failure and local instability can be studied by these models.

However, if the comprehensive damage of the laminate contributes considerably to the overall energy absorption, these models cannot be used [10]. Further, if delamination or debonding exists, specialized procedures must be implemented into the model to show this failure mechanism.

Tied connections are used with a force-based failure method to model the delamination in composite materials [11,12]. By this method, nodes on opposite sides of an interface where delamination is expected are tied together using any of a variety of methods including spring elements or rigid rods. If the forces produced by these elements exceed some criterion, the constraint is released. Reedy et al. applied the cohesive zone model (CZM) for the same reason. In this method instead of relying on simple spring properties the force-displacement response of the interfacial elements is based on classical cohesive failure behaviour [13]. Virtual crack closure technique is often used by researchers in the area of fracture mechanics. Energy release rates are calculated from nodal forces and displacements in the vicinity of a crack front.

Even though the method is sensitive to mesh refinement, but not so sensitive like the other fracture modelling techniques, which need more accuracy in calculating of stresses in the singular region near a crack front.

In this work the delamination behaviour in Mode-I (discussed previously) was modelled with two layers of shell elements in the box wall (see Figure 8.4). The thickness of each layer is equal to half of the total box wall thickness. The surface-to-surface tiebreak contact was used to model the bonding between the bundles of plies in the box walls. In this contact algorithm, the tiebreak works for nodes which are initially in contact. The failure of the bonding between these bundles takes place when the following failure criterion is fulfilled:

$$\left[\frac{|\sigma_n|}{NFLS}\right]^2 + \left[\frac{|\sigma_s|}{SFLS}\right]^2 \geq 1 \qquad (8.12)$$

where NFLS and SFLS are the normal tensile and shear stresses at failure.

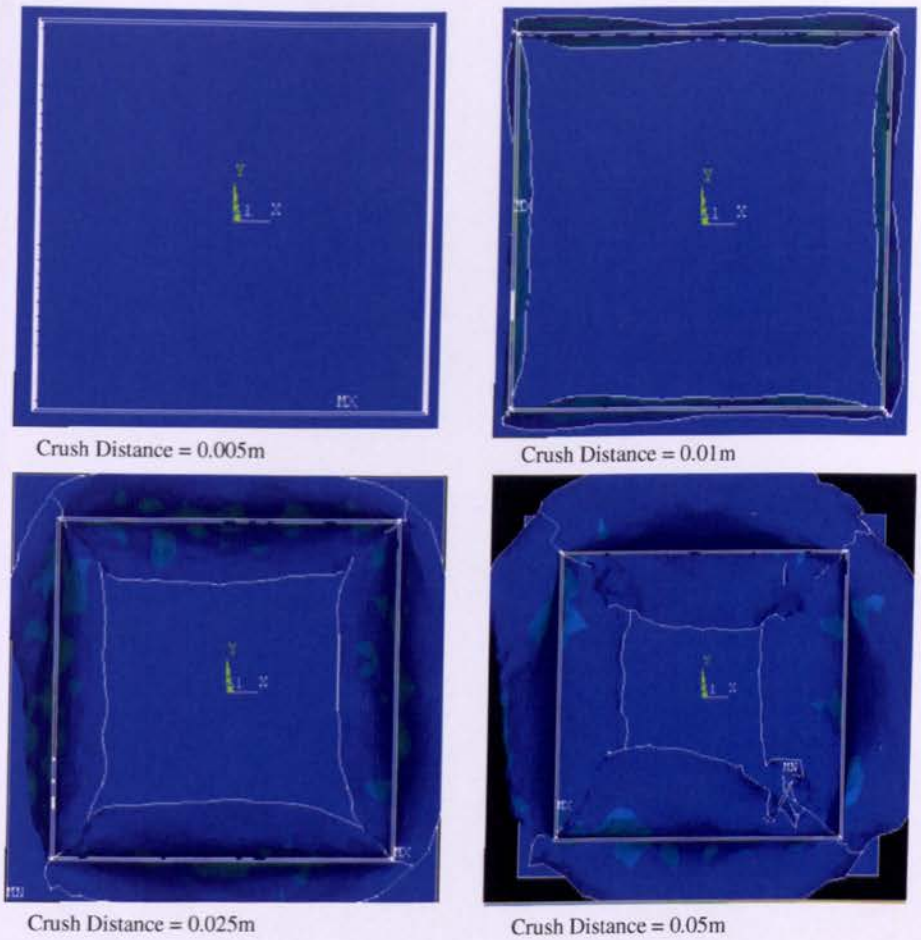

Fig. 8.4. Mode-I delamination growth in finite element modelling of CFRP composite box structures. The inserts show von Mises stress distribution at various stages (Plane view of crushed box).

In Figure 8.5 the comparison of deformed shape of composite box and in Figure 8.6 the comparison of force-crush distance between two models of single-layer-element and double-layer-shell element are shown. Results indicate that the difference in mean forces between the two FE models is less than 15%, respectively. Regarding the Mode-I crack propagation in woven CFRP composite box during the crushing process, this technique was applied to models $[0/45]_2$ and $[0]_4$.

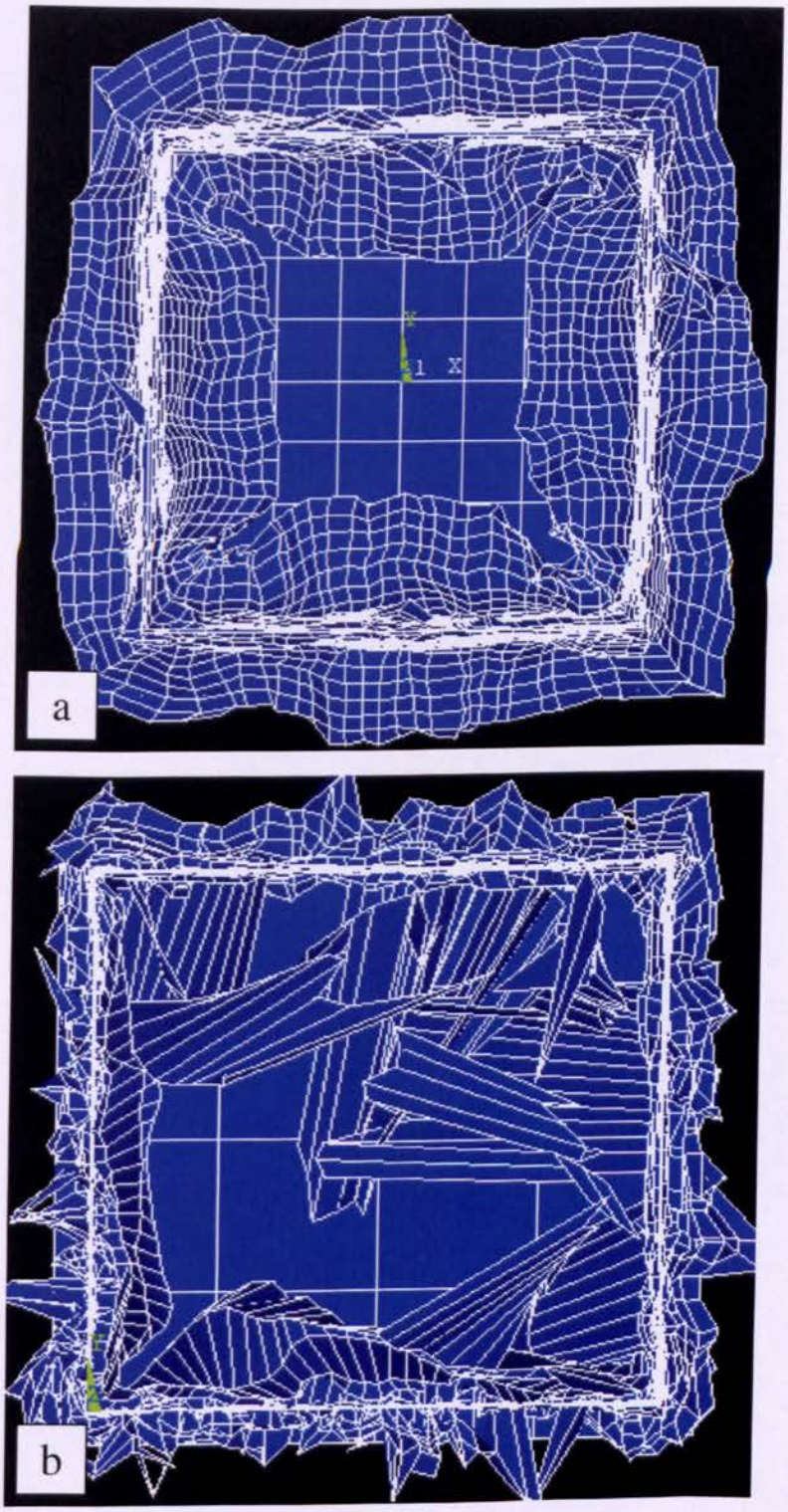

Fig. 8.5. The comparison of final element deformation (a) single-layer-shell element and (b) double-layer-shell element in crushing process of CFRP composite box structures. (Plane view of crushed box).

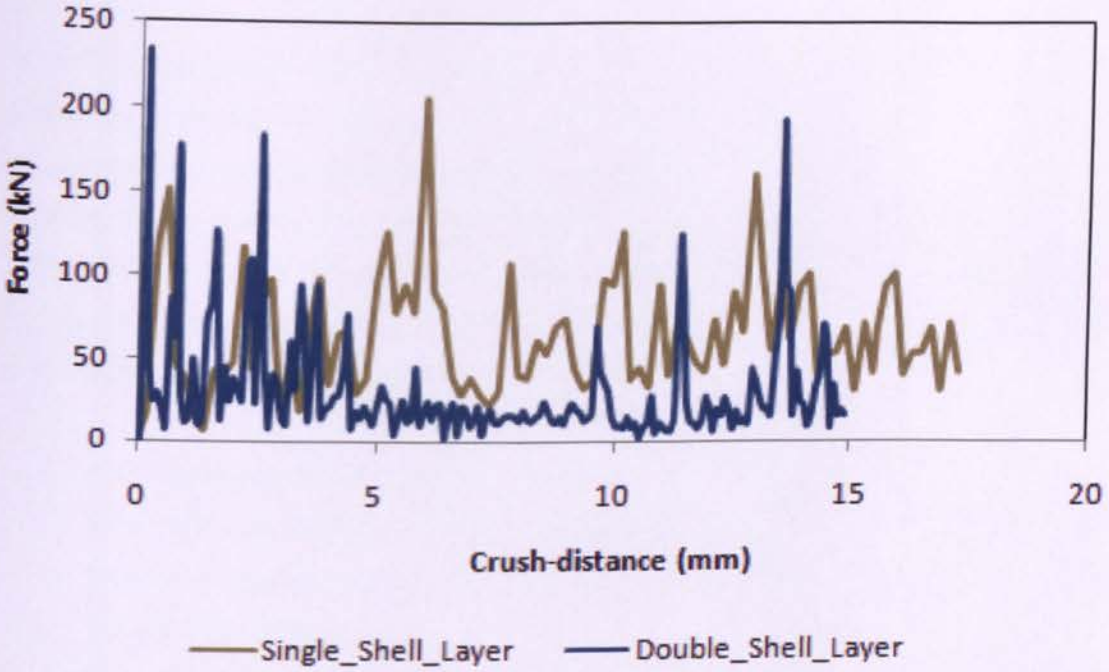

Fig. 8.6. Comparison of force-crush distance between single-layer-shell and double-layer-shell CFRP composite box.

8.3.4. Contact modelling

Apart from geometry, meshing, selection of element types and material models, the declaration of the contact interface types between the interacting parts of each model plays an equally important role in the finite element modelling. Specifying contact between the parts of each model ensures that the finite element code prevents penetration between the geometric boundaries of the parts during their movement and progressive deformation [14]. In total six different types of contact interface were used in the modelling of the axial and off-axis compression of the GFRP and CFRP boxes:

1. The "rigidwall_planar" type was used in all finite element models for the contact between the composite box and the stationary rigid platen of the press test machine in order to prevent penetration of the boundary of the lower test machine head by the box specimen nodes.
2. The "rigidwall_geometric_flat_motion" type was used in the case of quasi-static compression tests only for the contact between the composite box and the constantly moving upper head of the press. Apart from penetration avoidance, this interface was used during the post-processing phase for the creation of the load–displacement curve, since the contact force between the moving press head and the compressed specimen is the crushing load of the load curve.
3. The "automatic_single_surface" type was used in all finite element models to prevent penetration of the deformed box boundary by box its own nodes.
4. The "eroding_single_surface" type was used in all models for the same reason as the previous interface type, but also because the boundary surface of box was eroded during the compression due to element deletion at the various stages of box collapse.
5. The "eroding_surface_to_surface" type was used in the case of the quasi-static tests for the modelling of collapse mode I, selected for the contact between the shell elements corresponding to the two bundles of plies of the splayed box wall laminate that were eroded during the axial and off-axis compression due to element deletion.
6. The "tiebreak_surface_to_surface" type was also used in the case of the quasi-static tests for the modelling of collapse mode I, to model the bonding between the bundles of plies of the composite box wall laminate.

The number of contact interface types used in each model depended upon the type of collapse modelled.

8.3.5. Boundary conditions

All degrees of freedom of the crash boxes were fixed at the bottom end and all degrees of freedom were free at the upper ends which were subjected to compressive force by the rigid striker.

The contact between the rigid plate and the specimens was modelled using a *nodes impacting surface* with a friction coefficient of 0.25 for GFRP and 0.35 for CFRP which was measured experimentally to avoid lateral movements. To prevent the penetration of the crushed box boundary by its own nodes, a *single surface* contact algorithm without friction was used.

To simulate the quasi-static condition, the loading velocity of 1 m/s was applied to the rigid striker. However, the real crushing speed was too slow for the numerical simulation.

The explicit time integration method is only conditionally stable, and therefore by using the real crushing speed, a very small time increment was required.

In this study to decrease the time step increment the mass density of all materials was scaled-up by factors of 100 and 1000 with the same applied velocity. In both cases the response of internal energy was very similar and the kinetic energy was negligible in comparison to internal energy (see Figure 8.7).

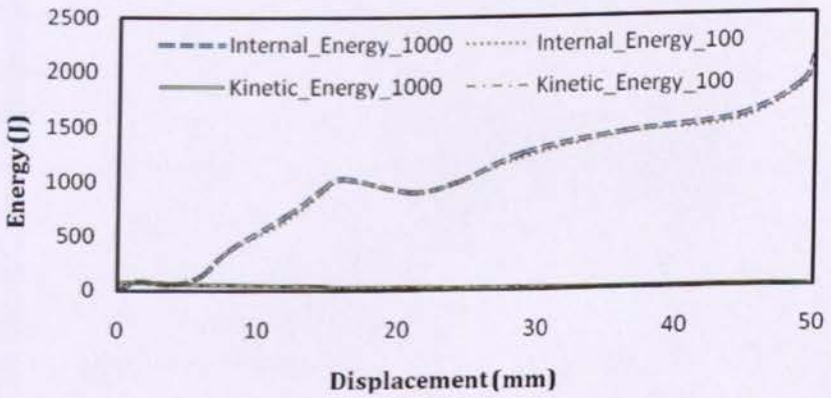

Fig. 8.7. Effect of mass scaling on the internal and kinetic energy in quasi-static simulation of off-axis loading of 5°.

For satisfying quasi-static condition not only the total kinetic energy has to be very small compared to the total internal energy over the period of the crushing process but also the crushing force-displacement response must be independent from the applied velocity.

8.4. Results and discussion

8.4.1. Axial crushing

In this chapter, the finite element modelling of the axial collapse of GFRP and CFRP composite crush box, using the LS-DYNA code was presented in detail. Although the response of this structure in compressive loading was rather complex from macro- and microscopic point of view, the computed results from the simulation model approached to a satisfactory degree the results obtained by the corresponding experimental work. This was shown at first by means of a series of photographs and computer pictures that enabled the macroscopic comparison between the calculated and the experimentally observed collapse of the composite crush box and subsequently by comparing the calculated load/displacement curve and main crushing characteristics to the ones obtained by the experimental work.

The deformed shape of the FEA model for GFRP-$[0/90]_{10}$ lay-up is shown in Figure 8.8. The similarity between the FEA simulation and experimental work shown are very good. In Figure 8.9 the force-crush distance of $[0/90]_{10}$ lay-up which was extracted from the FEA model is compared with the experimental results.

Interpreting the shape of the load/displacement graphs, the first linear part of each graph corresponds to an initial elastic deformation stage, during which the load rises sharply at a steady rate up to maximum collapse load, F_{max}. In the second stage the force fluctuates around a mean crushing load F_m and the composite box is capable of absorbing large amounts of deformation energy while collapsing in a relatively stable behaviour.

In the simulation modelling this corresponds to erosion/deletion of the highly distorted and collapsed shell elements, and also modelling of the laminate parts respectively.

Certainly, the high level of discretisation which is necessary for obtaining accurate results from the finite element model caused more intensive fluctuations in the numerical load/displacement graph, compared to the experimental result.

The difference in mean force between the FEA model and experiment is less than 8%. The energy absorption computed from FEA is 14.5 kJ/kg while the value from experiment is 15.8 kJ/kg, a difference of less than 9 %.

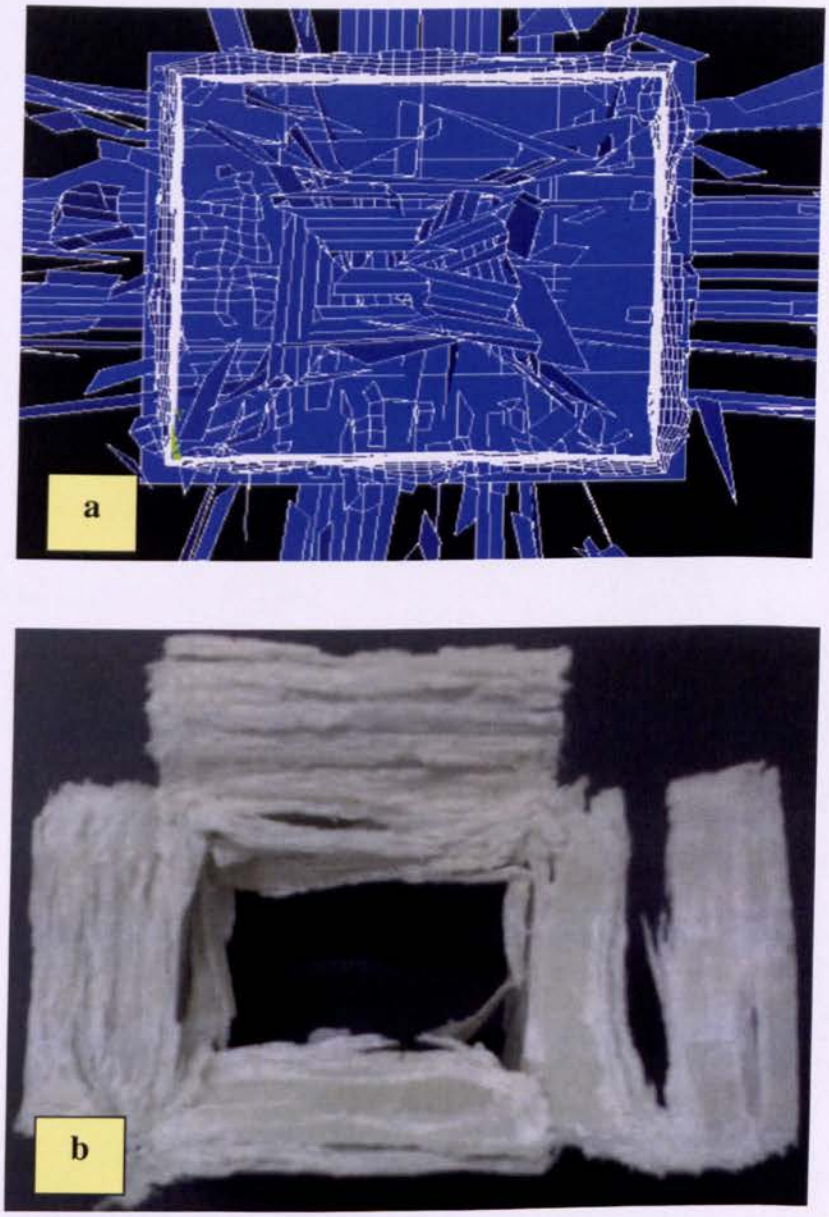

Fig. 8.8. Comparison of final deformed shape of the GFRP $[0/90]_{10}$ lay-up box in plain view. a) FEA result, b) experiment.

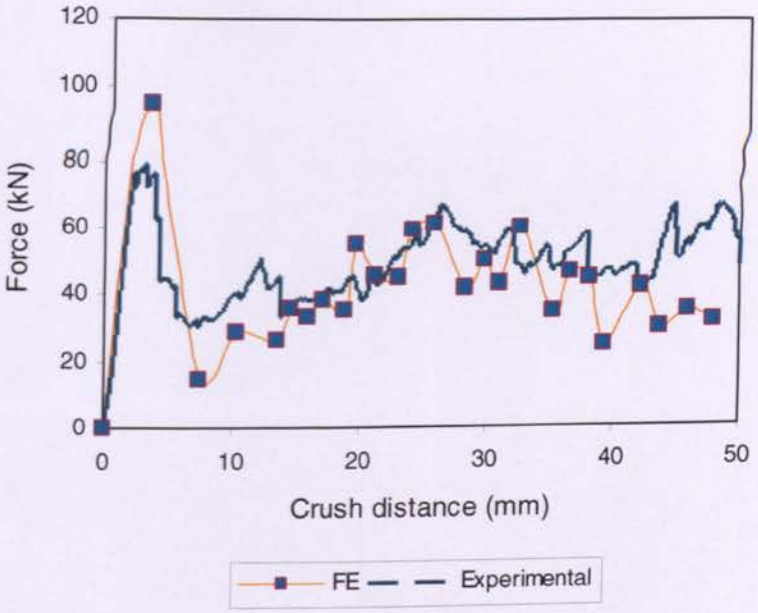

Fig. 8.9. Comparison of experimental and FE results for GFRP composite box with $[0/90]_{10}$ lay-up.

In Figures 8.10 and 8.11 various crushing processes and the force-crush distance of all lay-ups of CFRP composite box which were extracted from the FEA models are compared with the experimental results. The difference in mean forces and energy absorption between the FEA models and experiments are less than 5% in all models (see Table 8.1).

Table 8.1. Comparison of experimental, and FEA mean force results of each laminate design of CFRP composite box. LB/BF= Lamina bending/brittle fracture and BU/TS= Local buckling/transverse shearing.

Laminate Lay-up	**Cushing failure mode**	F_m (Exp.) kN	F_m (FEA) kN
$[0]_4$	LB/BF	65	60
$[0/45]_2$	LB/BF	67	65
$[45]_4$	BU/TS	52	55

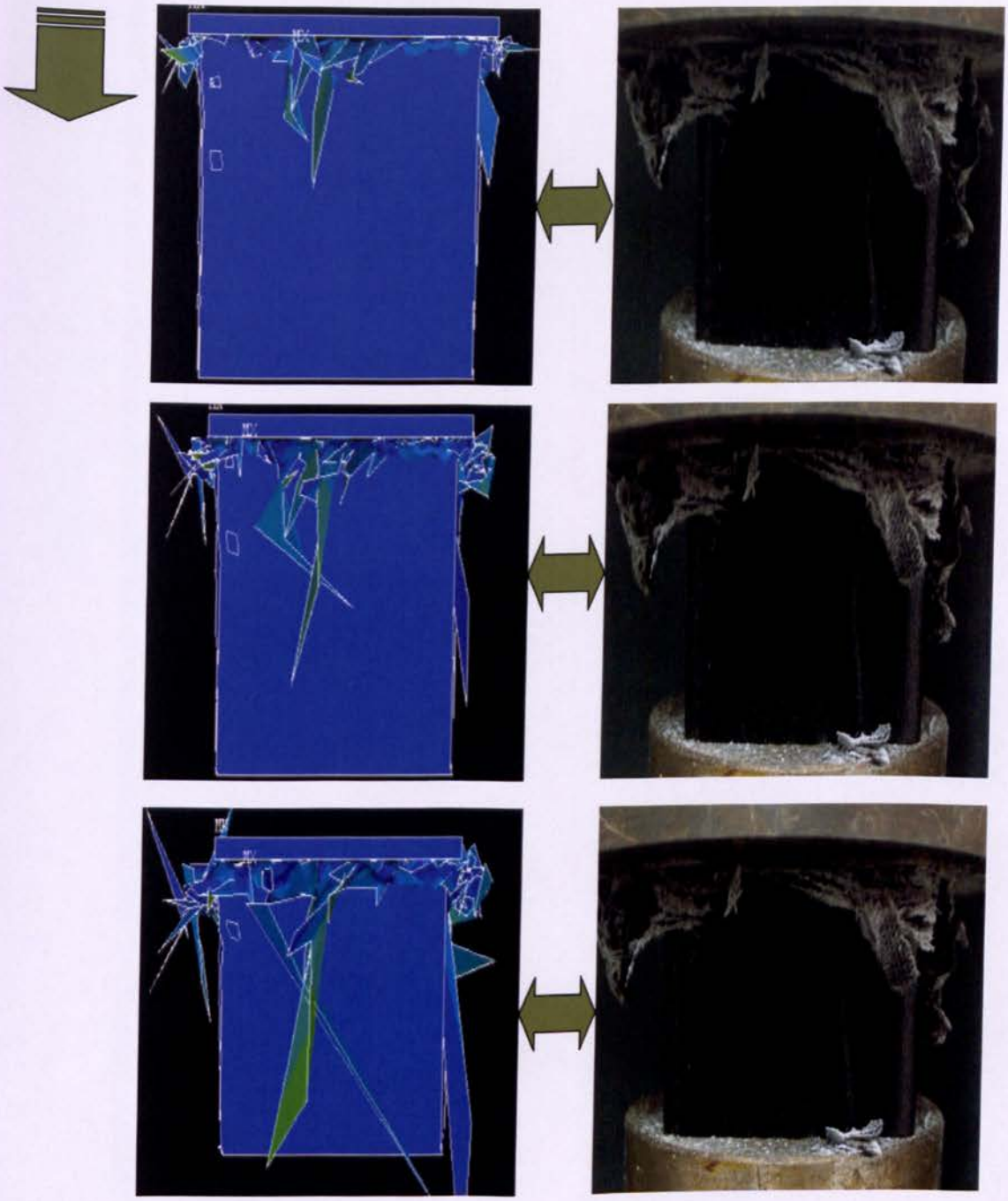

Fig.8.10. Various stages of crushing process of CFRP composite box of $[0]_4$. The inserts show von Mises stress distribution at various stages.

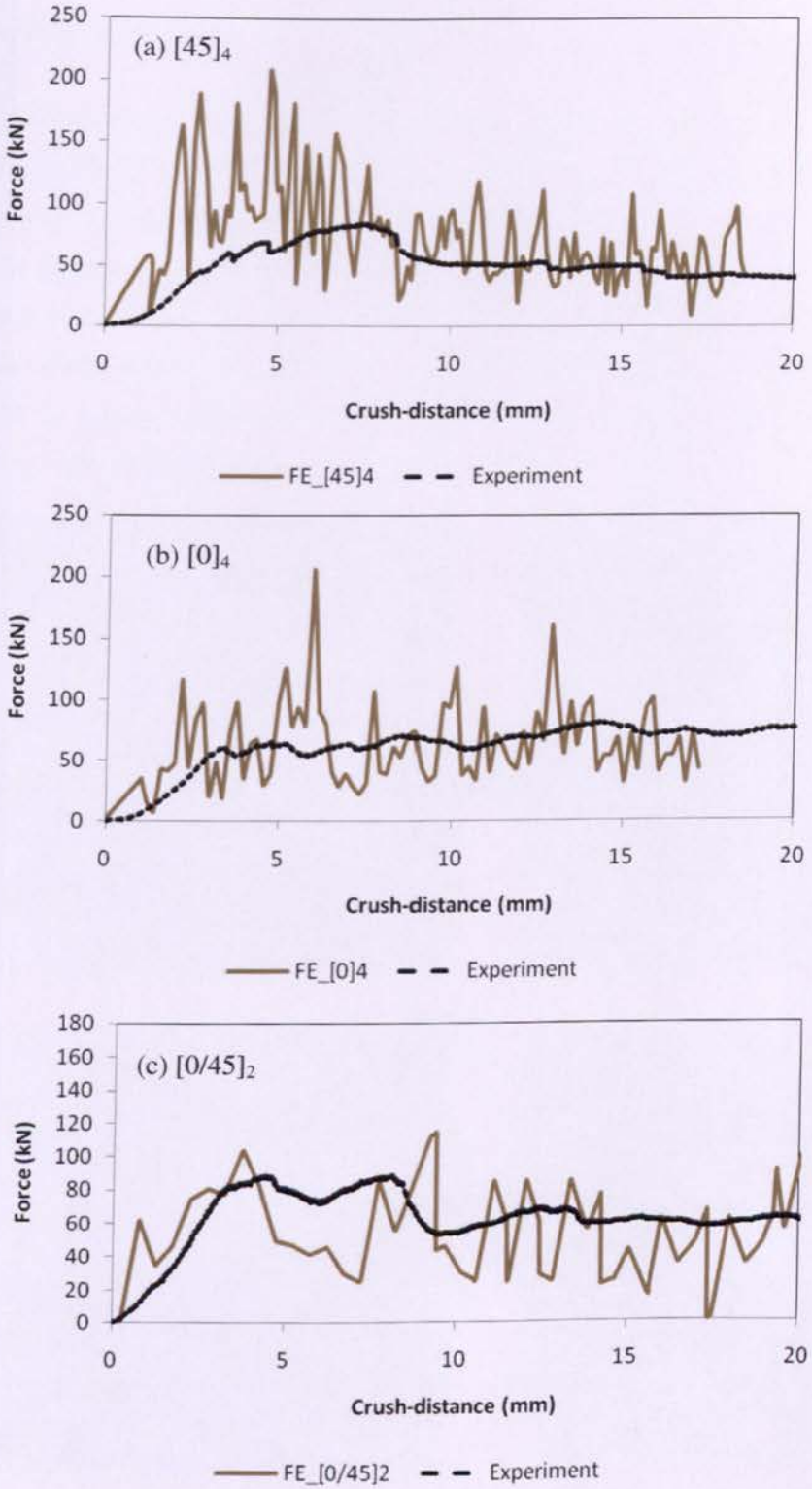

Fig.8.11. Comparison of experimental and FE force-crush distance results for twill/weave CFRP composite box with a) $[45]_4$, b) $[0]_4$ and c) $[0/45]_2$ lay-ups.

8.4.2. Off-axis crushing

In this analysis each composite box was modelled according to the relevant angle of off-axis loading (see Figure 8.12). The trigger mechanism was modelled by reducing the thickness of the first row of shell elements at the top of each box. The GFRP composite box model was based on Belytschko-Lin-Tsay quadrilateral shell elements. This shell element is based on a combined co-rotational and velocity strain. All surfaces of the model were meshed using quadratic shell elements and the size of an element was 2.5×2.5mm. The striker was modelled as a rigid block using solid elements. Other details of the finite element (FE) modelling were similar to those used for axial crushing modelling.

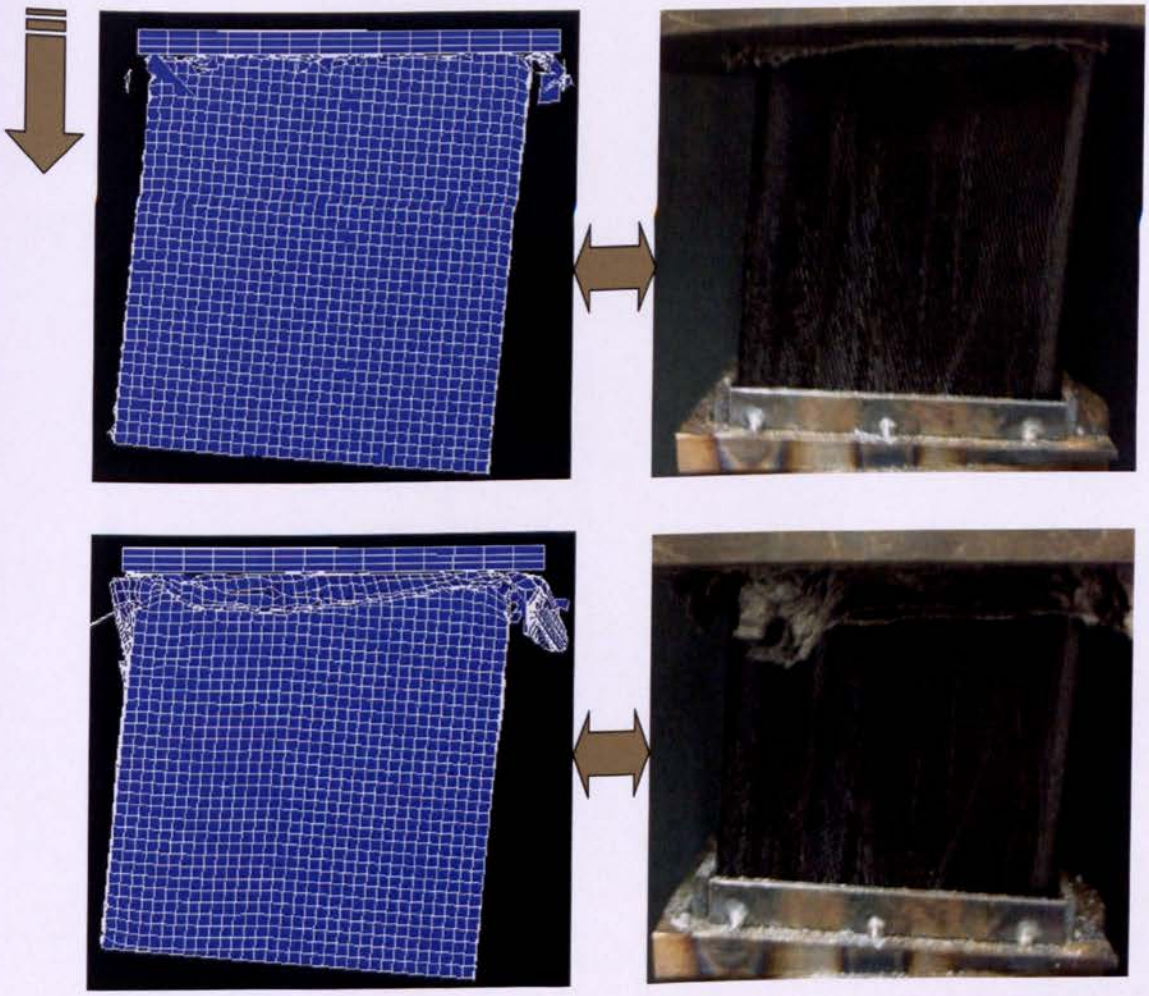

Fig. 8.12. Various stages of 5° off-axis angle at crushing process of GFRP composite box structures.

In Figure 8.13 the force-crush distance of all off-axis loading angles which were extracted from the FEA models are compared with the experimental results. The difference in mean forces and energy absorption between the FEA models and experiments are less than 10% in all models (see Table 8.2). The comparison between the FE final deformed shape and experimental results are presented in Figure 8.14. These results indicate the good agreement with the relevant experimental ones.

Table 8.2. Comparison of experimental and FEA mean force (F_m) results of each laminate design.

Off-axis loading angle	F_m (Exp.) (kN)	F_m (FEA) (kN)	Error (%)
Axial crushing	50±2	45	10
5°	50±2	47	6
10°	60±2	57	5
20°	38.0±2	35	8
30°	20.0±1	22	-10

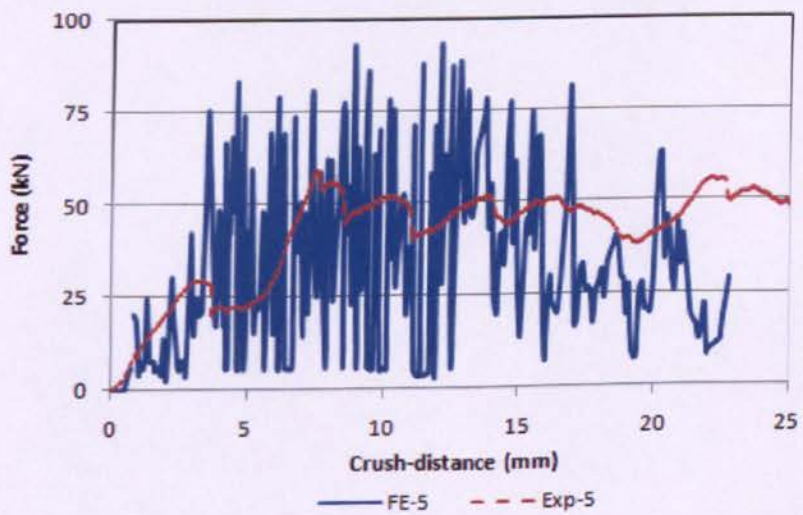

Continued…

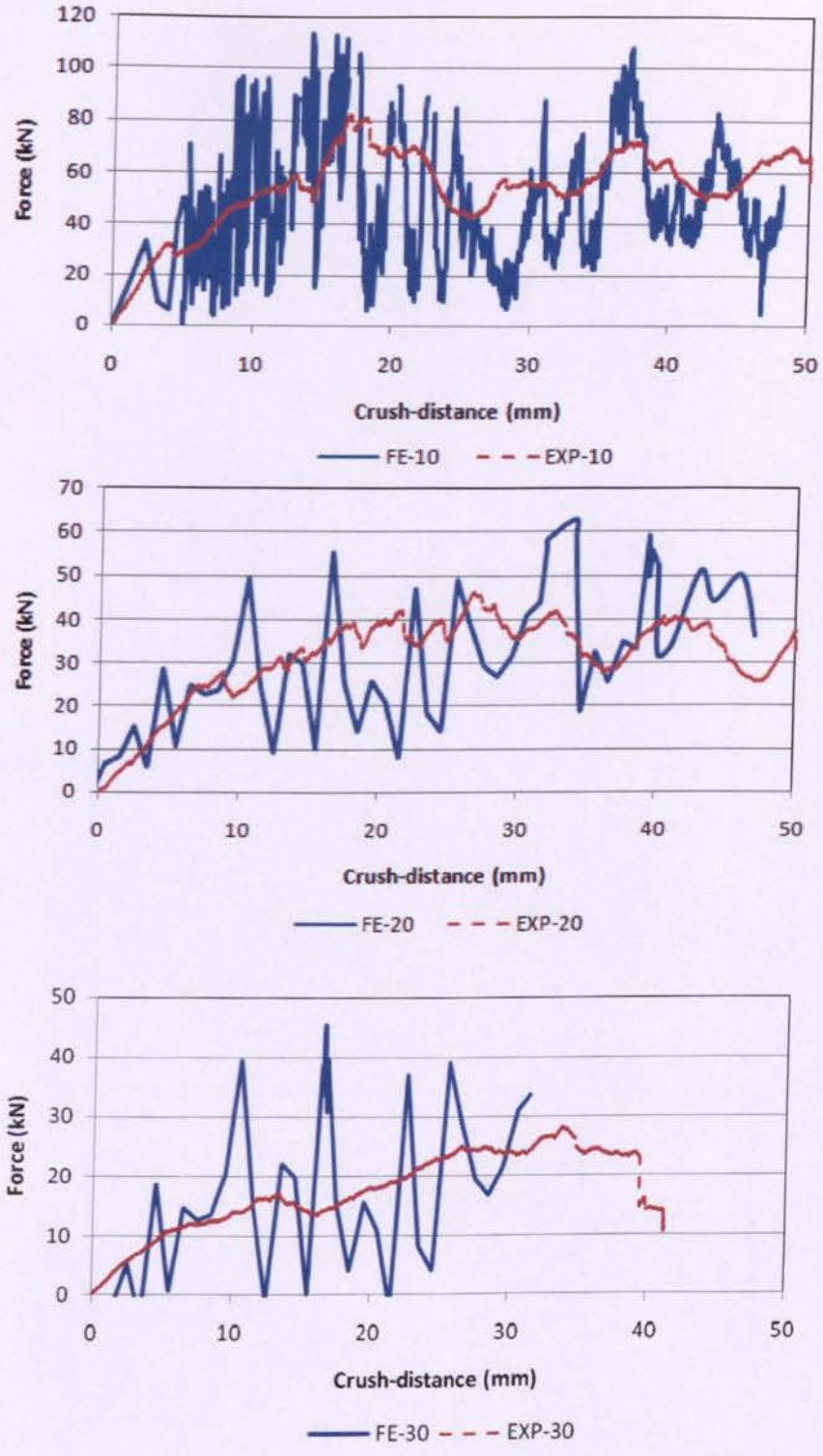

Fig. 8.13. Comparison of experimental and FE force-crush distance results for woven GFRP composite box under various off-axis loading.

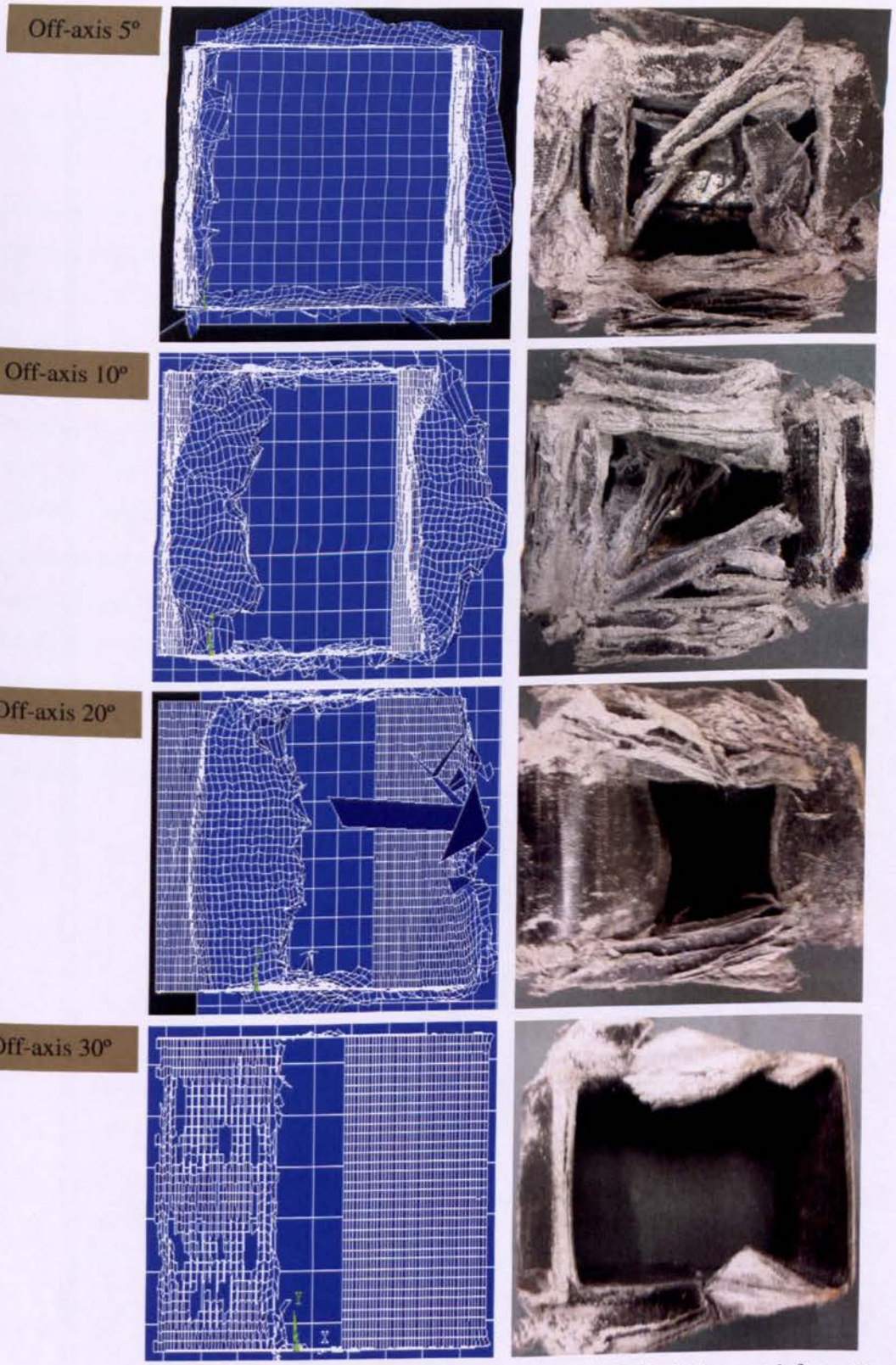

Fig. 8.14. Comparison of plane view of experimental and FE final element deformation results for woven GFRP composite box under various off-axis loading.

8.5. Conclusion

In this chapter analyses in which the crushing characteristic of thin-walled GFRP and CFRP composite crush components were simulated to find the response of various lay-ups subjected to quasi-static axial and off-axis compression loading, using LS-DYNA finite element code are described. After analysing the results a good agreement between the final element deformation from FE and experimental results was found. Regarding the higher crushing rate in comparison with real one in experiment and also some technical requirements in solution time, the force-crush distance diagrams from the FE analysis showed some overestimations in comparison with relevant experimental results. However, the mean crushing forces obtained from the FE analysis were close enough to the experimental ones with error of less than 12%. A new technique of tiebreak contact was applied in the FE simulation to model the delamination crack growth and consequently make the crushing process as similar as to the experimental one. This technique was used for those composite boxes which had shown the crushing process with lamina bending mode which and consequently propagation of Mode-I opening crack in box wall section. In this case each composite box was modelled using double-layer-shell-elements and the difference between the force-crush distance diagrams from the double-layer-shell-element box and the single-shell-element box was less than 10%.

References

[1] LS-DYNA User's Manual (Non-linear Dynamic Analysis of Structures in Three Dimensions), Livermore Software Technology Corporation, 1997, Livermore, USA.

[2] Zienkiewicz OC, Taylor RL. Finite element method. Upper Saddle River, NJ: Prentic-Hall; 1996.

[3] Chang FK and Chang KY. A progressive damage model for laminated composites containing stress concentrations. *J Compos Mater,* 1987;21:809-833.

[4] Farley GL, Jones RM. Prediction of the energy-absorption capability of composite tubes. *J Compos Mater.* 1992;26(3):388–404.

[5] Hamada H, Ramakrishna SA. FEM method for prediction of energy absorption capability of crashworthy polymer composite materials. *J Reinf Plast Compos* 1997;16(3):226–42.

[6] Kindervater CM. Crash resistant composite helicopter structural concepts thermoset and thermoplastic corrugated web designs. In: Proceedings of the AHS national technical specialists meeting on advanced rotorcraft structures, Williamsburg, VA, 1995.

[7] Fleming DC, Vizzini AJ. Off-axis energy absorption characteristics of composites for crashworthy rotorcraft design. *J Am Helicopter Soc* 1996;41(3):239–46.

[8] Williams JG, Hadavinia H. A Cohesive zone global energy analysis of an impact loaded bi-material strip in shear. *International Journal of Fracture*, 2006;38(1-4): 197-209.

[9] Marzi S, Ramon-Villalonga L, Poklitar M, Kleiner F. Usage of cohesive elements in crash analysis of large, bonded vehicle structures. LSDYNA Anwenderforum, Bamberg 2008.

[10] Fleming DC. Delamination modelling of composite for improved crash analysis. *J Compos Mater* 2001;35(19):1777–92.

[11] Kohlgruber D, Kamoulakos A. Validation of numerical simulation of composite helicopter sub-floor structures under crash loading. In: Proceedings of the 54th American helicopter society annual forum, Washington, DC, May 20–22 1998.

[12] Kerth S, Dehn A, Ostgathe M, Maier M. Experimental investigation and numerical simulation of the crush behaviour of composite structural parts. In: Proceedings of the 41st international SAMPE symposium and exhibition, 1996. p. 1397–408.

[13] Pinho ST, Camanho PP and de Moura MF. Numerical simulation of the crushing process of composite materials. IJ Crash, 2004;9(3):263-276.

[14] Mamalis AG, Manolakos DE, Ioannidis MB, Papapostolou DP. Static and dynamic axial collapse of CFRP square tubes: Finite element modelling. *Composite Structures*, 2006;74:213-225.

Chapter 9:

Conclusion & Future works

9.1. Conclusion

In the present work, the effects of interlaminar fracture toughness on the progressive energy absorption of composite structures under quasi-static loading have been investigated. In this regard, Mode-I, Mode-II and mixed-Mode I/II interlaminar fracture toughness of various FRP composites with different laminate designs were studied experimentally to investigate the relationship between interlaminar crack propagation and the energy absorption capability and crushing modes of composite box structures.

The combination of brittle fracture, lamina bending, local buckling and transverse shearing crushing modes was found in the experimental studies. New analytical solutions based on friction, bending and fracture mechanisms were proposed to predict the mean crushing force for each of these failure modes. The crushing process of composite boxes was also investigated by finite element software LS-DYNA and the results were verified with the relevant experimental and analytical results.

The final conclusions of this work can be summarised as follows,

Mode-I interlaminar fracture toughness and energy absorption of composite box structures

It was found that the interlaminar fracture toughness for GFRP interface fracture planes of 0/90, 90/90 and 0/45 are clustered close to each other while the equivalent value for +60/–60 interface plane is much lower. This shows that the specific energy absorptions (SEA) of fibre orientations which are laminated with $0/\theta$ angles are close together. In the lamina bending crushing mode of CFRP composite crush box, due to through-the-thickness transverse stress, Mode-I interlaminar fracture will occur. However, this fracture mode was not observed in laminate design of $[45]_4$. Choosing a suitable fibre orientation in the interface plane is one of the main factors for improving the energy absorption of composite crush boxes in progressive failure.

Mode-II interlaminar fracture toughness and energy absorption of composite box structures

It was shown that the total interlaminar fracture toughness in Mode-I and Mode-II of 0/0 is higher than the equivalent values of 0/45 and 45/45 interface planes of CFRP composites, but 0/45 box has the highest SEA. This indicates that the effect of other mechanisms such as

friction and bending will increase as the total fracture energy increase beyond a certain limit. It can be seen the CFE increases as the total interlaminar fracture toughness in Mode-I and Mode-II increases. The $[0]_4$ lay-up has the highest CFE. This is due to its lower initial maximum collapse force compared with other fibre orientations. This situation is more suitable for crashworthiness design cases which need to absorb the energy with a lower initial collapse force but not necessarily with the highest energy absorption capability.

Mixed-Mode I/II interlaminar fracture toughness and off-axis crashworthiness of composite box structures

The brittle fracture mode was observed for composite box in axial crushing and off-axis loading of 5°. The energy absorbing capability at this off-axis loading was almost the same as energy absorption of composite box under axial loading. Two fracture mechanisms of bundle fracture and crack propagation in Mode-II were found for all composite boxes at various off-axis loading. Due to crack propagation in mixed-Mode I/II and more friction and bending resistance at one side of the composite box which first contacted the crushing platen, the amount of SEA at off-axis loading of 10° was the maximum.

Effects of delamination failure in crashworthiness analysis of hybrid composite box structures

In all hybrid composite boxes the lamina bending crushing mode was observed. In this case the main central interwall crack which is similar to Mode-I crack delamination starts to propagate at four sidewalls of each composite box. In lamina bending mode, the main central crack causes to shape lamina bundles which has a significant role on absorbing the crushing energy. Earlier it was shown that the fibre orientation at the interface planes has a significant effect on Mode-I interlaminar fracture toughness.

Also in this failure mode the fronds splitting due to lamina bundle bending is similar to interlaminar crack propagation in Mode-II. The G_{IC} and G_{IIC} of initiation are more influential than the G_{IC} and G_{IIC} of propagation in the energy absorption mechanism. The Mode-I and Mode-II initiation values were chosen to quantify the effect of Mode-I and Mode-II fracture toughness on energy absorption of composite box. From this relationship it was found that the hybrid laminate designs which showed higher fracture toughness in Mode-I and Mode-II delamination tests, were able to absorb more energy as a composite box in crushing process. The assembled boxes from two channels with the $[0]_4$ lay-up bonded by epoxy adhesive

showed roughly the same SSCS as the simple box. The assembled box stiffened with a V-shape stiffener has 4% higher SSCS relative to its higher mean force in comparison with simple box.

Theoretical prediction of mean crushing force in progressive failure of composite box structures

The contribution of each failure mechanism to the energy dissipation of composite box in various crushing mode were studied. In brittle fracture/ lamina bending crushing mode the highest value which plays an important role on energy absorption during crushing process is for axial splitting and after that for bundle fracture. It should be mentioned these mechanisms are coupled together and they act at the same time in a crushing process. This fact shows higher resistance for delamination crack growth in different delamination modes directly affect on the bending and friction resistance of internal and external fronds against the crushing load.

Finite Element analysis of progressive failure crushing of composite box structures

After analysing the results good agreement was found between the final element deformation from FE and the experimental results. Regarding the higher crushing rate in comparison with real one in experiment and also some technical requirements in solution time, the force-crush distance diagrams from the FE analysis showed some overestimations in comparison with relevant experimental results. However, the mean crushing forces obtained from FE were close enough to experimental ones with error of less than 12%. A new technique of tiebreak contact was applied in the FE simulation to model the delamination crack growth and consequently make the crushing process as similar as to the experimental one. This technique was used for those composite boxes which had shown the crushing process with lamina bending mode which and consequently propagation of Mode-I opening crack in box wall section. In this case each composite box was modelled using double-layer-shell-elements and the difference between the force-crush distance diagrams from the double-layer-shell-element box and the single-shell-element box was less than 10%.

9.2. Critical appraisal

The main objective of this research was to study the effects of interlaminar fracture toughness on the progressive energy absorption of composite material structures under quasi-static loading. Regarding the strain rate sensitivity of FRP composite materials, the impact (dynamic loading) test is the real and true analysis to study the energy absorption tendency of composite material structures. However in future work various delamination failure tests should be investigated under impact loading. Delamination failure occurs with other intralaminar failures (*e.g.* fibre breakage) during a crushing process. In this regard, coupling of all mechanisms together is more reliable to find the relationship between fracture toughness and energy absorption capability of the composite tubular structures.

9.3. Future work

The future works for this research can be summarised as follow,

- Experimental studies on tubular structures under impact loading to find their energy absorption capabilities during the impact event. New tubular structures need to be investigated by many factors such as geometry optimisation, material characterisation, manufacturing and repairing process and loading conditions.

- Experimental studies on dynamic interlaminar fracture toughness under various delamination modes. In this case, the new relationship will be found to investigate the effects of dynamic interlaminar fracture toughness on the energy absorption of composite tubular structures.

- An improved continuum damage mechanics model of new types of composite materials (*i.e.* 3D-woven composites) coupled with delamination model to represent the true behaviour of composite structures under impact loading.

- An improved explicit dynamic Finite Element (FE) code for the analysis of delamination in composite structures using interface elements. The interface element modelling technique is applied to fracture toughness based delamination problems in the DCB, ENF and MMB tests to predict the delamination behaviour under impact loading.

- Experimental and numerical studies on intralaminar fracture failures (*e.g.* fibre/matrix debonding and fibre breakage) coupled with interlaminar fracture failures to investigate their effects on the energy absorption of the composite material structures.

Publications

Journals

- H. Ghasemnejad, H. Hadavinia, A. Aboutorabi, *"Effect of delamination failure on the crashworthiness of hybrid composite box structures"*, In Materials and Design, accepted, (*2010*).
- H. Ghasemnejad, H. Hadavinia, "Off-axis crashworthiness characteristic of woven glass/epoxy composite box structures", *'Journal of Reinforced Plastic and Composites'*, In-press, (2010).
- A. Aboutorabi, H. Ghasemnejad, H. Hadavinia, *"Analytical Approach for Progressive Failure Crushing Modes of woven FRP composite box structures"*, *'Journal of World Engineering'*, In-press, (2010).
- H. Hadavinia, H. Ghasemnejad, *"Effects of Mode-I and Mode-II interlaminar fracture toughness on the energy absorption of CFRP twill/weave composite box sections"* in 'Composite Structures', 89(2) pp. 303-314, (*2009*).
- H. Ghasemnejad, B.R.K. Blackman, H. Hadavinia, B Sudall, *"Experimental studies on fracture characterisation and energy absorption of GFRP composite box structures"* in 'Composite Structures', 88(2) pp. 253–261, (*2009*).
- H. Ghasemnejad, H. Hadavinia, E. Lewis, *"Crushing behaviour of CFRP composite structure"* in 'Key Engineering Materials', 385-387, pp. 85-88, (*2008*).

Conferences

- H. Ghasemnejad, H. Hadavinia, A. Ordys, *"Coupling of interlaminar fracture toughness and crashworthiness in woven CFRP composite box structures"*, Composites 2009-2nd ECCOMAS Thematic Conference on the Mechanical Response of Composites, 1-3 April, Imperial College, London, UK, (*2009*).
- H. Ghasemnejad, B.R.K. Blackman, H. Hadavinia, *"Crashworthiness of Composite Thin-walled GFRP and CFRP Box Structures"*, ESIS 2008, 5th International Conference on the Fracture of Polymers, Composites and Adhesives, September, les Diablerets, Switzerland, (*2008*).
- H. Ghasemnejad, H. Hadavinia, E. Lewis, *"Crushing behaviour of CFRP composite structure"*, The 7th international conference on fracture and damage mechanics (FDM08), 9-11 September, Seoul, Korea, (*2008*).
- H. Ghasemnejad, H. Hadavinia, A. Aboutorabi, *"Study on energy absorption of GFRP composite crash box"*, Tenth International Conference on Structures Under Shock and Impact, 14 - 16 May, The Algarve, Portugal, (*2008*).

Composite Structures 88 (2009) 253–261

Contents lists available at ScienceDirect

Composite Structures

journal homepage: www.elsevier.com/locate/compstruct

Experimental studies on fracture characterisation and energy absorption of GFRP composite box structures

H. Ghasemnejad [a], B.R.K. Blackman [b], H. Hadavinia [a,*], B. Sudall [a]

[a] Faculty of Engineering, Kingston University, London, UK
[b] Department of Mechanical Engineering, Imperial College, London, UK

ARTICLE INFO

Article history:
Available online 8 April 2008

Keywords:
Interlaminar fracture toughness
Specific energy absorption
Fibre orientation

ABSTRACT

Interlaminar fracture toughness of composite materials plays an important role in the specific energy absorption (SEA) characteristics of crushing composite materials. In this regard the effect of fibre orientation and stacking sequence on the composite crash box design is sought by studying their effects on the interlaminar fracture toughness. In order to achieve this, glass fibre/epoxy orientations of $[\pm 60]_{10}$, $[0_2/\pm 45]_S$, $[0/90]_{10}$ and $[0/90]_{5S}$ were studied experimentally. Tensile, shear, double cantilever beam (DCB) and axial crush box specimens from different lay-ups were made and tested under quasi-static conditions to determine the mechanical properties, interlaminar fracture toughness (G_{IC}) and SEA. It was shown that the interlaminar fracture toughness of glass fibre/epoxy affects the frond bending resistance due to the main central interwall crack in a progressive crushing failure and consequently SEA. A higher interlaminar fracture toughness between laminates will enhance the SEA in the axial crushing of the composite box.

1. Introduction

The high energy absorbing capabilities of fibre reinforced polymer composite (FRP) materials is one of the main factors in their application in automotive and aerospace structures. They also provide other functional and economic benefits such as enhanced strength, durability, weight reduction and hence lower fuel consumption. For structural vehicle crashworthiness, FRP composites are able to collapse in a progressive, controlled manner which results in high specific energy absorption in the event of crash. Unlike metals and polymers, the progressive energy absorption of composite structures is dominated by extensive micro-fracture instead of plastic deformation [1–4]. The highest energy absorption of composite tubes occurs in two progressive crushing mechanisms which are brittle fracture and lamina bending [4,5]. These two crushing mechanisms absorb energy due to interlaminar and intralaminar crack growth and fracturing of lamina bundles. During progressive collapse, the sources of energy absorption are mainly from [5,6]:

- Frictional resistance between wedge and fronds and between fronds and platen: about 45% of total energy.
- Frond bending due to delamination between plies: about 40%.
- Interwall crack propagation: about 12%.
- Axial splitting between fronds: about 3%.

Various fracture mechanisms such as fibre breakage and buckling, matrix cracking and crushing, debonding at the fibre–matrix interface and especially plies delamination play important roles on progressive failure mode and energy absorption of composite tubes. Warrior et al. [7] studied the influence of toughened resins, thermoplastic resin additives, through-thickness stitching and thermoplastic interleaving on the interlaminar fracture toughness (G_{IC}) and the SEA for continuous filament random mat (CoFRM) and 0/90 non-crimp fabric (NCF) E-glass reinforced polyester composite tubes. They reported that all above mentioned factors increase G_{IC}, but only toughened resin and through-thickness stitching can increase SEA. In general a tougher matrix gives a higher G_{IC}, for the composite and this is a benefit in crashworthiness design [8]. Farley [9] concluded that matrix stiffness has only a small effect on energy absorption of materials which crush by a brittle fracture and transverse shearing mechanism, and more effect of matrix stiffness is considered by lamina bending mechanism. Cauchi Savona and Hogg [10] studied the relation between sustained crushing stress of glass fibre reinforced plastic composite plates with their Mode-I and Mode-II fracture toughness properties. According to their results, materials which show low Mode-I and Mode-II fracture toughness, yield low crushing energies. Solaimurugan and Velmurugan [11,12] recently have studied the effect of stitching, fibre orientation and stacking sequence on G_{IC}, SEA, and of progressively crushing of glass/polyester composite cylindrical shells under axial compression. They reported that axial fibres placed close to the outer surface of tube led to more petal

* Corresponding author. Tel.: +44 20 8547 8864; fax: +44 20 8547 7992.
E-mail address: h.hadavinia@kingston.ac.uk (H. Hadavinia).

0263-8223/$ - see front matter © 2008 Elsevier Ltd. All rights reserved.
doi:10.1016/j.compstruct.2008.04.006

Nomenclature

a	crack length	V_f	volume fraction
b	side of box	X_t	longitudinal tensile strength
C	compliance	X_c	longitudinal compressive strength
CFE	crush force efficiency	Y_t	transverse tensile strength
DCB	double cantilever beam	Y_c	transverse compressive strength
E	Young's modulus	ν	Poisson's ratio
F	force	σ_1	longitudinal stress
F_{max}	initial maximum force	σ_2	transverse stress
F_m	mean force	σ_{12}	transverse shear stress
G_{12}	shear modulus	β	weight factor
G_{IC}	Mode-I interlaminar fracture toughness	δ	displacement
GFRP	glass fibre reinforced plastic	σ_u	ultimate tensile stress
SEA	specific energy absorption	θ	fibre orientation
S	shear strength	Δ	extension correction factor for DCB sample
t	thickness	α	trigger angle

formation and stable crushing process, while axial fibres close to inner surface tube cause higher energy absorption. Furthermore, the energy absorption in the form of circumferential delamination increases for higher values of Mode-I fracture toughness. They also reported that stitching increases the Mode-I interlaminar fracture toughness which causes higher energy absorption of cylindrical tube. Farley [13] studied the static crushing process of graphite/epoxy and Kevlar/epoxy square cross section tubes to investigate the effect of geometry on energy absorption of composite materials. He reported that energy absorption of graphite/epoxy and Kevlar/epoxy tubes is a non-linear function of (b/t) where b is the side of the box and t is the wall thickness. It was reported that the energy absorption increased with decreasing b/t ratio. Generally, the highest energy absorption occurs when the thickness of all types of tubes is in the range of 2–3 mm [8]. Farley and Jones [14] also reported that in quasi-static crushing of glass/epoxy tube with fibre orientation of $[0/\pm\theta]_S$, by increasing θ the energy absorption capability of tube increases non-linearly however, as θ increases, the energy absorption capability of the carbon/epoxy tube decreases non-linearly. Generally, they reported that fibre orientation of $[0/\pm45]$ is preferred for glass fibre epoxy tubes. Schmueser and Wickliffe [15] showed that SEA of carbon–epoxy, glass–epoxy and aramid–epoxy $[0_2/\pm\theta]$ specimens all generally increase with increasing θ. Jimenez et al. [16] have concluded that the bevel trigger mechanism with angle of 60 shows the highest energy absorption in composite profiles.

The present work is mainly focused on the effect of fibre orientation and stacking sequence on G_{IC} and SEA. The DCB and crash box specimens were made and tested with different lay-ups but with the same geometry and material. The experimental results were compared together to find the relationship between G_{IC} and SEA.

2. Experimental studies

Five different types of test were conducted to characterize the mechanical characteristic of a GFRP material. These were tensile, shear, double cantilever beam (DCB), fibre volume fraction determination and quasi-static crush box tests. All tensile, shear, DCB and fibre volume fraction tests were carried out in accordance with the relevant standards [17–20]. All specimens were manufactured from glass fibre material of density 2.1 g/cm^3 with epoxy resin.

2.1. Mechanical properties

A separate panel was made for each type of test and specimens were cut from the panel for testing. The dimensions of each panel were determined by the size and quantity of specimen required for each test. As three types of test specimen had the same dimensions, this simplified the manufacturing process as they could all be prepared in the same way, using the same templates and equipment. Five specimens were made for each test which meant the panels from which they were to be cut would need to be 125 mm wide by the required length, 250 mm. With allowances for machining and possible defects around the edge these numbers were rounded up to 300 × 200 mm. The thickness of each specimen was 2 mm with 250 mm length and 25 mm width. All specimens were cured first in a curing cycle of 30 min at 60 °C with a heating rate of 3–5 °C/min and the temperature was held at 125 °C for 60 min. Tensile tests were carried out on specimens with [0] and [90] lay up with the aim of finding Young's modulus, E_1 and E_2, Poisson's ratio ν_{12} and ν_{21}, and the ultimate tensile strengths according to BS ISO 2747 standard [17]. There are several test methods for measuring the shear modulus of composite materials. The $[\pm45°]_S$ tensile shear test was chosen for the shear testing as this type of test can be carried out using a conventional tensile testing machine. The state of stress in each laminate was not pure shear but a combination of normal stresses, in addition to desired shear stress. Firstly, the shear stress–strain responses of many composite materials are non-linear, and may exhibit strain softening characteristics, due to rearrangement of dislocations. So, although the biaxial stress in the specimen is likely to cause the measured value of shear strength to be lower than the true value, the reduction may be small because of the non-linear softening response. Secondly, the magnitudes of the interlaminar stresses for laminates containing lamina with high orthotropic ratios are a maximum at ply angles of 15–25°, and the interlaminar stresses for 45° ply angles are considerably smaller. These tests were conducted in accordance with BS ISO 14129 standard [18]. The tests were carried out on a Denison–Mayes 100 kN universal testing machine with crosshead speed of 2 mm/min. For measuring Young's modulus in the axial and transverse direction a biaxial rosette strain gauge Showa N22-FA-8 with a resistance of 120 Ω and gauge length of 8 mm was placed at the central part of the specimen and for measuring the shear modulus a 0/45/90 rosette strain gauge was used.

The fibre volume fraction of the GFRP was determined by the resin burn-off method. It is particularly suitable for GFRP composite because glass is resistant to oxidation at elevated temperatures. This test followed ASTM D 3171 standard [19]. Three small specimens of composite, approximately 15 × 15 × 2 mm, were cut from a larger panel. The width, thickness and length were measured in three places using a micrometer, a mean average taken and the volume of the specimen calculated. Three ceramic crucibles were

weighed on scales accurate to one hundredth of a gram. The composite specimens were then placed one on each crucible and the crucible and specimen weighed together. The mass of the composite was obtained from subtracting this value from the weight of the crucible. The mass of the composite was divided by its volume to calculate the specimen's density. The three crucibles containing the specimens were then placed in a preheated oven at 500 °C for 5 h. This high temperature 'burns-off' the epoxy matrix leaving just the fibres behind. After 5 h the specimens are removed and re-weighed. This mass is subtracted from the crucible mass to obtain the weight of the fibres in the specimen. The results show excellent correlation with each other. The fibre volume fraction for this material was found to be 40.3%. The manufactures reported value of fibre volume fracture for this composite was 39%, which closely matches to the experimental results. A summary of the findings for these tests are reported in Table 1.

2.2. Determination of Mode-I fracture toughness

The fabrication of each DCB specimen was laid-up according to the laminate design of each composite crush box which will be discussed later. The mid-plane interface was 0/90, 90/90, 0/45 and +60/−60 to determine the Mode-I interlaminar fracture toughness for three fracture locations. For determining the Mode-I interlaminar fracture toughness G_{IC}, BS ISO 15024 standard [20] was followed together with the corrections developed elsewhere to take into account for the end-block, DCB arm bending and root rotation [21–24]. The recommended specimen size is at least 125 mm long and 20–25 mm wide with an initial crack length (i.e. length of the insert from the load line) of 50 mm (see Fig. 1). For curing the specimens the temperature was initially raised to 60 °C and held for 30 min and then the temperature was increased to 125 °C and held for 60 min. This stepped heat-up meant the heat was raised gradually to 125 °C instead of quickly, allowing the epoxy matrix to fully infuse the reinforcement before hardening. After curing, the specimen was left in the oven to cool to room temperature. Each specimen was labelled prior to testing with the specimen lay-up and specimen number. White paint was applied to both longitudinal edges of each specimen and allowed to dry. The painted sides were then marked with a fine pen at the edge of the polymer insert to indicate the edge of the precrack. To aid in recording crack growth, the first 5 mm from the insert were marked every 1 mm with a thin pen line and the next 55 mm were marked at 5 mm intervals. Hence crack growth was recorded for 60 mm along the specimens. The load end-blocks were bonded to the DCB specimens using Betamate 1493 adhesive at the end containing the insert. Load was applied to the specimens through end-blocks to propagate the crack (see Fig. 2a). A travelling optical microscope was used to accurately measure the length of the initial crack. The travelling microscope, with 10× magnification, slides along a horizontal scale similar to that used on callipers. A cross-hair is lined up with the path of the load through the hinges (load line). The position of the microscope was noted to the nearest tenth of a millimetre. The travelling microscope was then moved, by turning a knob, to the end of the polymer insert, sighted using the prementioned pen line. The position of the microscope was again noted, and the difference of these two measurements gave the initial crack length. Loading was carried out at a constant crosshead displacement rate of 2 mm/min. The position of the crack tip was monitored through the microscope as the crack advanced. When the crack first visibly propagated, the displacement of the crosshead was recorded. As the crack propagation past the subsequent marked lines, the crack length and crosshead displacement were recorded. Force at each crack length was retrospectively obtained from the force–displacement diagram to calculate G_{IC}.

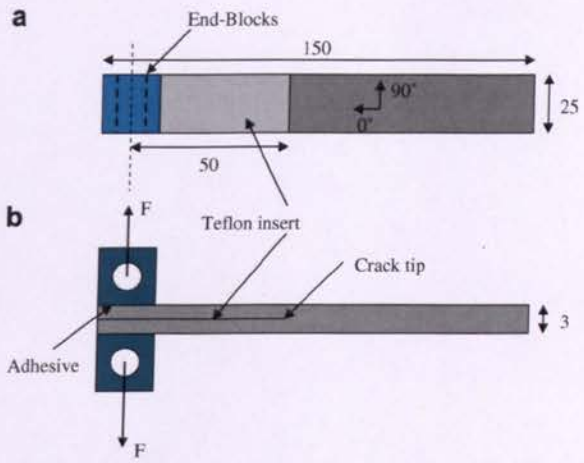

Fig. 1. Double cantilever beam (DCB) specimen: (a) plane view; (b) side view (all dimensions in mm).

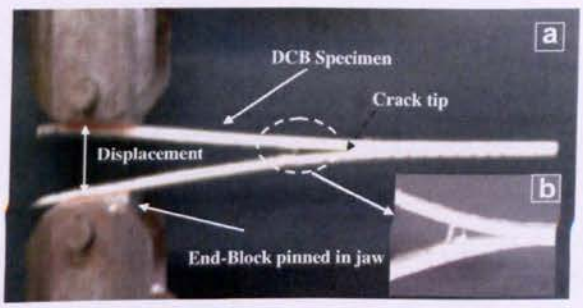

Fig. 2. (a) GFRP DCB test specimen in universal testing machine. (b) Fiber bridging across the interface layers.

2.3. Composite crush box

The crush box specimens were made of glass fibre/epoxy by hand lay-up with various fibre orientations which are following the same lay ups as described in DCB tests in the previous section. A cardboard template was made for marking out the panel plies on the prepreg roll. The 0° and 90° angle plies were marked using a set square and the 45° and ±60° angle plies were marked using a protractor to orientate the template on the roll and achieve the required fibre direction. The pieces were then labelled with fibre direction and angle to avoid later confusion. Once marked out, the panel plies were cut from the roll using a sharp Stanley knife and steel ruler. The two protective layers covering each ply of

Table 1
Material properties of the GFRP

E_1 (GPa)	E_2 (GPa)	G_{12} (GPa)	v_{12}	UTS 0° (MPa)	UTS 90° (MPa)	Shear strength (MPa)	V_f (%)
35.1	9.6	4	0.32	807	21.3	97.9	40.3

prepreg were removed and the first layer was placed around a rigid wooden mould covered with a non-stick polymer sheet. The layer then covered with another sheet of non-stick polymer to prevent contamination and a roller was used to roll and shape the material around the mould as flat as possible, and removing any air pockets. The polymer sheet was then removed and the second ply was laid-up on top of the first ply according to desired lay-up. Four laminate with fibre orientations of $[\pm 60]_{10}$, $[0_2/\pm 45]_5$, $[0/90]_{10}$ and $[0/90]_{5S}$ were chosen for composite boxes. The 0 direction coincides with the axial axis of the crush box. Once the boxes had been successfully laid-up, they were placed between four pre-cut aluminium plates to keep them flat during the curing process. The plates were pre-treated with a mould cleaner to remove grease and debris and a monocoat wax was applied to prevent escaped epoxy from the prepreg bonding to the metal plates. The plates were then covered in non-stick polymer sheets to further decrease the chance of epoxy bonding to the plates. The plates were placed on either side of the uncured composite, then covered top and bottom with three sheets of 'breather cloth' and placed inside a heat resistant polymer bag. The breather cloth has the appearance of cotton wool and allows air to circulate around the bag preventing the formation of air pockets. The bagging material was cut from a roll and was open at either end. A high temperature, double-sided epoxy tape was used to seal the ends. Once sealed, an air suction valve is inserted through the bag and a pipe connected the valve to a vacuum pump. The vacuum pump was used to evacuate the bag, with the aid of the breather cloth. This has the effect of pressing the aluminium plates tightly together and forcing the plies of prepreg together, allowing good adhesion between the plies and eliminating air that could cause voids in the composite. The pressure gauge was inserted via a second valve to monitor the pressure in the bag. This can be used to ensure the correct pressure is applied to the bag (following the manufacture's guidelines). The pressure gauge was also used to measure any pressure drop in the vacuum bag once the pump had been switched off and hence to check if the bag was properly sealed. All composite boxes were cured for 30 min at 65 °C and then for 120 min at 130 °C. Then they were cut to the required lengths. The dimensions of all boxes were the same and chosen according to the previous reported works which have shown progressive failure [14]. The b/t ratio was 26.7 mm with thickness of about 3 mm and the total length was 100 mm. To avoid stress concentration at the box corners, an internal fillet with a radius of 6 mm was inserted at the internal corners of the box. Also one end of specimens was bevelled to make a trigger for progressive crushing with an angle of 60° (Fig. 3). Each specimen was crushed between two parallel plates for 50 mm stroke using Universal Testing Machine with 500 kN load cell. The crush speed was set at 2 mm/min, the same speed as used for the DCB tests. For each test configuration three specimens were tested. The force–crush distance diagrams were recorded automatically for each test.

3. Results and discussion

3.1. Mode-I interlaminar fracture toughness

The Mode-I interlaminar fracture toughness G_{IC}, for each fibre orientation was calculated using the modified beam theory (MBT) method and the modified compliance calibration (MCC) method [20–25]. For MBT method, the cube root of compliance, $C^{1/3}$, was plotted as a function of crack length, a. The intercept with the x-axis was considered as the crack length correction, Δ. The G_{IC} value was calculated from:

$$G_{IC} = \frac{3F\delta}{2b(a + |\Delta|)} \tag{1}$$

In the MCC method, a least squares plot of a/t as a function of the cube root of the compliance, $C^{1/3}$, is generated using the visually observed delamination onset values and all the propagation values. The slope of this line is A [25]. The G_{IC} value was then obtained from:

$$G_{IC} = \frac{3F^2C^{\frac{2}{3}}}{2Abt} \tag{2}$$

The experimental G_{IC} results obtained from MBT and MCC for different fibre orientation are shown in Table 2. A sample experimental resistance curve (i.e. G_{IC} versus crack length) is shown in Fig. 4. Transverse cracking of θ-oriented lamina at interface caused some fibre bridging for most of DCB tests as shown in Fig. 2b. The development of fibre bridging caused the force to continuously increase as the crack advanced resulting in a rising R-curve. Regarding the results and recommendations of other works on DCB-tests on

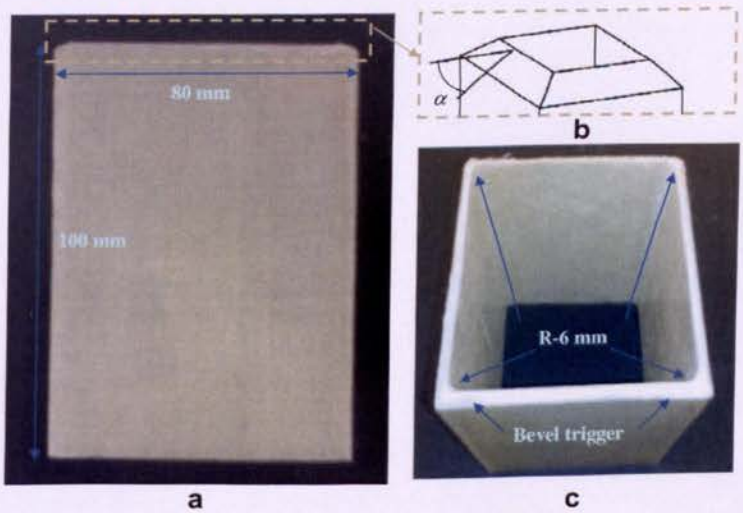

Fig. 3. GFRP composite box: (a) front view, (b) trigger mechanism and (c) top view. Internal fillets of 6 mm were introduced at the internal corners.

Table 2
Interlaminar fracture toughness obtained from DCB tests for various interface fibre orientations

Laminate lay-up	Fracture plane interface	G_{IC} (kJ/m^2)	
		MCC	MBT
$[0/90]_{10}$	0/90	0.923	1.243
$[0_2/\pm45]_5$	0/45	0.884	1.060
$[0/90]_{5S}$	90/90	0.778	1.168
$[\pm60]_{10}$	+60/−60	0.449	0.541

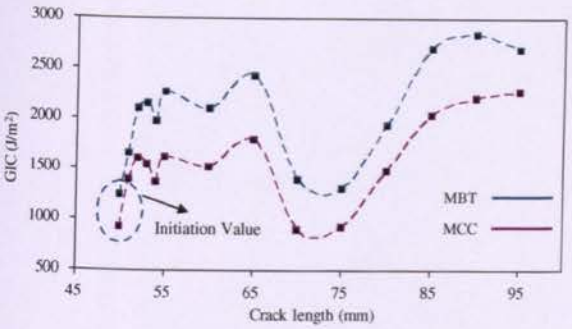

Fig. 4. Resistance curve (R-curve) in a DCB specimen with 0/90 fracture plane interface using MBT and MCC methods.

multidirectional laminates [26–28], G_{IC} values of initiation were considered as interlaminar fracture toughness.

Three different methods to determine crack length for the initiation values from the precrack as the distance between the force–displacement and the precrack are considered. The first non-linearity (NL) method determines the point of deviation from linearity, by sketching a straight line from the origin. The second uses the visual observation (VIS) which is the first point at which the crack is observed to move from the tip of the Teflon insert. The last is the MAX/5%, a point on the force–displacement curve at which the compliance has increased by 5% of its initial value. In this work the visual observation (VIS) was chosen to determine the initiation crack length. It was observed that fibre orientation in the layers adjacent to crack plane affects the G_{IC}. Mode-I interlaminar fracture toughness of the interface layers of 0/90 showed the highest values of G_{IC} for all tested specimens, and the interlaminar fracture toughness of interface layers of +60/−60 showed the lowest value. The combination of $0/\theta$ and θ/θ at interface layers caused the maximum interlaminar fracture toughness.

3.2. Progressive crushing process

Three main crushing modes in accordance with Farley and Jones [14] classification are categorised for progressive failure of composite box in crushing process. The first one is fragmentation mode which is characterised by a wedge-shaped laminate cross section with one or multiple short interlaminar and longitudinal cracks. The second one is lamina bending mode which is shaped with long interlaminar, intralaminar, and parallel to fibre cracks. This mechanism causes the formation of continuous fronds which spread inwards and outwards. The third one is the combination of fragmentation and lamina bending modes and it is called brittle fracture mode. Different modes of crush were observed during quasi-static crush test. As can be seen in Fig. 5, the combination of two distinct crush modes, fragmentation and lamina bending, were observed for all the specimens. This mode (the brittle fracture mode) is an ideal crushing mechanism to dissipate the energy during crushing in composites [9]. For fibre orientation of $[0/90]_{5S}$ and $[\pm60]_{10}$, the fronds were broken into short pieces. Other two fibre orientations $[0_2/\pm45]_5$ and $[0/90]_{10}$ showed more interlaminar separation in crushing process.

At the initial stages of the crushing, four axial cracks were formed at corners of each box which caused bending of the internal and external fronds. It was observed that the external fronds were longer than internal fronds. No axial tear was observed during the crush process. The deformation of all boxes was elastic at the beginning of crushing process while the load increased rapidly to its maximum. Because of the friction between crushing plate and deformed fronds, the debris wedge was shaped. After this a lot of interlaminar and intralaminar cracks were formed in the crush zone (Fig. 6). The crack continued to propagate along the main central interwall (Fig. 7), and lamina bundles were formed. The load dropped from its peak and stabilised around a mean force, F_m. The magnitude of the mean force depends on the propagation of the interlaminar and intralaminar cracks. In this stage which is called post-crushing regime, the internal and external fronds were buckled when the applied force reached a critical value. The energy absorption and the force stability of composite boxes are related to fracture behaviour of the main central interwall crack (Fig. 7). The main central crack which causes to shape lamina bundles has an important role on resistance against crushing energy. The propagation of this crack is similar to crack propagation in Mode-I delamination in composite laminates discussed earlier in Section 2.2 that the fibre orientation at the interface planes has significant effect on Mode-I interlaminar fracture toughness. Also the SEA varied with fibre orientation and fracture behaviour of the main interlaminar cracks. These evidences show that the fracture behaviour of a central interlaminar opening crack is correlated to Mode-I interlaminar fracture toughness.

As discussed previously, the fibre orientation and consequently interlaminar fracture toughness affect on progressive crushing modes. For those fibre orientations which show higher fracture energy from DCB test, higher mean force and absorbed energy were observed during crushing. Obviously the resistance crack propagation contributes to greater energy absorption. As the material and geometry are the same for all specimens; the effect of friction on the dissipation of energy can be assumed to be approximately the same in all crushing processes. The experimental results of force–crush distance for all lay ups are shown and compared in Fig. 8. The results show that the $[0_2/\pm45]_5$ has the highest mean force and consequently highest energy absorption in comparison with other lay-ups. This high energy absorption is related to high Mode-I interlaminar fracture toughness. The lowest interlaminar fracture toughness from DCB tests was observed for $[\pm60]_{10}$ lay-up. This was reflected on the lowest values of mean force and energy absorption in the crash box with the same lay-ups.

Variation of specific energy absorption (SEA) from crush test versus Mode-I interlaminar fracture toughness, G_{IC}, from DCB tests for various lay-ups is plotted in Fig. 9. It can be seen that the interlaminar fracture toughness for interface fracture planes of 0/90, 90/90 and 0/45 are clustered close to each other while the equivalent value for +60/−60 interface plane is much lower. This shows that the specific energy absorptions (SEA) of fibre orientations which are laminated with $0/\theta$ angles are close together. Choosing a suitable fibre orientation in the interface plane is one of the main factors for improving the energy absorption of composite crush boxes in progressive failure. The ratio between initial maximum collapse force and mean force is known as the crush force efficiency (CFE), and the higher value of this parameter, the better energy absorption capability. The crush force efficiency (CFE) of all composite crush boxes was also obtained and the results are shown in Table 3. The $[0/90]_{10}$ lay-up has the highest CFE. The reason comes from its lower initial maximum collapse force compared with other fibre orientations. This situation is more suitable for crashworthiness

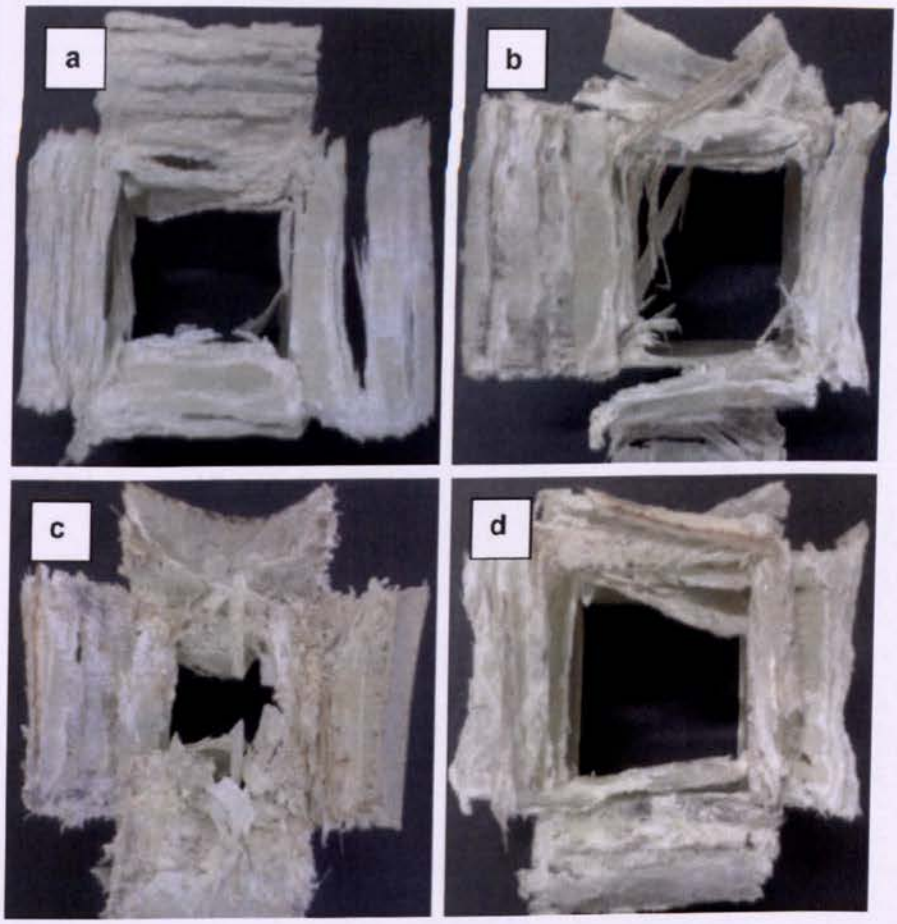

Fig. 5. Plane view of crushed GFRP composite box: (a) $[0/90]_{10}$; (b) $[0/90]_{5S}$; (c) $[0_2/\pm45]_S$; (d) $[\pm60]_{10}$.

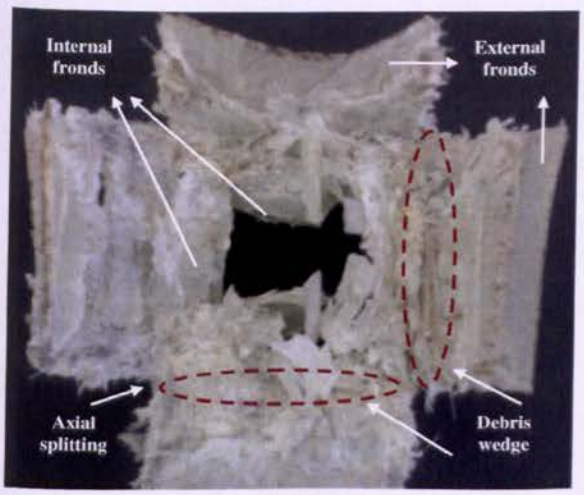

Fig. 6. Crush zone of GFRP composite box (plain view).

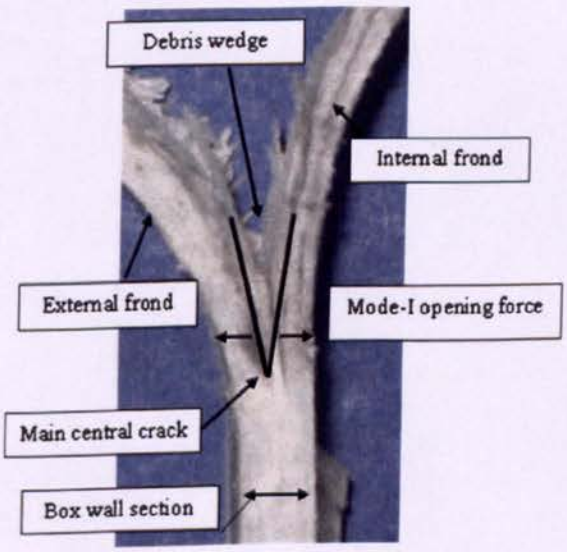

Fig. 7. Mode-I interlaminar crack propagation at the middle of box wall.

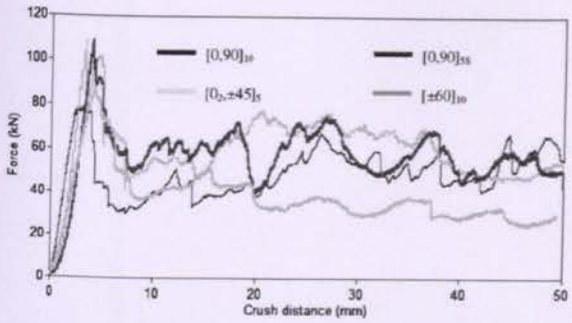

Fig. 8. The comparison of force–crush distance in a square crash box for various lay-ups.

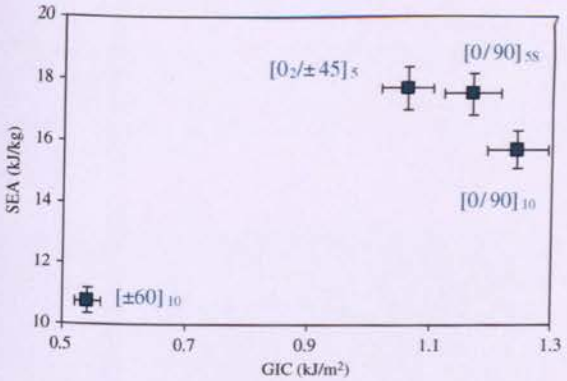

Fig. 9. Variation of specific energy absorption (SEA) with interlaminar fracture toughness, G_{IC}(SBT) for various box lay-ups.

Table 3
Comparison of SEA and Mode-I interlaminar fracture toughness

Lay up	F_{max} (kN)	F_m (kN)	CFE (%)	SEA (kJ/kg)	G_{IC} (kJ/m²) MCC
$[0/90]_{10}$	78	52	67	15.8	0.923
$[0/90]_{5S}$	110	60	55	17.5	0.778
$[0_2/\pm45]_S$	105	61	58	17.7	0.884
$[\pm60]_{10}$	87	38	43	10.8	0.449

design cases which need to absorb the energy with a lower initial collapse force but not necessarily with the highest energy absorption capability.

4. Finite element studies

4.1. Finite element model

The GFRP composite box was modelled with various lay-ups using finite element software ANSYS/LSDYNA [29]. The size of outer cross section of the composite box was 80 × 100 mm with a thickness of 3 mm. The bevel trigger mechanism was modelled in accordance with the experiments with a trigger angle of 60° (see Fig. 3). The GFRP composite box model was based on Belytschko–Lin–Tsay quadrilateral shell elements. All surfaces of the model were meshed using quadratic shell element and the size of an element was 2.5 × 2.5 mm. The striker was modelled as a rigid block using solid element (Fig. 10). The composite layers were modelled by defining the integration points which are placed equally through the thickness in each layer. For each layer the material properties, thickness and fibre orientation were defined. To simulate the quasi-static condition, the velocity of 1 m/s was applied to the rigid striker. The real crushing speed was too slow for the numerical simulation. The explicit time integration method is only conditionally stable, and therefore by using real crushing speed, very small time increments was required to use. For satisfying quasi-static condition firstly the total kinetic energy has to be very small compared to the total internal energy over the period of the crushing process. Secondly, the crushing force–displacement response must be independent from the applied velocity [29]. For the aim of computational efficiency, the density of rigid striker and composite box were scaled-up by a factor of 1000. By using this factor, the quasi-static condition was satisfied during the crushing analysis.

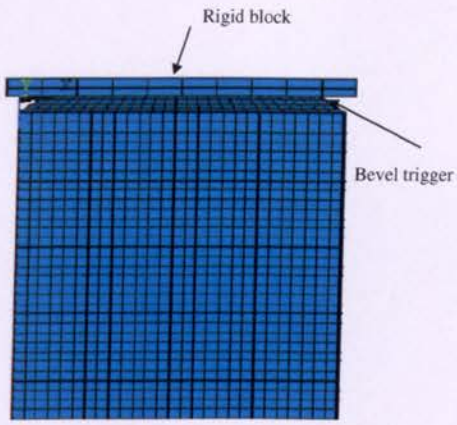

Fig. 10. Finite element model of GFRP composite box in LS-DYNA.

4.2. Material modelling

Material model 54 of LS-DYNA was selected to model the damage of GFRP composite box. In ANSYS this material model follows the Chang and Chang [30] failure criterion which is the modification of the Hashin's failure criterion for assessing lamina failure. In this model as described below all material properties of lamina are examined using the following laws to determine the failure characteristic [31]:

- Tensile fibre failure mode: (fibre rupture)
  If $\sigma_1 > 0$

$$\text{then } e_f^2 = \left(\frac{\sigma_1}{X_t}\right)^2 + \beta\left(\frac{\sigma_{12}}{S}\right) - 1 \quad \begin{cases} e_f^2 \geq 0 & \text{failed} \\ e_f^2 < 0 & \text{elastic} \end{cases} \tag{3}$$

  where β is a weighting factor for shear term in tensile fibre mode and its range is 0–1 and σ_1 is stress in the fibre direction and σ_{12} is transverse shearing stress. When lamina failure occurs, all material constants are set to zero.
- Compressive fibre failure mode: (fibre buckling)
  If $\sigma_1 < 0$

$$\text{then } e_c^2 = \left(\frac{\sigma_1}{X_c}\right)^2 - 1 \quad \begin{cases} e_c^2 \geq 0 & \text{failed} \\ e_c^2 < 0 & \text{elastic} \end{cases} \tag{4}$$

  After lamina failure by fibre buckling E_1, v_{12} and v_{21} are set to zero.
- Tensile matrix failure: (matrix cracking under transverse tension and in-plane shear)
  If $\sigma_2 > 0$

$$\text{then } e_m^2 = \left(\frac{\sigma_2}{Y_t}\right)^2 + \beta\left(\frac{\sigma_{12}}{S}\right) - 1 \quad \begin{cases} e_m^2 \geq 0 & \text{failed} \\ e_m^2 < 0 & \text{elastic} \end{cases} \tag{5}$$

where σ_2 is stress in normal to the fibre direction. After lamina failure by matrix cracking, E_2, v_{21} and G_{12} are set to zero.

- Compressive matrix failure mode: (matrix cracking under transverse compression and in-plane shear)

If $\sigma_2 < 0$

$$\text{then } e_d^2 = \left(\frac{\sigma_2}{2S}\right)^2 + \left[\left(\frac{Y_c}{2S}\right)^2 - 1\right]\frac{\sigma_2}{Y_c} + \left(\frac{\sigma_{12}}{S}\right)^2 \quad \begin{cases} e_d^2 \geq 0 & \textit{failed} \\ e_d^2 < 0 & \text{elastic} \end{cases} \tag{6}$$

In this work the weight factor β which is defined as the radio between shear stress and shear strength is set to 1. The material properties of GFRP were obtained from experimental work reported in Table 1.

4.3. Boundary conditions and contact algorithms

All degrees of freedom of the crash boxes were fixed at the bottom end and all degrees of freedom were free at the upper end which is subjected to impact by the rigid striker. The following contact algorithms were used to simulate the crushing process in quasi-static condition:

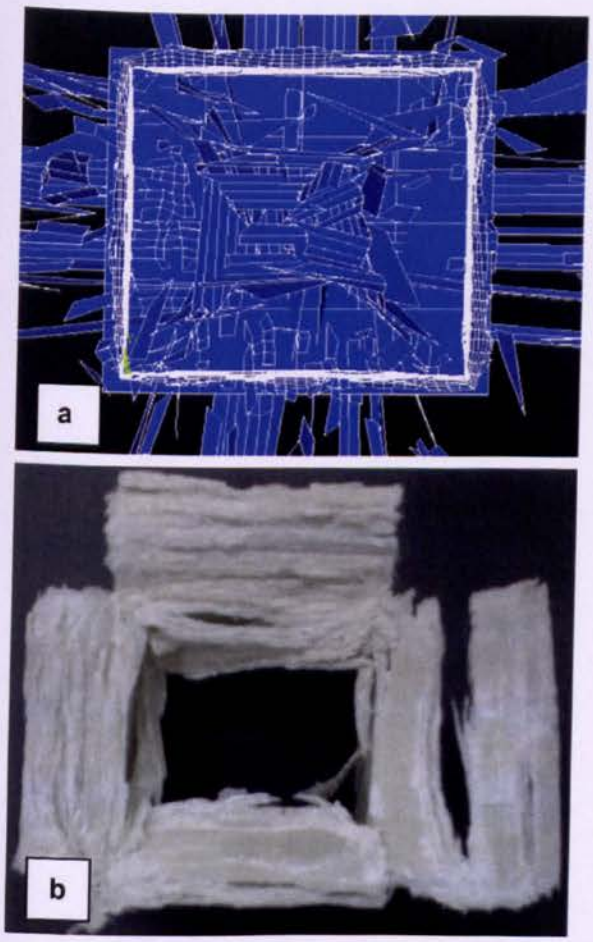

Fig. 11. Comparison of final deformed shape of the GFRP $[0/90]_{10}$ lay-up box in plane view: (a) FEA results; (b) experiment.

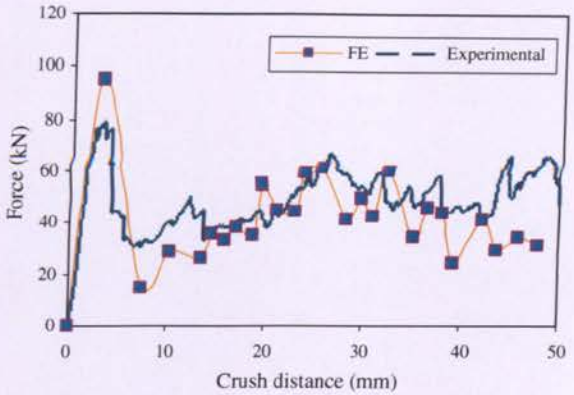

Fig. 12. Comparison of experimental and FE results for GFRP composite box with $[0/90]_{10}$ lay-up.

- The automatic_single_surface algorithm was used to prevent the penetration of the deformed composite box boundary with its own nodes.
- The automatic_node_to_surface algorithm with friction coefficient of 0.25 was used for the contact between rigid striker and composite box.

4.4. Verification of FE results

The deformed shape of FEA model for $[0/90]_{10}$ lay-up is shown in Fig. 11. The similarity between the FEA simulation and experimental work shown in Fig. 5a are very good. In Fig. 12, the force–crush distance of $[0/90]_{10}$ lay-up extracted from FEA model is compared with the experimental results. The difference in mean dynamic force between the FEA model and experiment is less than 8%. The energy absorption computed from FEA is 14.5 kJ/kg while the value from experiment is 15.8 kJ/kg, a difference of less than 9%.

5. Conclusion

In this paper, the effect of fibre orientation on the interlaminar fracture toughness, G_{IC}, and specific energy absorption, SEA, of GFRP composite crush boxes was investigated. It was shown that the fibre orientation at interface fracture plane affects the interlaminar fracture toughness of GFRP composite materials.

The interlaminar fracture toughness of interface fracture planes of 0/90, 90/90 and 0/45 are close together while +60/−60 behave quite differently. The interface plane of 0/90 showed the maximum interlaminar fracture energy while it was a minimum for the +60/−60 interface plane.

It was shown that the specific energy absorption in axial crushing of composite box depends on the interlaminar fracture toughness between laminates and the higher the Mode-I fracture toughness, the higher SEA. However, this relationship is not linear. The SEA of those fibre orientations which have a combination of 0/θ angles are close together because of the similar interlaminar fracture toughness at interface fracture plane. In summary suitable composite structures designs which are subjected to the crushing forces can be achieved by properly choosing the laminate lay-up which gives the highest interlaminar fracture toughness and consequently an improved SEA.

References

[1] Hull D. A unified approach to progressive crushing of fibre reinforced tubes. Compos Sci Technol 1991;40:377–421.

[2] Farley G, Jones R. Crushing characteristics of continuous fibre reinforced composite tubes. J Compos Mater 1992;26:37–50.
[3] Fairfull A, Hull D. Energy absorption of polymer matrix composite structures: frictional effects. In: Wierzbicki T, Jones D, editors. Structural failure. John Wiley and Sons; 1989. p. 255–79 [Chapter 8].
[4] Mamalis AG, Manolakos DE, Demosthenous GA, Ioannidis MB. The static and dynamic collapse of fibreglass composite automotive frame rails. Compos Struct 1996;34:77–90.
[5] Mamalis AG, Manolakos DE, Demosthenous GA, Ioannidis MB. The static and dynamic axial crumbling of thin-walled fibreglass composite square tubes. Compos Pt B: Eng 1997;28(4):439–51.
[6] Saito H, Inai R, Yokoyama A, Hamada H. Basic study of progressive crushing mechanism. Key Eng Mater 2000;177–180:321–6.
[7] Warrior NA, Turner TA, Robitaille F, Rudd CD. The effect of interlaminar toughening strategies on the energy absorption of composite tubes. Compos Pt A 2004;35:431–7.
[8] Jacob GC, Fellers JF, Simunovic S, Starbuck M. Energy absorption in polymer composites for automotive crashworthiness. J Compos Mater 2002;36:813–50.
[9] Farley GL. Energy absorption in composite materials for crashworthy structures. In: Matthews FL, Buskell NCR, Hodgkingson JM, Mortan J, editors. In: Proceedings of the ICCM, vol. 6. London: Elsevier Science Publishers Limited. p. 3.57–3.66.
[10] Cauchi Savona S, Hogg PJ. Effect of fracture thoughness properties on the crushing of flat composite plates. Compos Sci Technol 2006;66:2317–28.
[11] Solaimurugan S, Velmurugan R. Influence of fibre orientation and stacking sequence on petalling of glass/polyester composite cylindrical shell under axial compression. Int J Solid Struct 2007;44:6999–7020.
[12] Solaimurugan S, Velmurugan R. Progressive crushing of stitched glass/polyester composite cylindrical shells. Compos Sci Technol 2007;67:422–37.
[13] Farley GL. Energy absorption capability and scalability of square cross-section composite tube specimens. J Am Helicopter Soc 1989:59–62.
[14] Farley GL, Jones RM. Energy absorption capability of composite tubes and beams. NASA TM-101634, AVSCOM TR-89-B-003; 1989.
[15] Schmueser DW, Wickliffe LE. Impact energy absorption of continuous fiber composite tubes. J Eng Mater Technol 1987;109:72–7.
[16] Jimenez MA, Miravete A, Larrode E, Revuelta D. Effect of trigger geometry on energy absorption in composite profiles. Compos Struct 2000;48:107–11.
[17] BS EN ISO 2747. Glass fibre reinforced plastics-tensile test. London: British Standard Institute; 1998.
[18] BS EN ISO 14129. Fibre reinforced plastics composite-determination of the in-plane shear stress/shear strain response, including the in-plane shear modulus and strength by the ±45 tension test method. London: British Standard Institute; 1998.
[19] ASTM D 3171-99. Standard test method for constituent content of composite materials. Annual book of ASTM standards. West Conshohocken, PA: ASTM; 2002.
[20] BS EN ISO 15024:2001. Fibre-reinforced plastic composites. Determination of mode I interlaminar fracture toughness, G_{IC}, for unidirectional reinforced materials. BSI; 2002.
[21] Blackman BRK, Brunner AJ. Mode I fracture toughness testing of fibre reinforced polymer composites: unidirectional versus cross ply lay up. In: Brown MW, de la Rios ER, Miller KJ, editor. ECF-12 fracture from defects. EMAS; 1998. p. 1471–5.
[22] Hashemi S, Kinloch AJ, Williams JG. Corrections needed in double-cantilever beam tests for assessing the interlaminar failure of fibre-composites. J Mater Sci Lett 1989;8:125–9.
[23] Hashemi S, Kinloch AJ, Williams JG. The analysis of interlaminar fracture in uniaxial fiber–polymer composites. P R Soc Lond A: Mater 1990;427:173–99.
[24] Williams JG. End corrections for orthotropic DCB specimens. Compos Sci Technol 1989;35:367–76.
[25] Shetty MR, Vijay Kumar KR, Sudhir S, Raghu P, Madhuranath AD. Effect of fibre orientation on Mode-I interlaminar fracture toughness of glass epoxy composites. J Reinforced Plastic Compos 2000;19:606–20.
[26] Choi NS, Kinloch AJ, Willams JG. Delamination fracture of multidirectional carbon-fiber/epoxy composites under mode I, mode II and mixed mode I/II loading. J Compos Mater 1999;33(1):73–100.
[27] de Morais AB. Double cantilever beam testing of multidirectional laminates. Compos Pt A: Appl Sci 2003;A34(12):1135–42.
[28] Pereira AB, de Morais AB. Mode I interlaminar fracture of carbon/epoxy multidirectional laminates. Compos Sci Technol 2004;64(13–14):2261–70.
[29] Santosa SP, Wierzbicki T, Hanssen AG, Langseth M. Experimental and numerical studies of foam-filled sections. Int J Impact Eng 2000;24:509–34.
[30] Chang FK, Chang KY. A progressive damage model for laminated composites containing stress concentrations. J Compos Mater 1987;21:809–33.
[31] LS-DYNA user's manual. Non-linear dynamic analysis of structures in three dimensions. Livermore, USA: Livermore Software Technology Corporation; 1997.

Composite Structures 89 (2009) 303–314

Contents lists available at ScienceDirect

Composite Structures

journal homepage: www.elsevier.com/locate/compstruct

Effects of Mode-I and Mode-II interlaminar fracture toughness on the energy absorption of CFRP twill/weave composite box sections

H. Hadavinia *, H. Ghasemnejad

Faculty of Engineering, Kingston University London, London SW15 3DW, UK

ARTICLE INFO

Article history:
Available online 20 August 2008

Keywords:
Interlaminar fracture toughness
Specific energy absorption
Laminate design
Crush box
LS-DYNA

ABSTRACT

Mode-I and Mode-II interlaminar crack growth affect the failure modes of the progressive crushing of composite box structures. These failure modes which are known as lamina bending, brittle fracture, transverse shearing and local buckling contribute to specific energy absorption (SEA) of composite box. In this regard, the effect of laminate lay-up of the composite crush box was sought by studying their effects on Mode-I and Mode-II interlaminar fracture toughness. The double cantilever beam (DCB), three-point-end-notched flexure (3ENF) and axial crush box specimens were fabricated from carbon/epoxy twill–weave fabrics of $[0]_4$, $[45]_4$ and $[0/45]_2$ and they were tested under quasi-static condition to determine the interlaminar fracture toughness in Mode-I (G_{IC}), Mode-II (G_{IIC}) and SEA of each lay-up. It was shown that interlaminar crack propagation in Mode-I and Mode-II contributes significantly on the type of the progressive crushing mode and SEA. The interfaces of 0/45 and 0/0 have higher Mode-I and Mode-II interlaminar fracture toughness and as a result the crushed box with these lay-ups showed a higher energy absorption capability in comparison with crush box lay-up of $[45]_4$. An analytical solution was proposed to predict the mean crushing force for each failure mode. The crushing process of composite boxes was also simulated by finite element software LS-DYNA and the results were verified with the relevant experimental results.

1. Introduction

The brittle nature of most fibre reinforced polymer (FRP) composites accompanying other forms of energy absorption mechanisms such as fibre breakage, lamina bending, and buckling, matrix cracking and crushing, debonding at the fibre–matrix interface and especially plies delamination which occurs due to shear and tensile separation between fronds, play important roles on progressive failure mode and energy absorption capability of composite boxes.

In design of energy absorbers structures from FRP materials, the main source of energy absorption is due to four crushing modes and their combinations during progressive failure of composite crush box [1]. The first mode is *transverse shearing* (fragmentation) which is characterised by a wedge-shaped laminate cross section with one or multiple short interlaminar and longitudinal cracks. In this mechanism interlaminar crack propagation and bundle fracture control the energy absorption. The second mode is *lamina bending* which is developed from long interlaminar, intralaminar, and parallel to fibre cracks. This mechanism causes the formation of continuous fronds which spread inwards and outwards. Friction and inter/intra laminar fracture controls the energy absorption of lamina bending mode. The third mode is *brittle fracturing* mode which is a combination of transverse shearing and lamina bending crushing modes. In this mode the length of the interlaminar cracks are between 1 and 10 laminate thickness. In this case the main energy absorption mechanism is fracturing of lamina bundles. The highest energy absorption of composite tubes has been observed in brittle fracture and lamina bending crushing modes [2]. The fourth mode is *local buckling* which occurs in brittle FRP composites when (i) the interlaminar stresses are small relative to the strength of the matrix, (ii) the matrix has a higher failure strain than the fibre, and (iii) the matrix exhibits plastic deformation under high stress.

During progressive collapse, frond bending following the growth of a main central interwall crack due to delamination in the side wall causes a significant amount of energy absorption. The main central interwall cracks are Mode-I interlaminar crack propagation. Sliding occurs between lamina bundles during frond bending, and they dissipate the energy in Mode-II crack propagation.

The effects of delamination fracture toughness on the energy absorption of composite materials and structures have been investigated by other researchers [3–8]. Savona et al. [3] studied the relation between specific sustained crushing stress (SSCS) of GFRP composite plates with their Mode-I and Mode-II fracture

* Corresponding author. Tel.: +44 20 8547 8864; fax: +44 20 8547 7992.
E-mail address: h.hadavinia@kingston.ac.uk (H. Hadavinia).

0263-8223/$ - see front matter © 2008 Elsevier Ltd. All rights reserved.
doi:10.1016/j.compstruct.2008.08.004

Nomenclature

a	crack length
a_e	effective crack length
b	side of box
C	compliance
CFE	crush force efficiency
CFRP	carbon fibre reinforced plastic
DCB	double-cantilever beam
3ENF	three-point-end-notched flexure
E	Young's modulus
F	load
F_{max}	initial maximum load
F_m	mean load
G_{12}	shear modulus
G_{IC}	Mode-I interlaminar fracture toughness
G_{IIC}	Mode-II interlaminar fracture toughness
h	ENF specimen half-thickness
L	half span of ENF specimen
SEA	specific energy absorption
t	crush box wall thickness
V_f	fibre volume fraction
U_e	external work
U_f	energy dissipated by friction
U_b	energy dissipated in bending
U_{bu}	energy dissipated in local buckling
U_{bf}	energy dissipated by bundle fracture
U_c	energy dissipated in axial splitting
U_d	energy dissipated by delamination
U_s	energy dissipated in shear deformation
$U_{LB/BF}$	energy dissipated for lamina bending/brittle fracture crushing modes
$U_{BU/TS}$	energy dissipated for local buckling/transverse shearing crushing modes
x	sliding distance on the platen
Y	geometry factor
z	crushing distance
ν	Poisson's ratio
λ	crush length of a single stroke
β	weight factor
μ	coefficient of friction
δ	displacement
σ_u	ultimate tensile stress
σ_b	flexural strength
τ_s	shear strength
θ	fibre orientation
φ	semi-angle of the wedge
Δ	crack length correction factor in DCB test

toughness properties. According to their results, materials which show Mode-I and Mode-II interlaminar fracture toughness absorb low crushing energy. They also showed that the G_{IC} and G_{IIC} of initiation are more influential than theG_{IC} and G_{IIC} of propagation on the energy absorption mechanism. Solaimurugan and Velmurugan [4] had studied the effect of stitching, fibre orientation and stacking sequence on G_{IC}, SEA, and progressively crushing of glass/polyester composite cylindrical shells under axial compression. They reported that axial fibres placed close to the outer surface of the tube led to more petals formation and stable crushing process, while axial fibres close to inner surface of the tube cause higher energy absorption. Furthermore, the energy absorption during delamination increases when Mode-I fracture toughness is higher. They also reported that through-thickness stitching increases the Mode-I interlaminar fracture toughness which increases energy absorption of cylindrical tube. Warrior et al. [5] studied the influence of toughened resins, thermoplastic resin additives, through-thickness stitching and thermoplastic interleaving on the interlaminar fracture toughness (G_{IC}) and the SEA for continuous filament random mat (CoFRM) and 0/90 non-crimp fabric (NCF) E-glass reinforced polyester composite tubes. They reported that all above mentioned factors increase G_{IC}, but only toughened resin and through-thickness stitching can increase SEA. A comprehensive review of the effect of fibre type, matrix type, fibre architecture, specimen geometry, process conditions, fibre volume fraction and testing speed on energy absorbing capabilities of composite crash elements are reported in [6]. It was shown that in general, a tougher matrix gives a higher G_{IC} for the composite and this has a positive effect on their crash performance. Farley [7] concluded that matrix stiffness has a minor effect on energy absorption of materials which crushed by a brittle fracture and transverse shearing mechanism, but the effect of matrix stiffness is more important in lamina bending mechanism. Ghasemnejad et. al. [8] recently studied the effect of Mode-I interlaminar fracture toughness on the energy absorption of laminated GFRP composite box made from various fibre orientations. They concluded that using suitable laminate design for composite box improves interlaminar fracture toughness and consequently energy absorption capability. They also showed that the variation of specific energy absorption (SEA) with interlaminar fracture toughness (G_{IC}) is non-linear for various box lay-ups.

Jimenez et al. [9] experimentally studied the energy absorption capability of a unidirectional box section, and an I-section made of alternating layers of mat and fabric. For each one of the two profiles, six different trigger geometries were analysed. They showed that the I-section is a good candidate for being considered for energy absorption applications. They also concluded that when studying a trigger geometry, slight modifications (as the bevel angle of a bevel trigger) can result in important variations of the results. Elgalai et al. [10] examined the crushing behaviour of axially crushed composite corrugated carbon fibre/epoxy and glass fibre/epoxy tubes. A series of experiments was conducted for tubes with corrugation angle ranging from 10° to 40°. Their results showed that the crushing behaviour of composite corrugated tube is sensitive to the change in corrugation angle and fibre type. Alkateb et al. [11] experimentally examined the behaviour of composite elliptical thin walled cones with the same ellipticity ratio and different vertex angles subjected to quasi-static axial crushing. They showed that the catastrophic failure mode is avoided by deviating from the elliptical tubular shape to the elliptical conical one. A significant enhancement in load carrying capacity and energy absorption capability were seen in the case of elliptical conical shells. Melo et al. [12] looked at the effect of the processing conditions (with or without vacuum) on the specific energy absorption capacity of composite tubes under quasi-static compression load. Their test results showed that, among the conditions considered, tubes of circular cross section fabricated under applied vacuum display the highest level of specific energy absorbed. Mahdi and Kadi [13] implemented artificial neural networks (ANN) technique in the prediction of the crushing behaviour and energy absorption characteristics of laterally loaded glass fibre/epoxy composite elliptical tubes.

Zarei et al. [14] performed dynamic crash tests in order to determine the crash behavior of woven fiberglass/polyamide thermoplastic composite crash boxes. The LS-DYNA explicit finite element code was used for modelling. They compared the crash performance of the optimum composite crash box with an optimum aluminium tube. Lee et al. [15] performed the tensile and

compressive tests of glass/epoxy composites with 1–200 s^{-1} strain rates which are typical strain rate range during automobile crash accidents in order to measure the strength variation with respect to strain rate.

This study is mainly focused on the effect of fibre orientation on G_{IC}, G_{IIC} and SEA of twill/weave fabric CFRP. The DCB, 3ENF and crush box specimens were made from carbon/epoxy twill-weave fabrics of $[0]_4$, $[45]_4$ and $[0/45]_2$ and they were tested under quasi-static condition. The experimental interlaminar fracture toughness in Mode-I (G_{IC}) and Mode-II (G_{IIC}) were measured and their effect on the progressive crushing mode and SEA were investigated. The crushing process of composite boxes was also simulated by finite element software LS-DYNA and the results were verified by experimental results.

2. Experimental procedure

The mechanical characteristics of carbon/epoxy twill-weave fabrics were obtained in accordance with the relevant standards [16–19]. These tests were tensile, shear, fibre volume fraction, coefficient of friction, double-cantilever beam (DCB), 3-point-end-notched flexure (3ENF) and quasi-static crush box. All specimens were manufactured from twill/weave fabric CFRP material of density 1.8 g/cm^3 with epoxy resin. For twill/weave composite it was observed that crack propagation along the weft yarns is associated with more resistance than propagation along the warp direction [20]. In this regard, the weft direction was coincided with the longitudinal axis of composite boxes which crack propagates. Details of the test procedures were explained elsewhere [8]. A summary of the findings for tensile, shear and fibre volume fracture are summarised in Table 1.

2.1. Preparation of DCB and 3ENF specimens

The lamination of DCB and 3ENF beams was laid-up according to the laminate design of $[0]_4$, $[0/45]_2$ and $[45]_4$ with respect to weft direction. The mid-plane interfaces were, respectively, 0/0, 0/45 and 45/45 to determine the Mode-I and Mode-II interlaminar fracture toughness along the respective fracture planes. The crack propagation was set along the weft direction which was defined as 0 direction (see Fig. 1).

For determining the Mode-I interlaminar fracture toughness, G_{IC}, BS ISO 15024 standard [19] was followed. Also the corrections for the end-block, DCB arm bending and root rotation were considered [21]. The recommended specimen size is at least 150 mm long and 20–25 mm wide with an initial crack length (i.e. the length of the insert from the load line) of 50 mm (see Fig. 2a).

The 3ENF specimens were made according to ESIS protocol [22] with the width of 20 mm and the total length of 160 mm, while the thickness varied from 5 to 6 mm. This thickness is required to avoid large displacement, plastic deformation and intraply damage. A precrack length of 55 mm from the free end of specimen was inserted using a Teflon film (see Fig. 2b). Loading was carried out at a constant crosshead displacement rate of 2 mm/min. The details of specimen preparation and testing method were explained in [8]. However, due to rapid crack propagation without any clear mouth opening in 3ENF Mode-II tests, the initiation fracture toughness is more accurate than propagation. Force at each crack length was retrospectively obtained from the recorded force–displacement diagram to calculate G_{IC} and G_{IIC} (Fig. 3).

Table 1
Material properties of the twill/weave CFRP

E_1 (GPa)	E_2 (GPa)	G_{12} (GPa)	ν_{12}	$\sigma_u 0°$ (MPa)	$\sigma_u 90°$ (MPa)	τ_s (MPa)	V_f (%)	μ	σ_b (MPa)	
61	58	3.4	0.1	634	560	94	45	0.41	$[0]_4$	555
									$[0/45]_2$	570
									$[45]_4$	320

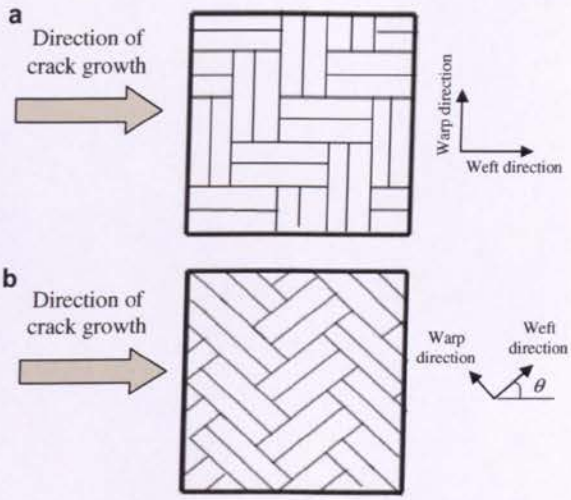

Fig. 1. Direction of crack propagation in (a) 0° and (b) 45° ply.

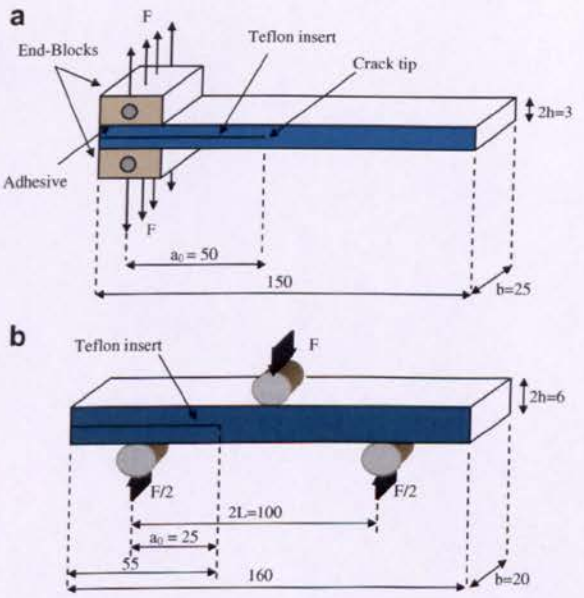

Fig. 2. Geometries of (a) DCB and (b) 3ENF specimens (all dimensions in mm).

2.2. Composite crush box

The crush box specimens were made of the carbon/epoxy twill-weave fabric by hand lay-up with fibre orientations in accordance to those used in DCB and 3ENF tests as described in the previous section. The 0° direction which coincided with the axial axis of the crush box was parallel to weft direction (Fig. 4). All details of specimen preparation and testing method were reported in [8].

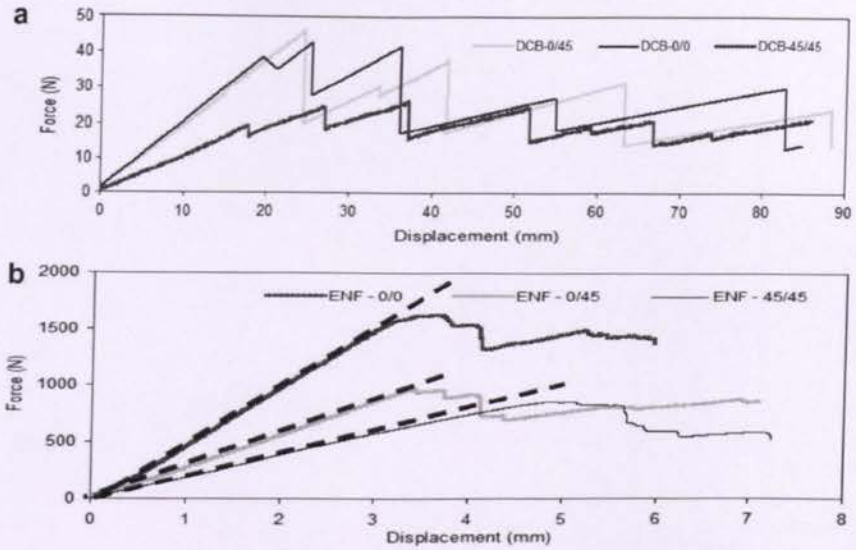

Fig. 3. Force–load line displacement from (a) DCB and (b) 3ENF tests for various mid-plane interfaces.

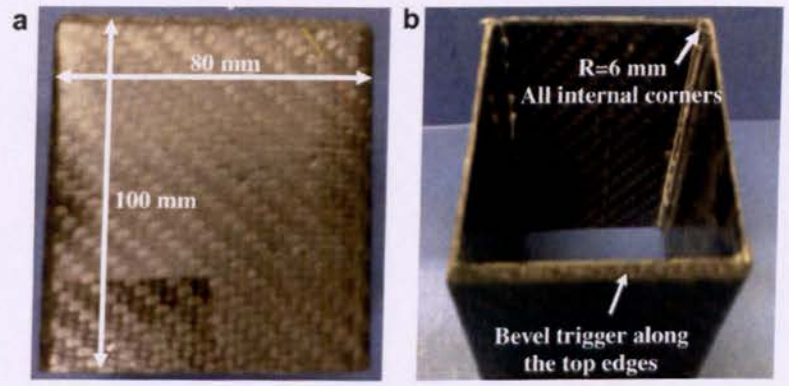

Fig. 4. CFRP composite crush box specimen: (a) front view and (b) top view. Internal fillets of 6 mm were introduced at the internal box corners. The box wall thickness is $t = 3$ mm.

Each specimen was crushed at the rate of 2 mm/min between two parallel platens for 50 mm stroke using a Universal Testing Machine with 500 kN load cell. For each test configuration three specimens were tested. The force–crush distance diagrams were recorded automatically for each test.

3. Experimental results and discussion

3.1. Mode-I interlaminar fracture toughness

The Mode-I interlaminar fracture toughness G_{IC}, for each fibre orientation was calculated using the *modified beam theory* (*MBT*) and the *modified compliance calibration* (*MCC*) methods [21]. The MBT and MCC methods were calculated from Eqs. (1) and (2), respectively:

$$G_{IC} = \frac{3F\delta}{2b(a+|\Delta|)} \tag{1}$$

$$G_{IC} = \frac{3F^2C^{\frac{2}{3}}}{2Abt} \tag{2}$$

The experimental G_{IC} results obtained from MBT and MCC for different fibre orientation are reported in Table 2. The experimental resistance curves (i.e. G_{IC} versus crack length) are presented in Fig. 5. Various reasons such as intra-laminar delamination, mixed mode fracture, fibre-bridging, micro-cracking, residual stresses, or a combination of these effects of θ-oriented lamina at interface caused the development of transverse intralaminar and unstable crack propagation in DCB tests. In all DCB tests intra-laminar delamination, fibre–matrix debonding and/or fibre breakage were observed in fracture surface areas as shown in Fig. 6. The development of transverse cracking also caused the force to show several continuous increases after initial crack propagation resulting in a rising R-curve (see Fig. 7). Regarding the results and recommendations of other works on DCB-tests on multidirectional laminates [23,24], G_{IC} values of initiation are reported as interlaminar fracture toughness. The experimental results show that fibre orientation in the layers adjacent to crack plane affects the G_{IC}. Mode-I interlaminar fracture toughness of the interface layers of (0/45) showed the highest values of G_{IC}, and interface layers of (45/45) showed the lowest value.

Table 2
Interlaminar fracture toughness obtained from DCB and 3ENF tests for various interface fibre orientations

Laminate lay-up	Fracture plane interface	G_{IC} (MCC), kJ/m^2	G_{IC} (MBT), kJ/m^2	G_{IIC} (CCM), kJ/m^2	G_{IIC} (SBT), kJ/m^2
$[0]_4$	0/0	0.9	1.0	2.0	2.4
$[0/45]_2$	0/45	1.2	1.3	1.6	1.5
$[45]_4$	45/45	0.7	0.7	1.2	0.9

MCC: modified compliance calibration, MBT: modified beam theory, CCM: compliance calibration method, SBT: simple beam theory.

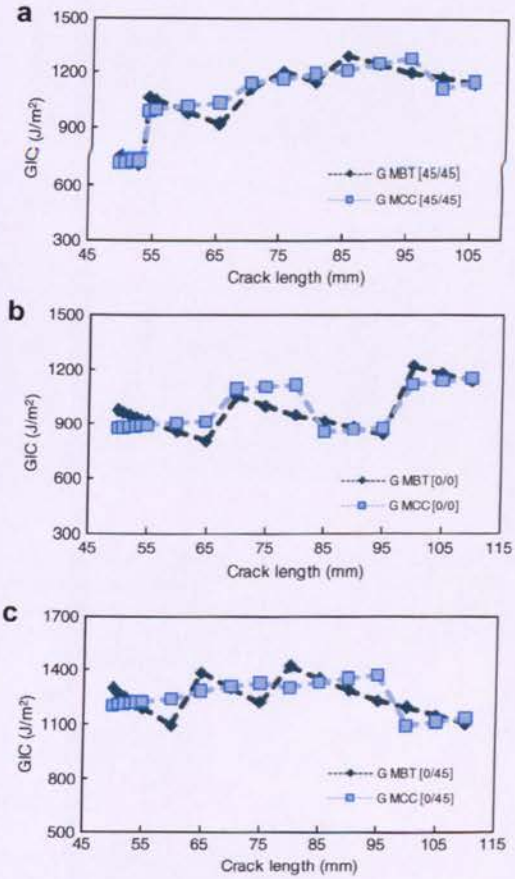

Fig. 5. Resistance curve (R-curve) in DCB specimens with (a) 45/45, (b) 0/0 and (c) 0/45 fracture plane interfaces using MBT and MCC methods. (a) Interface of 45/45, (b) interface of 0/0, and (c) interface of 0/45.

3.2. Mode-II interlaminar fracture toughness

The Mode-II interlaminar fracture toughness, G_{IIC}, can be measured by three-point-end-notched flexure (3ENF), the end-loaded split (ELS) and the four-point-end-notched flexure (4ENF) tests [25]. Because of a simple 3ENF test setup, this method is the most used [26]. Measuring the Mode-II fracture toughness from film inserts yields a higher toughness than from precracks. This is in contrast to Mode-I testing where fibre bridging causes higher fracture toughness from precracks [27]. In this work as the initiation values of G_{IC} and G_{IIC} is more relevant than propagation values, the 3ENF

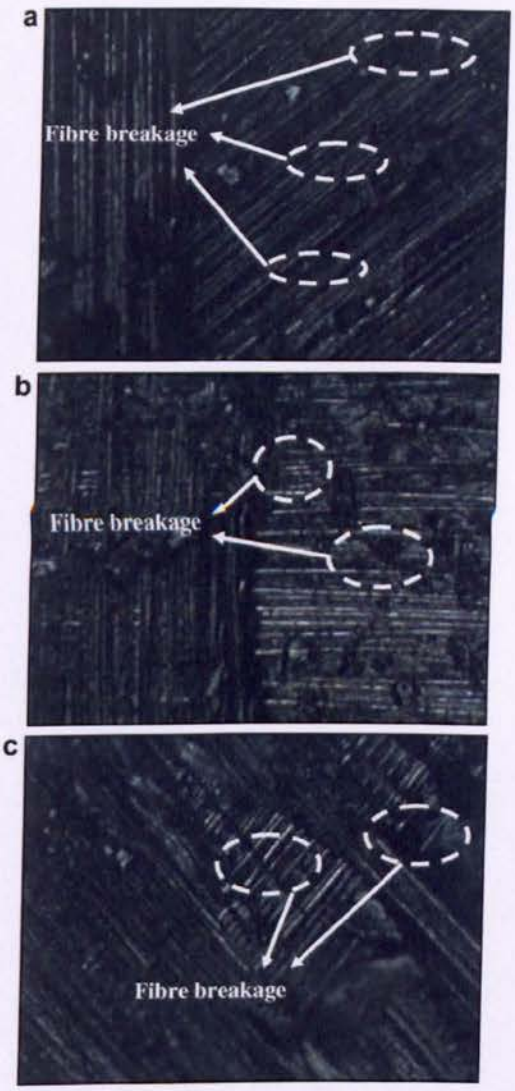

Fig. 6. Optical micrograph from fracture surface of DCB specimens showing fibre breakage combination of intralaminar: (a) 0/45 interface, (b) 0/0 interface and (c) 45/45 interface.

test method is used to study the effect of Mode-II fracture toughness on the energy absorption of composite box.

Using classical simple beam theory (SBT), the load-point compliance in the 3ENF specimen is [25]

$$C = \frac{\delta}{F} \tag{3}$$

$$C = \frac{2L^3 + 3a^3}{8E_1 bh^3} \tag{4}$$

Using the compliance equation

$$G = \frac{F^2}{2b}\frac{dC}{da} \tag{5}$$

The interlaminar fracture toughness can be found in Eqs. (3)–(5):

$$G_{IIC} = \frac{9F\delta a^2}{2b(2L^3 + 3a^3)} \tag{6}$$

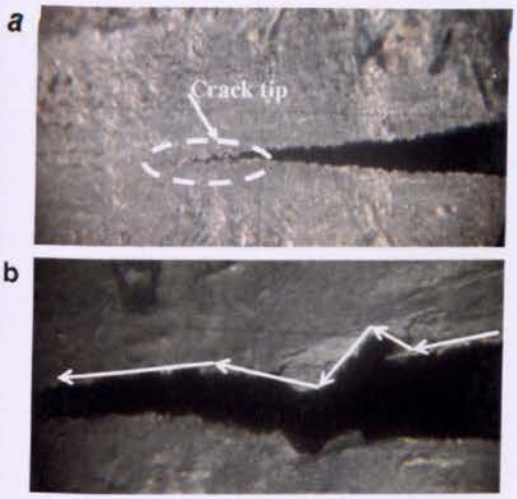

Fig. 7. Transverse cracking in DCB specimen: (a) at crack tip and (b) typical pattern of crack propagation.

Table 3
Comparison of experimental SEA and summation of Mode-I and Mode-II interlaminar fracture toughness

Laminate lay-up	F_{max} (kN)	F_m (kN)	CFE (%)	SEA (kJ/kg)	G_T[a] (kJ/m^2)
$[0]_4$	67	65	97	25	5
$[0/45]_2$	87	67	77	26	4.4
$[45]_4$	85	52	61	20	3.6

[a] Under the assumption that $G_T = G_{IC} + 2G_{IIC}$ for box lay-ups of $[0/45]_2$ and $[0]_4$ and $G_T = 3\ G_{IIC}$ for box lay-up of $[45]_4$ as no Mode-I crack was observed in this lay-up.

Various other methods of the *compliance calibration method* (*CCM*), the *corrected beam theory* (*CBT*) and the *corrected beam theory* (CBT^{WW}) after Wang and Williams [28] are used to calculate the Mode-II interlaminar fracture toughness, G_{IIC}. In *CCM* compliance is based on the least squares linear regression as [27]

$$CN_1 = A + ma^3 \tag{7}$$

where N_1 is a large displacement correction factor and A and m are data fitting constants. Thus, G_{IIC}, becomes

$$G_{IIC} = \frac{3mF^2a^2}{2b}\frac{F'}{N_1} \tag{8}$$

where F is an additional large displacements correction factor which was found negligible in 3ENF tests [27].

In this work *simple beam theory* (SBT) and *Corrected Calibration Method* (CCM) were used to determine the Mode-II fracture toughness. Due to the difficulties in defining the exact position of crack initiation, the non-linearity (NL) and the 5% offset are used to find the crack initiation. The results of Mode-II delamination fracture toughness, G_{IIC}, using non-linearity (NL) for each interface, were presented in Table 2. The Mode-II interlaminar fracture toughness of the interface layers of (0/0) showed the highest values of G_{IIC} for all specimens, and for interface layers of (45/45) showed the lowest value. The experimental resistance curves of G_{IIC} versus crack length are presented in Fig. 8.

3.3. Progressive crushing process of crush box

Each composite box was crushed between two parallel platen for 50 mm stroke using a Universal Testing Machine with 500 kN load cell. The crush speed was set at 2 mm/min, the same speed as used for the DCB and 3ENF tests. For each test configuration three specimens were tested. The force–crush distance diagrams were recorded automatically for each test.

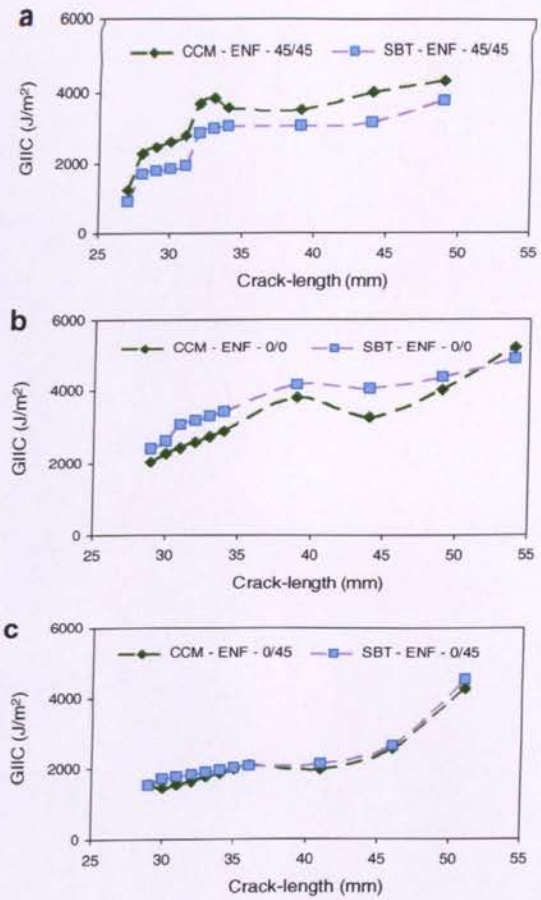

Fig. 8. Resistance curve (R-curve) in 3ENF specimens with (a) 45/45, (b) 0/0 and (c) 0/45 fracture plane interfaces using *CCM* and *SBT* methods.

The combinations of three distinct crushing modes were observed during quasi-static crush tests. As can be seen in Fig. 9, the combination of lamina bending and brittle fracture modes were observed for fibre orientations of $[0]_4$ and $[0/45]_2$ and also the combination of transverse shearing and local buckling was found for laminate design of $[45]_4$. The combination of lamina bending and brittle fracture crushing modes showed the highest energy absorption in comparison with the other observed modes. This high energy absorption is caused by a larger crush area and therefore a higher potential to absorb energy by frictional effects at the platen/specimen interface. The force–crush distance of lamina bending crushing mode showed majority of serrations with small amplitude. This situation causes to increase the required stresses to initiate crack propagation and consequently high energy absorption. In brittle fracture and lamina bending many interlaminar and intralaminar cracks were formed in the crush zone.

The deformation of all boxes was elastic at the beginning of crushing process while the load increased rapidly to its maximum. At the initial stages of the crushing, four axial cracks were formed at the corners of each box which caused splitting of the transverse fibres and bending of the internal and external fronds. It was

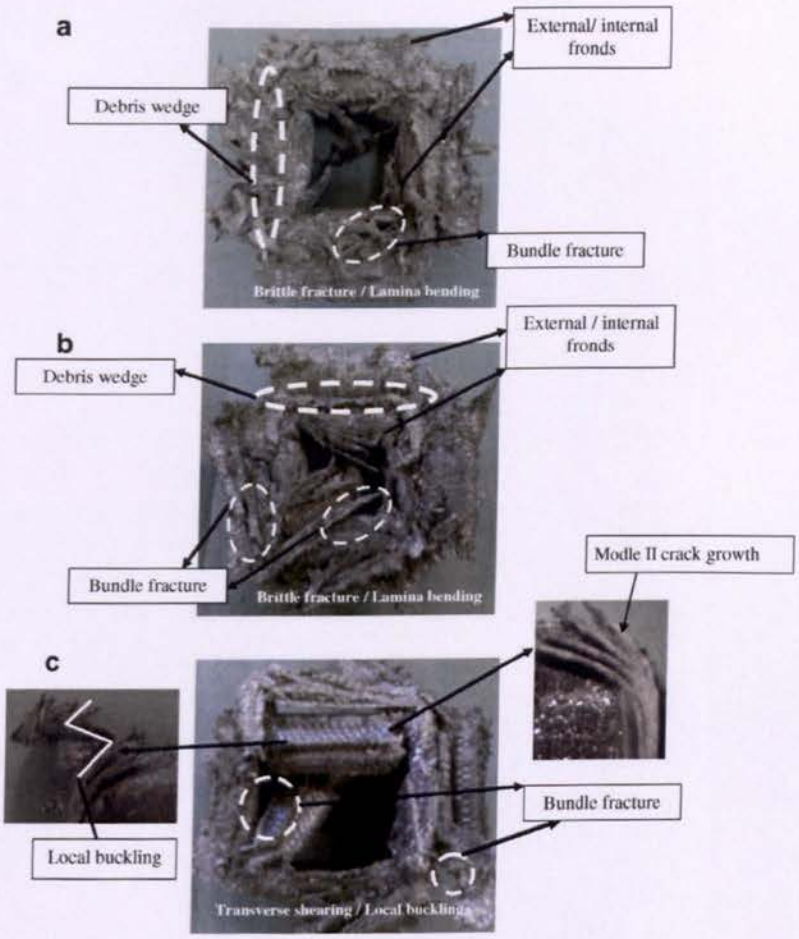

Fig. 9. Plane view of crushed CFRP composite box. (a) $[0]_4$, (b) $[0/45]_2$, and (c) $[45]_4$.

observed that the external fronds were nearly the same size as internal fronds. For all boxes except laminate design of $[45]_4$ the main cracks started and continued to propagate along the central interwall, and lamina bundles were formed (see Fig. 10). At this stage the load dropped from its peak and stabilised around a mean force, F_m. The magnitude of the mean force depends on the propagation of the interlaminar and intralaminar cracks. In this stage which is called post-crushing regime, the internal and external fronds were buckled when the applied force reached a critical value. In crushing of $[0]_4$ and $[0/45]_2$ boxes, some lamina bundle fracture mechanisms were observed during frond bending as the central crack interwall propagated. In crushing of $[45]_4$ box, local buckling and many lamina bundle fracture and short interlaminar Mode-II crack propagation occurred (Fig. 9c). In this case the interlaminar stresses are small relative to the strength of the matrix and no Mode-I crack growth will occur. This situation yields to shape local buckling crushing mode with many bundle fractures in transverse shearing mode.

In lamina bending mode, the main central crack causes to shape lamina bundles which has a significant role on absorbing the impact energy. The propagation of this type of cracks is the same as crack propagation in Mode-I delamination in composite laminates discussed earlier. We saw that the fibre orientation at the interface planes has a significant effect on Mode-I interlaminar fracture toughness (see Fig. 5). Also in this failure mode the fronds splitting

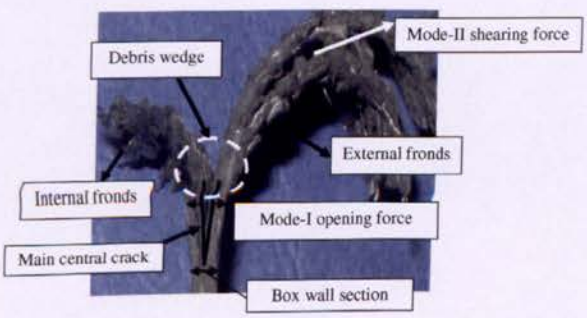

Fig. 10. Mode-I interlaminar crack propagation at the central interwall in $[0/45]_2$ and $[0]_4$ boxes.

due to lamina bundle bending is similar to interlaminar crack propagation in Mode-II (see Fig. 10). The G_{IC} and G_{IIC} of initiation are more influential than theG_{IC} and G_{IIC} of propagation in the energy absorption mechanism [3]. Hence, the Mode-I and Mode-II initiation values were chosen to quantify the effect of Mode-I and Mode-II fracture toughness on energy absorption of composite box. Regarding the fracture toughness study in previous sections,

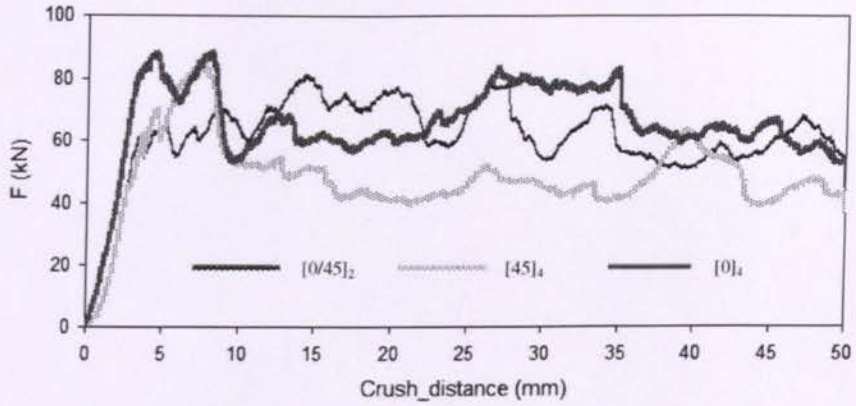

Fig. 11. Comparison of force–crush distance of CFRP composite boxes with different layup.

the interface of 0/45 showed the highest Mode-I fracture toughness and the interface of 0/0 showed the highest Mode-II fracture toughness while the lowest of both Mode-I and Mode-II fracture toughness was observed along interface of 45/45.

In the lamina bending crushing mode due to through the thickness transverse stress, Mode-I interlaminar fracture will occur. However, this fracture mode was not observed in laminate design of $[45]_4$ (see Fig. 9c). The combination of local buckling and transverse shearing crushing modes was more likely to shape than other crushing modes. In combination of lamina bending and brittle fracture modes, the high friction and the high fracture toughness values far outweigh other crushing mechanisms in absorbing the crushing energy.

The experimental results of force–crush distance for all lay-ups are compared in Fig. 11. The results show that $[0/45]_2$ has the highest mean force and consequently the highest energy absorption capability in comparison with other lay-ups. Owning to no frond bending and low frictional effect this was reflected on the lowest values of mean force and energy absorption in the crush box of $[45]_4$ lay-ups.

Variation of specific energy absorption (SEA) from crush test versus a summation of G_{IC} and G_{IIC} for various lay-ups is plotted in Fig. 12a. It can be seen that the total interlaminar fracture toughness in Mode-I and Mode-II of 0/0 is higher than the equivalent values of 0/45 and 45/45 interface planes, but 0/45 box has the highest SEA. This shows that the effect of other mechanisms such as friction and bending will increase as the total fracture energy increase beyond a certain limit. It should be mentioned that due to absence of Mode I crack in 45/45 laminated crushed box during quasi-static crushing tests, G_{IC} for this lay-up was not considered in Fig. 12. The summary of the results are presented in Table 3. Choosing a suitable fibre orientation at the interface plane is one of the main factors for improving the energy absorption of composite crush boxes in progressive failure.

The ratio between initial maximum collapse force and mean force is known as the crush force efficiency (CFE) and the higher the value of this parameter, the better energy absorption capability. The experimental crush force efficiency (CFE) of all composite crush boxes was obtained and the results of CFE versus interlaminar fracture toughness for various lay-ups are shown in Fig. 12b. It can be seen the CFE increases as the total interlaminar fracture toughness in Mode-I and Mode-II increases. The $[0]_4$ lay-up has the highest CFE. This is due to its lower initial maximum collapse force compared with other fibre orientations. This situation is more suitable for crashworthiness design cases which need to absorb the energy with a lower initial collapse force but not necessarily with the highest energy absorption capability [29].

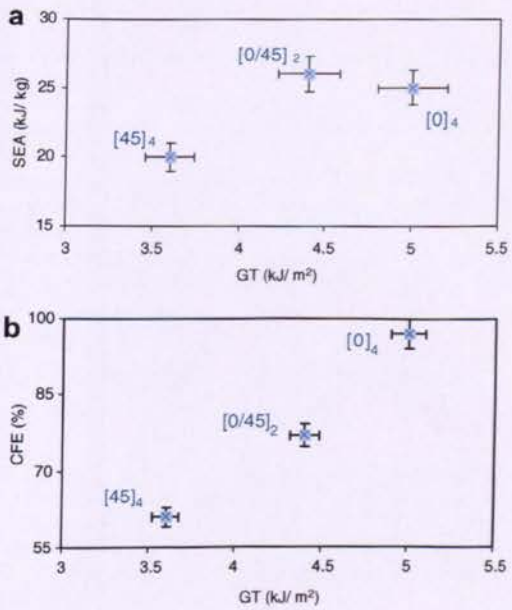

Fig. 12. (a) Variation of specific energy absorption (SEA) and (b) crush force efficiency (CFE) versus summation of interlaminar fracture toughness in Mode-I and Mode-II, i.e., $G_T = G_{IC} + 2G_{IIC}$ for boxes with $[0/45]_2$ and $[0]_4$ lay-ups and $G_T = 3G_{IIC}$ for boxes with $[45]_4$ lay-up.

4. Analytical solution

The CFRP composite boxes showed combination of progressive crushing failure of lamina bending/brittle fracture and local buckling/transverse shearing modes. Other analytical solutions were proposed for the prediction of static and dynamic mean force of composite tubular specimens in axial crushing [2,4]. In the following two analytical models based on energy balance approach will be introduced to obtain the mean crushing force, F_m, in axial crushing of square composite box.

The external work of crushing platen is dissipated by mechanisms of friction, bending, fracture and shear deformation. The idealised crush zone for our analytical model is shown in Fig. 13.

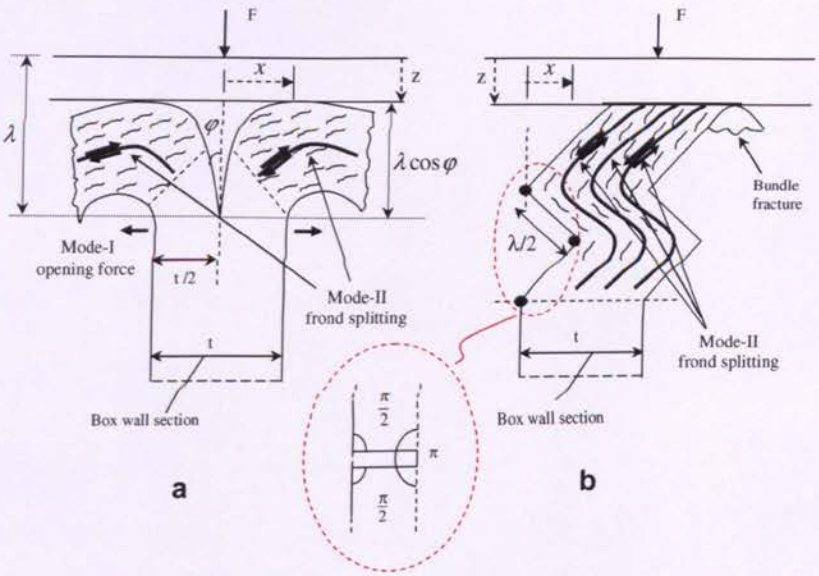

Fig. 13. Ideal crush zone: (a) Lamina bending/brittle fracture crushing mode and (b) local buckling/transverse shearing crushing mode.

The applied external work by force F during the crush distance z is

$$U_e = F \cdot z \tag{9}$$

where $z = \lambda - \lambda\cos\varphi$ is the crush distance as shown in Fig. 13 and λ is the crush length of a single stroke. The maximum work done by external force happens when $\phi = \pi/2$, $z = \lambda$.

The energy dissipated by friction between crushing platen and the debris inside the internal and external fronds in *lamina bending/brittle fracture* crushing mode can be obtained from

$$U_f = 2\left(\mu \cdot \frac{F}{2} \cdot x\right) = \mu \cdot F \cdot x \tag{10}$$

where $x = \lambda\sin\varphi$. The experimentally measured coefficient of friction is $\mu = 0.41$.

The energy dissipated by frond bending was calculated by assuming that the whole cross-section of the frond will reach to the flexural bending stiffness, σ_b. The bending moment per unit width of internal and external fronds is $M = 2\left[2\int_0^{\frac{t}{2}}\sigma_b y dy\right] = \frac{\sigma_b t^2}{8}$.

The flexural strengths, σ_b, for each lay-ups of CFRP were measured from 3PB experiments and the results are listed in Table 1. The energy dissipated in bending for combination of *lamina bending/brittle fracture* crushing mode at stationary hinge lines is

$$U_b = \int_0^{\frac{\pi}{2}} \frac{\sigma_b (4b) t^2 d\varphi}{8} \tag{11}$$

Hence, the dissipated energy due to bending becomes

$$U_b = \frac{\pi b t^2 \sigma_b}{4} \tag{12}$$

The energy dissipated by interlaminar crack propagation in Mode-I and Mode-II is calculated from interlaminar fracture energies. In lamina bending/brittle fracture mode there is one interwall Mode-I crack at the centre of each side wall of the box and one Mode-II cracks in each internal and external fronds as shown in Fig. 10. Therefore,

$$U_d = 4b\lambda(G_{IC} + 2G_{IIC}) \tag{13}$$

The Mode-I and Mode-II interlaminar fracture toughness were measured experimentally by DCB and 3ENF tests as discussed earlier.

Dissipated energy by axial splitting at the four corners of the box for *lamina bending/transverse shearing* crushing mode is calculated based on the stress intensity factor,

$$G = \frac{K^2}{E_z} \tag{14}$$

where K is the stress intensity factor given by

$$K = Y\sigma\sqrt{\pi\lambda} \tag{15}$$

At fibre splitting we assume $\sigma = \sigma_u$. The crack assumed to propagate similar to a crack growth in a single edge notched (SEN) plate where $Y = 1.12$. Therefore, the dissipated energy in axial splitting for a fracture area of $A = 4t\lambda$ is

$$U_c = \frac{5\pi t\lambda^2\sigma_u^2}{E_z} \tag{16}$$

where E_z is Young's modulus in axial direction of the crush box.

The energy dissipated in shear deformation of matrix during steady-state progressive crushing was estimated from

$$U_s = \frac{1}{2}\int_V \tau\gamma dV = \frac{1}{2}\int_V \frac{\tau^2}{G_{12}} dV \tag{17}$$

By assuming during the crushing process the shear stress will reach to its maximum shear strength value of the laminate, $\tau = \tau_s$, the energy dissipated in shear deformation of laminate is

$$U_s = \frac{2bt\lambda\tau_s^2}{G_{12}} \tag{18}$$

Dissipated energy due to bundle fracture was obtained by replacing the crush distance, λ with the width of box, $b/2$.

$$U_{bf} = \frac{1.25\pi t b^2 \sigma_u^2}{E_y} \tag{19}$$

The fracture area of $A = 8\left(\frac{t}{2}\right)\left(\frac{b}{2}\right) = 2bt$ was assumed for eight internal and external fronds with crack growth assumed to be half the width of the side wall as observed in the experiments and E_y is Young's modulus in transverse direction of the crush box.

The energy balance for the crushing process during a single stroke crush distance is

$$U_e - U_f = U_b + U_d + U_c + U_s + U_{bf} \quad (20)$$

Substituting from Eqs. (9), (10), (12), (13), (16), (18) and (19) in Eq. (20), the energy dissipated by *lamina bending/brittle fracture* crushing mode, $U_{LB/BF}$, is

$$U_{LB/BF} = F(1-\mu)\lambda = \frac{\pi bt^2\sigma_b}{4} + 4b\lambda(G_{IC} + 2G_{IIC}) + \frac{5\pi t\lambda^2\sigma_u^2}{E_z} + \frac{2bt\lambda\tau_s^2}{G_{12}} + \frac{1.25\pi tb^2\sigma_u^2}{E_y} \quad (21)$$

Therefore, the mean oscillatory crushing force in a stable progressive crush is

$$F = \frac{1}{(1-\mu)}\left[\frac{\pi bt^2\sigma_b}{4\lambda} + 4b(G_{IC} + 2G_{IIC}) + \frac{5\pi t\lambda\sigma_u^2}{E_z} + \frac{2bt\tau_s^2}{G_{12}} + \frac{1.25\pi tb^2\sigma_u^2}{E_y\lambda}\right] \quad (22)$$

A single stroke crush distance for lamina bending case can be found from Eq. (22) by setting $\partial F/\partial\lambda = 0$

$$\lambda = \sqrt{\frac{bt\sigma_b E_y + 5b^2\sigma_u^2}{20\sigma_u^2}\frac{E_z}{E_y}} \quad (23)$$

The mean force during the progressive crushing can be found by calculating λ from Eq. (23) and substituting in Eq. (22).

According to experimental results for *local buckling/transverse shearing* crushing mode, interwall Mode-I opening crack was not observed in the crushed box. In this case the energy dissipated by friction between crushing platen and fronds when the hinge folded completely can be obtained from (see Fig. 13),

$$U_f = \mu \cdot F \cdot x = \mu \cdot F \cdot \lambda \quad (24)$$

The energy dissipated in bending for *local buckling/transverse shearing* mode happens in three hinge lines can be summed

$$U_{bu} = (4b)\int_0^{\varphi} M\,d\varphi = (4b)\sum_{i=1}^{3} M\varphi \quad (25)$$

In this situation, the rotational angles at the hinge lines are assumed to be $\pi/2$, π and $\pi/2$, respectively (see Fig. 13). For this crushing mode the dissipated energy in local buckling is

$$U_{bu} = \frac{\pi bt^2\sigma_b}{2} \quad (26)$$

In this mode during crushing, box side walls were locally buckled and three Mode-II interlaminar fracture cracks were observed in *local buckling/transverse shearing* in bundles (see Fig. 9c).

The dissipated energy in delamination is calculated from

$$U_d = 4b\lambda(3G_{IIC}) = 12b\lambda G_{IIC} \quad (27)$$

Dissipated energy due to bundle fracture can be obtained from Eq. (19).

Dissipated energy due to axial splitting and shear deformation of matrix remains as before and can be calculated from Eqs. (16) and (18). Assuming the maximum work done, $U_e = F\lambda$, the total energy balance can be written as

$$U_e - U_f = U_{bu} + U_d + U_c + U_s + U_{bf} \quad (28)$$

Finally, the dissipated energy by *local buckling/transverse shearing*, $W_{BU/TS}$ crushing mode can be obtained by substituting from Eqs. (16), (18), (19), (26) and (27) in Eq. (28) as

$$U_{BU/TS} = F\lambda(1-\mu) = \frac{\pi bt^2\sigma_b}{2} + 12b\lambda G_{IIC} + \frac{5\pi t\lambda^2\sigma_u^2}{E_z} + \frac{2bt\lambda\tau_s^2}{G_{12}} + \frac{1.25\pi tb^2\sigma_u^2}{E_y} \quad (29)$$

The crush length of a single stroke due to lamina bending can be found from Eq. (29) by setting $\partial F/\partial\lambda = 0$

$$\lambda = \sqrt{\frac{bt\sigma_b E_y + 2.5b^2\sigma_u^2}{10\sigma_u^2}\frac{E_z}{E_y}} \quad (30)$$

The results of mean force from experimental and theoretical solutions are summarised in Table 4. The results are in good agreement and the discrepancy between experimental and theoretical results is less than 8%.

Table 4
Comparison of experimental, FEA and analytical mean force results of each laminate design

Laminate lay-up	Cushing failure mode	F_m(Exp.), kN	F_m (FEA), kN	F_m (Anal.), kN
$[0]_4$	LB/BF	65	60	59.4
$[0/45]_2$	LB/BF	67	65	59.3
$[45]_4$	BU/TS	52	55	58.5

LB/BF, lamina bending/brittle fracture and BU/TS, local buckling/transverse shearing.

5. Finite element studies

Morozov and Thomson [30] simulated the crush response of a glass fabric reinforced thin-walled laminated structural component using the finite element software PAM-CRASH. They treated the orthotropic ply as a quasi-homogeneous layer that includes progressive damage to model material fracture. Han et al. [31] were carried out a comprehensive numerical investigation to evaluate the response and energy absorbing capacity of hybrid composite tubes made of unidirectional pultruded tube over wrapped with ±45 braided fibre-reinforced plastic under quasi-static compression and axial dynamic impact loadings. They looked at the influence of the tube's length, thickness and type of braid, as well as the loading conditions on the crushing behavior of the tubes. They observed although the pultruded tube, which had the highest stiffness among the tubes considered, produced the highest magnitude of energy absorption capacity, it exhibited a non-symmetric failure mode followed by a longitudinal splitting.

In this work the CFRP composite box was modelled with various lay-ups using finite element software ANSYS/LSDYNA [32]. The size of outer cross-section of the composite box was 80 × 80 mm with a thickness of 3 mm. The CFRP composite box model was based on Belytschko–Lin–Tsay quadrilateral shell elements. All surfaces of the model were meshed using quadratic shell element and the size of an element was 2.5 × 2.5 mm. The striker was modelled as a rigid block using solid element. The composite layers were modelled by defining the integration points which are placed equally through the thickness in each layer. Material model 54 of LS-DYNA was selected to model the damage of CFRP composite box. In ANSYS this material model follows the Chang-Chang [33] failure criterion which is the modification of the Hashin's failure criterion for assessing lamina failure. The detail of failure model can be found in [8].

To simulate the quasi-static condition, the velocity of 1 m/s was applied to the rigid striker. However, the real crushing speed was too slow for the numerical simulation. The explicit time integration method is only conditionally stable, and therefore by using real crushing speed, very small time increment was required. For satisfying quasi-static condition not only the total kinetic energy has to be very small compared to the total internal energy over the period of the crushing process but also the crushing force–displacement response must be independent from the applied velocity [34]. For

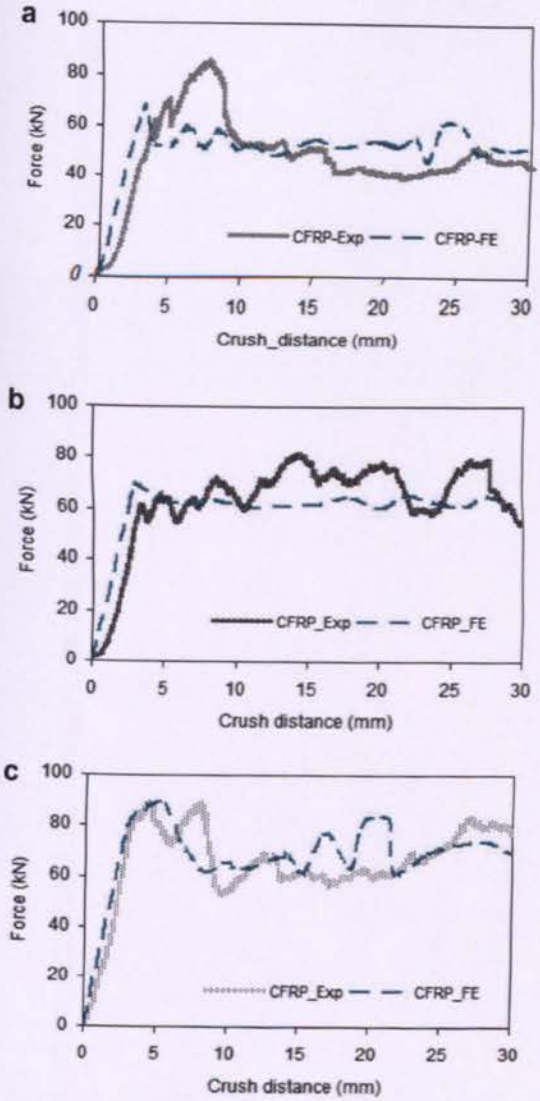

Fig. 14. Comparison of experimental and FE force–crush distance results for twill/weave CFRP composite box with (a) $[45]_4$, (b) $[0]_4$ and (c) $[0/45]_2$ lay-ups.

the aim of computational efficiency, the density of rigid striker and composite box were scaled-up by a factor of 1000. By using this factor, the quasi-static condition was satisfied during the crushing analysis.

In Fig. 14 the force–crush distance of all lay-ups which were extracted from FEA model is compared with the experimental results. The difference in mean forces and energy absorption between the FEA models and experiments are less than 5% in all models (see Table 4).

6. Conclusion

In this work, the effect of fibre orientation on the interlaminar fracture toughness in Mode-I and Mode-II, and specific energy absorption of carbon/epoxy twill-weave composite box was studied. It was shown that the laminate design at interface fracture plane affects the interlaminar fracture toughness of woven CFRP composite materials. The combination of lamina bending/brittle fracture crushing mode was observed for the lay-ups of $[0]_4$ and $[0/45]_2$. In this case a combination of Mode-I and Mode-II affect the energy absorption of woven CFRP composite box. In laminate design of $[45]_4$, only Mode-II crack propagation was observed in the side walls which contribute to the creation of a combination of local buckling/transverse shearing crushing mode.

The specific energy absorption in axial crushing of composite box depends on the interlaminar fracture toughness between laminates. The creation of Mode-I central interwall crack caused to increase the contact area between the platen and the box and consequently the energy dissipated by the friction has been increased.

It was shown that the total interlaminar fracture toughness in Mode-I and Mode-II of 0/0 interface plane is higher than the equivalent values of 0/45 and 45/45 interface planes, but 0/45 box has the highest specific energy absorption (SEA). This shows that the effect of other mechanisms such as friction and bending will increase as the total fracture energy increases beyond a certain limit. However, the crush force efficiency (CFE) increased as the total interlaminar fracture toughness in Mode-I and Mode-II increased. The $[0]_4$ lay-up has the highest CFE. This is due to its lower initial maximum collapse force compared with other fibre orientations.

References

[1] Farley GL, Jones R. Crushing characteristics of continuous fibre reinforced composite tubes. J Compos Mater 1992;26:37–50.
[2] Mamalis AG, Manolakos DE, Demosthenous GA, Ioannidis MB. The static and dynamic collapse of fibreglass composite automotive frame rails. Compos Struct 1996;34:77–90.
[3] Savona SC, Hogg PJ. Effect of fracture toughness properties on the crushing of flat composite plates. Compos Sci Technol 2006;66:2317–28.
[4] Solaimurugan S, Velmurugan R. Influence of fibre orientation and stacking sequence on petalling of glass/polyester composite cylindrical shell under axial compression. Int J Solid Struct 2007;44:6999–7020.
[5] Warrior NA, Turner TA, Robitaille F, Rudd CD. The effect of interlaminar toughening strategies on the energy absorption of composite tubes. Composites: Part A 2004;35:431–7.
[6] Jacob GC, Fellers JF, Simunovic S, Starbuck M. Energy absorption in polymer composites for automotive crashworthiness. J Compos Mater 2002;36:813–50.
[7] Farley GL. Energy absorption in composite materials for crashworthy structures. In: Matthews FL, Buskell NCR, Hodgkingson JM, Morton J, editors. Proceedings of the ICCM, vol. 6. London: Elsevier Science Publishers Limited; 1987. p. 3.57–66.
[8] Ghasemnejad H, Blackman BRK, Hadavinia H, Sudall B. Experimental studies on fracture characterisation and energy absorption of GFRP composite box structure. Compos Struct 2009;88(2):253–61.
[9] Jiménez MA, Miravete A, Larrodé E, Revuelta D. Effect of trigger geometry on energy absorption in composite profiles. Compos Struct 2000;48(1–3):107–11.
[10] Elgalai AM, Mahdi E, Hamouda AMS, Sahari BS. Crushing response of composite corrugated tubes to quasi-static axial loading. Compos Struct 2004;66(1–4):665–71.
[11] Alkateb M, Mahdi E, Hamouda AMS, Hamdan MM. On the energy absorption capability of axially crushed composite elliptical cones. Compos Struct 2004;66(1–4):495–501.
[12] Melo JDD, Silva ALS, Villena JEN. The effect of processing conditions on the energy absorption capability of composite tubes. Compos Struct 2008;82(4):622–8.
[13] Mahdi E, Kadi H. Crushing behavior of laterally compressed composite elliptical tubes: experiments and predictions using artificial neural networks. Compos Struct 2008;83(4):399–412.
[14] Zarei H, Kröger M, Albertsen H. An experimental and numerical crashworthiness investigation of thermoplastic composite crash boxes. Compos Struct 2008;85(3):245–57.
[15] Lee DG, Lim TS, Cheon SS. Impact energy absorption characteristics of composite structures. Compos Struct 2000;50(4):381–90.
[16] BS EN ISO 2747. Glass Fibre reinforced plastics-tensile test. British Standard Institute, London; 1998.
[17] BS EN ISO 14129. Fibre reinforced plastics composite-determination of the in-plane shear stress/shear strain response, including the in-plane shear modulus and strength by the ±45 tension test method. British Standard Institute, London; 1998.
[18] ASTM D 3171-99. Standard test method for constituent content of composite materials. Annual book of ASTM standards, West Conshohocken, PA; 2002.
[19] BS EN ISO 15024:2001. Fibre-reinforced plastic composites. Determination of mode I interlaminar fracture toughness, G_{IC}, for unidirectional reinforced materials. BSI; 2002.

[20] Alif N, Carlsson LA, Boogh L. The effect of weave pattern and crack propagation direction on mode I delamination resistance of woven glass and carbon composites. Composites Part B 1998;29(B):603–11.
[21] Williams JG. End corrections for orthotropic DCB specimens. Compos Sci Technol 1989;35:367–76.
[22] Davies P, editor. Protocols for interlaminar fracture testing of composites. In: Proceedings of European Structural Integrity Society (ESIS) Polymers and Composites Task Group; 1993.
[23] Choi NS, Kinloch AJ, Willams JG. Delamination fracture of multidirectional carbon–fiber/epoxy composites under mode I, mode II and mixed mode I/II loading. J Compos Mater 1999;33(1):73–100.
[24] Pereira AB, de Morais AB. Mode I interlaminar fracture of carbon/epoxy multidirectional laminates. Compos Sci Technol 2004;64(13–14):2261–70.
[25] Russel AJ, Street KN. Factor affecting the interlaminar fracture energy of graphite/epoxy laminates. In: Hayashi T, Kawata K, Umekawa S, editors. Progress in Science and Engineering of Composites. ICCM-IV. Tokyo: ASM International; 1982. p. 279–86.
[26] Davies P, Sims GD, Blackman BRK, Brunner AJ. Comparison of test configurations for determination of mode II interlaminar fracture toughness: results from international collaborative test programme. Plastic Rubber Comp 1999;28:432–7.
[27] Moore DR, Pavan A, Williams JG, editors. Fracture mechanics testing methods for polymers, adhesives and composites. ESIS Publication 28. Elsevier Science Ltd.; 2001.
[28] Wang Y, Williams JG. Corrections for mode II fracture toughness specimens of composite materials. Comp Sci Technol 1992;43:251–6.
[29] Ghasemnejad H, Hadavinia H, Marchant DR, Aboutorabi A. Energy absorption of thin-walled corrugated crash box in axial crushing. J Struct Durability Health Monitor 2008;4(1):29–46.
[30] Morozov EV, Thomson VA. Simulating the progressive crushing of fabric reinforced composite structures. Compos Struct 2006;76(1–2):130–7.
[31] Han H, Taheri F, Pegg N, Lu Y. A numerical study on the axial crushing response of hybrid pultruded and ±45° braided tubes. Compos Struct 2007;80(2):253–64.
[32] LS-DYNA user's manual (non-linear dynamic analysis of structures in three dimensions). Livermore Software Technology Corporation, Livermore, USA; 1997.
[33] Chang FK, Chang KY. A progressive damage model for laminated composites containing stress concentrations. J Compos Mater 1987;21:809–33.
[34] Santosa SP, Wierzbicki T, Hanssen AG, Langseth M. Experimental and numerical studies of foam-filled sections. Int J Impact Eng 2000;24:509–34.

Materials and Design xxx (2009) xxx–xxx

Contents lists available at ScienceDirect

Materials and Design

journal homepage: www.elsevier.com/locate/matdes

Effect of delamination failure in crashworthiness analysis of hybrid composite box structures

H. Ghasemnejad *, H. Hadavinia, A. Aboutorabi

Faculty of Engineering, Kingston University London, SW15 3DW, UK

ARTICLE INFO

Article history:
Received 9 July 2009
Accepted 22 September 2009
Available online xxxx

Keywords:
Delamination
Crashworthiness
Hybrid
Composite
Finite element modelling

ABSTRACT

In the present paper the effects of delamination failure of hybrid composite box structures on their crashworthy behaviour will be studied and also their performance will be compared with non-hybrid ones. The combination of twill-weave and unidirectional CFRP composite materials are used to laminate the composite boxes. Delamination study in Mode-I and Mode-II with the same lay-ups was carried out to investigate the effect of delamination crack growth on energy absorption of hybrid composite box structures. The end-loaded split (ELS) and double-cantilever beam (DCB) standard test methods were chosen for delamination studies. In all hybrid composite boxes the lamina bending crushing mode was observed. Regarding the delamination study of hybrid DCB and ELS the variation of the specific energy absorption (SEA) versus summation of G_{IC} and G_{IIC} were plotted to combine the effect of Mode-I and Mode-II interlaminar fracture toughness on the SEA. From this relationship it was found the hybrid laminate designs which showed higher fracture toughness in Mode-I and Mode-II delamination tests, will absorb more energy as a hybrid composite box in crushing process. The crushing process of hybrid composite boxes was also simulated by finite element software LS-DYNA and the results were verified with the relevant experimental result.

1. Introduction

Crashworthiness of fibre-reinforced polymer (FRP) composite materials and structures is classified on how they deform, fail and absorb the crashing energy in a controllable behaviour. The energy absorbing capabilities of FRP composite structures have been investigated in literature by studying the effect of fibre type, matrix type, fibre architecture, specimen geometry, process conditions, fibre volume fraction and testing speed under axial loading [1]. In axial crushing of composite box the crushing energy is absorbed by four main mechanism of crushing modes and their combinations during progressive failure. These crushing modes are transverse shearing (fragmentation), lamina bending, brittle fracturing and local buckling [2].

Fracture mechanism is the most important factors which affects the energy absorbing capability of the structure. In previous works [3–7] the effect of interlaminar fracture toughness on the energy absorption of composite structures in axial crushing have been studied. Ghasemnejad et al. [3] studied the effect of Mode-I interlaminar fracture toughness on the energy absorption of GFRP composite box. They showed that during progressive collapse, frond bending following the growth of a main central interwall crack due to delamination in the side wall causes a significant amount of energy absorption. The main central interwall cracks are Mode-I interlaminar crack propagation. They also concluded that using suitable laminate design for composite box improves interlaminar fracture toughness and consequently energy absorption capability. The variation of specific energy absorption (SEA) with interlaminar fracture toughness is non-linear for different lay-ups.

Hadavinia and Ghasemnejad [4] studied the effect of Mode-I and Mode-II interlaminar fracture toughness on the energy absorption of laminated CFRP composite box. According to their results in combination of lamina bending/brittle fracture crushing mode, creation of crack propagation in Mode-I and Mode-II causes absorption of a higher crushing energy relative to combination of local buckling/transverse shearing crushing mode which has only Mode-II interlaminar crack propagation. More recently Ghasemnejad and Hadavinia [5] have investigated the off-axis crashworthy behaviour of Woven GFRP composite box structures. They found two fracture mechanisms of bundle fracture and delamination crack propagation in Mode-II for all composite boxes at various off-axis loading. Due to crack propagation in mixed-Mode I/II and more friction and bending resistance at one side of composite box which firstly contacted the crushing platen, the amount of SEA at off-axis loading of 10° was the maximum in comparison with other off-axis crushing loadings.

Savona and Hogg [6] considered the relation between specific sustained crushing stress (SSCS) of GFRP composite plates with their Mode-I and Mode-II fracture toughness properties. According

* Corresponding author. Tel.: +44 20 8547 4738; fax: +44 20 8547 7992.
E-mail address: h.ghasemnejad@kingston.ac.uk (H. Ghasemnejad).

0261-3069/$ - see front matter © 2009 Published by Elsevier Ltd.
doi:10.1016/j.matdes.2009.09.043

Nomenclature

a	crack length (mm)	X_t	longitudinal tensile strength (MPa)
b	side of box (mm)	X_c	longitudinal compressive strength (MPa)
C	compliance (mm/N)	Y_t	transverse tensile strength (MPa)
E	Young's modulus (GPa)	Y_c	transverse compressive strength (MPa)
ELS	end-loaded split	σ_1	longitudinal stress (MPa)
F	force (kN)	σ_2	transverse stress (MPa)
F_m	mean force (kN)	σ_{12}	transverse shear stress (MPa)
G_{12}	shear modulus (GPa)	σ_u	ultimate tensile stress (MPa)
G_{IC}	mode-I interlaminar fracture toughness (J/m^2)	σ_b	flexural strength (MPa)
G_{IIC}	mode-II interlaminar fracture toughness (J/m^2)	τ_s	shear strength (MPa)
SEA	specific energy absorption (kJ/kg)	β	weight factor
t	thickness (mm)	ν	Poisson's ratio
V_f	fibre volume fraction	Δ_{clamp}	end-clamp correction factor

to their results, materials which have a lower Mode-I and Mode-II interlaminar fracture toughness, absorb a lower crushing energy. They also showed that the G_{IC} and G_{IIC} of initiation are more influential than the G_{IC} and G_{IIC} of propagation on the energy absorption mechanism.

Warrior et al. [7] studied the influence of toughened resins, thermoplastic resin additives, through-thickness stitching and thermoplastic interleaving on the interlaminar fracture toughness (G_{IC}) and the SEA for continuous filament random mat (CoFRM) and 0/90 non-crimp fabric (NCF) E-glass reinforced polyester composite tubes. They reported that all above mentioned factors increase G_{IC}, but only toughened resin and through-thickness stitching can increase SEA.

Most of these works have studied the effect of interlaminar fracture toughness on the crushing process of non-hybrid composite tubes. Several works have investigated the effects of hybridisation of composite materials on the energy absorbing capabilities of composite crash elements such as box. Mahdi et al. [8] investigated the crushing behaviour and energy absorption efficiency of hybrid and non-hybrid natural fibre composite solid cones. They found that for non-hybrid specimens, longitudinal cracks initiated at the cone small end turns out to be the dominating failure mechanism. They also showed that hybridisation of the coir fibre/polyester with oil palm fibre/polyester alters the mode of failure to non-catastrophic.

Han et al. [9] evaluated the response and energy absorbing capacity of hybrid composite tubes made of unidirectional pultruded tube over wrapped with ±45° braided fibre-reinforced plastic (FRP). They found that the pultruded tube with the highest stiffness among the tubes considered, produced the highest magnitude of energy absorption capacity. Hufenbach et al. [10] investigated the strain rate dependent material properties and failure behaviour of composites with hybrid multi-layered flat bed weft knitted fibre reinforcements consisting of different fibre combinations such as glass–glass, glass–aramid and glass–polyethylene. They demonstrated that the material phenomena of textile reinforced composites under highly dynamic loading as well as the determination of time dependent deformation and fracture characteristic affected by different knitting materials.

In this paper the effects of delamination failure of hybrid composite box structures in their crashworthy behaviour are studied and their performance are compared with non-hybrid ones. The combination of twill-weave and unidirectional CFRP composite materials are used to laminate the composite boxes. Delamination study in Mode-I and Mode-II with the same lay-ups was carried out to investigate the effect of delamination crack growth on energy absorption of hybrid composite box structures. The end-loaded split (ELS) and double-cantilever beam (DCB) standard test methods were chosen for delamination studies. It is shown that hybrid laminate design can significantly increase the interlaminar fracture toughness and consequently energy absorbing capability of composite material structures. The crushing process of hybrid composite box was of laminate design of $[T0/U0]_7$ also simulated by finite element software

Table 1
Material properties of the woven (a) Unidirectional-CFRP and (b) Woven CFRP composite materials.

E_1 (GPa)	E_2 (GPa)	G_{12} (GPa)	υ_{12}	$\sigma_u 0°$ (MPa)	$\sigma_u 90°$ (MPa)	τ_s (MPa)	V_f (%)
(a)							
138 ± 12	10.5 ± 1	6.3 ± 0.4	0.1	330 ± 14	32 ± 4	147 ± 14	42
(b)							
61 ± 5	58 ± 6	3.4 ± 0.3	0.2	634 ± 15	560 ± 21	94 ± 11	55

Table 2
Interlaminar fracture toughness obtained from DCB tests for various interface fibre orientations.

Laminate lay-up	Fracture plane interface	G_{IC} (MCC) (J/m^2)	G_{IC} (MBT) (J/m^2)	$G_{IProp.}$ (MCC) (J/m^2)	$G_{IProp.}$ (MBT) (J/m^2)
$[T0/U0]_7$	T0//U0	480 ± 20	450 ± 20	400 ± 20	400 ± 20
$[T0/U90]_7$	T0//U90	510 ± 20	530 ± 20	420 ± 20	420 ± 20
$[T90/U0]_7$	T90//U0	500 ± 20	480 ± 20	430 ± 30	430 ± 20
$[T90/U90]_7$	T90//U90	440 ± 20	430 ± 10	400 ± 20	400 ± 10
$[T90]_{10}$	T90//T90	620 ± 20	610 ± 20	600 ± 20	600 ± 20
$[U90]_{16}$	U90//U90	350 ± 20	340 ± 10	400 ± 20	400 ± 10

MCC: Modified Compliance Calibration Method and MBT: Modified Beam Theory.

Please cite this article in press as: Ghasemnejad H et al. Effect of delamination failure in crashworthiness analysis of hybrid composite box structures. J Mater Design (2009), doi:10.1016/j.matdes.2009.09.043

LS-DYNA and the FE result is verified by relevant experimental result.

2. Experimental studies

2.1. Determination of Mode-I interlaminar fracture toughness

The mechanical characteristics of carbon/epoxy twill-weave and unidirectional fabrics were obtained in accordance with the relevant standards [11–15]. These tests were tensile, shear, fibre volume fraction, coefficient of friction (see Table 1), double-cantilever beam (DCB) (Table 2 and Fig. 3), end-loaded split (ELS) (Table 4 and Fig. 6) and quasi-static crush box.

All specimens were manufactured from unidirectional and twill/weave fabric CFRP materials of density 1.4 g/cm^3 and 1.8 g/cm^3 with epoxy resin. For twill/weave composite it was observed that crack propagation along the weft yarns is associated with more resistance than propagation along the warp direction. For

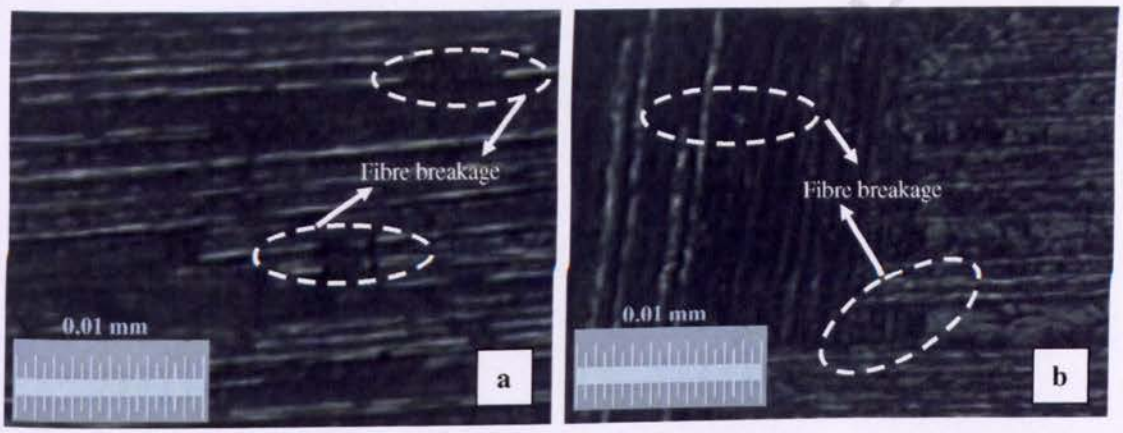

Fig. 1. Optical micrograph from fracture surface of Hybrid DCB specimens showing fibre breakage of intra-laminar T0//U0 interface, (a) fracture surface of T0 and (b) fracture surface of U0.

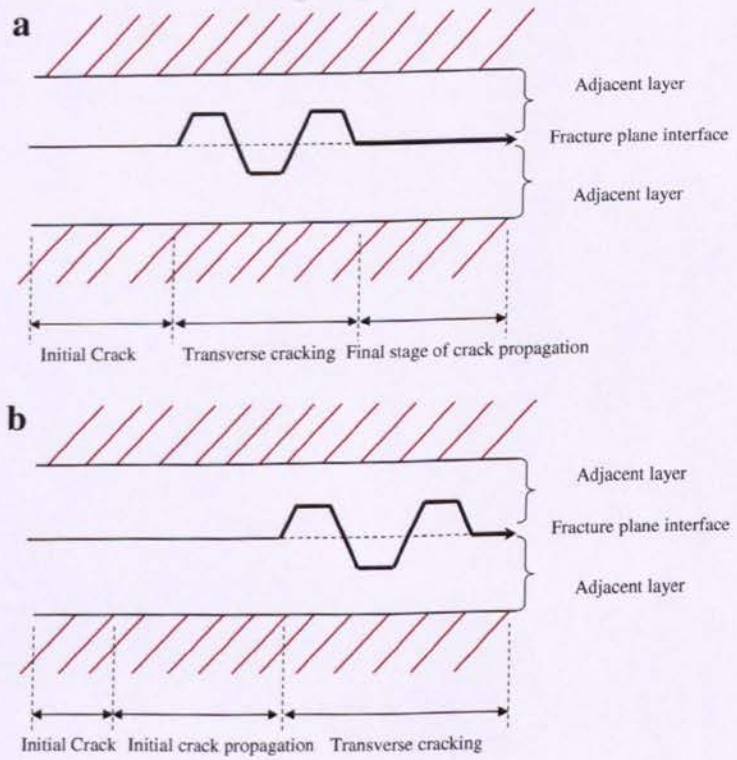

Fig. 2. Typical crack propagation in Mode-I delamination at fracture plane interface.

Please cite this article in press as: Ghasemnejad H et al. Effect of delamination failure in crashworthiness analysis of hybrid composite box structures. J Mater Design (2009), doi:10.1016/j.matdes.2009.09.043

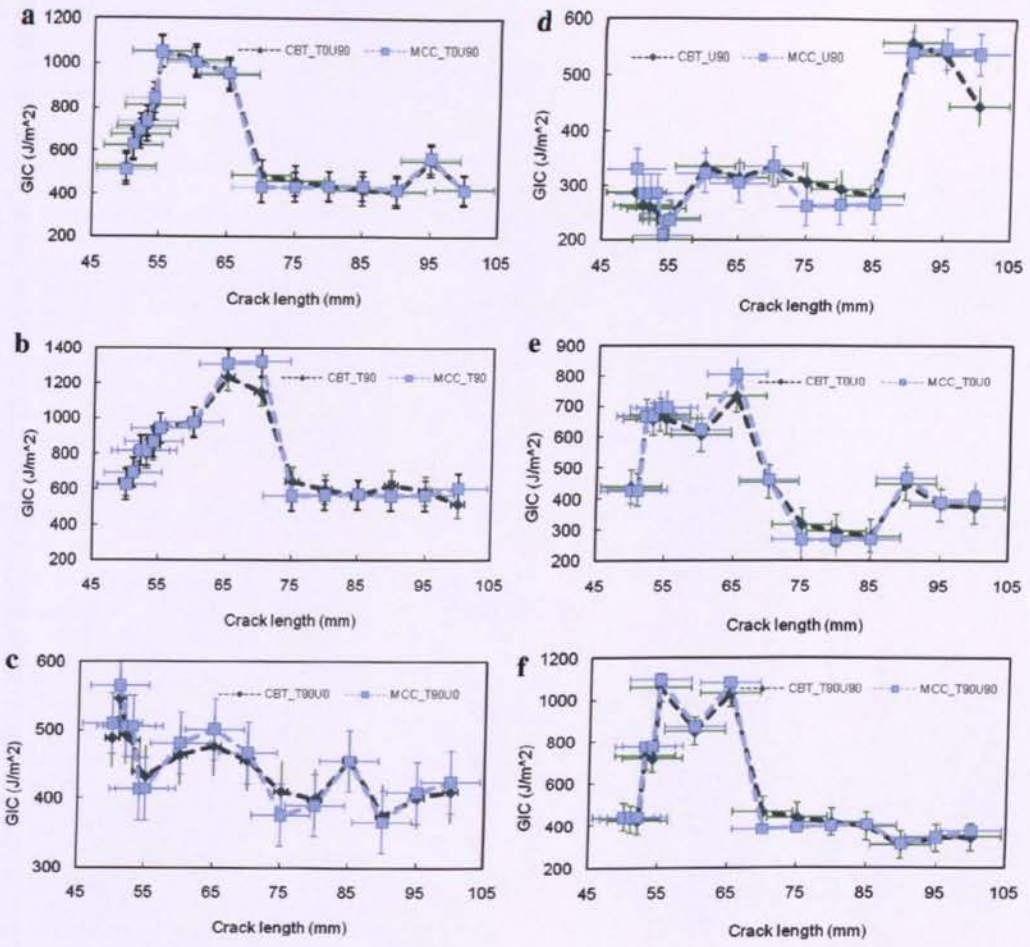

Fig. 3. Resistance curve (*R*-curve) in DCB specimens with various fracture plane interfaces using MBT and MCC methods.

Table 3
Various lay-ups of hybrid composite box structures.

Hybrid composite box lay-ups
$[T0/U0]_7$
$[T0/U90]_7$
$[T90/U0]_7$
$[T90/U90]_7$
[a] $[T90]_{10}$
[a] $[U90]_{16}$

T = Twill-weave and *U* = Unidirectional CFRP materials.
[a] Non-hybrid CFRP composite box.

determining the Mode-I interlaminar fracture toughness G_{IC}, BS ISO 15024 standard [14] was followed together with the corrections developed elsewhere to take into account for the end-block, DCB arm bending and root rotation [16–19]. The recommended specimen size is at least 125 mm long and 20–25 mm wide with an initial crack length (i.e. length of the insert from the load line) of 50 mm. Loading was carried out at a constant crosshead displacement rate of 2 mm/min. The position of the crack tip was monitored through the travelling microscope as the crack advanced. When the crack first visibly propagated, the displacement of the crosshead was recorded. As the crack propagation past the subsequent marked lines, the crack length and crosshead displacement were recorded. For each test configuration four specimens were tested. For all interface planes of DCB specimens the development

Table 4
Interlaminar fracture toughness obtained from ELS tests for various interface fibre orientations.

Laminate lay-up	Fracture plane interface	G_{IIC} (ECM) (J/m^2)	G_{IIC} (CBT) (J/m^2)	$G_{IIProp.}$ (ECM) (J/m^2)	$G_{IIProp.}$ (CBT) (J/m^2)
$[T0/U0]_7$	T0//U0	800 ± 30	1200 ± 40	1300 ± 30	1700 ± 40
$[T0/U90]_7$	T0//U90	900 ± 30	1000 ± 40	2500 ± 30	2600 ± 40
$[T90/U0]_7$	T90//U0	1200 ± 40	1300 ± 30	2500 ± 40	2700 ± 30
$[T90/U90]_7$	T90//U90	900 ± 30	1500 ± 40	2000 ± 20	3000 ± 40
$[T90]_{10}$	T90//T90	1100 ± 30	1300 ± 40	3200 ± 30	3300 ± 40
$[U90]_{12}$	U90//U90	800 ± 30	1000 ± 30	1200 ± 30	1300 ± 30

ECM: Experimental Calibration Method and CBT: Corrected Beam Theory.

Please cite this article in press as: Ghasemnejad H et al. Effect of delamination failure in crashworthiness analysis of hybrid composite box structures. J Mater Design (2009), doi:10.1016/j.matdes.2009.09.043

of transverse cracking also caused the force to show several continuous increases after initial crack propagation resulting in a rising *R*-curve. Various reasons such as intra-laminar delamination, mixed mode fracture, fibre bridging, micro-cracking, residual stresses, or a combination of these effects of θ-oriented lamina at interface caused the development of transverse intra-laminar and unstable crack propagation in DCB tests (see Fig. 1). Transverse cracking for interface planes of T90//U90, T0//U0, T90//T90, T90//U0 and T0//U90 happened at the beginning of delamination growth (see Fig. 2a) while this process for interface plane of U90//U90 happened at the end of delamination crack growth (see Fig. 2b). The results of Mode-I delamination fracture toughness, G_{IIC}, using non-linearity (NL) for each interface, were presented in Fig. 3 and Table 2.

For comparison between the energy absorption of hybrid composite box and non-hybrid one, two types of composite box were made from twill-weave and unidirectional CFRP materials. The lay-ups of different hybrid composite boxes are presented in Table 3.

2.2. Determination of Mode-II interlaminar fracture toughness using ELS specimen

The Mode-II interlaminar fracture toughness, G_{IIC}, can be measured by three-point- end-notched flexure (3ENF), the end-loaded split (ELS) and the four-point-end-notched flexure (4ENF) tests [20]. Measuring the Mode-II fracture toughness from film inserts yields a higher toughness than from precracks. This is in contrast to Mode-I testing where fibre bridging causes higher fracture toughness from precracks [21]. The fabrication of hybrid twill-weave and unidirectional CFRP ELS specimens were laid-up according to the laminate design of each hybrid composite crush box. The mid-plane interface of hybrid CFRP ELS specimens were T0//U0, T0//U90, T90//U0 and T90//U90, and for non-hybrid CFRP ELS specimens were T90//T90 and U0//U0 to determine the Mode-II interlaminar fracture toughness. In twill-weave specimens the weft direction was defined as 0° direction.

The ELS specimens were made and tested according to ESIS protocol [15] with the width of 20 mm and the total length of 160 mm, while the thickness varied from 5 to 6 mm. This thickness is required to avoid large displacement, plastic deformation and intra-ply damage. A precrack length of 60 mm from the free end of specimen was inserted using a Teflon film of thickness 13 μm (see Fig. 4). The position of the crack tip was monitored through the travelling microscope as the crack advanced. Loading was carried out at a constant crosshead displacement rate of 2 mm/min. Force at each crack length was retrospectively obtained from the recorded force–displacement diagram to calculate G_{IIC} (see Figs. 5 and 6). For each test configuration four specimens were tested. Three different methods to determine crack length for the initiation values from the precrack as the distance between the force–displacement and the precrack are considered. The first non-linearity (NL) method determines the point of deviation from linearity, by sketching a straight line from the origin. The second uses the visual observation (VIS) which is the first point at which the crack is observed to move from the tip of the Teflon insert. The last is the MAX/5%, a point on the force–displacement curve at which the compliance has increased by 5% of its initial value. In this work the visual observation (VIS) was chosen to determine the initiation crack length. Due to the difficulties in defining the exact position of crack initiation, the non-linearity (NL) and the 5% offset are used to find the crack initiation. The slop of plot of the compliance versus the cube of the delamination length (a^3) is used to find the interlaminar fracture toughness using ECM.

In this work *Corrected Beam Theory* (CBT) and *Experimental Calibration Method* (ECM) were used to determine the Mode-II fracture toughness. The CBT method was calculated from Eq. (1), respectively:

$$G_{II} = \frac{9F\delta}{2B}\left[\frac{(a+\Delta_{II})^2}{3(a+\Delta_{II})^3 + (L+\Delta_{clamp})^3}\right]\cdot\frac{f}{N} \quad (1)$$

where $\Delta_{clamp} = 2\Delta_{II}$ is the end-clamp effect and f and N are the correction factors for large displacement and end-block effects [18,22].

Because of some difficulties in curve fitting in ECM some undesirable discrepancies were found between the *R*-curve obtained from two methods for interface layers of (T0//U0) and (T90//U90).

The Mode-II interlaminar fracture toughness of the interface layer of (T90//T90) and (T90//U0) CFRP composite material showed the highest values of G_{IIC} for all specimens, and for interface layers of (U0//U0) unidirectional CFRP composite material showed the lowest value. The experimental resistance curves of hybrid CFRP composite materials of G_{IIC} versus crack length are presented in Fig. 7. The results of Mode-II delamination fracture toughness, G_{IIC}, using non-linearity (NL) for each interface, were presented in Table 3. The propagation value of fracture toughness in Mode-II was also measured from obtained *R*-curve of each ELS specimen. This value for fracture interface planes of U90//U90 and T90//T90 was found as an average of *R*-curve.

2.3. Composite crush box

The crush box specimens were made of the hybrid woven and unidirectional carbon/epoxy by hand lay-up with fibre orientations in accordance to those used in DCB and ELS tests as described in the previous section. The 0° direction which coincided with the axial axis of the crush box was parallel to weft direction. Each specimen was crushed at the rate of 2 mm/min between two parallel platens for 50 mm stroke using a Universal Testing Machine with 500 kN load cell. For each test configuration three specimens were tested. The force-crush distance diagrams were recorded automatically for each test.

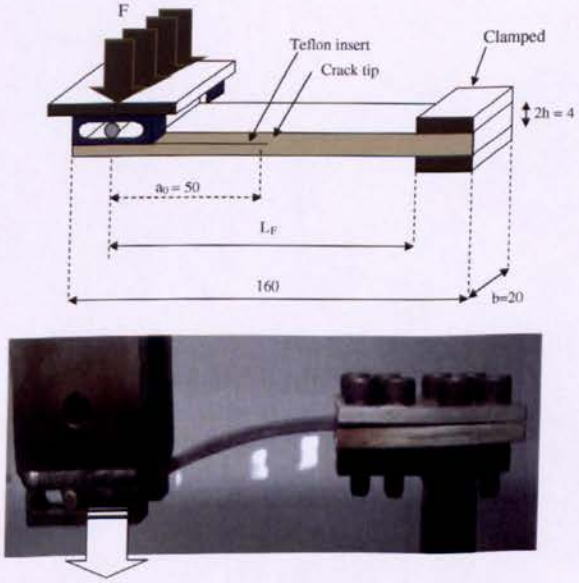

Fig. 4. ELS specimen for Mode-II delamination testing (all dimensions in mm).

Please cite this article in press as: Ghasemnejad H et al. Effect of delamination failure in crashworthiness analysis of hybrid composite box structures. J Mater Design (2009), doi:10.1016/j.matdes.2009.09.043

2.4. Progressive crushing process of hybrid composite crush box

For all hybrid composite crush boxes the lamina bending crushing mode was observed. The lamina bending mode is shaped with long interlaminar, intra-laminar, and parallel to fibre cracks. This mechanisms cause the formation of continuous fronds which spread inwards and outwards. Friction and inter/intra-laminar fracture controls the energy absorption of lamina bending mode. In lamina bending crushing modes higher energy absorption is observed in comparison with the other observed modes. This high energy absorption is caused by a larger crush area and therefore a higher potential to absorb energy by bending and frictional effects at the platen/specimen interface (see Fig. 8).

The comparison of force-crush distance behaviour of hybrid composite boxes together with non-hybrid ones from twill-weave and unidirectional CFRP materials are compared in Fig. 9. This comparison shows that hybrid composite boxes absorb higher energy than non-hybrid unidirectional CFRP composite boxes, while in some cases this energy absorption capability is lower than the relevant capability in non-hybrid woven CFRP composite box.

The hybrid boxes with laminate designs of $[T0/U0]_7$ and $[T90/U0]_7$ absorbed the highest crushing energy in all hybrid composite boxes. On the other hand, energy absorption of hybrid boxes with lay-ups of $[T0/U90]_7$ and $[T90/U90]_7$ was almost the same as pure unidirectional CFRP composite box. It should be emphasised that, the weight of all composite boxes is the same *i.e.*, 158 ± 2 gr.

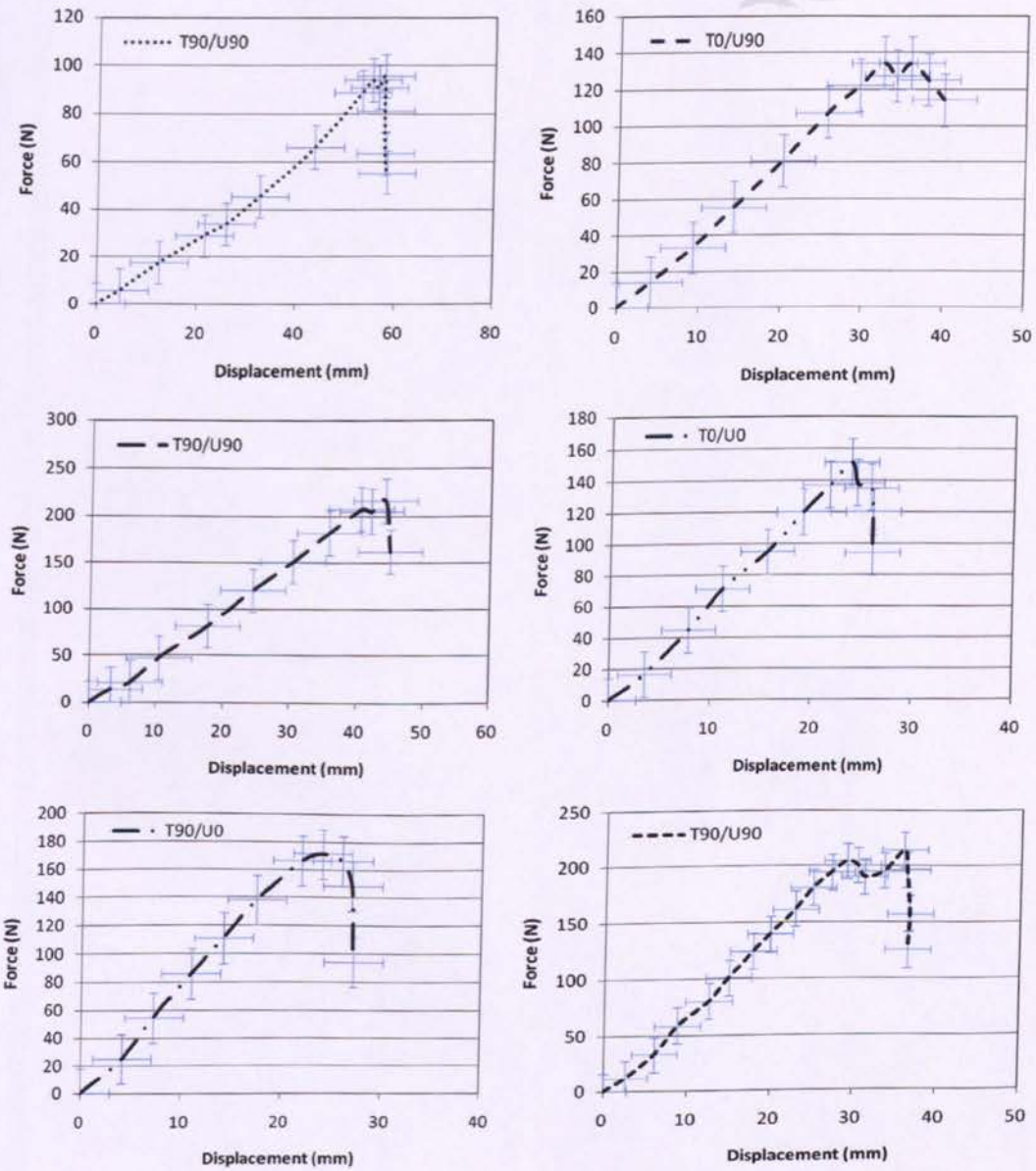

Fig. 5. Force–load line displacement from ELS tests for various mid-plane interfaces.

Please cite this article in press as: Ghasemnejad H et al. Effect of delamination failure in crashworthiness analysis of hybrid composite box structures. J Mater Design (2009), doi:10.1016/j.matdes.2009.09.043

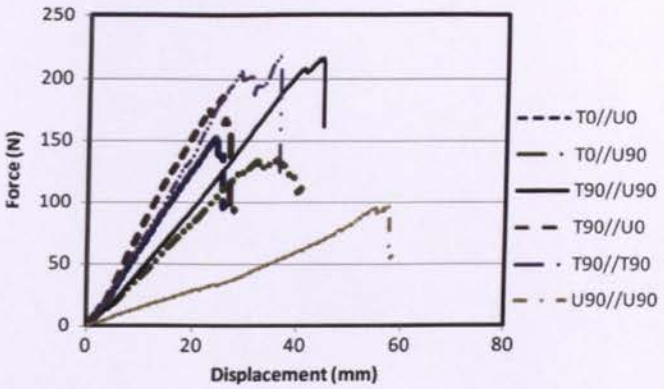

Fig. 6. Comparison of force–load line displacement from ELS tests for various mid-plane interfaces.

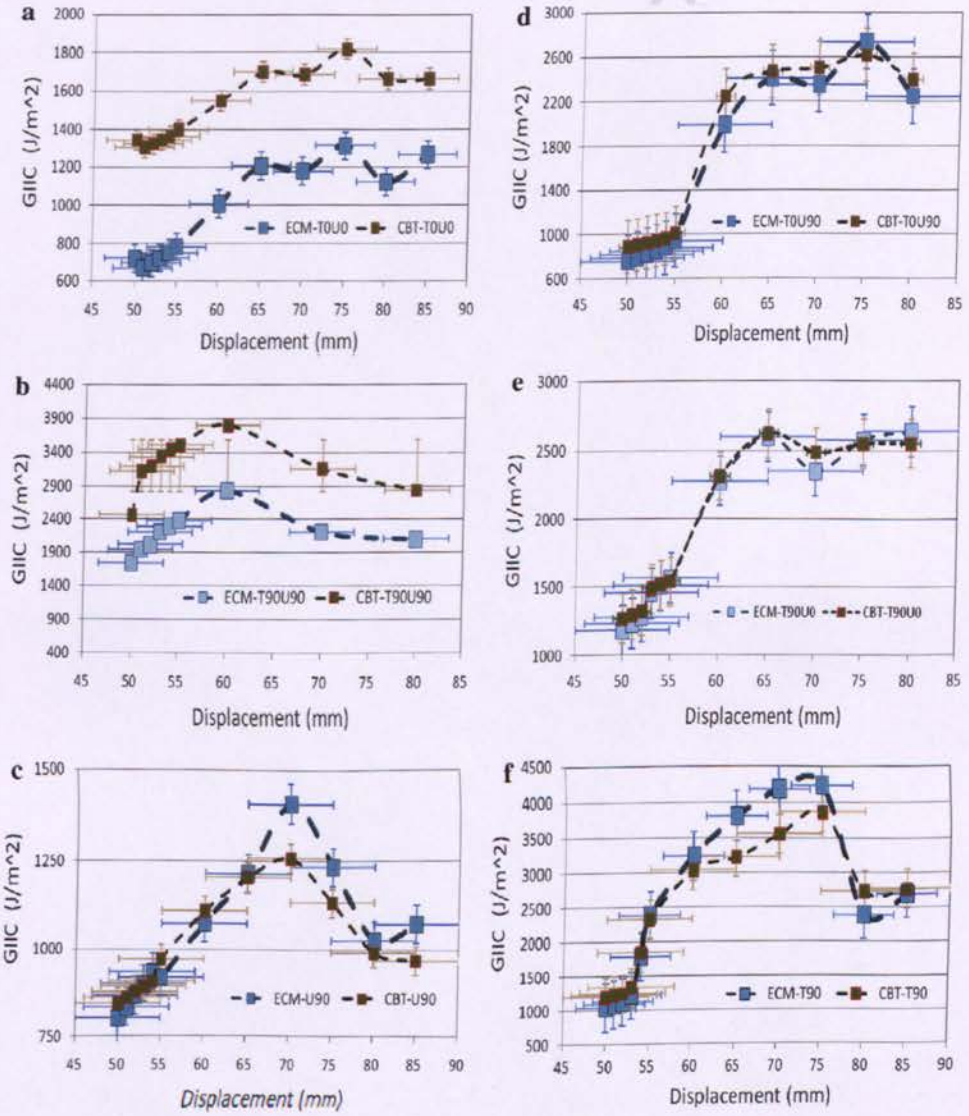

Fig. 7. Resistance curve (*R*-curve) in ELS specimens with various fracture plane interfaces using ECM and CBT methods.

Please cite this article in press as: Ghasemnejad H et al. Effect of delamination failure in crashworthiness analysis of hybrid composite box structures. J Mater Design (2009), doi:10.1016/j.matdes.2009.09.043

Comparing the mean force results of all hybrid boxes to non-hybrid composite box indicates that the mean force for pure composite box made of Unidirectional CFRP is the lowest value (*i.e.*, F_m = 78 kN), while the mean force of hybrid boxes with laminate designs of $[T90/U0]_7$ and $[T0/U0]_7$ are about 120 and 138 kN, respectively. The non-hybrid composite box with laminate design of $[T90]_{10}$ showed higher energy absorption capability in comparison with composite boxes with laminate design of $[T0/U90]_7$, $[T90/U90]_7$ and $[U90]_{16}$.

In all composite boxes the lamina bending crushing mode was observed. In this case the main central interwall crack which is similar to Mode-I crack delamination starts to propagate at four sidewalls of each composite box. This situation causes to shape lamina bundles and resistance against the crushing load. In lamina bending mode, the main central crack causes to shape lamina bundles which has a significant role on absorbing the crushing energy. Earlier it was shown that the fibre orientation at the interface planes has a significant effect on Mode-I interlaminar fracture toughness.

Also in this failure mode the fronds splitting due to lamina bundle bending is similar to interlaminar crack propagation in Mode-II (see Fig. 10).

The G_{IC} and G_{IIC} of initiation are more influential than the G_{IC} and G_{IIC} of propagation in the energy absorption mechanism [6]. The Mode-I and Mode-II initiation values were chosen to quantify the effect of Mode-I and Mode-II fracture toughness on energy absorption of composite box. Regarding the delamination study of hybrid DCB and ELS the variation of SEA versus summation of G_{IC} and G_{IIC} and a root mean square of $\sqrt{G_{IC}^2 + 2G_{IIC}^2}$ were plotted in Fig. 11 to combine the effect of Mode-I and Mode-II interlaminar fracture toughness on the SEA. The values of G_{IIC} were doubled as during the lamina bending two crack propagations in Mode-II were observed in internal and external fronds.

From these relationships it is found the hybrid laminate designs which showed higher fracture toughness in Mode-I and Mode-II delamination tests, will absorb more energy as a composite box in crushing process. However, other mechanisms such as bending

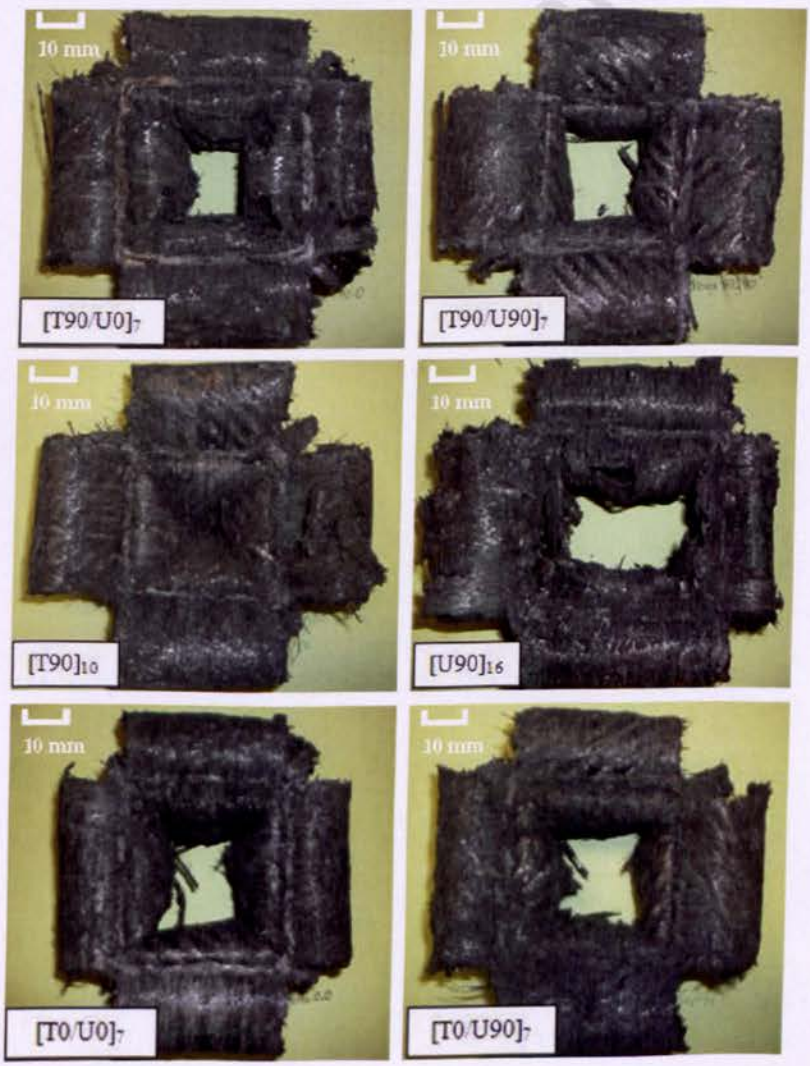

Fig. 8. Lamina bending crushing mode of various lay-ups of hybrid composite box.

Please cite this article in press as: Ghasemnejad H et al. Effect of delamination failure in crashworthiness analysis of hybrid composite box structures. J Mater Design (2009), doi:10.1016/j.matdes.2009.09.043

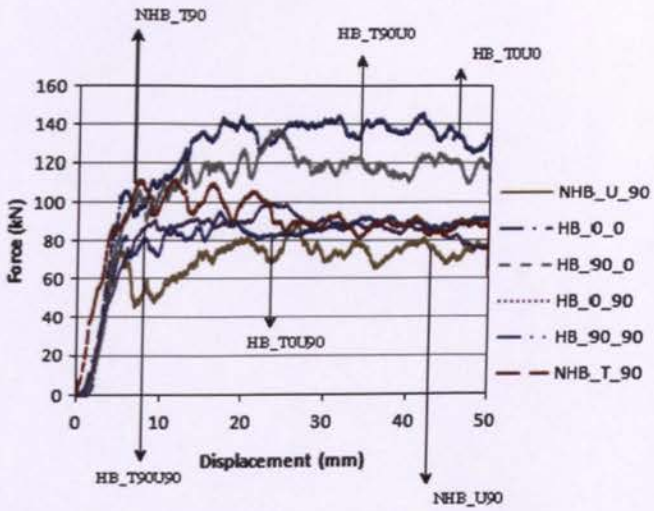

Fig. 9. The comparison of force-crush distance in a hybrid composite crush box for various lay-ups.

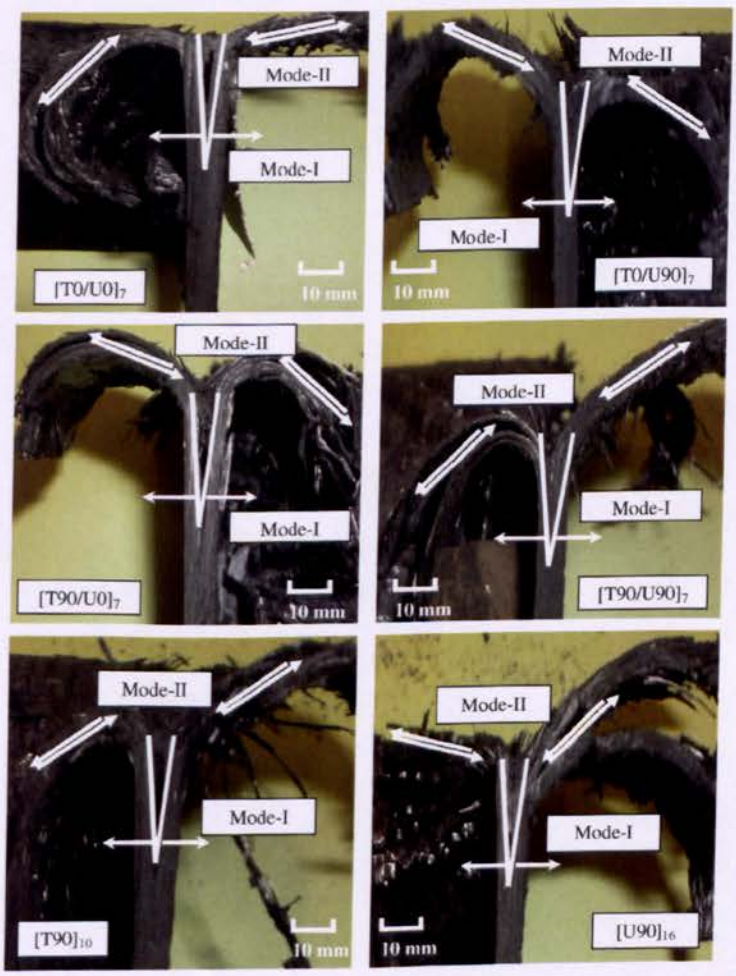

Fig. 10. Mode-I and Mode-II interlaminar crack propagation at the central interwall in all composite boxes.

Please cite this article in press as: Ghasemnejad H et al. Effect of delamination failure in crashworthiness analysis of hybrid composite box structures. J Mater Design (2009), doi:10.1016/j.matdes.2009.09.043

and friction are significantly contributing to energy absorption. For hybrid box with laminate design of $[T0//U0]_7$ these mechanisms are more dominant in absorbing the crushing energy.

As a result, delamination crack growth in Mode-I and Mode-II cannot far outweigh the bending and friction mechanisms in energy absorption. Many other intra-laminar fracture mechanisms such as fibre/matrix debonding, fibre breakage and matrix cracking are also contributing in dissipating the crushing energy.

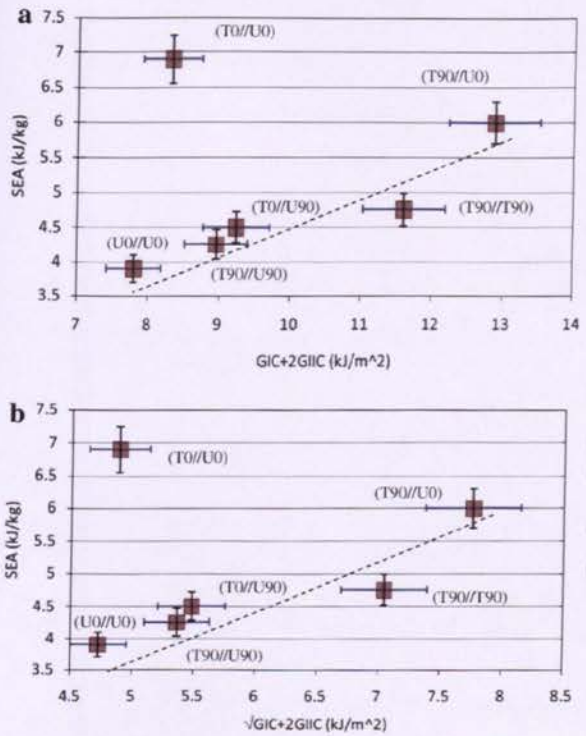

Fig. 11. Variation of SEA versus (a) $G_{IC} + G_{IIC}$ and (b) $\sqrt{G_{IC}^2 + 2G_{IIC}^2}$.

3. Finite element studies

The hybrid composite box was modelled with various lay-ups using finite element software LSDYNA [17]. The size of outer cross section of the composite box was 80 × 80 mm with a thickness of 3 mm. Trigger mechanism was modelled by reducing the thickness of the first row of shell elements at the top of each box.

The hybrid composite box model was based on Belytschko-Lin-Tsay quadrilateral shell elements. This shell element is based on a combined co-rotational and velocity strain. All surfaces of the model were meshed using quadratic shell element and the size of an element was 2.5 × 2.5 mm. The striker was modelled as a rigid block using solid element.

The delamination failure mode needs three-dimensional representation of the constitutive equation and kinematics, and cannot be treated in thin shell theory. The delamination failure mode requires micro-mechanical modelling of the interface between layers and cannot be treated in thin shell theory that deals with stresses at macro levels. Thus, debonding and delamination are usually ignored when thin shell element are used to model failure in composite modelling. In this work the delamination behaviour in Mode-I (discussed previously) was modelled with two layers of shell elements in the box wall. The thickness of each layer is equal to half of the total box wall thickness. The surface-to-surface tiebreak contact was used to model the bonding between the bundles of plies in the box walls. In this contact algorithm, the tiebreak works for nodes which are initially in contact. The failure of the bonding between these bundles takes place when the following failure criterion is fulfilled:

$$\left[\frac{|\sigma_n|}{NFLS}\right]^2 + \left[\frac{|\sigma_S|}{SFLS}\right]^2 \geqslant 1 \qquad (2)$$

where σ_n and σ_s are normal and shear stress, respectively acting on the interface surface while NFLS and SFLS are the normal tensile and shear stresses at failure.

Material model 54 of LS-DYNA was selected to model the damage of hybrid composite box. The Chang–Chang failure criterion which is the modification of the Hashin's failure criterion was chosen for assessing lamina failure. The post-failure conditions in the Material 54 model are somewhat different from the original Chang–Chang equations. In this model four failure modes are categorised. These failure indicators are appointed on total failure for the laminas, where both the strength and

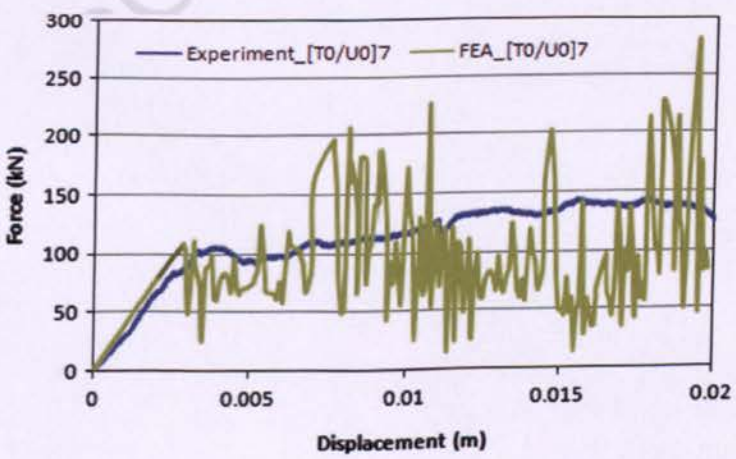

Fig. 12. Comparison of experimental and FE results for hybrid composite box with $[T0/U0]_7$ lay-up.

Please cite this article in press as: Ghasemnejad H et al. Effect of delamination failure in crashworthiness analysis of hybrid composite box structures. J Mater Design (2009), doi:10.1016/j.matdes.2009.09.043

the stiffness are set equal to zero after failure is encountered. In this model as described below all material properties of lamina are checked using the following laws to determine the failure characteristic [23].

- Tensile fibre failure mode: (fibre rupture)

If $\sigma_1 > 0$

$$\text{then } e_f^2 = \left(\frac{\sigma_1}{X_t}\right)^2 + \beta\left(\frac{\sigma_{12}}{\tau_S}\right)^2 - 1 \quad \begin{cases} e_f^2 \geq 0 & \text{failed} \\ e_f^2 < 0 & \text{elastic} \end{cases} \tag{3}$$

where β is a weighting factor for shear term in tensile fibre mode and its range is $0-1$ and σ_1 is stress in the fibre direction and σ_{12} is transverse shearing stress. When lamina failure occurs, all material constants are set to zero.

- Compressive fibre failure mode: (fibre buckling)

If $\sigma_1 < 0$

$$\text{then } e_c^2 = \left(\frac{\sigma_1}{X_c}\right)^2 - 1 \quad \begin{cases} e_c^2 \geq 0 & \text{failed} \\ e_c^2 < 0 & \text{elastic} \end{cases} \tag{4}$$

After lamina failure by fibre buckling E_1, ν_{12} and ν_{21} are set to zero.

- Tensile matrix failure: (matrix cracking under transverse tension and in-plane shear)

If $\sigma_2 > 0$

$$\text{then } e_m^2 = \left(\frac{\sigma_2}{Y_t}\right)^2 + \left(\frac{\sigma_{12}}{\tau_S}\right)^2 - 1 \quad \begin{cases} e_m^2 \geq 0 & \text{failed} \\ e_m^2 < 0 & \text{elastic} \end{cases} \tag{5}$$

where σ_2 is stress in normal to the fibre direction. After lamina failure by matrix cracking, E_2, ν_{21} and G_{12} are set to zero.

- Compressive matrix failure mode: (matrix cracking under transverse compression and in-plane shear)

If $\sigma_2 < 0$

$$\text{then } e_d^2 = \left(\frac{\sigma_2}{2\tau_S}\right)^2 + \left[\left(\frac{Y_c}{2\tau_S}\right)^2 - 1\right]\frac{\sigma_2}{Y_c} + \left(\frac{\sigma_{12}}{\tau_S}\right)^2 - 1 \quad \begin{cases} e_d^2 \geq 0 & \text{failed} \\ e_d^2 < 0 & \text{elastic} \end{cases} \tag{6}$$

In this work the weight factor β which is defined as the radio between shear stress and shear strength is set to 1. The material properties of unidirectional and woven CFRP were obtained from experimental work reported in Table 1.

The contact between the rigid plate and the specimens was modelled using a *nodes impacting surface* with a friction coefficient of 0.35 which was measured experimentally to avoid lateral movements.

To prevent the penetration of the crushed box boundary by its own nodes, a *single surface* contact algorithm without friction was used. To simulate the quasi-static condition, the loading velocity of 1 m/s was applied to the rigid striker. However, the real crushing speed was too slow for the numerical simulation. The explicit time integration method is only conditionally stable, and therefore by using real crushing speed, very small time increment was required. In this study to decrease the time step increment the mass density of all materials was scaled-up by factors of 100 and 1000 with the same applied velocity. In both cases the response of internal energy was very similar with one another and the kinetic energy was negligible in comparison to internal energy. For satisfying quasi-static condition not only the total kinetic energy has to be very small compared to the total internal energy over the period of the crushing process but also the crushing force–displacement response must be independent from the applied velocity.

In Fig. 12 the force-crush distance of hybrid box with laminate design of $[T0//U0]_7$ which was extracted from FEA model is compared with the experimental result. The termination of the FEA was set when the crosshead displacements reach the value of 20 mm. However, the experimental crush distance was about 50 mm. This setting was applied to get the convergence between experimental and FE results in minimum overall calculation time. The difference in mean force and energy absorption between the FEA models and experiment is less than 10%. The comparison between final element deformation from FE and relevant experimental results are presented in Fig. 13.

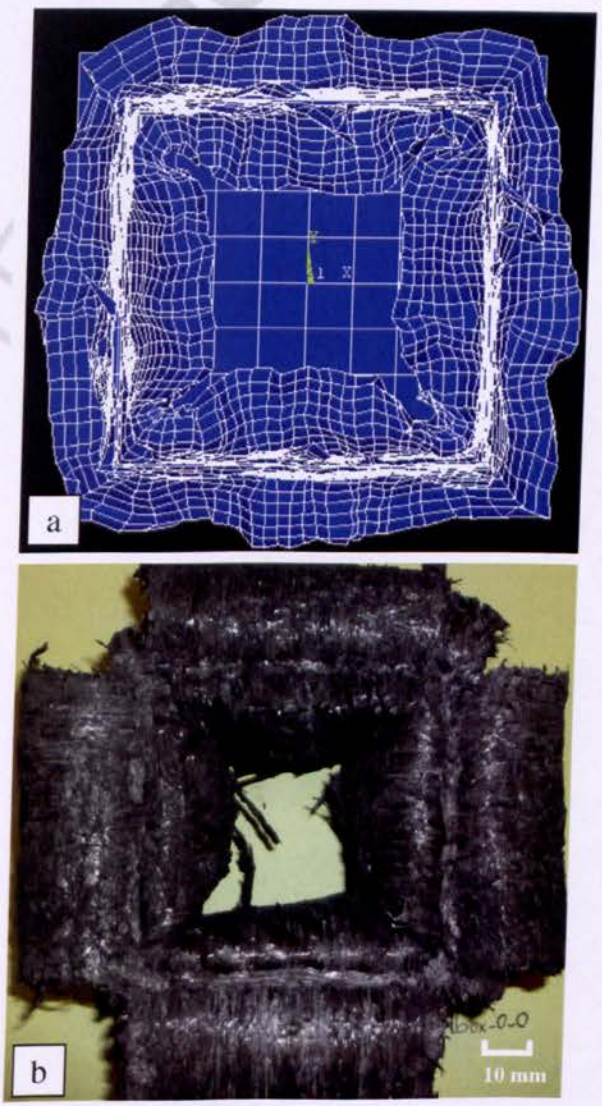

Fig. 13. Comparison of final deformed shape of the hybrid $[T0/U0]_7$ lay-up box in plan view. (a) FEA result and (b) experiment.

Please cite this article in press as: Ghasemnejad H et al. Effect of delamination failure in crashworthiness analysis of hybrid composite box structures. J Mater Design (2009), doi:10.1016/j.matdes.2009.09.043

4. Conclusion

In present work the delamination study in Mode-I and Mode-II was carried out to investigate the effect of delamination crack growth on energy absorption of hybrid composite box structures. In all hybrid composite boxes the lamina bending crushing mode was observed. In this case the main central interwall crack which is similar to Mode-I crack delamination starts to propagate at four sidewalls of each composite box. In lamina bending mode, the main central crack causes to shape lamina bundles which has a significant role on absorbing the crushing energy. Earlier it was shown that the fibre orientation at the interface planes has a significant effect on Mode-I interlaminar fracture toughness. Also in this failure mode the fronds splitting due to lamina bundle bending is similar to interlaminar crack propagation in Mode-II. The G_{IC} and G_{IIC} of initiation are more influential than the G_{IC} and G_{IIC} of propagation in the energy absorption mechanism. The Mode-I and Mode-II initiation values were chosen to quantify the effect of Mode-I and Mode-II fracture toughness on energy absorption of composite box. From this relationship it is found the hybrid laminate designs which showed higher fracture toughness in Mode-I and Mode-II delamination tests, are able to absorb more energy as a composite box in crushing process.

References

[1] Farley G, Jones R. Crushing characteristics of continuous fibre reinforced composite tubes. J Compos Mater 1992;26:37–50.
[2] Mamalis AG, Manolakos DE, Demosthenous GA, Ioannidis MB. Crashworthiness of composite thin-walled structural components. 1st ed. Publisher CRC; 1998.
[3] Ghasemnejad H, Blackman BRK, Hadavinia H, Sudall B. Experimental studies on fracture characterisation and energy absorption of GFRP composite box structure. Compos Struct 2008;88(2):253–61.
[4] Hadavinia H, Ghasemnejad H. Effects of mode-I and mode-II interlaminar fracture toughness on the energy absorption of CFRP twill/weave composite box sections. Compos Struct 2008;89(2):303–14.
[5] Ghasemnejad H, Hadavinia H. Off-axis crashworthiness characteristic of woven glass/epoxy composite box structures. in press.
[6] Savona SC, Hogg PJ. Effect of fracture toughness properties on the crushing of flat composite plates. Compos Sci Technol 2006;66:2317–28.
[7] Warrior NA, Turner TA, Robitaille F, Rudd CD. The effect of interlaminar toughening strategies on the energy absorption of composite tubes. Composites Part A 2004;35:431–7.
[8] Mahdi E, Hamouda ASM, Sen AC. Quasi-static crushing behaviour of hybrid and non-hybrid natural fibre composite solid cones. Compos Struct 2004;66:647–63.
[9] Han H, Taheri F, Pegg N, Lu Y. A numerical study on the axial crushing response of hybrid pultruded and ±45° braided tubes. Compos Struct 2007;80:253–64.
[10] Hufenbach W, Gude M, Ebert C. Hybrid 3D-textile reinforced composites with tailored property profiles for crash and impact applications. 2009;69:1422–6.
[11] BS EN ISO 2747. Glass fibre reinforced plastics-tensile test. London: British Standard Institute; 1998.
[12] BS EN ISO 14129. Fibre reinforced plastics composite-determination of the in-plane shear stress/shear strain response, including the in-plane shear modulus and strength by the ±45 tension test method. London: British Standard Institute; 1998.
[13] ASTM D 3171-99. Standard test method for constituent content of composite materials. West Conshohocken (PA): Annual Book of ASTM Standards; 2002.
[14] BS EN ISO 15024:2001. Fibre-reinforced plastic composites. Determination of mode I interlaminar fracture toughness, G_{IC}, for unidirectional reinforced materials. BSI; 2002.
[15] Davies P, editor. Protocols for interlaminar fracture testing of composites. ESIS-Polymers and Composites Task Group; 1993.
[16] Blackman BRK, Brunner AJ,. Mode I fracture toughness testing of fibre reinforced polymer composites: unidirectional versus cross ply layup. In: Brown MW, de la Rios ER, Miller KJ, editors. ECF-12 Fracture from defects. EMAS; 1998. p. 1471–5.
[17] Hashemi S, Kinloch AJ, Williams JG. Corrections needed in double-cantilever beam tests for assessing the interlaminar failure of fibre-composites. J Mater Sci Lett 1989;8:125–9.
[18] Hashemi S, Kinloch AJ, Williams JG. The analysis of interlaminar fracture in uniaxial fiber–polymer composites. Proc Roy Soc Lond A Mater 1990;427:173–99.
[19] Williams JG. End corrections for orthotropic DCB specimens. Compos Sci Technol 1989;35:367–76.
[20] Russel AJ, Street KN. Factor affecting the interlaminar fracture energy of graphite/epoxy laminates. In: Hayashi T, Kawata K, Umekawa S, editors. Progress in science and engineering of composites. Tokyo: ICCM-IV, ASM International; 1982. p. 279–86.
[21] Moore DR, Pavan A, Williams JG, editors. Fracture mechanics testing methods for polymers, adhesives and composites. ESIS Publication 28. Elsevier Science Ltd.; 2001.
[22] de Moura MFSF, de Morais AB. Equivalent crack based analysis of ENF and ELS tests 2008;75:2584–96.
[23] LS-DYNA user's manual (non-linear dynamic analysis of structures in three-dimensions). Livermore (USA): Livermore Software Technology Corporation; 1997.

Please cite this article in press as: Ghasemnejad H et al. Effect of delamination failure in crashworthiness analysis of hybrid composite box structures. J Mater Design (2009), doi:10.1016/j.matdes.2009.09.043